ADA 268232

DIFFUSION IN ORDERED ALLOYS

DIFFUSION IN ORDERED ALLOYS

A volume in the Electronic, Magnetic, and Photonic
Materials Division Monograph Series
sponsored by the TMS Chemistry and Physics of Materials Committee
and the ASM Atomic Transport Committee.

This symposium was held November 3 and 4, 1992 at the
TMS Annual Meeting in Chicago, Illinois.

This work relates to the Department of the Navy Grant N00014-92-J-1921 issued by the Office of Naval Research. The United States Government has a royalty-free license throughout the world in all copyrightable material contained herein.

Edited by
B. Fultz, R.W. Cahn, and D. Gupta

A Publication of
TMS
Minerals • Metals • Materials

A Publication of The Minerals, Metals & Materials Society
420 Commonwealth Drive
Warrendale, Pennsylvania 15086
(412) 776-9000

Printed in the United States of America
Library of Congress Catalog Number 93-78948
ISBN Number 0-87339-234-3

TMS
Minerals · Metals · Materials

PREFACE

Diffusion in ordered alloys and intermetallic compounds has received little attention in recent years, even though it lies at the heart of many fundamental and practical problems. As opposed to *diffusion in dilute* alloys or solid solutions, atom movements in ordered alloys are affected by the state of order in the material. Conversely, atom movements change the state of order, either locally, leading to large diffusional correlation factors, or globally, leading to order-disorder transformations. Diffusion controls the sequence of compound formation during the intermixing of pure elements, and affects properties such as creep, hydrogen embrittlement, and stability against electromigration. These topics form the scope of this book.

This book originated with the Symposium on Diffusion in Ordered Alloys and Intermetallic Compounds, held during the 1992 fall meeting of The Metals, Minerals, and Materials Society (TMS) in Chicago. The goal of this symposium was to bring together scientists having interests in basic and applied problems ranging from diffusional correlation factors, to effects of diffusion on microstructural evolution and on the properties of ordered alloys. The speakers and the topics were selected to match the scope of the nascent book, and the editors, and authors worked together to ensure broad coverage without overlap. The editors thank the authors for accommodating the needs of the book, and the selfless referees for helping them to do so.

One of us (B.F.) is indebted to Ms. Pamela Albertson for her help in managing manuscripts and communications with authors. The editors gratefully acknowledge the support for the Symposium provided by the Office of Naval Research (S. Fishman) and the Oak Ridge National Laboratory (C. T. Liu).

Brent Fultz
California Institute of Technology

Robert Cahn
Cambridge University

Dave Gupta
IBM Thomas J. Watson Research Center

TABLE OF CONTENTS

ATOM MOVEMENTS

ORDER-DISORDER TRANSFORMATIONS

DIFFUSION COUPLES

DIFFUSION AND PROPERTIES

ATOM MOVEMENTS

Diffusion in Ordered Binary Alloys: A Microscopic Approach

Ching C. Wang and Sheikh A. Akbar

Department of Materials Science and Engineering
The Ohio State University
Columbus, Ohio 43210 USA

Abstract

Diffusion in ordered binary alloys has been treated using the pair-approximation of the Path Probability Method (PPM) based on an atomistic model. The effect of the atomic interaction on the ordering behavior and its influence on transport properties have been clarified. Compositional dependences of both the intrinsic diffusion and interdiffusion coefficients, correlation factor, and thermodynamic factor agree very well with results from Monte Carlo simulations. The calculated properties also show qualitative agreement with the experimental data on diffusivity, activity, and creep in NiAl system.

Diffusion in Ordered Alloys
Edited by B. Fultz, R.W. Cahn, and D. Gupta
The Minerals, Metals & Materials Society, 1993

I. Introduction

Diffusion in ordered alloys recently has been the subject of considerable interest due largely to the increasing demand for the understanding of high temperature behavior of the ordered intermetallic compounds. In comparison with the disordered solid solution alloys, theoretical treatment of diffusion in ordered alloys are much more complicated because of the atomic interactions between the diffusing species. In other words, atomic jump in an ordered alloy strongly depends on the nature of ordering in the immediate environment at the microscopic level. Considering diffusion via the vacancy mechanism, when diffusing atoms exchange with vacancies, they tend to leave behind traces of disordered region and locally deviate from thermodynamic equilibrium. In order to maintain thermodynamic equilibrium, the migration of atoms must occur in a way or sequence to compensate or minimize the increase of energy during the diffusion. As a result, diffusion in ordered alloys is strongly correlated; the degree of correlation (or order) is a function of composition and temperature, and this considerably complicates the theoretical treatment of diffusion.

Diffusion in ordered alloys tends to be much slower than in disordered alloys, and is often characterized with the existence of a sharp minimum in the diffusion coefficient versus composition curve and a sharp maximum in the activation energy versus composition curve around the stoichiometric composition. Slow rates of diffusion bring with them the associated advantage of improved microstructural stability and improved creep strength at elevated temperatures, especially when creep is controlled by a diffusion mechanism. Apart from its technical importance, this problem of diffusion is also quite challenging theoretically. In the past two decades, the theoretical treatment of diffusion in ordered alloys has mostly been developed as an extension to Manning's random alloy model in the framework of the nearest-neighbor pair-wise interactions. Bakker [1] and Stolwijk [2] have extended Manning's random alloy model to include long- and short-range order and their results show good agreement with the numerical simulations by the Monte Carlo method. However, these approaches do not provide an analytical expression for the calculation of the thermodynamic state of order as a function of composition and temperature. In the treatment of diffusion in ordered alloys, one requires firstly to construct an exact analytical expression for the change of the free energy of the system to be minimized, and secondly to derive the Onsager equation. A combined approach based on the Path Probability Method [3] and the Cluster Variation Method [4] offers a unique opportunity to treat these problems [5,6].

The Cluster Variation Method (CVM), a static version of the Path Probability Method (PPM), can calculate the thermodynamic equilibrium state of order as a function of temperature and composition. The PPM, on the other hand, can derive the Onsager equation for diffusion analytically based on atomistic models [7,8]. Such analytical expressions are quite helpful in identifying measurable quantities (e.g. diffusion coefficient, ionic conductivity, etc.) in terms of fundamental microscopic parameters such as jump frequencies and interatomic interactions. If sufficient information is available on these quantities, specific predictions can be made or, conversely, diffusion experiments can be used to evaluate these atomistic parameters for which there is no straightforward calculation or measurement. It has recently been demonstrated [9] that by fitting the PPM equations to demixing experiments in oxide solid solutions, it is possible to self-consistently evaluate microscopic parameters.

Although some limitations have been found to appear in the original formalism of the PPM as applied to transport problems where the motion of individual particles is at stake (e.g., the calculation of the correlation factor), significant improvements have recently been made by changing some of the averaging processes. A full account of this problem can be found in references [5,10]. Here, for simplicity, the original formalism will be used. The objective of this paper is to show how the PPM can be used to treat diffusion problems in ordered alloys using the well established pair-approximation. The effect of atomic interactions on the ordering behavior and its influence on transport properties will be illustrated and compared with the existing Monte Carlo simulations [11] and experimental results in ordered intermetallic compounds such as NiAl. Compositional dependences of intrinsic diffusion and interdiffusion coefficients will be illustrated and their implication on the high temperature creep behavior of NiAl will be addressed. Also, an attempt is made to deal with diffusion in some ordered alloys where a maximum in diffusivity versus composition curve is observed. This paper is primarily an extension of our recent work on diffusion in ordered alloys and intermetallic compounds [6], and some results are directly taken from that reference.

II. Theoretical Background

A. Equilibrium distribution of atoms

In this section, relevant results of the CVM [4] are briefly reviewed, as the equilibrium treatment of the CVM forms the basis for the PPM calculation of transport properties. The role of the Cluster Variation Method is to calculate the equilibrium state or distribution of atoms of a system using the variation principle common to other equilibrium statistical mechanics. The equilibrium state is represented by the most probable state specified by the state variables $\{a\}$ which make the free energy $F\{a\} = E\{a\} - TS\{a\}$, a minimum, or the partition function $Q\{a\} = \exp[-F\{a\}/kT]$, a maximum. The choice of the state variables $\{a\}$ or the calculation of energy $E\{a\}$, and the evaluation of entropy $S\{a\}$ are the basic ingredients of the CVM. In its general form, the CVM represents a hierarchy of approximations, and the degree of approximation can be systematically improved.

In a binary alloy AB, for example, if atoms interact only with their nearest neighbors, the total energy E{a} of the system can be given by specifying the number of atomic pairs such as A-A, A-B and B-B. The entropy S{a} can be evaluated by counting the number of ways of rearranging these fixed number of pairs on a given lattice (details can be found in Ref. 4). When these pairs are taken as state variables, the treatment is called the pair-approximation (equivalent to the Bethe-approximation).

Based on the pair-approximation of the CVM, the variables required to specify a state are x_i's, which indicate the probability of finding the *i*th species on a lattice site, and y_{ij}'s, which represent the equilibrium values of the probability of finding i-j pairs. For a binary alloy, the state variables fulfill the following relations:

$$1 = \sum_i x_i \tag{1}$$

$$x_i = \sum_j y_{ij} \tag{2}$$

where, i and j = A, B, and *v*, the vacancy. With the assumption that interactions exist only between nearest neighbors, these state variables for a given composition and temperature are determined by the pairwise interaction energy ε_{ij} ($\varepsilon_{ij} > 0$ is taken as attractive). In other words, the state variables for a given composition are determined as a function of temperature in terms of ε_{ij} under the equilibrium condition. For an ordered alloy, the state variable y_{ij}'s can be expressed as:

$$y_{ij} = q_i q_j e^{s_i - s_j} K_{ij}^{-1} \tag{3a}$$

$$K_{ij} = e^{-\beta \varepsilon_{ij}} \tag{3b}$$

where, q_i and s_i are determined by a set of simultaneous equations

$$x_i = q_i \sum_j q_j K_{ij}^{-1} \tag{4a}$$

$$s_i = \frac{2\omega}{2\omega - 1} \ln \frac{\sum_j q_j e^{s_i - s_j} K_{ij}^{-1}}{\sum_j q_j e^{s_j - s_i} K_{ji}^{-1}} \tag{4b}$$

These variables represent the short-range and long-range order, respectively.

Instead of using values of individual ε_{ij}, it is more convenient to introduce an effective interaction energy parameter ε of the form:

$$4\varepsilon = 2\varepsilon_{AB} - (\varepsilon_{AA} + \varepsilon_{BB}) \tag{5}$$

Although interactions involved with vacancies are often assumed zero ($\varepsilon_{AV} = \varepsilon_{BV} = \varepsilon_{VV} = 0$), these can also be treated indirectly through differences among ε_{ij}'s as defined in Eq. (5). It is important to note that the value of ε can be positive or negative. In the case of binary solid solution, negative in ε corresponds to positive deviation from the ideal solution in terms of thermodynamic activity, and vice versa. In the present paper where the case with positive value of ε is considered, the effective interaction energy parameter ε, sometime referred to as "ordering energy", also gives the measure of the critical temperature T_c of the order-disorder transformation. In the pair-approximation of the CVM, T_c at the stoichiometric composition with a negligible vacancy concentration is given in terms of the lattice coordination number (2ω) as [12]

$$2\varepsilon/kT_c = \ln[\omega/(\omega - 1)] \tag{6}$$

Equation (6) serves to normalize the value of ε with respect to kT_c. In a bcc lattice with $2\omega = 8$, for example, ε/kT_c has a value of 0.144.

B. Atomistic calculation of transport properties

The essence of an atomistic theory of diffusion within the linear approximation of the Onsager formalism is to derive the flux equations in a multicomponent system. For a binary alloy AB, at uniform temperature, the Onsager equations derived by the PPM can be expressed as

$$J_A = - L_{AA}\,\alpha'_A - L_{AB}\alpha'_B \tag{7a}$$

$$J_B = - L_{BA}\alpha'_A - L_{BB}\alpha'_B \tag{7b}$$

Here, J_A and J_B represent the fluxes of A and B atoms respectively, and α'_i (i = A, B) represents the generalized chemical potential gradient of the *i*th species ($\alpha_i = \beta\mu_i$, where $\beta = 1/kT$ and μ_i is the chemical potential).

Based on the PPM, the Onsager matrix coefficients L_{ij}'s can be expressed in terms of two parameters: the static and kinetic parameters, i.e., the interatomic interactions (ε_{ij}), and the jump frequencies of constituents (w_i). For diffusion by the vacancy mechanism, L_{ij}'s are derived as

$$L_{AA} = w_A y_{AV} W_A f_{AA} \tag{8a}$$

$$L_{AB} = w_A y_{AV} W_A f_{AB} \tag{8b}$$

$$L_{BA} = w_B y_{BV} W_B f_{BA} \tag{8c}$$

$$L_{BB} = w_B y_{BV} W_B f_{BB} \tag{8d}$$

where

$$w_i = \theta \exp(-\beta u_i) \tag{9}$$

$$W_i = \left[\frac{\sum_j y_{ij} e^{-\beta e_{ij}}}{x_i} \right]^{2\omega-1} \tag{10}$$

As explained in the previous section, the variables y_{ij}'s represent the equilibrium values of the probability of finding i-j pairs, obtained by the pair-approximation of the CVM, and, hence, y_{iv} represents the probability of finding a vacancy near an *i*th atom. This term is conveniently called the *vacancy availability factor* (VAF). Here, θ is the attempt frequency and u_i is the activation energy of motion. It is obvious that while w_i is the bare jump frequency, W_i represents the effect of the surroundings on the jumping atom and is called the *bond-breaking factor* (BBF).

The quantities f_{ij}'s, which are directly related to the appropriate L_{ij} in Eq. (8), constitute the so-called vacancy-wind effect or the physical correlation factor f_i^I (for random-walk motion, $f_i^I = 1$) defined as:

$$f_A^I = f_{AA} - f_{AB} C_A / C_B \tag{11a}$$

$$f_B^I = f_{BB} - f_{BA} C_B / C_A \tag{11b}$$

where, concentration C_i is defined as:

$$C_i = [\, x_{i(1)} + x_{i(2)}]/2 \tag{11c}$$

Here, $x_{i(1)}$ and $x_{i(2)}$ are the values of x_i on the two sublattices of the ordered system.

In general, although f_{ii} and f_{ij} ($i \neq j$) can be directly obtained by the PPM [6,13], the physical interpretation of these functions are rather complicated. In the limit of impurity diffusion, say, A in the host of B, f_{AA} refers to the impurity (or tracer) correlation factor. At the other limit of self diffusion (in pure crystal), f_{AA} is unity if the vacancy concentration is very low. f_{ij} ($i \neq j$), which is related to the cross terms of the Onsager matrix coefficients defined in Eq. (8), reflects the interference of the flux of the *j* atoms on the flux of the *i* atoms. This interference arises indirectly from the competition of atoms for the vacancies.

Equations (8 - 10) show precisely how the transport of an atom depends on the availability of a vacancy in its neighborhood, and how the motion is influenced by the surrounding atoms. It should be noted that for an ordered system with two distinct sublattices, bond-breaking factors can be introduced for each sublattice. However, the product of VAF and BBF in the system of Eq. (8) makes the Onsager coefficients invariant of the sublattice.

The Onsager matrix coefficient, L_{ij} can be related to the more familiar intrinsic diffusion coefficients as

$$D_{IA} = L_{AA}/C_A - L_{AB}/C_B \tag{12a}$$

$$D_{IB} = L_{BB}/C_B - L_{BA}/C_A \tag{12b}$$

From Eqs. (8) and (12), the intrinsic diffusion coefficient, for example, D_{IA}, can be expressed as [14]

$$D_{IA} = D_A f^I_A, \tag{13}$$

where, D_A is a hypothetical (or calculated) diffusion coefficient of an A atom which is making random walk.

It is important to note that D_{IA} and D_{IB} (or, more precisely, D_A and D_B) implicitly include the thermodynamic factor commonly recognized in the context of chemical diffusion in non-ideal multicomponent systems. Therefore, sometimes it is convenient to express D_{Ii} in the following form:

$$D_{Ii} = D^0_i \, \Phi \, f^I_i \tag{14}$$

where Φ accounts for deviation of the system from ideal solution behavior ($\Phi = 1$ for an ideal solution). The quantity D^0_i is the intrinsic diffusion coefficient of species *i* in the ideal solution. This kind of expression is especially helpful in the analysis of problem of diffusion in multicomponent systems.

The thermodynamic factor Φ is usually defined as

$$\Phi = \beta x_i \left[\partial \mu_i / \partial x_i\right] \tag{15}$$

Using the relationship, $C_A + C_B \cong 1$, equation (15) can be rewritten as [11]

$$\Phi = \beta C_A C_B \left[\partial(\mu_A - \mu_B)/\partial C_A\right] \tag{16}$$

which is more convenient for numerical differentiation. The chemical potential of *i*th species for an ordered alloy with negligible vacancies, can be derived by the CVM and is expressed as [15]

$$\mu_i = \beta\,(2\omega \ln q_i - 0.5(2\omega - 1) \ln [x_{i(1)} x_{i(2)}]) \tag{17}$$

Thus, the thermodynamic factor Φ can be calculated from equation (16) by determining μ_A-μ_B as a function of composition and performing a numerical differentiation. Furthermore, by taking the pure component as the standard state, the activity as a function of composition within the ordered phase region can be calculated by

$$a_i = \exp\,[\beta\,(\mu_i - \mu_{oi})] \tag{18}$$

where μ_{oi} is the chemical potential of pure *i*.

The PPM calculations will be divided into two parts for two different types of lattice. First, the simple cubic lattice will be employed so that our results can be directly compared with those obtained by Monte Carlo simulations. Then, in order to compare with the experimental results of diffusion coefficients in NiAl (CsCl-type bcc structure), the calculations will be extended to the bcc lattice. In both cases, interactions only between nearest neighbors will be assumed and designated as ε_{AA}, ε_{BB}, ε_{AB}. Further, interactions involved with vacancies *v* are assumed to be zero.

In the treatment of diffusion, in which the relative easiness of breaking bonds with its nearest neighbor atoms is to be considered, the difference of ε_{AA} and ε_{BB} has to be taken into account. Therefore, an extra parameter U is defined as

$$U = (\varepsilon_{AA} - \varepsilon_{BB})/(4\varepsilon) \tag{19}$$

This parameter is a measure of whether A-A or B-B bond is easier to break, and can be estimated from the energy of formation of vacancies.

From equations (8) and (12), the intrinsic diffusion coefficients can be expressed in the following form:

$$D_{IA} = \hat{w}_A y_{AV} [f_{AA} - C_A f_{AB}/C_B]/C_A \tag{20a}$$

$$D_{IB} = \hat{w}_B y_{BV} [f_{BB} - C_B f_{BA}/C_A]/C_B \tag{20b}$$

where

$$\hat{w}_i = w_i W_i \tag{20c}$$

The vacancy availability factors y_{AV} and y_{BV} are functions of temperature and composition, and can be evaluated by the CVM. However, in order not to introduce extra complications and conform to the approach taken by Zhang et al. [11] in their Monte Carlo computations, normalized intrinsic diffusion coefficients are defined as

$$\overline{D}_{IA} = D_{IA}/[C_V w_B] \quad (21a)$$

$$\overline{D}_{IB} = D_{IB}/[C_V w_B] \quad (21b)$$

and are called intrinsic diffusion coefficients per unit vacancy concentration. The interdiffusion coefficient of Darken's form [16], $\tilde{D}$, can be calculated directly from $\overline{D}_{IA}$ and $\overline{D}_{IB}$:

$$\tilde{D} = C_B \overline{D}_{IA} + C_A \overline{D}_{IB} \quad (22)$$

and similar to Eq. (14), the interdiffusion coefficient can be expressed in terms of the thermodynamic and correlation factors in the following form

$$\tilde{D} = \left(C_B \overline{D}^{o}_{A} f^{I}_{A} + C_A \overline{D}^{o}_{B} f^{I}_{B} \right) \Phi \quad (23)$$

For a given set of ε, U and temperature (or a normalized temperature in terms of ε/kT_C), both the intrinsic diffusion and interdiffusion coefficients can be calculated as a function of composition. It is important to note that the composition-dependence of the diffusivity in an ordered alloy is decided by the competition between the correlation and the thermodynamic factors [Eqs. (14) and (23)].

III. Results and Discussion

A. Comparison Between the PPM and Monte Carlo Simulations

As in the case of Monte Carlo (MC) simulations of Zhang et al. [11], the first part of our calculation was also carried out for a simple cubic (sc) lattice with U = 0, i.e., $\varepsilon_{AA} = \varepsilon_{BB}$. From equation (6), the normalized critical temperature for the sc lattice is calculated to be $\varepsilon/kT_C = 0.203$. Note that in comparison with Zhang et al.[11], our definition of the ordering energy differs from theirs by a factor of 4. Being symmetrical, only the results for the A component are shown here; those for the B component can be obtained simply by substituting B for A in the figures.

Figure 1a shows the composition dependence of the thermodynamic factor Φ at various values of ε/kT. Note that lower temperature corresponds to higher ε/kT. For $\varepsilon/kT \geq 0.203$, the ordered phase appears with the minima in Φ, corresponding to the order-disorder phase boundaries, and with the peaks or maxima at the stoichiometric composition. These results agree very well with that of the MC simulation [11], as shown in Fig. 1b.

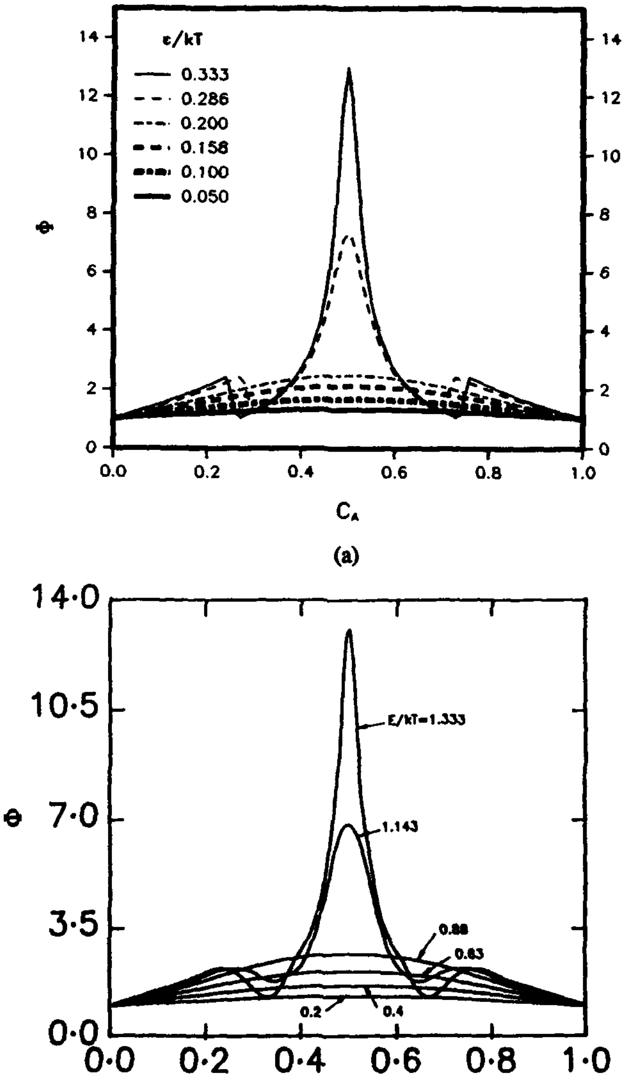

(b)

Fig. 1. Composition-dependence of the thermodynamic factor Φ at various values of ε/kT calculated by (a) the pair-approximation of the CVM and (b) Monte Carlo simulation[11].

Figure 2a shows the results of the intrinsic diffusion coefficient $\bar{D}_{IA}$ at various values of ε/kT as defined in equation (21). For ε/kT greater than 0.203, a minimum develops in the ordered region as expected. Again, these results agree very well with that of MC simulation, as shown in Fig. 2b. There are minor differences, though, especially in the region where C_A approaches 1.

With the results of $\overline{D}_{IA}$ and $\overline{D}_{IB}$, the interdiffusion coefficient $\tilde{D}$ can be obtained using Eq. (22), and the results are shown in Fig. 3a. Similar results obtained by MC simulation are shown in Fig. 3b. Despite the maximum in the thermodynamic factor, a minimum in $\tilde{D}$ develops in the ordered region, suggesting that other factors may dominate in the diffusion process. Figure 4 shows the composition-dependence of the physical correlation factor f_A^I at various values of ε/kT. In all cases, the decrease of f_A^I to a minimum indicates the increase in ordering as C_A approaching the stoichiometric composition, or, in other words, the tendency of atoms to reverse jumps becomes stronger in order to preserve local order. For $\varepsilon/kT > 0.203$, a deep cusp manifests the so called physical correlation effects, which is reflected in the slowing down of atomic migration due to preservation of local order as can be seen in Figs. 3. The effect of correlation factor, therefore, overshadows that of thermodynamic factor and, hence, dominates the interdiffusion processes in the ordered region.

B. Comparison with the Experimental Data on NiAl System

It is known that NiAl is an ordered compound with CsCl-type structure and exits over a wide range of compositions [17]. The stoichiometric alloy retains its structure up to its melting point of 1638°C. From equation (6), the ordering energy ε can be estimated to be 0.55 kcal/mol. For simplicity, the ratio of bare jump frequencies (w_{Ni}/w_{Al}) is set to be unity. The calculations were carried out by choosing different values of $\varepsilon_{Ni-Ni}/\varepsilon_{Al-Al}$ or U. Here, the ratio of $\varepsilon_{Ni-Ni}/\varepsilon_{Al-Al}$ were estimated to be 1.5 from the cohesive energies of Ni and Al [18]. It should be noted that our fitting of parameters or curves *are not meant to be exact*, since the present model does not take into account the variation of lattice parameters and the vacancy concentration (therefore, interatomic interactions) as a function of composition. Also, the pair-approximation of the CVM does not accurately predict phase boundaries in intermetallic alloys; it is necessary to use higher-order approximations.

Figure 5 shows the comparison of the calculated activity of Ni with the experimental data for NiAl at 1000°C, in the range of $C_{Ni} = 0.4 - 0.6$. The thin-solid curve represents the activity of Ni obtained by Hanneman and Seybolt [19], converted from experimental activity of Al [20] by Gibbs-Duhem integrations. In light of the fact that this calculation is carried out using the pair-approximation with nearest neighbor interactions, the agreement is quite satisfactory. For the purpose of comparison, activity of Ni calculated with $\varepsilon = 0.80$

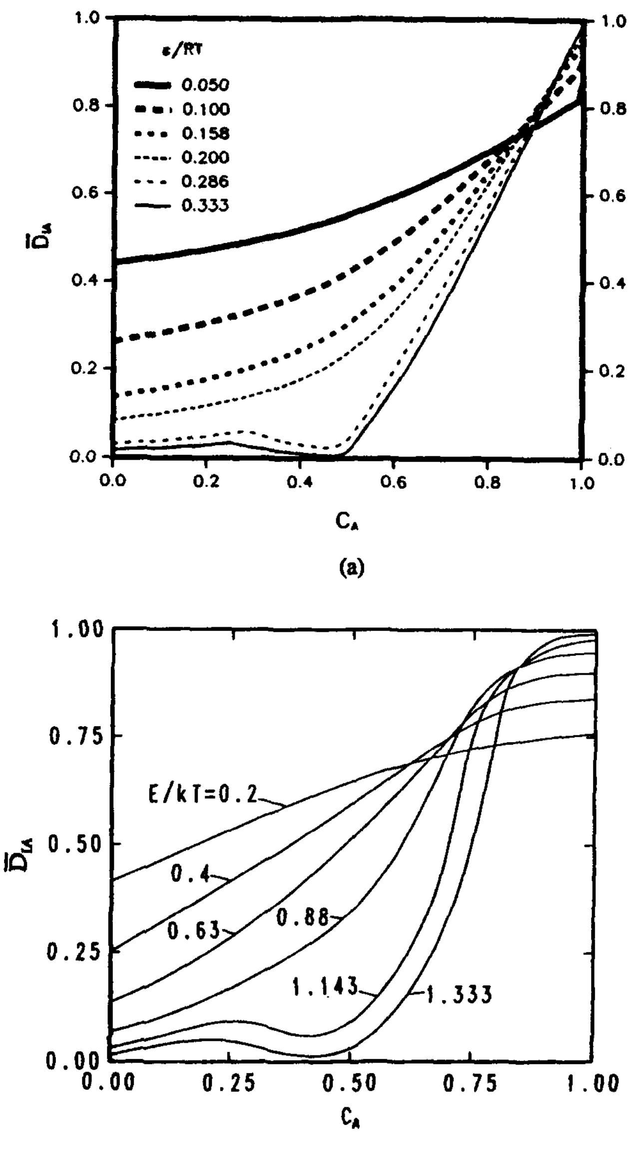

(a)

(b)

Fig. 2. Composition-dependence of the intrinsic diffusion coefficient $\overline{D}_{IA}$ at various ε/kT calculated by (a) the PPM and (b) Monte Carlo simulation [11].

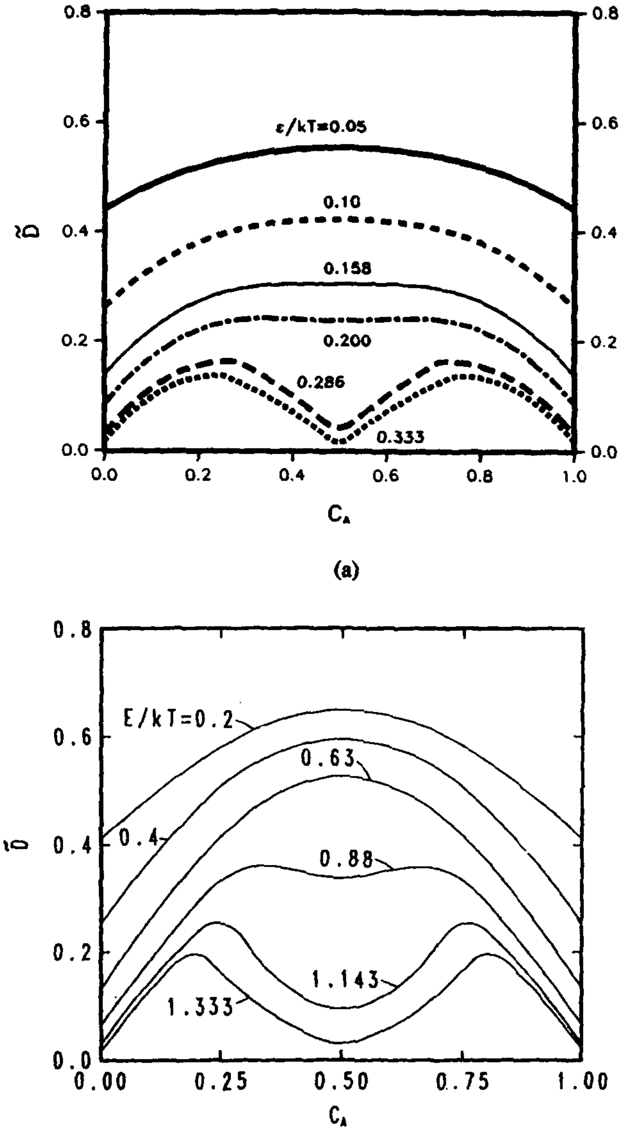

(a)

(b)

Fig. 3. Composition-dependence of the interdiffusion coefficient $\tilde{D}$ at various values of ε/kT calculated by (a) the PPM and (b) Monte Carlo simulation [11].

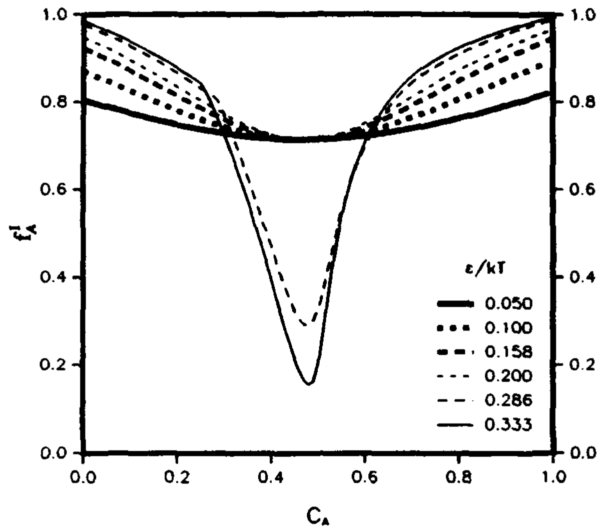

Fig. 4. Composition-dependence of the physical correlation factor f_A^I at various values of ε/kT calculated by the PPM.

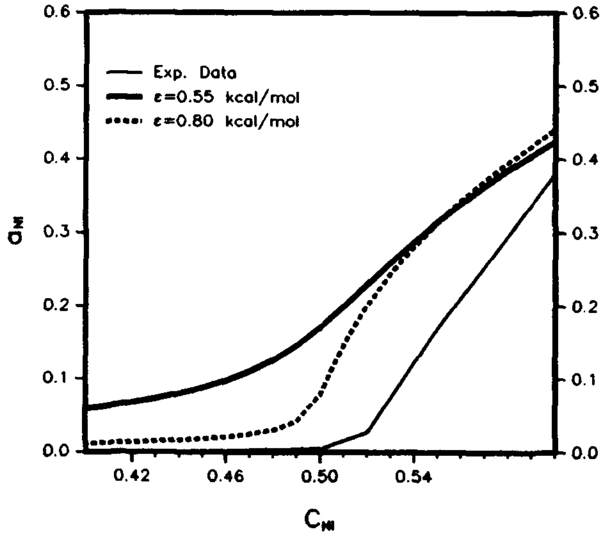

Fig. 5. Comparison of the calculated activity of Ni with the experimental data for NiAl at 1000°C in the range of C_{Ni} = 0.4 - 0.6 [15]. The thick-solid line is calculated with ε = 0.55 kcal/mol, while the dotted line with ε = 0.80 kcal/mol.

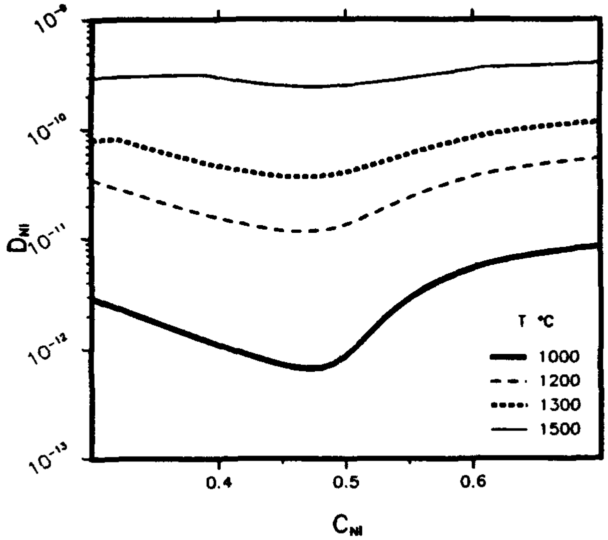

Fig. 6. Composition-dependence of the intrinsic diffusion coefficient of Ni, D_{Ni}, in NiAl at various temperatures, calculated with U = 0.73.

kcal/mol is also plotted as the dotted curve. It can be seen that the agreement with experimental data is better for higher ε, suggesting that the actual ordering energy may be higher than that estimated by the pair-approximation [Eq. (6)].

Figure 6 shows the composition-dependence of the intrinsic diffusion coefficient of Ni calculated with U = 0.73 at various temperatures as indicated. Note that minima are observed near the stoichiometric composition for all temperatures below 1638°C, which qualitatively agree with experimental results [21] shown in Fig. 7. It should also be noted that the minimum occurred is not centered at the stoichiometric composition, a behavior also observed in the ordered AuCd [22]. Traditionally, the interpretation of this off-stoichiometric behavior is based on the argument of the change of defect structure across the stoichiometric composition. Our calculations suggest that both the magnitude and the sign of U play a significant role in determining the location of the minimum. In our calculations, the positive value of U means that vacancies tend to distribute in the Ni-rich region which makes the minimum off-stoichiometric.

An important implication of the present results is the high temperature creep behavior of ordered alloys where diffusion mechanism is operative. It has been found in NiAl that the activation energy for steady-state creep as a function of composition exhibits a maximum at

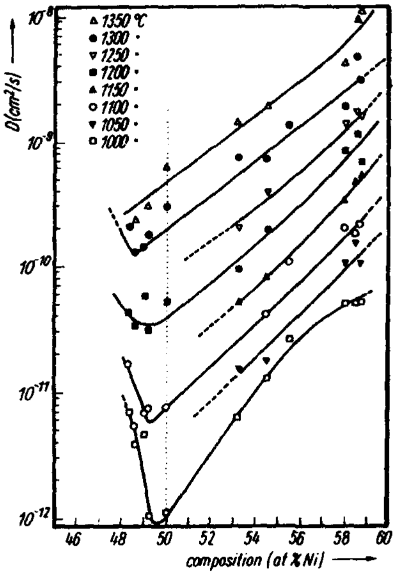

Fig. 7.
Composition-dependence of the intrinsic diffusion coefficient of Ni measured at various temperatures [20].

elevated temperatures [23,24]. Also, Shankar and Siegle [25] have found that the activation energy for interdiffusion shows similar composition-dependence, a behavior predicted by both the PPM and Monte Carlo simulation. The similarity between the composition-dependence of the activation energy for diffusion and steady-state creep at high temperatures implies the diffusional nature of the high-temperature creep in the ordered NiAl.

In some ordered binary alloys, a maximum in the diffusion coefficient vs. composition curve is exhibited. In Ti-Al system, for example, interdiffusion coefficient vs. composition curves exhibit maxima in both the Ti_3Al and TiAl phases [26]. According to Eq. (23), it is suspected that, unlike in the case of NiAl where f_i^I dominates the diffusion process, Φ may become dominant in systems such as Ti-Al. In order to verify this latter conjecture, further calculations in composition-dependence of the interdiffusion coefficient was carried out in a hypothetical ordered alloy AB with bcc-type lattice at various values of Θ, as shown in Fig.8. Note that only the contribution of Θ was considered in the calculation because: (i) composition-dependence of the thermodynamic factor Φ in an ordered alloy always exhibit a maximum, and (ii) Φ is fixed by ε for a given temperature and is independent of Θ. It can be seen that minima in composition-dependence of the diffusion coefficient persist for Θ in the range of 10^{-3} and 10^{3}. In other words, based on the present model, it is suggested that significant difference in jump frequencies of the constituent components may not result in a maximum in composition-dependence of diffusion coefficient observed in some ordered

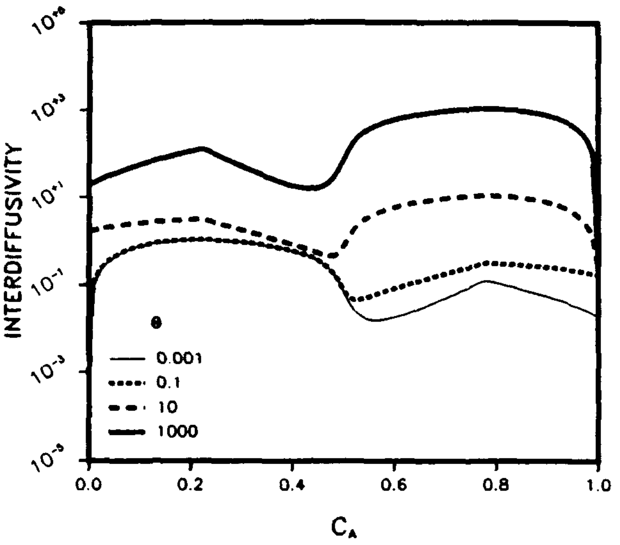

Fig. 8. Composition-dependence of the interdiffusion coefficient for a binary alloy AB with an ordered bcc lattice calculated at a normalized temperature $\varepsilon/kT = 0.4$ ($\varepsilon/kT_C = 0.144$) at various values of Θ.

alloys. The enhanced diffusion around the stoichiometric composition may arise from some other factors, which affect the thermodynamic and/or correlation factors. Note that since in the present model interactions involved with vacancies are assumed zero ($\varepsilon_{AV} = \varepsilon_{BV} = \varepsilon_{VV} = 0$), further work on the diffusion in ordered alloys may need to include non-zero ε_{iV}. At this stage, however, our conclusion is that either there exist some other factors which affect the thermodynamic and/or correlation factors, or the pair-approximation of the PPM is not capable of predicting this behavior.

IV. Conclusion

The treatment of diffusion in ordered alloys based on the Path Probability Method gives insights at an atomic level. The atomic interaction is shown to have significant influence on transport properties and its derived phenomena such as the high-temperature creep in ordered alloys. Although an exact quantitative fitting or assessment of parameters is not given in the present approach, the comparisons with the Monte Carlo simulation and experimental results serve to show how the PPM can be used to deal with the complex phenomenon of diffusion in ordered alloys. The composition-dependence of the diffusivity is shown to be decided by the competition between the thermodynamic and the correlation factors. Within the pair-approximation of the PPM, such a competition leads to a minimum behavior in the diffusivity in agreement with some binary alloys, but fails to predict the reverse behavior observed in others.

References

1. H. Bakker, Philos. Mag. **A40**, 525 (1979).
2. N.A. Stolwijk, Phys. Stat. Solidi. B, **105**, 223 (1981).
3. R. Kikuchi, Prog. Theor. Phys. (Kyoto), Suppl. No. **35**, 1-64 (1966).
4. R. Kikuchi, Phys. Rev., **81**, 988 (1951).
5. H. Sato, S. A. Akbar and G. E. Murch, in Diffusion in Solids: Recent Developments, p. 67, edited by M. A. Dayananda and G. E. Murch, TMS-AIME, Detroit, MI, U.S.A., 1984.
6. C. C. Wang and S. A. Akbar, "Diffusion in Ordered Alloys and Intermetallic Compounds," submitted to Acta Metall. (1992).
7. H. Sato, Materials Transactions, Jpn. Inst. Metals, **32**, 509 (1991).
8. S. A. Akbar, J. Mater. Sci., **27**, 3125 (1992).
9. C. C. Wang and S. A. Akbar, "Determination of Atomistic Parameters Combining Theory and Experiments of Demixing in (Co,Mg)O," submitted to J. Am. Ceram. Soc. (1992).
10. H. Sato and R. Kikuchi, Phys. Rev. B, **28**, 648 (1983).
11. L. Zhang, W.A. Oates, and G.E. Murch, Philos. Mag. A, **58**, 937 (1988).
12. K. Gschwend, H. Sato and R. Kikuchi, J. Chem. Phys., **71**, 284 (1979).
13. C. C. Wang, "Degradation of Multicomponent Oxides under Oxygen Potential Gradients," Ph.D. Dissertation, The Ohio State University, Columbus, OH, 1993.
14. A.R. Allnatt and E.L. Allnatt, Philos. Mag. A, **49**, 625 (1984).
15. R. Kikuchi and H. Sato, J. Chem. Phys., **51**, 161 (1969).
16. J.R. Manning, "Diffusion Kinetics for Atoms in Crystals," Van Nostrand-Reinhold, Princeton, New Jersey (1968).
17. M. Hansen, *Constitution of Binary Alloys*, McGraw-Hill Pub. Co. (1958), pp.118.
18. R. Hultgren, R.L. Orr, P.D. Anderson, and K.K. Kelley, *Selected Values of Thermodynamic Properties of Metals and Binary Alloys*, Wiley, New York (1963).
19. R.E. Hanneman and A.U. Seybolt, Trans. TMS-AIME, **245**, 434 (1969).
20. A. Steiner and K.L. Komarek, Trans. TMS-AIME, **230**, 786 (1964).
21. G.E. Hancock and B.R. McDonnell, Phys. Stat. Solidi. (a)**4**, 143 (1971).
22. D. Gupta, D. Lazarus, and D.S. Lieberman, Phys. Rev., **153**, 863 (1967).
23. R.R. Vandervoort, A.K. Mukherjee, and J.E. Dorn, Trans. ASM, **59**, 931 (1966).
24. W.J. Yang and R.A. Dodd, Metal Sci. J., **7**, 41 (1973).
25. S. Shankar and L.L. Seigle, Met. Trans. A, **9A**, 1467 (1978).
26. K. Ouchi, Y. Iijima and K. Hirano, *Titanium '80, Science and Technology*, Vol. 1, pp. 559, edited by H. Kimura and O. Izumi, TMS-AIME, Proc. Fourth Int. Conf. on Titanium, 19-22 May 1980, Kyoto, Japan.

Atomistic Approach to Diffusion in Ordered Alloys

Hiroshi Sato and Huanbo Zhang

School of Materials Engineering
Purdue University
West Lafayette, Indiana 47907-1289 USA

Abstract

Atomistic approach to diffusion processes in ordered systems by means of the pair approximation of the Path Probability method (PPM) of irreversible statistical mechanics is critically reviewed in the light of recent progress in the understanding of the treatment. The treatment of diffusion even by means of the pair approximation of the original PPM eventually leads to results corresponding to the point (mean field) approximation. This is traced to the fact that, in the PPM, the averaged motion of an assembly of particles is treated as flow. The troubles can thus be removed by changing the formalism of the PPM into that of dealing with the motion of a single particle in the assembly of particles. The characteristic change of the diffusion coefficient with composition is due to a drastic decrease in the physical correlation factor (the percolation efficiency) in the ordered region, in addition to the increase in the activation energy. In the original PPM, the percolation efficiency is determined only by the development of the long range order, while, after conversion, it is shown that the change of the short range order is responsible for the change of the percolation efficiency.

Diffusion in Ordered Alloys
Edited by B. Fultz, R.W. Cahn, and D. Gupta
The Minerals, Metals & Materials Society, 1993

I. Introduction

Earlier, Kikuchi and Sato derived expressions for the tracer diffusion coefficients in binary ordered systems composed of A and B atoms by means of the pair approximation of the PPM [1,2], and showed that the tracer diffusion coefficient of B, D_B, is expressed by means of the harmonic mean of two components, $D_{B,I}$ and $D_{B,II}$, as

$$\frac{1}{D_B}=\frac{1}{2}\left(\frac{1}{D_{B,I}}+\frac{1}{D_{B,II}}\right) \tag{1}$$

where $D_{B,I}$ ($D_{B,II}$) may be interpreted as a component of the diffusion coefficient when a B^* (tracer of B) atom jumps from a I sublattice into a II sublattice (from a II into a I) site and the smaller one practically determines D_B. This is a convenient concept and has been widely quoted. However, it has been found that a systematic deviation of the calculated values of tracer correlation factor from those obtained by Monte Carlo simulation method in the disordered region exists, but the agreement has been found to be restored when the long range order develops [3,4]. Here, we examine the cause of such discrepancies with the results of the Monte Carlo simulation in the light of recent progress in the understanding of the treatments.

Phenomenological approaches which agree well with results of the Monte Carlo simulation method were developed later [3,4]. We prefer, however, the treatment by means of the PPM in examining the discrepancies, because the treatment of the PPM does not include any further ad hoc assumptions other than those models initially assigned, or any further approximations other than those inherent in the treatment, and all the derivations are made analytically. Therefore, the cause of improper results, if any, can be traced in a straightforward fashion. The PPM is an extension of the Cluster Variation Method (CVM) of equilibrium statistical mechanics to include time, t, in the treatment. The nature of approximation and the validity of the CVM in dealing with equilibrium properties are well known.

In the following, we show, step by step, why the discrepancies between the PPM and the Monte Carlo simulation in the treatment of flow should arise, and how these troubles can be removed in the pair approximation by a change of the averaging process which has been called the conversion processes [5-9].

II. Treatment of Diffusion in Ordered Systems by Means of the Original PPM in the Pair Approximation

Here, we adopt a so-called lattice gas model. This corresponds to the vacancy model of diffusion commonly adopted. Two species of atoms, A and B, occupy the lattice sites. Unoccupied lattice sites are "vacancies," and an atom can jump into a nearest neighboring unoccupied site. We assume nearest neighbor pairwise interactions, ε_{AA}, ε_{BB} and ε_{AB}, with $4\varepsilon=2\varepsilon_{AB}-(\varepsilon_{AA}+\varepsilon_{BB})$, but no interactions between those associated with vacancies, or $\varepsilon_{AV}=\varepsilon_{BV}=\varepsilon_{VV}=0$. Here, we define that A and B are attractive if $\varepsilon>0$. These are called the static parameters which determine the distribution of atoms under equilibrium conditions. In addition, we need to assume basic jump frequencies for A and B atoms which determine the probabilities of jumps of atoms into nearest neighboring vacant sites, w_A and w_B, as $w_A = \theta_A \exp(-\frac{u_A}{kT})$ and $w_B = \theta_B \exp(-\frac{u_B}{kT})$, where θ_A and θ_B represent the attempt frequencies, u_A and u_B represent the activation energy characteristic of A and B atoms, respectively. The effect of surroundings due to the interaction with nearest neighboring atoms (which we call the bond breaking factor) is to be accounted for in addition to u_A and u_B (see below). These are called the kinetic parameters. In kinetics, a jump of an atom into a nearest neighboring vacancy corresponds to an interaction with its nearest neighboring atom in statics. No more assumptions than these are required. The flow is calculated as the difference in the number of particles jumping across the reference plane between those in the plus direction and the minus direction towards the driving force. In the derivation, no further ad hoc assumptions are introduced other than the pair approximation of the PPM. Interactions introduce a certain equilibrium distribution among A and B atoms at a specified temperature. In the CVM-PPM formalism in deriving flow, this distribution is calculated by the (pair approximation of) CVM. Jumps of atoms under the driving force which do not change the equilibrium distribution of atoms are calculated by the PPM. The Onsager equation thus derived corresponds to the parallel displacement of an equilibrium distribution (the motion of a certain cross section of the specimen) under the driving force. Details of the treatment are given elsewhere [1,2].

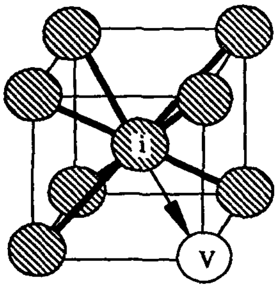

Fig. 1. Effect of bond breaking as an atom of the ith species jumps into a vacancy. Thick lines indicate the bonds [7].

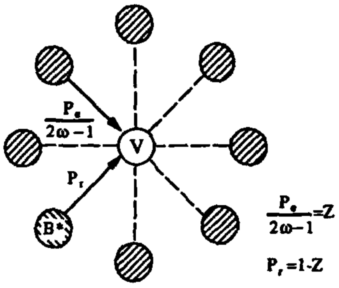

Fig. 2. Definition of Z in terms of P_e and P_r [7].

The change in the distribution causes the change in the local activation energy because an atom should break interactions (bonds) with the nearest neighboring atoms when it jumps into a vacancy (Fig. 1). This term is introduced as the bond breaking factor. The average of the activation energy thus depends on the distribution and composition, and this is calculated by the CVM. In addition, the introduction of the bond breaking factor creates the fluctuation of the activation energy from place to place because of the fluctuation in the distribution and makes the motion of a particle deviate from that of random walk. This creates the correlated motion of particles and the associated correlation factor, f, (physical correlation factor or the percolation efficiency) becomes small compared to one even in the disordered state. This term, however, has not been taken into account by the PPM. A sharp drop in the percolation efficiency in the well ordered region where atomic sites are divided into two makes the diffusion coefficient in the ordered system extremely small, although the increase in the average activation energy in the ordered region also contributes to the decrease in the diffusion coefficient.

The distribution of vacancies affects the diffusion process [1,2]. Although $\varepsilon_{AV} = \varepsilon_{BV} = \varepsilon_{VV} = 0$ is assumed, due to the difference in ε_{AA} and ε_{BB}, vacancies prefer to stay next to A or B depending on

$$U \equiv \frac{\varepsilon_{AA} - \varepsilon_{BB}}{4\varepsilon} \lessgtr 0 \tag{2}$$

A finite, non-zero value of U thus makes the behavior asymmetric[#] with respect to the equiatomic composition [1,2]. We, however, often assume U to be zero in order to make the calculations simpler [10,11]. Under this assumption, the distribution of vacancies becomes homogeneous.

By means of the pair approximation of the PPM, the tracer diffusion coefficient of B, D_B, and the two components, $D_{B,I}$ and $D_{B,II}$, defined in Eq.(1) are expressed as

$$D_B = 4w_B V_B W_B f \tag{3}$$

$$\begin{aligned} D_{B,I} &= 4w_B V_{B,I} W_{B,I} f_I \\ D_{B,II} &= 4w_B V_{B,II} W_{B,II} f_{II} \end{aligned} \tag{4}$$

with

$$\frac{1}{W_B} = \frac{1}{2}\left(\frac{1}{W_{B,I}} + \frac{1}{W_{B,II}}\right) \tag{5}$$

$$1/f = \frac{1}{2}\left(1/f_I + 1/f_{II}\right) \tag{6}$$

$$V_B = \left(x_{B,I} V_{B,I} + x_{B,II} V_{B,II}\right)/(2x_B) \tag{7}$$

where, V_B, W_B and f are the vacancy availability factor, effective jump frequency factor, and the (physical) correlation factor [2]. Here, $W_{B,I}$, and $W_{B,II}$ represent the bond breaking factor for a B^* on the I and II sublattices on the average, respectively. f_I and f_{II} are (physical) correlation factors for diffusion in the I and the II sublattices, respectively. $V_{B,I}$, for example, corresponds to the probability of finding vacancies at the nearest neighbor of a B^* atom on the I sublattice. The composition of B on the I (II) sublattice is specified by $x_{B,I}$ ($x_{B,II}$), and x_B is the average concentration of the species B

$$x_B = \left(x_{B,I} + x_{B,II}\right)/2 \tag{8}$$

[#] If $U = 0$ and $\theta_A = \theta_B$, and $u_A = u_B$ can be assumed, D_A and D_B become symmetric with respect to each other at the equiatomic composition.

If the sublattice I corresponds to the B sublattice, $W_{B,I}$ is small (the bond breaking factor becomes significant) and, based on Eq. (1), D_B is practically represented by $D_{B,I}$. At the same time, under the same condition in the well ordered state, $f_I << f_{II}$, so that f is practically represented by f_I. Therefore, the diffusion coefficient in the ordered system can be estimated from the dependence of $W_{B,I}$ on composition with the scaling factor f_I which depends only on the long range order even without a complicated calculation by means of the PPM.

It is to be noted that the pair approximation works only for crystal lattices which can be divided into two equivalent sublattices such as the two dimensional honeycomb lattice (2Dhc) ($2\omega=3$, where 2ω corresponds to the coordination number), the two dimensional square lattice (2Dsq, $2\omega=4$) and the body centered cubic lattice (bcc, $2\omega=8$), etc. The face centered cubic lattice (fcc, $2\omega=12$), for example, is divided into four equivalent sublattices and conclusions obtained by the pair approximation are not readily applicable. Indeed, the tetrahedron approximation is required for treatments with approximation higher than the point approximation here. Treatments for diffusion using approximations higher than the pair approximation are very complicated to handle in the PPM (The triangle approximation of the PPM which is applicable to problem of flow has been completed [12]) while the point approximation tends to give physically incorrect results as is well known in the calculation of phase diagrams. Because of this situation, systematic calculations of diffusion coefficients in binary systems by means of the PPM have been limited to the treatment by the pair approximation.

The fact that the diffusion process can be considered as two parallel circuits as shown in Eq. (1) is essentially based on the concept of microscopic reversibility under the equilibrium condition. In the CVM-PPM formalism, diffusion is treated to take place always under the equilibrium condition, and this concept of the transposed lattice can be readily proved [2].

Expressions of Eq. (4) indicate that the diffusion coefficients, $D_{B,I}$, etc., are determined by two factors of different nature, $W_{B,I}$, etc. and f_I, etc. The factors $W_{B,I}$, etc., representing the average bond breaking factors, indicate the increase in the (intrinsic) activation energy in the ordered state and are calculated essentially by the pair approximation of the CVM. These factors are determined by the distribution of atoms and the space correlation of the distribution is represented by that of the pair approximation. On the other hand, the correlation factors, f_I, etc., represent the character of flow and are determined by the PPM part of the theory. In Eq. (6), f_I, etc., depend only on the long range order and are insensitive to the short range order. In other words, the degree of approximation in calculating the time correlation by the PPM is reduced to that of the point approximation. It is to be reminded here that the temperature dependence of the correlation factor affects the Arrhenius plot. In other words, the temperature dependence of the correlation factor, $\partial \ln f / \partial (1/T)$, also contributes to the apparent activation energy.

The fundamental equation of flow in the PPM, which depends linearly on the driving force, has the form

$$
\begin{aligned}
\Psi_i &= -\dot{\alpha}_i + \sum_j Q_j \psi_{ji} \\
&= -(1 - \sum_j Q_j \psi_{ji} / \dot{\alpha}_i)\dot{\alpha}_i = -f_i \dot{\alpha}_i
\end{aligned}
\tag{9}
$$

Here, Ψ_i is a normalized flow (the flow under the driving force divided by the flow in one direction under the equilibrium condition) of an assembly of the ith species, Q_j indicates the distribution of atoms which surround a tagged species of i atoms, ψ_{ji} indicates the deviation from equilibrium with respect to the j-i pairs in the direction of the driving force, α_i is the generalized chemical potential divided by kT, $\dot{\alpha}_i$ indicates the driving force for the ith species and f_i defines the correlation factor. Therefore, the term $\sum_j Q_j \psi_{ji} / \dot{\alpha}_i$ represents a strain in the distribution created by an external force $\dot{\alpha}_i$ and this strain makes the correlation factor f_i smaller than one. Equation (9) indicates that the flow corresponds to the parallel displacement of a plane with particles in the equilibrium distribution under the driving force. In such a case, the time correlation of the motion of particles corresponds to that of the average, and hence to that of the point approximation. This is the reason that the time correlation treated by the PPM is reduced to that of the point approximation irrespective of the degree of approximation used to treat the problem of flow. It is noted that this difficulty is not limited to the PPM, but is found to be common to treatments of flow for an assembly of particles and is due to the procedure in which the averaged flow (by means of the ensemble averaging) of an assembly is handled [6].

Equation (9) further leads to

$$
f_i = \frac{(2\omega - 1)Z_i}{2 + (2\omega - 3)Z_i} \tag{10}
$$

where

$$
Z_i = \sum_j \frac{Q_j \hat{w}_j}{\hat{w}_i + \hat{w}_j} \tag{11}
$$

and $\hat{w}_i$, etc. means the jump frequency of the ith species with the bond breaking factor ($\hat{w}_i = w_i \cdot W_i$), etc. In terms of Z, the physical situation of deriving the correlation factor becomes especially clear. In Fig. 2, a situation which represents Z_i is shown when a tagged atom B^* at the central site has just replaced the position with a vacancy and is ready to jump back into the vacancy it has left behind. Then the probability for a jump back is denoted by P_r, and a jump of an atom at a surrounding into the vacancy represents the escape probability, P_e, of the vacancy as noted in Fig. 2. Based on Eq. (11),

$$
\begin{aligned}
P_{ir} &= 1 - Z_i \\
P_{ie} &= (2\omega - 1)Z_i
\end{aligned}
\tag{12}
$$

and f_i is connected to Z_i as Eq. (10). The larger is the normalized jump back probability, τ, which is defined as

$$\tau = \frac{P_r}{P_e + P_r} \tag{13}$$

the smaller is the correlation factor, which is represented based on Eq. (10) in terms of τ as $f = (1-\tau)/(1+\tau)$. In ordered systems, because of the microscopic reversibility, Eq. (9) can be represented by flows in two parallel circuits as

$$\begin{aligned} \Psi_i(\mathrm{I}) &= -\dot{\alpha}_i + \sum_j Q_j(\mathrm{II})\, \psi_{ji}(\mathrm{I}) \\ \Psi_i(\mathrm{II}) &= -\dot{\alpha}_i + \sum_j Q_j(\mathrm{I})\, \psi_{ji}(\mathrm{II}) \end{aligned} \tag{14}$$

Here, $\Psi_i(\mathrm{I})$ and $\Psi_i(\mathrm{II})$ represent the flow through the I sublattice and that through the II sublattice respectively, and $Q_j(\mathrm{II})$ and $Q_j(\mathrm{I})$ represent the probability of finding the jth species of atoms on the II and I sublattices, respectively. Each equation in Eq. (14) is equivalent to that in Eq. (9) in the disordered state, and similar arguments as Eqs. (10)-(13) follow. If the central site in Fig. 2 represents the I site and the surrounding sites the II sites, the B^* atom which jumped out tends to go back to the I *site immediately*. This makes the value of $f_{B,I}$ and hence f_B small. In this way, it is understood that the composition dependence of f_i is enhanced in the region where the long range order exists.

III. Conversion Process

In Section 2, the reason that the degree of approximation in the time correlation is reduced to the point approximation is stated to be due to the fact that the averaged motion of an assembly of particles is treated. In order to remove the trouble, therefore, it is necessary to convert the treatment of flow from that of dealing with the averaged motion of an assembly of particles to that of following the motion of a single particle in the assembly.

In the pair approximation of the PPM, the conversion process mentioned in Section 1 can be performed by replacing some of the results of the ensemble averaging process in the PPM by those of the time averaging process. This procedure consists of two processes, the instantaneous distribution conversion process [8,9] and the time conversion process [7]. The former deals with the effect of the local fluctuation of the distribution of particles around the tagged particle, and the latter deals with the approach to the equilibrium after the tagged atom replaces its position with a vacancy. In this form, it is clear that, when a particle replaces its position with a vacancy, the particle is not in equilibrium with the rest of the system, and the local equilibrium concept does not strictly apply. In the CVM-PPM formalism, however, it is considered that the equilibrium is maintained (as a result of the ensemble averaging process and thus the local equilibrium concept holds) and this leads the time correlation to the point approximation [12]. After the application of the instantaneous distribution conversion process, the equation of flow corresponding to Eq. (14) is obtained as [9]

$$\Psi_i(\alpha) = -\dot{\alpha}_i + \sum_j Q_j(\beta)\,\psi_{ji}(\alpha)$$

$$\Psi_i(\beta) = -\dot{\alpha}_i + \sum_j Q_j(\alpha)\,\psi_{ji}(\beta) \qquad (15)$$

Here, i represents a single, tagged tracer atom i, Q(β) and Q(α) represents species of atoms of the surrounding of an A atom (preferred by B atoms) and that of a B atom (preferred by A atoms) respectively in distribution with the short range order, and the relation is represented by the Bethe short range order in lieu of the sublattices I and II. However, the two sites are not equivalent [9]. The separation in two parallel circuits similar to Eq. (14) is in accordance with the microscopic reversibility. The correspondence of $\Psi_i(\alpha)$, $\psi_{ji}(\alpha)$ and $Q_j(\beta)$ to $\Psi_i(I)$, $\psi_{ji}(I)$ and $Q_j(II)$, and of $\Psi_i(\beta)$, $\psi_{ji}(\beta)$ and $Q_j(\alpha)$ to $\Psi_i(II)$, $\psi_{ji}(II)$ and $Q_j(I)$ is clear. The time conversion process indicates how the information from distant atoms can be accumulated with time for a jumped atom to reestablish the equilibrium with the surroundings (τ increases with time and then saturates [13]). This process improves the degree of approximation of the time correlation from that of the point approximation (the jump back probability τ is independent of time t) to that of the pair approximation [13] (The conversion process in the approximation higher than the pair has not been carried out). After the conversion process, the expression for f in terms of the long range order in the original PPM is now expressed in terms of the short range order with a proper degree of approximation for the time correlation. Diffusion coefficients are no longer separated into two components in terms of I and II sublattices, but into two components in terms of two virtual sublattices with their sites surrounded by two kinds of surroundings of the short range order, as pointed out above.

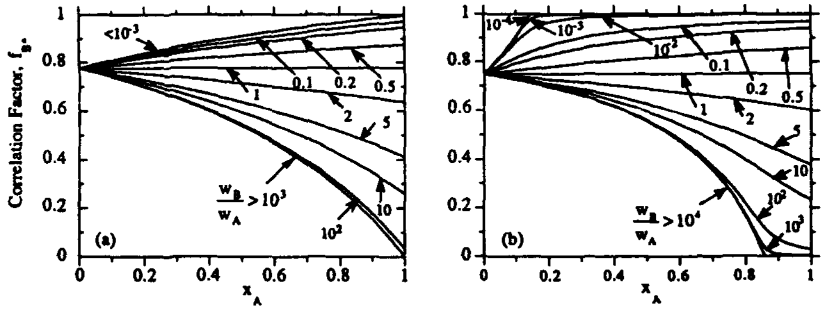

Fig. 3 The composition dependence of f_{B^*} for an ideally disordered alloy of bcc lattice as a function of w_B / w_A (a) Calculation based on original PPM, (b) after the time conversion [7].

Details of the conversion process are given in References [5-9] (also see Appendix). Here, only some results of the conversion process are shown. Since the conversion process deals with the motion of a single particle, the calculation is directly related to that of the tracer correlation factor or the diffusion coefficient of a tracer particle. In Fig. 3, we show how the percolation limit appears by applying the time conversion process [7]. Here, results of the calculation of the tracer correlation factor of B, or f_{B^*}, as a function of composition for different values of w_B / w_A by the original PPM with and without the time conversion process are compared, assuming that the binary system A-B is an ideal solution (no interactions among constituents exists, and, hence, no instantaneous distribution conversion process is required). The (time) conversion process converts the value of the tracer correlation factor for self diffusion from $(2\omega-1)/(2\omega+1)$ to $(2\omega-2)/2\omega$. The most remarkable difference is the appearance of the percolation limit of the motion of B (f_{B^*} becomes zero) at the composition $x_B = 1/(2\omega-1)$ in the system where only B can move (in the limit $w_B / w_A \rightarrow \infty$). The value of the percolation limit coincides with the calculation by the pair approximation of the CVM [14] and this indicates that, by the conversion process, the degree of approximation for the calculation of the time correlation improves to that of the pair approximation [7].

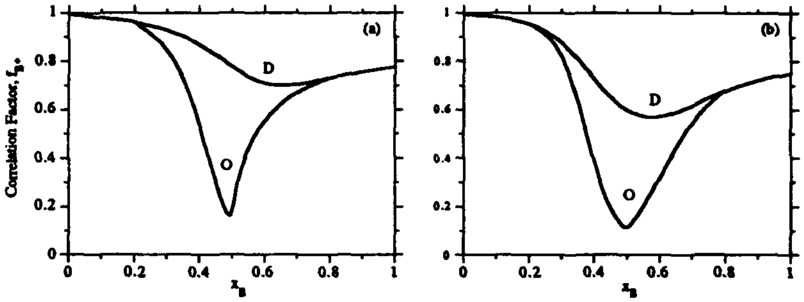

Fig. 4 The composition dependence of f_{B^*} in the ordered binary alloy of bcc lattice at $T / T_c = 0.5$ calculated by the pair approximation of (a) original PPM and (b) PPM after the conversion process [9].

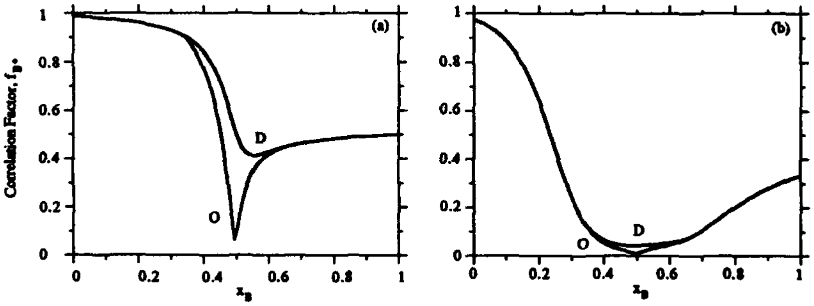

Fig. 5 The composition dependence of f_{B^*} in an ordered binary alloy of 2Dhc lattice at $T / T_c = 0.5$ calculated by the pair approximation of (a) original PPM and (b) PPM after the conversion process [9].

On the other hand, for systems with fluctuations in the distribution such as the existence of short range order, the instantaneous distribution conversion process plays an important role [9]. In Figs. 4 and 5, calculated results of the composition dependence of f_B for bcc and 2Dhc with and without the conversion process are shown. Here, U=0 is assumed and the temperature

T is normalized with respect to T_c of the order-disorder transition at the equiatomic composition, which is given by

$$2\varepsilon / kT_c = \log[\omega / (\omega - 1)] \tag{16}$$

Interaction parameters are normalized with respect to T_c and $\theta_A = \theta_B$, $u_A = u_B$ are also assumed for simplicity. The curves O and D refer to two different cases based on the different values of the short range order calculated. O indicates the normal case where the development of the short range order with T accompanies that of the long range order. The curve D refers to the case for the development of short range order only, calculated by keeping the degree of the long range order at zero. For bcc, the results of the original PPM and those after the conversion processes are not very different. On the other hand, for 2Dhc, a remarkable change is observed. This difference is due to the fact that, in a low dimensional case like 2Dhc, the development of the short range order outside the range of the long range order is significant. This shows how results after the conversion process are sensitive to the short range order. In Fig. 6, we show the results of the Monte Carlo simulations made by Murch for corresponding cases [9]. The results agree reasonably well with those of the PPM with conversion and justify the correctness of the interpretation given above. The systematic deviation of the results of the original PPM from those by the Monte Carlo simulation [3,4] is almost completely removed. As in the case of the CVM, the pair approximation gives good qualitative results also in the PPM.

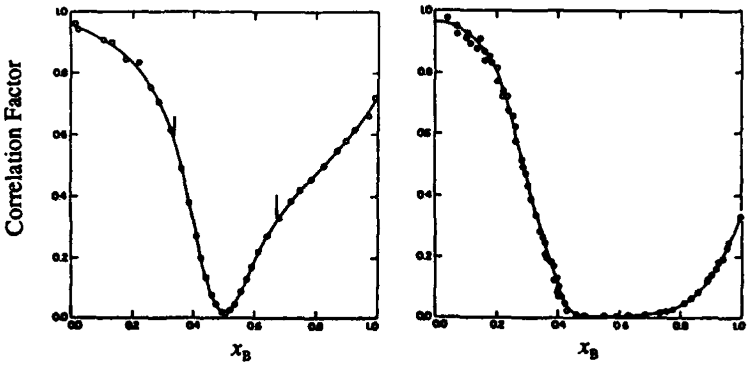

(a) (b)

Fig. 6. The composition dependence of f_B. in the ordered alloys of (a) bcc and (b) 2Dhc at $T/T_c = 0.5$ calculated by the Monte Carlo simulation method [9]. Arrows in (a) indicate the phase boundaries.

The expression obtained by the conversion process indicates that the behavior of diffusion can be estimated roughly by means of the calculation of the short range order (distribution of atoms which surround a B) by the CVM in such cases where the application of the pair approximation of the PPM is not feasible as the face centered cubic lattice.

It should be pointed out that this type of trouble in dealing with the time correlation in the PPM does not explicitly appear in applications in which the system is considered to be homogeneous so that all the particles can be considered to behave in the same fashion [10,11,15,16] (or the indistinguishability among particles can be applied [3]). However, the trouble appears explicitly in the treatment of flow, where a flow is defined in terms of the time correlation of the motion of a single particle.

IV. Onsager Matrix

The conversion process is related to the motion of a single particle in the assembly. However, the Onsager matrix is for an assembly of particles. In order to calculate the Onsager matrix elements, therefore, it is necessary to convert the results of conversion again into those of an assembly without losing the effect of conversion.

The Onsager equation derived by the original PPM for assemblies of particles represents a parallel displacement of a plane of particles with the equilibrium distribution by the driving force. Under such a situation, the flow represents an assembly of several independent parallel stationary flows. Therefore, for particles inside these individual flows, the instantaneous distribution and the time conversion processes are applied individually. These independent flows include a number of the same species of particles. The indistinguishability among particles of the same species in these independent flows makes the time conversion process among these particles ineffective[17]. Therefore, the time conversion process is eliminated for these particles. By following these processes, the Onsager matrix for an assembly of atoms can be calculated without reducing the degree of approximation to the point approximation, and the Haven ratio can be calculated with the pair approximation. The ionic conductivity of the binary system for the assembly of ions has thus been calculated successfully [11].

Acknowledgment

The authors appreciate the help of Dr. A. Datta in preparing the manuscript. The work was supported by a grant from the Department of Energy DE-FG02-84ER-45133.

Appendix

For ordered systems, Ref. 9 should be referred to. There are some mistakes there. For the present purpose, Eqs. (47) and (52b) in Ref. 9 should be replaced by

$$\frac{1}{\Psi_j} = \frac{x_A}{\Psi_j^{\alpha}} + \frac{x_B}{\Psi_j^{\beta}} \qquad (47)$$

$$\hat{w}_{B\bullet}(\alpha) = \theta_B e^{-\beta u_B} \left\{ \frac{y_{AA} e^{-\beta \varepsilon_{BA}} + y_{AB} e^{-\beta \varepsilon_{BB}}}{x_A} \right\}^{2\omega-1}$$

$$\hat{w}_{B^*}(\beta) = \theta_B e^{-\beta u_B} \left\{ \frac{y_{BA} e^{-\beta e_{BA}} + y_{BB} e^{-\beta e_{BB}}}{x_B} \right\}^{2\omega-1} = \hat{w}_B \tag{52b}$$

$$\hat{w}_A = \theta_A e^{-\beta u_A} \left\{ \frac{y_{AA} e^{-\beta e_{AA}} + y_{AB} e^{-\beta e_{AB}}}{x_A} \right\}^{2\omega-1} = \hat{w}_A(\alpha)$$

References

[1] R. Kikuchi and H. Sato, J. Chem. Phys. 51, 161 (1969).

[2] R. Kikuchi and H. Sato, J. Chem. Phys. 57, 4962 (1972).

[3] H. Bakker, Phil. Mag. A40, 525 (1979).

[4] N. A. Stolwijk, Phys. Stat. Sol. B105, 223 (1981).

[5] H. Sato, Materials Transactions, JIM 32, 509 (1991)

[6] H. Sato, "Non Debye Relaxation Process of Hopping Ionic Conduction in Lattice Gas Models: An Application of the Path Probability Method," Progress in Theoretical Physics, special issue: Fundamentals and Applications of the Cluster Variation Method and the Path Probability Method, to be published.

[7] H. Sato and R. Kikuchi, Phys. Rev. B28, 648 (1983).

[8] H. Sato, Non Traditional Methods in Diffusion, eds. G. E. Murch, H. K. Birnbaum and J. R. Cost, TMS (1984), pp. 203-235.

[9] H. Sato, S. A. Akbar and G. E. Murch, Diffusion in Solids: Recent Developments, eds. M. A. Dayananda and G. E. Murch, TMS (1985), pp. 345-369.

[10] K. Gschwend, H. Sato and R. Kikuchi, J. Chem. Phys. 69, 5005 (1978).

[11] K. Gschwend, H. Sato, R. Kikuchi, H. Iwasaki and H. Maniwa, J. Chem. Phys. 71, 2844 (1979).

[12] J.K. McCoy, R. Kikuchi, K. Gschwend and H. Sato, Phys. Rev. B25, 1734 (1982)

[13] H. Sato, "Examination of the Concept of Local Equilibrium," Defects and Diffusion Forum, Proc. DIMAT-92, to be published.

[14] H. Sato, A. Arrott and R. Kikuchi, J. Phys. Chem. Solids 10, 19 (1959).

[15] T. Ishikawa, K. Wada, H. Sato and R. Kikuchi, Phys. Rev. A. 33, 4164 (1986)

[16] K. Wada, T. Ishikawa, H. Sato and R. Kikuchi, Phys. Rev. A. 33, 4170 (1986)

[17] H. Sato, S. A. Akbar and T. Ishii, Solid State Ionics 28-30, 138 (1988).

Short Range Ordering Kinetics under Special Consideration of Correlation Effects

G. Yu and K. Lücke

Institut für Metallkunde und Metallphysik
Rheinisch-Westfälische Technische Hochschule Aachen
W-5100 Aachen, Germany

Abstract

Based on the simple pair model analytical expressions for the kinetics of first and second shell short range order formation in binary alloys have been derived for three cubic lattices (sc, bcc and fcc). Comparison to Monte-Carlo simulations demonstrated that the ordering kinetics is strongly influenced by the correlation of the successive vacancy jumps and allowed the determination of the corresponding correlation factors [1]. It was further shown that in all three lattices the establishment of the first pair variable P_{AB} during isothermal annealing after a small temperature change obeys an exponential time law, independent of the second shell interaction. The evaluated relaxation time given by $\tau=\nu_X/m_X$ yields a simple relationship too: the efficiency constant m_X depends only on the mobility ratio ν_A/ν_B of the two components. The development of the second pair variable P_{AB2}, however, follows a more complex kinetics which depends on the relevant parameters.

Diffusion in Ordered Alloys
Edited by B. Fultz, R.W. Cahn, and D. Gupta
The Minerals, Metals & Materials Society, 1993

1. Introduction

Order and disorder occur wherever there are materials. The kinetics of ordering and disordering processes becomes ever more interesting for studying and controlling the properties of systems far from the equilibrium produced by the modern material processing methods [1-4].

In the recent paper of the present authors [1] (hereafter denoted as Ref.I), the kinetics of the short range order (SRO) formation by the motion of vacancies in binary fcc alloys had been studied by using the nearest neighbour (NN) interaction pair model. Two methods were used: (i) By modifying and extending the analytical treatment described mainly by Radelaar [5], the rate equations for the atom ordering and the vacancy re-distribution and the solutions of these equations could be derived explicitely, and (ii) by applying Monte-Carlo simulations (MCSs) the correlation effects of vacancy migration with respect to the ordering could be introduced into the analytical treatment. These investigation revealed that the SRO formation during isothermal annealing after a small temperature change follows first order kinetics and that, due to the correlation effect, the relaxation times happen to be a simple function of the mobility ratio of the two components. It was further shown that the treatment for the high temperature range which is known to yield a good approximation for the pair model may be extended to the low temperature range and that this linear behavior exists nearly over the whole temperature range where SRO occurs.

In this paper again the kinetics of SRO formation is discussed. Compared to Ref.I, two important extensions are made:

--- Analytical treatments similar to those in Ref.I as well as the corresponding MCSs are carried out for the other kinds of cubic lattices; this appears to be helpful especially for understanding the general existence of the correlation effect in all diffusional phenomena.

--- The next nearest neighbour (NNN) interaction is considered both in the analysis and in the MCSs for the binary fcc alloys, so that the limitation of the pair model and the validity of its results can more thoroughly be discussed. But here only some main results are given. Further details of the analytical derivations and the MCSs results are published elsewhere in Ref.[6].

2. Analytical treatment of SRO formation

2.1 NN interaction in general lattices

In the following the derivation of the kinetics of the SRO formation in fcc lattices as given in detail in Ref.I is extended to general lattices. The pair variable P_{XY} (X, $Y=A$, B or V for vacancy), i.e. the concentration of A-B bonds, is defined as $P_{AB}=N_{AB}/zN$ with z being the coordination number of the first shell ($z=12$ for fcc lattices). N and N_{XY} denote the total number of the lattice sites and that of the X-Y bonds, respectively. Considering $C_V \ll 1$ we have $P_{XA}+P_{XB}+P_{XV}=C_X \approx P_{XA}+P_{XB}$ with C_X being the concentration of the component X.

The successive jumps of vacancies are considered to be the elementary process of ordering. The jump frequency of an X atom is written as

$$\nu_X=\nu_X^0\exp\left(-\frac{V_{\{g\}}}{k_BT}\right) \qquad (1)$$

where ν_X^0 is the attack frequency of the X atom and $V_{\{g\}}$ denotes the energy barrier in the special configuration identified by $\{g\}$. In Ref.I $V_{\{g\}}$ is set equal to the difference $V_{\{g\}}^{+}-V_{\{g\}}^{0}$ of the configurational energy in the saddle point position and in the initial lattice site position. For calculating $V_{\{g\}}^{0}$ by using the NN interaction pair model, the lattice sites which surround the site exchange pair, the jumping atom and the vacancy, must be divided into 3 groups: α sites being adjacent to only the jumping atom, β sites adjacent to only the vacancy and γ sites adjacent to both. Calling the number of α or β sites q, the number of γ sites is given by $r=z-q-1$. For the 2-dimensional hexagonal lattice (see Fig.1) one has $z=6$, $q=3$ and $r=2$. If the jumping atom is an X atom and the α, β and γ sites are occupied by i, j and k X atoms, respectively, we obtain for the difference of the configurational energy between saddle point position and ground state

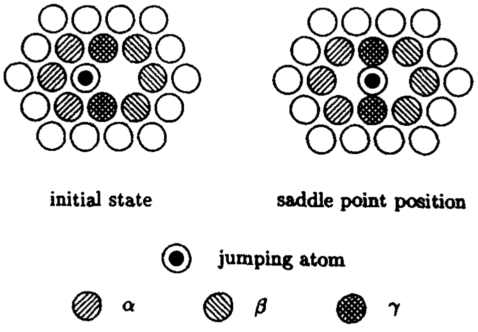

Fig. 1 Three groups of different NN sites around the exchange pair

Type of lattice	Coordi-nation-number z	Number of α, β sites q	Number of γ site r	Correlation factor for diffusion f_D	Efficiency constant $m_A(\phi=1)$	Correlation factor for ordering $f_A(\phi=1)$
2D square	4	3	0	0.47	-	-
2D hexagonal	6	3	2	0.56	-	-
sc	6	5	0	0.65	1.54	0.39
bcc	8	7	0	0.73	1.33	0.43
fcc	12	7	4	0.78	1.26	0.68

Table 1 Characteristic parameters for different kinds of lattices. The correlation factors for self-diffusion f_D are taken from [15] and the correlation factors for ordering f_A are evaluated from the present simulation by using $f_A=z/(2qm)$.

$$V_{\{g\}}=V^{+}_{\{X,k\}}-V^{0}_{\{X,ijk\}}=kE^{+}_{XX}+(r-k)E^{+}_{AB}-(i+k)E_{XX}-(z-1-i-k)E_{AB} \tag{2}$$

E_{XY} is the interaction energy of the bond *X-Y* and $E_{XY}{}^{+}$ is that between an *X* atom in saddle point position and a *Y* atom in the γ sites. In the case $r=0$, the configurational energy at the saddle point position $V_{\{g\}}{}^{+}$ is independent of the environment, and we have the alternative expression

$$V_{\{g\}}=V_{\{X,ijk\}}=V^{+}_{X}-iE_{XX}-(z-1-i)E_{AB} \tag{2a}$$

As in Ref.I the interaction between vacancies and atoms is neglected.

The averaging of $\nu_{\{g\}}=\nu_{\{X,ijk\}}$ over all i, j and k gives the mean jump frequency

$$N_X\nu_X=\sum_{ijk}P_{\{X,ijk\}}\nu_{\{X,ijk\}} \tag{3}$$

with $P_{\{X,ijk\}}$ being the probability of the occurence of the configuration $\{X, ijk\}$. As shown in Ref.I this will lead to

$$\nu_X=z\frac{P_{VX}}{C_X}\bar{\nu}_X\left[1+\frac{P_{VAB}}{P_{VX}}\left(e^{\eta_X-\eta^{+}_{X}}-1\right)\right]^{r}h_X^{q} \tag{4}$$

where

$$\eta_X=\frac{E_{XX}-E_{AB}}{k_BT}\ ,\quad \eta^{+}_{X}=\frac{E^{+}_{XX}-E^{+}_{AB}}{k_BT}\ ,\quad \eta=\frac{\eta_A+\eta_B}{2}\ ,\quad h_X=1+\frac{P_{AB}}{C_X}\left(e^{\eta_X}-1\right)$$

are abbreviations and $\tilde{\nu}_X$ represents the jump frequency of the *X* atom in the pure metal *X* independent of the individual configuration. We have generally $\tilde{\nu}_X=\nu_0^X\exp\{[(z-1)E_{XX}-rE_{XX}^{+}]/k_BT\}$ and for the case of $r=0$ $\tilde{\nu}_X=\nu_0^X\exp\{[(z-1)E_{XX}-V_X^{+}]/k_BT\}$. The quantity P_{VAB} is defined in Table 2 as the probability of having a *Y* atom at a γ site near an *A-V* pair. It represents a three-body probability which, as in Ref.I, is approximated by pair probabilities. It is to be noted that we may write $\nu_X=C_V\mu_X$ with μ_X being the jump frequency of a vacancy to an *X* atom. The exact value of μ_X depends on the state of order and is given for high temperatures in Ref.I.

For the configuration *{X,ijk}* each successful jump of an *X* atom will change the number of the *A-B* bonds N_{AB} by the value *i-j*. This gives the average rate of change due to jump of *X* atoms

$$\dot{N}_{AB}^X=-\dot{N}_{XX}^X=\dot{N}_{VX}^X=zNf_X\sum_{ijk}(i-j)P_{\{X,ijk\}}\nu_{\{X,ijk\}} \tag{5}$$

Here instead of $\nu_{\{X,ijk\}}$ the product $f_X\nu_{\{X,ijk\}}$ is introduced. f_X denotes thus the correlation factor which describes the different efficiencies of the various atom jumps for ordering. Further evaluation and considering relationships like

$$\dot{P}_{AB}=\frac{\dot{N}_{AB}^A+\dot{N}_{AB}^B}{zN},\quad \dot{P}_{VA}=\frac{\dot{N}_{AB}^A-\dot{N}_{AB}^B}{zN} \tag{6}$$

finally yields a set of completed non-linear rate equations

$$\dot{P}_{AB}=\omega[C_AC_B-P_{AB}+(1-e^{-(\eta_A+\eta_B)})P_{AB}^2]+s\dot{P}_{VA} \tag{7}$$

and

$$\dot{P}_{VA}=\frac{q}{z}C_Af_A\nu_A+\omega_1P_{AB}-\omega_0\frac{P_{VA}}{C_V} \tag{8}$$

with the abbreviations

$$\omega=\frac{2q}{z}h_A^{-1}h_B^{-1}\frac{f_Af_B\nu_A\nu_B}{C_Af_A\nu_A+C_Bf_B\nu_B} \tag{9a}$$

$$s=\frac{C_Af_A\nu_A-C_Bf_B\nu_B}{C_Af_A\nu_A+C_Bf_B\nu_B} \tag{9b}$$

$$\omega_0=\frac{q}{z}(C_Af_A\nu_A+C_Bf_B\nu_B) \tag{9c}$$

$$\omega_1=\frac{q}{z}\left[\frac{C_Bf_B\nu_B}{C_B+P_{AB}(e^{\eta_B}-1)}-\frac{C_Af_A\nu_A}{C_A+P_{AB}(e^{\eta_A}-1)}\right] \tag{9d}$$

As discussed in Ref.I the term $\dot{P}_{VA}$ in Eq.(7) is negligably small because of $C_V \ll 1$ and can be omitted. Furthermore, for high temperatures one has $\eta_X \to 0$ and $h_X \to 1$, so that as an approximation for high temperature an uncoupled linear rate equation is obtained

$$\dot{P}_{AB} = -\frac{2q}{z} \frac{f_A f_B \nu_A \nu_B}{C_A f_A \nu_A + C_B f_B \nu_B} \Delta P_{AB} = -\frac{\Delta P_{AB}}{\tau} \tag{10}$$

$\Delta P_{AB} = P_{AB}(t) - P^{*}_{AB}$ denotes the deviation of P_{AB} from its equilibrium value

$$P^{*}_{AB} = C_A C_B \{1 + \frac{4C_A C_B (1 - e^{-(\eta_A + \eta_B)})}{[1 + \sqrt{1 - 4C_A C_B (1 - e^{-(\eta_A + \eta_B)})}]^2}\} \approx C_A C_B [1 + C_A C_B (\eta_A + \eta_B)] \tag{11}$$

which follows from Eq.(7) by setting $\dot{P}_{AB} = 0$. The values for z and q for various lattices are given in Tab.1. The re-distribution rate of vacancies $\dot{P}_{VA}$ will be considered in [6].

2.2 NN and NNN interaction in fcc lattices

In the following treatment the fcc lattice is considered as an example. But, as in the case of only NN interaction treated in Sec.2, the method can easily be extended to the other kinds of lattices.

In the case of taking into account only NN interactions, 3 groups of lattice sites (α, β and γ) are to be distinguished. If also the NNN interaction is taken into account, one has to consider seven different kinds (i to vii) of positions among all NN and NNN sites of the exchange pair, the jumping X atom and the vacancy, for the fcc lattice (which increases to eight for general lattices). This is illustrated in Fig.2 and explained in Table 2. In Fig.2 the jumping atom (1) and the vacancy (2) are each positioned in the centre of a cube in such a way that their NNs are situated on the middle of the edge of the cube. Then NNNs are on the lines through the centre parallel to the edge. In Table 2 the probabilities of finding a Y atom for all 7 groups are listed. Obviously P_{VXY}, Q_{VXY} and R_{VXY} present three-body-probabilities (XYV).

The jump frequency of an X atom in the special configuration having χ_i X atoms at the i-th position is obtained by using Eq.(1). Compared to Eq.(2) we have here

$$\begin{aligned} V_{\{g\}} = {} & \chi_i E^{*}_{XX} + (4 - \chi_1) E^{*}_{AB} - (\chi_1 + \chi_2 + \chi_4) E_{XX} - [11 - (\chi_1 + \chi_2 + \chi_4)] E_{AB} \\ & - (\chi_5 + \chi_6) E_{XX2} - [6 - (\chi_5 + \chi_6)] E_{AB2} \end{aligned} \tag{12}$$

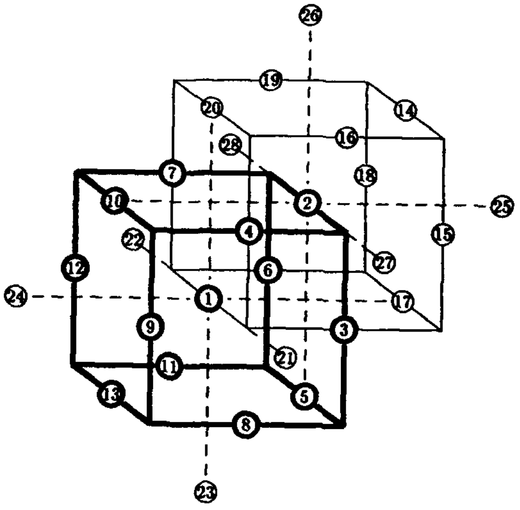

Fig. 2 Different positions around a site exchange pair in an fcc lattice as listed in Tab. 2: Each site situated at the edge of a cube is a NN and situated at the end of the dashed line is a NNN of the site 1 or 2, respectively. Cube and NN positions around site 1 are emphazised.

Type of position	Number of the site in Fig.2	Relation to the X atom	Relation to the vacancy	Probability of having a Y atom
X atom	1			
vacancy	2			
i (γ)	3,4,6,7	NN	NN	P_{VXY}/P_{VX}
ii (α)	8,9,11,12,13	NN	>NNN	P_{XY}/C_X
iii (β)	14,15,16,18,19	>NNN	NN	P_{VY}/C_V
iv (α)	5,10	NN	NNN	Q_{VXY}/P_{VX}
v (β)	17,20	NNN	NN	R_{VXY}/P_{VX}
vi	21,22,23,24	NNN	>NNN	P_{XYZ}/C_X
vii	25,26,27,28	>NNN	NNN	P_{VYZ}/C_V

Table 2 Seven groups of the NN and NNN sites around the exchange pair X-V

The additional subscript *2* indicates the corresponding quantity with respect to the second shell, e.g., E_{XY2} denotes the interaction energy of an *X* atom with *Y* atom on a NNN site. Also here the interaction between vacancies and atoms is assumed to be so small that it is negligible even compared to the second shell atomic interaction. Instead of Eq.(4) we have for the mean jump frequency of the *X* atom

$$\nu_X=12\frac{P_{VX}}{C_V}\tilde{\nu}_X h_X^5 h_{X2}^4\left[1+\frac{P_{VAB}}{P_{VX}}\left(e^{\eta_X-\dot{\eta}_X}-1\right)\right]^4\left[1+\frac{Q_{VAB}}{P_{VX}}\left(e^{\eta_X}-1\right)\right]^2\left[1+\frac{R_{VAB}}{P_{VX}}\left(e^{\eta_{X2}}-1\right)\right]^2 \quad (13)$$

with the probability variables being listed in Table 2 and the abbreviations

$$\eta_{X2}=\frac{E_{XX2}-E_{AB2}}{k_BT}\ , \quad h_{X2}=1+\frac{P_{AB2}}{C_X}\left(e^{\eta_X}-1\right)$$

Each jump of an *X* atom in the configuration $\{\chi_i\}$ causes the change of N_{AB} by the value $(\chi_2+\chi_4-\chi_3-\chi_5)$ as well as the change of N_{AB2} by the value $(\chi_5+\chi_6-\chi_4-\chi_7)$. This gives us the rate of change of *A-B* NN as well as *A-B* NNN bonds due to the jump of an *X* atom

$$\dot{N}_{AB}^X=12Nf_X\sum\nolimits_{\{X,\ \chi_i\}}(\chi_2+\chi_3-\chi_4-\chi_5)P_{\{X,\chi_i\}}\nu_{\{X,\chi_i\}} \quad (14)$$

and

$$\dot{N}_{AB2}^X=6Nf_{X2}\sum\nolimits_{\{X,\ \chi_i\}}(\chi_5+\chi_6-\chi_4-\chi_7)P_{\{X,\chi_i\}}\nu_{\{X,\chi_i\}} \quad (15)$$

where f_{X2} denotes the correlation factor for jumps of *X* atoms with respect to the second shell ordering. Then, in analogy to the treatments in Sec.2.1, rate equations are obtained. These as well as solutions of them will be analytically derived in [6].

3. Monte Carlo Simulation

3.1 Method

The principal method and the algorithm of the present MC simulation of the SRO kinetics is described in detail in [7-9]. In the present paper three cubic lattices are considered. The rigid computer crystal for the simulation is composed of $60\times60\times60$ elementary cells, i.e. $N=216000$ for sc, $N=432000$ for bcc and $N=864000$ for fcc respectively. These sites are occupied by N_A *A* and N_B *B* atoms according to the given composition C_X. Only a single site remains vacant ($N_V=1$ and $C_V\sim10^{-5}$), and the movement of atoms occurs by the migration of this vacancy. The periodical boundary condition is used.

For each attempted jump two random numbers are required; i.e., the first serves for the determination of the jump direction among all z possibilities and the second for checking the success of the jump. The attempted jump actually takes place if the normalized frequency $\nu_{(g)}/\nu_{max}$ in the direction selected by the first random number is larger than the second number between 0 and 1 (ν_{max} is the largest of the values $\nu_{(g)}$). For calculating $\nu_{(g)}$ we have from Eq.(2) for cases without consideration of the NNN interaction

$$\nu_{(g)}=\tilde{\nu}_X \exp[-(11-i-k)\eta_X+(4-k)\eta_X^+] \tag{16}$$

In this case we have to only count the number i and k. For the case with NNN interaction in fcc lattices we obtain from Eq.(11)

$$\nu_{(g)}=\tilde{\nu}_X \exp[-(11-\chi_1-\chi_2-\chi_4)\eta_X-(4-\chi_5-\chi_6)\eta_{X2}+(4-\chi_1)\eta_X^+] \tag{17}$$

Here three numbers χ_1, $(\chi_2+\chi_4)$ and $(\chi_5+\chi_6)$ must be determined.

Each simulation run is designed as an isothermal annealing at a selected temperature $T=(E_{AA}+E_{BB}-2E_{AB})/(2\eta k_B)$ after quenching from $T=\infty$. The dependence of the ordering kinetics on the energy parameters η_X and η_X^+ has been discussed in Ref.I and [10]. In this paper they are set constant $\eta_A=\eta_B=\eta=0.15$ and $\eta_A^+=\eta_B^+=0.3$. By varing C_A and the ratio $\tilde{\nu}_A/\tilde{\nu}_B$, as well as η_2 (using $\eta_2=\eta_{A2}=\eta_{B2}$), the different sets of simulations hve been carried out, so that the dependence of the ordering kinetics on the concentration C_A and the mobility ratio $\phi=\nu_A/\nu_B$ as well as the influence of the NNN interaction can be dealt with. To demonstrate the ordering kinetics more illustratively the jump number n_A per A atom or n_B per B atom is used for the time scale and the normalized quantities

$$r=(P_{AB}-P_{AB}^*)/(P_{AB}^0-P_{AB}^*)\ , \qquad r_2=(P_{AB2}-P_{AB2}^*)/(P_{AB2}^0-P_{AB2}^*)$$

for the relative change of the SRO parameters.

3.2 NN SRO kinetics in three cubic lattices

The simulations lead for P_{AB} to final plateau values independent of ϕ, which show they are equilibrium values P_{AB}^*. Fig.3 gives an example. As can be seen from Fig.4 where P_{AB}^* vs η for fcc lattices is plotted, the pair model is a good approximation for fcc lattice only at high temperatures, but the tetrahedron models, either that by using cluster variation (CV) method [11] or that based on quasi-chemical theory [12], yield a satisfactory agreement with the present simulations. The application of the pair model to low temperature range will be discussed in detail in [10].

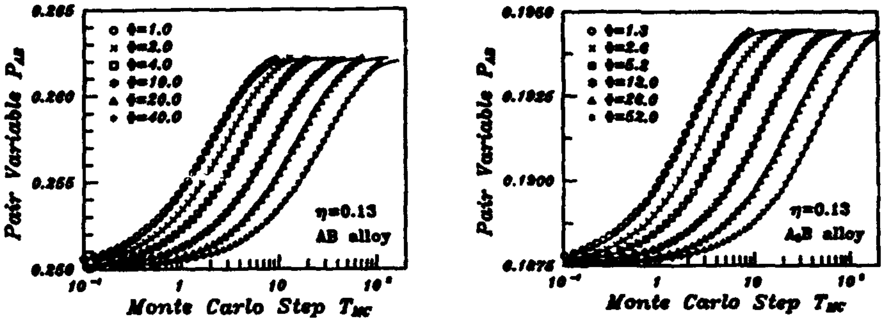

(a) (b)

Fig. 3 SRO parameter P_{AB} vs the annealing time for varying φ in fcc lattices

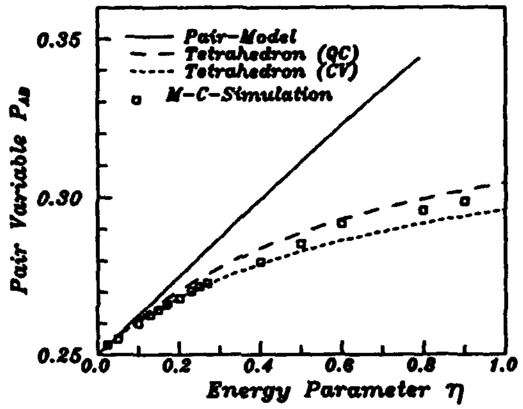

Fig. 4 Dependence of the equilibrium values for P_{AB} on the energy parameter η in fcc lattices

Considering the kinetics, for all cases of only NN interaction investigated in this work, a first order reaction

$$r=\exp(-\frac{t}{\tau})=\exp(-\frac{n_A}{m_A})=\exp(-\frac{n_B}{m_B}) \tag{18}$$

is observed as a very good approximation. Here we obviously have $m_X=\tau\nu_X$ from $n_X=t\nu_X$. This simple exponential rule is demonstrated by the examples of Figs.5a to 5c where for sc, bcc and fcc lattices the plots log(r) vs n_A for $C_A=0.25$ and varying φ yield the straight lines. The deviations from the straight lines at large n_A are not of principal nature but only due to insufficient averaging. m_A here gives the number of jumps per A atom required for reducing the deviation of P_{AB} from the equilibrium value P_{AB}^* by a factor 1/e and the straight lines indicate that it is constant. m_A^{-1} and the corresponding m_B^{-1}, which will thus be denoted as efficiency constants, are then determined by fitting the $r(n_A)$ curves by an exponential.

The relationship between the resulting m_A values and the relevant parameters is illustrated in Figs.6 for sc, bcc and fcc alloys. The solid curves $m_A^{-1}=f(\phi)$ are given by the equation

$$f(x)=\frac{a}{1+x}[1+b\exp(-c(x+\frac{1}{x}))] \qquad (19)$$

with $a=2.33$, $b=-0.41$ and $c=0.12$ which is obtained by fitting the results from MCSs in fcc lattices in Ref.I. Figs.6 show the rather astonshingly simple result that for all three cubic lattices and all applied values of the parameters η, η_X and C_X determining the SRO kinetics. The efficiency constant m_A approximately follows an universal function $f(\phi)$ in quite good approximation.

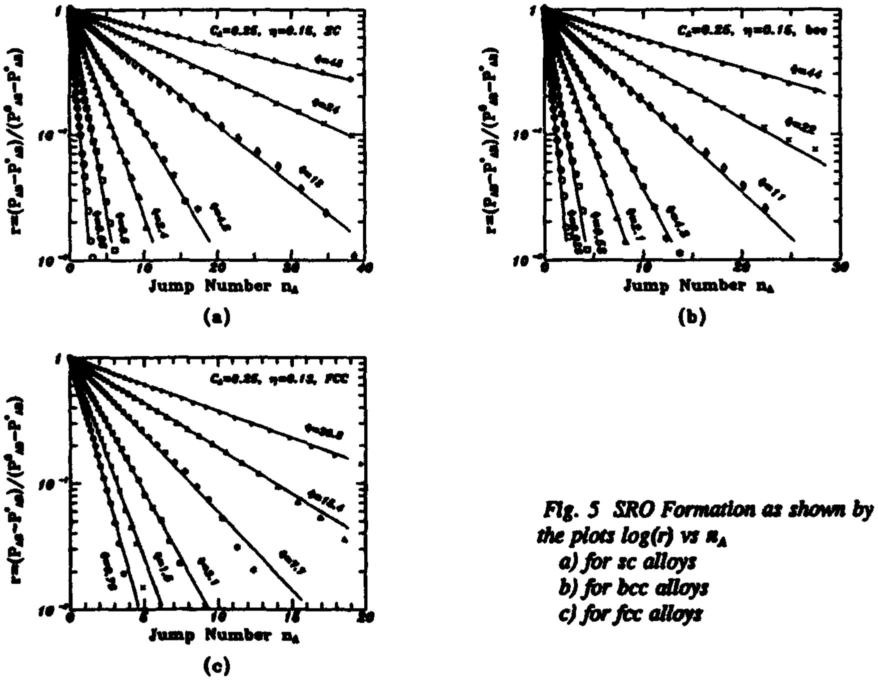

(a)

(b)

(c)

Fig. 5 SRO Formation as shown by the plots log(r) vs n_A
a) for sc alloys
b) for bcc alloys
c) for fcc alloys

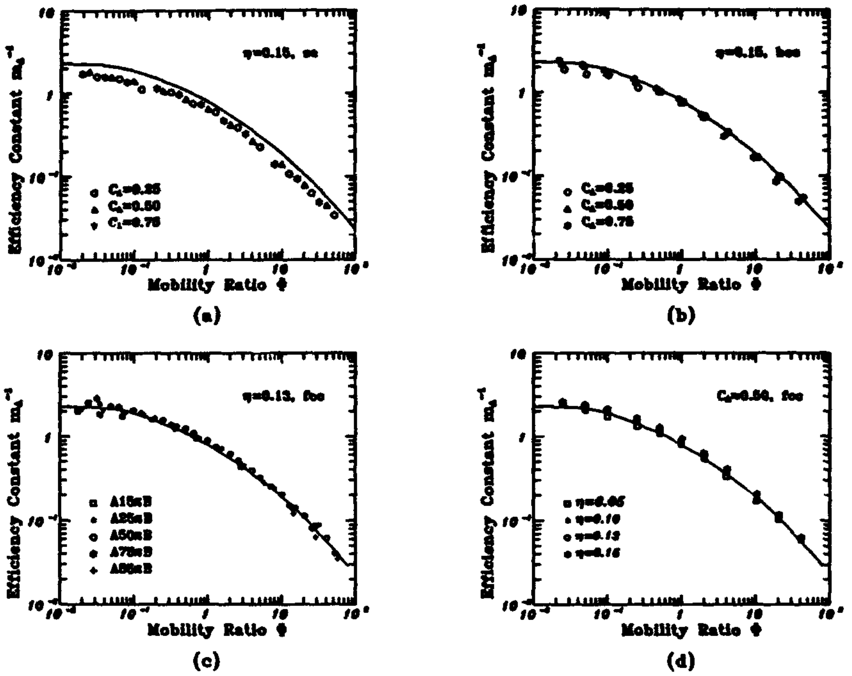

(a) (b)

(c) (d)

Fig. 6 The relationship between the efficiency constant m_A^{-1} and the mobility ratio ϕ, the concentration C_A and the energy parameter η. The solid curves are calculated from Eq.(19).

a) for sc alloys b) for bcc alloys c) and d) for fcc alloys

3.3 SRO kinetics under consideration of NNN interaction

Some results of the simulations for the fcc lattice considering also NNN interaction are demonstrated in Figs.7a to 7d by plotting P_{AB} and P_{AB2} against n_A for varying C_V, ϕ and η_2. It can be seen that the final values P^{*}_{AB} as well as P^{*}_{AB2} are independent of ϕ. However, P^{*}_{AB2} considerably decreases with the decreasing η_2 whereas the final values P^{*}_{AB} only slightly increase. It is to be mentioned that P_{AB2} changes also in the case of $\eta_2=0$ and reaches the plateau after about the same time with varying η_2.

The change of P_{AB} follows a first order kinetics also in the presence of NNN interaction, as illustrated in Fig.8 by plotting log(r) vs n_A for C_A=0.25 and η_2=-0.25η. Moreover, the resulting efficiency constant m_A is hardly changed by the NNN interaction: As to be seen from Fig.9, the values η_2=0, -0.25η and -0.5η lead to the same $m_A^{-1}=f(\phi)$. The development of P_{AB2} shows a more complex course and in general is non-exponential as will be discussed in [6].

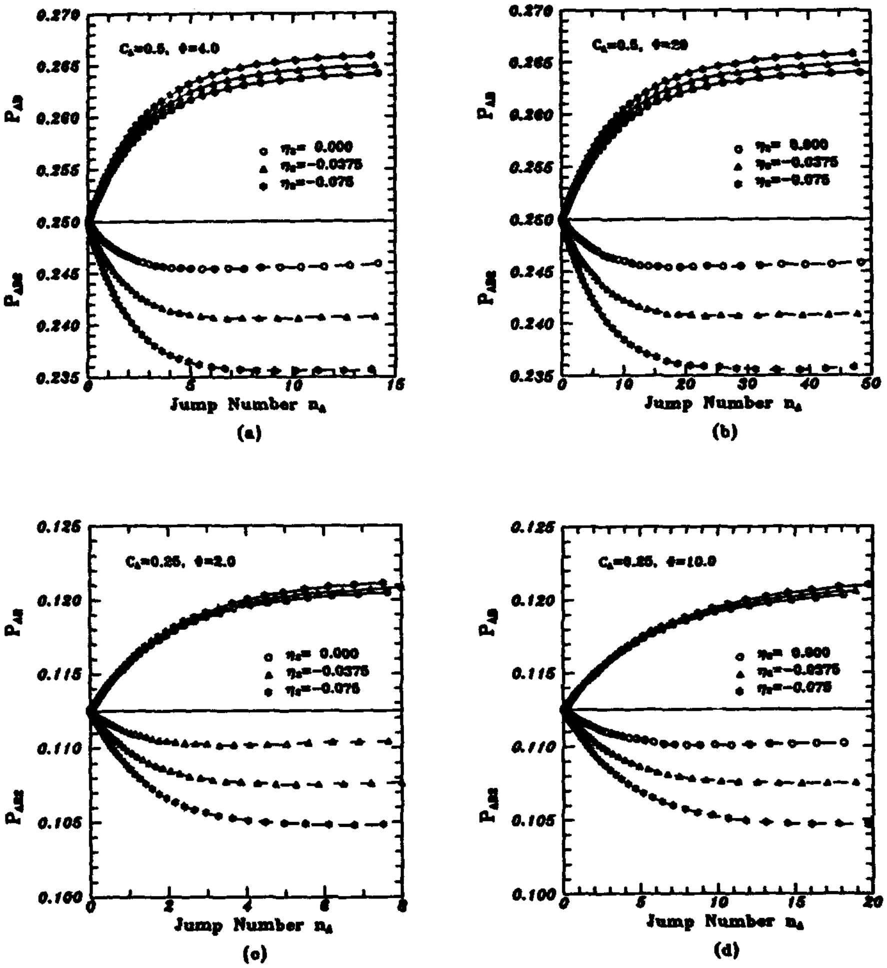

Fig. 7 Change of the pair variables P_{AB} and P_{AB2} during annealing for η=0.15
a) for C_A=0.50 and ϕ=4.0 b) for C_A=0.50 and ϕ=20.0
c) for C_A=0.25 and ϕ=2.0 d) for C_A=0.25 and ϕ=10.0

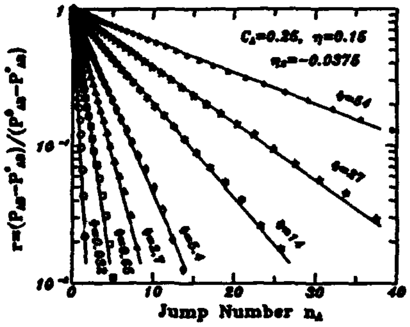

Fig. 8 SRO formation in fcc alloys taking into account the NNN interaction for $C_A=0.25$ and $\eta=0.15$

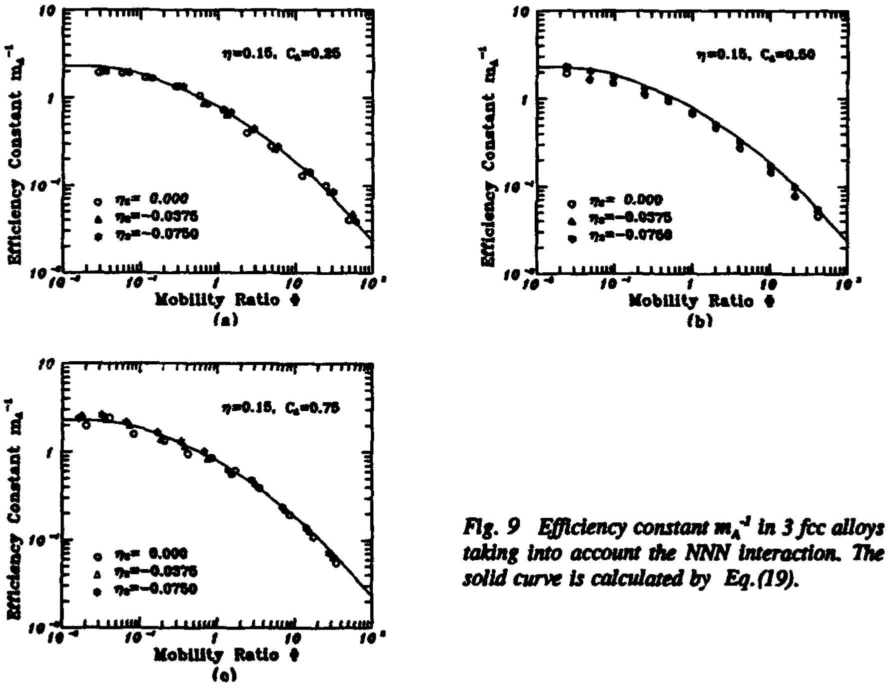

Fig. 9 Efficiency constant m_A^{-1} in 3 fcc alloys taking into account the NNN interaction. The solid curve is calculated by Eq.(19).

5. Discussion

The main results of the present MC simulations of three cubic lattices are (i) that the development of P_{AB} follows the first order kinetics for small temperature changes, and (ii) that the efficiency constant m_A is a function only of ϕ and not of C_A or η. The first of these results follows already from the analytical treatment leading to Eq.(10), but the second result is only obtained if in Eq.(10) the relationship

$$f_A\nu_A=f_B\nu_B=\nu_{AB} \tag{31}$$

is also fulfilled. As discussed in Ref.I it is this Eq.(31) that reveals the severe effects of the correlation of the successive vacancy jumps for the ordering and yields the essential insight into the mechanism of the ordering.

The concept of a correlation factor for processes due to the successive vacancy jumps originates from the consideration of the self-diffusion via vacancy migration [13]. There the correlation leads to a more than random probability for back jumping of the vacancies by which part of the prior displacement of the atom will be canceled. This can be expressed by a 'correlation factor' f_D for diffusion by which, compared to the random frequency, the actual jump frequency of the atoms is reduced. Since such a cancellation of prior atom jumps takes place generally in the case of vacancy controlled atom motion, correlation effects occur and strongly influence the kinetics of all such diffusional processes; e.g., for the self-diffusion in ideal superlattices, a relationship $f_D{}^A\nu_A=f_D{}^B\nu_B$ very similar to Eq.(31) must be obeyed [14].

But there is an essential difference between diffusion and ordering: In the ordering the A (or B) atoms are not distinguishable, so that as can directly be seen, vacancy motion by a chain of jumps of A (or B) atoms does not bring a change in the degree of order. This shows that the correlation effect must play a much more severe role in ordering than in (tracer) diffusion. In Table 1 both the correlation factors for self-diffusion in pure metal f_D [15] and the correlation factors for ordering $f_A(\phi=1)$ evaluated from the present simulation are listed. We recognize f_A considerably smaller in all three cubic lattices.

Since ordering ultimately consists only in the site exchange of an A and a B atom, both participants of ordering have to make the same contribution to the rate of ordering, no matter how much their mobilities differ. Thus, it is not ν_A or ν_B but the quantity ν_{AB} which determines the rate of ordering and which thus will be denoted as ordering frequency. This makes it clear, that in the case of a large mobility difference of the two components, the SRO kinetics is governed mainly by the diffusion of the slower component.

Introducing the expression Eq.(31) into Eq.(10) yields for the relaxation time

$$\frac{1}{\tau}=\frac{2q}{z}f_A v_A=\frac{2q}{z}f_B v_B=\frac{2q}{z}v_{AB} \tag{32}$$

This equation has the form which would also obtained for the direct site exchange mechanism and illustrates the similarity of the two mechanisms. Both mechanisms consist of an interchange of A and B atoms. In the case of direct interchange the exchange of sites occurs simultaneously by two neighbouring atoms, whereas in the vacancy mechanism the site exchange may be realized after a number of jumps of vacancies.

The applicability of the NN interaction pair model is discussed in two other articles of the present authors in two aspects: In [10] the treatment has been extended to include the low temperature range and in [6] to include the NNN interaction. In both cases, the analytical treatments as well as the simulations, were found to yield a first order kinetics of SRO formation after small temperature changes with a relaxation time obeying Eq.(32). This means that for small temperature change, Eqs.(10) and (30) and thus $m_A^{-1}=2qf_A/z$ are generally valid, for different kinds of lattices, for different concentrations, for cases including or excluding NNN interaction, and for the whole temperature range in which SRO exists. The reason why a non-zero NNN interaction does not influence the relaxation time (Fig.7) although it slightly changes the first shell equilibrium order, will be discussed in [6] in comparison to the detailed analytical derivations.

Finally it shall be estimated which temperature changes are permitted without destroying the first order kinetics. In the present simulation (as in [10] for the low temperature range), a temperature change of $|\Delta\eta|=0.15$ is found to still yield first order kinetics. From the defintion of η we can immediately write

$$\left|\frac{\Delta\eta}{\eta_{tr}}\right|=\left|\frac{\Delta T T_{tr}}{T(T+\Delta T)}\right|$$

Setting the transition temperature $T_{tr}<T$ and $\eta_{tr}=(2E_{AB}-E_{AA}-E_{BB})/(2kT_{tr})\approx 1.1$ [16], we easily find that e.g., for $T_{tr}\geq 300$ K the condition $|\Delta\eta|\leq 0.15$ is fulfilled for the whole existence range of SRO whenever $|\Delta T|\leq 60$K is satisfied. Most experiments on the SRO kinetics by means of the measurement of the SRO induced resistivity during the isothermal annealing after quenching [2,3], have been carried out within this temperature interval, typically one has $|\Delta T|\leq 30$K [2,3]. The present results thus deliver the fundamentals for the interpretation for these kinds of measurements.

The quantitative evaluation of $m_A^{-1}=f(\phi)$ clearly shows that m_A varies strongly with ϕ and only for $\phi=1$ m_A has the order of 1. This indicates thus that the traditional statement that generally m_A is nearly constant and about 1 is severely misleading and totally ignored the essential difference between an alloy and pure metals. It is just this ignorance which has led to false interpretations of experiments and has made the method of studying diffusion behaviors by measuring SRO kinetics disputed and hardly practicable. Nevertheless, the method of the measurement of the change of the SRO induced resistivity is especially valuable because, by different heat treatments, we may gain the infomation about the annealing-out of the quenched-in vacancies which occurs simultaneously during the SRO formation and directly influences the rate of ordering. If the mechanisms of both SRO formation and vacancy annihilation are cleared, the complete diffusion data can be obtained from such measurements [4].

References

[1] G. Yu and K. Lücke, *Acta metall.mater.* 40, 2523 (1992)

[2] W. Kohl, R.Scheffel, H. Heidsiek, and K. Lücke,
Acta metall.mater. 31, 1859 (1983);
W. Kohl, *Thesis* RWTH Aachen (1984)

[3] W. Pfeiler, *Acta metall. mater.* 36, 2417 (1988)

[4] G. Yu, *SRO Formation and Point Defect Behavious in Concentrated Alloys*
(in Germain) VDI Verlag, Düsseldorf (1991); *Phys. Rev. B* 46, 642 (1992)

[5] S. Radelaar, *J. Phys. Chem. Solids* 31, 219 (1970)

[6] G. Yu and K. Lücke, to be published

[7] G.E. Murch, *Phil. Mag.(A)* 45, 941 (1982)

[8] K. Binder (Ed.), *Application of the Monte Carlo Method in Statistical Physics*
Springer Verlag, Berlin (1983)

[9] U. Gahn and W. Pitsch, *Z. Metallk.* 78, 324 (1987)

[10] G. Yu and K. Lücke, to be published in *Phys.Rev. B*

[11] R. Kikuchi and H. Sato, *Acta metall. mater.* 22, 1099 (1974)

[12] Y.Y. Li, *J. Chem.Phys.* 17, 447 (1949)

[13] J.R. Manning, *Diffusion Kinetics for Atoms in Crystals* VAN Nostrand Com (1968);
Phys. Rev. B 4, 1111 (1971)

[14] R. Kikuchi and H. Sato, *J. Chem. Phys.* 57, 4962 (1972)

[15] C.P. Flynn, *Point Defects and Diffusion* Calrendon Press, Oxford (1972)

[16] U. Gahn, *J. Phys. Chem. Solids* 43, 977 (1982)

Diffusion in the Intermetallic Compounds TiAl and Co_2Nb

Helmut Mehrer, Wolfgang Sprengel, and Martin Denkinger

Institut für Metallforschung
Universität Münster, Wilhelm-Klemm-Strasse 10
D-4400 Münster, Germany

Abstract

Self-diffusion of titanium in the intermetallic compound γ-TiAl was investigated using the radiotracer method. The temperature dependence of the diffusivity is described by a pre-exponential factor of $1.53 \cdot 10^{-4}$ m^2s^{-1} and an activation enthalpy of 291 $kJmol^{-1}$. These values indicate that self-diffusion in γ-TiAl occurs via thermal vacancies. The radiotracer data are discussed together with available positron annihilation data, density measurements, and multiphase diffusion data for the Ti-Al system.

Solid state diffusion reaction in diffusion couples of Co and Nb has been studied using optical metallography and electron microprobe analysis. Parabolic growth constants for two of the three intermetallic compounds of the Co-Nb system have been determined. Interdiffusion coefficients for the cubic Laves phase Co_2Nb have been evaluated using the Boltzmann-Matano method. They are discussed together with density measurements in the Co-Nb system and with the scarce information on diffusion in other Laves phases available in the literature.

Diffusion in Ordered Alloys
Edited by B. Fultz, R.W. Cahn, and D. Gupta
The Minerals, Metals & Materials Society, 1993

1 Introduction

Diffusion in intermetallic compounds – despite of the progress achieved in recent years (for recent reviews and data collections see, e.g., [1-6]) – is an area which urgently needs further experimental efforts especially in view of the increasing importance of intermetallics as materials of advanced technology [7-11]. The present paper consists of two main parts:

In Section 2 we review available information on diffusion and defect structure on γ-TiAl including a recent radiotracer diffusion study from our laboratory. Titanium-aluminides are considered as highly promising light-weight alloys for structural applications at high temperatures. Their high-temperature strength is controlled by creep processes for which diffusion is a key property [12]. We report results of a study of self-diffusion of titanium in the single-phase intermetallic compound γ-TiAl, which has been published in more details elsewhere [14]. According to our knowledge this is the first radiotracer diffusion study performed on an intermetallic compound of the Ti-Al system. Furthermore, we discuss our tracer results in connection with a multiphase diffusion study available in the literature [15] and with information on the defect structure from positron annihilation and density measurements for this material.

In Section 3 we review results of a multiphase diffusion study in diffusion couples of Co and Nb from our laboratory, which have been partly published recently [17]. When diffusion couples of Co/Nb are annealed at high temperatures the formation and growth of three intermetallic phases can be observed. The growth kinetics of two of these phases, Co_2Nb and Co_7Nb_2, has been studied. Growth of the CoNb-phase also occurs. It is, however, so slow that its growth kinetics could not be determined by optical means. One of these phases is the cubic Laves phase with the approximate composition Co_2Nb. Laves phases are by far the largest class of intermetallic compounds. Some properties of Laves phases, and of alloys containing Laves phases have been recently reviewed by Livingston with an eye to their potential as high-temperature structural materials [13]. We will also report results about interdiffusion in the cubic Laves phase Co_2Nb and discuss these results in combination with the very scarce information available about diffusion and defect structure in Laves phase compounds.

2 Titanium self-diffusion, interdiffusion, and defect structure in the intermetallic compound γ-TiAl

2.1 The Ti-Al system

A recent version of the Ti-Al phase diagram [18] is shown in figure 1. Three intermetallic compounds are well-established in the Ti-Al system: a hexagonal compound Ti_3Al with DO_{19}-structure (also denoted as α_2) which can accomodate several atom percent off-stoichiometry, a tetragonal compound (γ-TiAl) with $L1_0$-structure (also denoted as CuAu(I)-structure) which can also accommodate several atom percent off-stoichiometry especially on the Al-rich side, and a stoichiometric compound $TiAl_3$ with tetragonal DO_{22}-

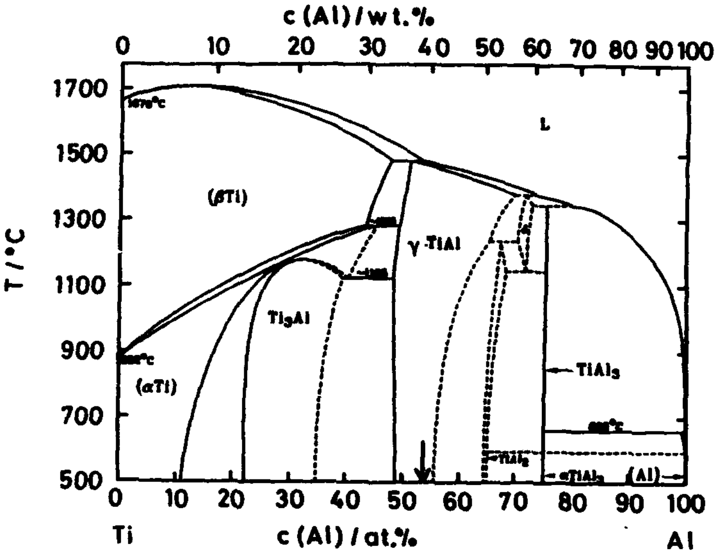

Figure 1: Phase diagram of the system Ti-Al according to [18]

structure. With respect to their potential for structural applications, intermetallic alloys with two-phase microstructure based on γ-TiAl and Ti$_3$Al have advantages over single-phase γ-TiAl alloys because they exhibit some macroscopic ductility. On the other hand, for a better understanding of the diffusional properties of the system diffusion data for the single-phase intermetallics are needed.

In our laboratory we have started diffusion work on the Ti-Al system. Here we report results for γ-TiAl. γ-TiAl can be considered as a slightly distorted face-centered (fcc) lattice with CuAu type order. The ratio between lattice parameters in the direction of the tetragonal axis and perpendicular to it has a value of about 1.02 [19].

2.2 Experimental procedure

Details of the experimental procedure have been already published elsewhere [14]. Therefore, we only highlight the main steps: Polycrystalline material of the compound γ-TiAl was prepared by a skull melting technique from Ti sponge and an Al electrode at the *Max-Planck-Institut für Eisenforschung in Düsseldorf.* According to chemical and electron microprobe analyses the composition was 46 at.% Ti and 54 at.% Al (see arrow in figure 1). In agreement with the phase diagram of figure 1, optical metallography and X-ray diffractometry indicated that the material was indeed single phase. The average grain size of the polycrystals was about 150 μm.

The diffusion experiments were performed with the tracer method utilizing the radioisotope ^{44}Ti, which was produced by irradiating a Sc-foil with protons in the compact cyclotron of the *Kernforschungszentrum Karlsruhe*. The aqueous solution of ^{44}Ti fluoride obtained after some radiochemistry was dropped onto the polished surface of the disk-shaped specimens and then dried by an infrared lamp. The diffusion anneals were carried out in ultra high vacuum at specified temperatures measured either by a thermocouple or by a pyrometer. Serial sectioning was accomplished with the help of a grinding device, which had been developed in our laboratory for the sectioning of brittle samples. The section thicknesses were determined from the sample diameters, the section weights, and the macroscopic density (3.70 g/cm^3) which was determined by the Archimedean method. The ^{44}Ti activities were measured using a well-type intrinsic Ge detector.

2.3 Results of ^{44}Ti diffusion

The diffusion condition is equivalent to a thin layer source, diffusing into a semi-infinite cylinder. The near-surface ranges of the penetration profiles shown in figure 2 can be described by the thin film solution of the diffusion equation,

$$c(x,t) = \frac{M}{\sqrt{\pi D^* t}} \exp\left(\frac{-x^2}{4 D^* t}\right) , \qquad (1)$$

where $c(x,t)$ is the tracer concentration at a depth x after a diffusion anneal of duration t. D^* is the tracer diffusion coefficient and M the initial amount of the tracer at the surface. For deeper penetrations, not shown in figure 2, deviations are observed which can be attributed to diffusion along grain boundaries. For further details the reader is referred to [14].

The temperature dependence of the diffusion coefficient is shown in figure 3. The solid line represents the following Arrhenius fit to the ^{44}Ti-data (triangles):

$$D^*_{Ti} = 1.53 \cdot 10^{-4} \exp\left(\frac{-291 \text{ kJmol}^{-1}}{RT}\right) \text{ m}^2\text{s}^{-1} . \qquad (2)$$

The dashed lines represent interdiffusion coefficients [15] and will be discussed later.

2.4 Discussion of diffusion and defect structure in γ-TiAl

According to our knowledge the present study is the first radiotracer self-diffusion experiment for a titanium aluminide. In addition there is only very scarce information on diffusion in other compounds of $L1_0$ type (CuAu type) structure (see, e.g., [3, 4]). In the binary Fe-Pt alloy system at about equiatomic composition an ordered $L1_0$-structure exists below 1573 K. The diffusion of ^{197}Pt in this alloy was studied by Kucera et al. [16]. Figure 4 shows in a *homologous* temperature scale a comparison of the present data with Pt self-diffusion in the isotypic $Fe_{50}Pt_{50}$-alloy. (Melting temperatures, T_m, have been used to normalize the temperature scale. For γ-TiAl instead of T_m the well-defined temperature of the peritectic decomposition (1708 K) has been used, which according to figure 1 is very close to the liquidus temperature anyway.) Also shown in figure 4 are self-diffusion data for several fcc metals and for indium parallel and perpendicular to its tetragonal

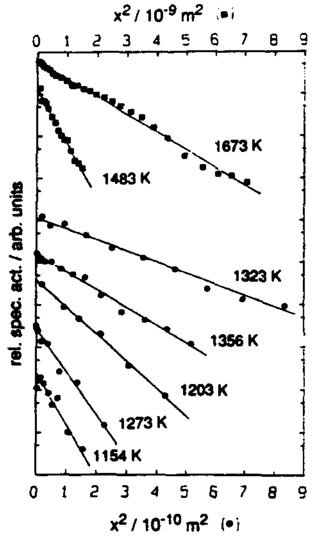

Figure 2: Concentration-depth profiles of ^{44}Ti in polycrystals of γ-TiAl

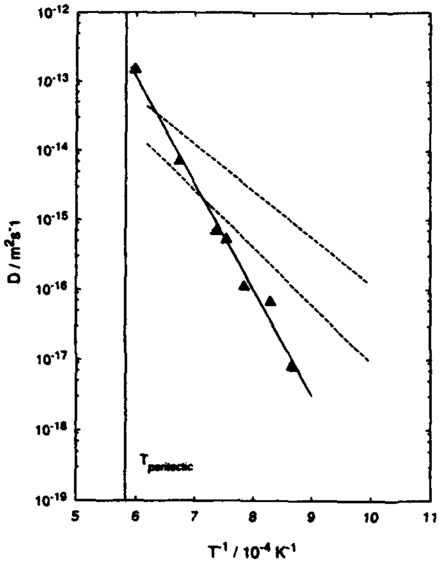

Figure 3: Arrhenius diagram of diffusion in γ-TiAl

axis. References of the self-diffusion data can be found, e.g., in [4].

Figure 4 shows the following:

- Titanium self-diffusion in γ-TiAl is similar to platinum self-diffusion in the isotypic $Fe_{50}Pt_{50}$ structure.
- Titanium self-diffusion in γ-TiAl lies within the 'diffusion spectrum' of fcc metals.
- Titanium self-diffusion in γ-TiAl is also similar to self-diffusion in both principal directions of indium.

These findings provide evidence that diffusion in γ-TiAl occurs via thermal vacancies. If the off-stoichiometry of the investigated material $Ti_{46}Al_{54}$ were accomodated by structural (also denoted as constitutional) vacancies as many as 4 percent of these defects would be necessary and then should be available as diffusion vehicles. The values of the pre-exponential factor and the activation enthalpy for Ti diffusion in equation (2) as well as the similarity of the diffusion behaviour to materials where thermal vacancies are well-established vehicles of diffusion (see figure 4) plead for a thermal vacancy mechanism and against significant contributions from structural vacancies.

Very recently Schaefer and coworkers [20] have studied the formation of thermal vacancies in $Ti_{49}Al_{51}$ using positron lifetime spectroscopy. An effective value for the formation enthalpy of vacancies of 1.38 eV (133 kJmol^{-1}) was deduced. Together with a normal

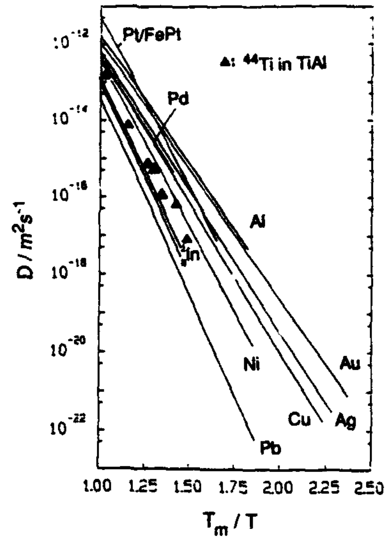

Figure 4: Self-diffusion in γ-TiAl and other materials in a homologous temperature scale

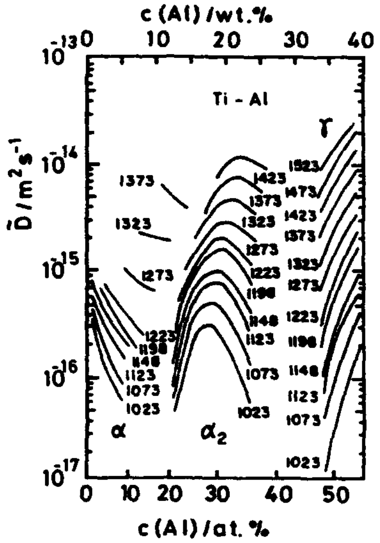

Figure 5: Interdiffusion coefficients determined from pure Ti and γ-$Ti_{46}Al_{54}$ diffusion couples by Hirano and Iijima[15]; (Diffusion data for the β-phase have been omitted)

value for the formation entropy the positron measurements suggest a vacancy concentration of about $1.6 \cdot 10^{-4}$ at. fraction near the peritectic decomposition temperature of γ-TiAl. This value is similar to typical vacancy concentrations near the melting temperatures in fcc metals (see, e.g., [24]).

Shirai and Yamaguchi [21] have reported a positron lifetime spectroscopy study on $Ti_{51}Al_{49}$, $Ti_{48}Al_{52}$ and $Ti_{44}Al_{56}$ compounds after electron irradiation, proton irradiation, and after deformation in compression. It is well-known that electron irradiation essentially generates vacancies and interstitials. In contrast to interstitials, vacancies can act as traps for positrons. After electron irradiation new positron lifetime components with lifetimes around 200 ps for $Ti_{44}Al_{56}$ and around 195 ps for $Ti_{51}Al_{49}$ were observed, which are distinctly different from the value of 152 ps observed in fully annealed compounds. The authors ascribe the higher lifetimes to positrons annihilating in radiation induced vacancies. The authors also conclude that there are no constitutional vacancies on either side of the stoichiometric composition in γ-TiAl because otherwise all positrons would be trapped in constitutional vacancies. The small fraction of vacancies introduced by electron irradiation (about 10^{-4}) could then cause no further change in positron lifetime. This conclusion is strongly supported by the above mentioned positron study of vacancies in thermal equilibrium and by practically the same value of about 200 ps deduced for the lifetime of positrons trapped in thermal vacancies [20].

Already in 1954 Elliot and Rostocker [22] had published a quantitative study of intensities of (220) and (110) X-ray diffraction lines from Al-rich off-stoichiometric γ-TiAl. They concluded that excess Al atoms replace Ti atoms but otherwise preserve long range $L1_0$ order. Recently, Vujic et al. [23] have determined lattice parameters a and c in γ-TiAl between 50 and 58 at.% Al from X-ray measurements. From the lattice parameter data they calculated X-ray densities assuming either constitutional vacancies on Ti sites or Al antisite atoms on Ti sites. From a comparison of gravimetric densities measured by the Archimedean method and the calculated X-ray densities they confirmed that no structural vacancies are present and that Al antisite atoms are the predominant structural defects.

Multiphase interdiffusion in the Ti-Al system especially on the Ti-rich side, has been studied by Hirano and Iijima [15] on diffusion couples of pure Ti and γ-$Ti_{46}Al_{54}$ using electron probe microanalysis and the Boltzmann-Matano method. Figure 5 shows interdiffusion coefficients from the work of Hirano and Iijima [15]. In the γ-TiAl phase, the interdiffusion coefficient increases with increasing Al content. In figure 3 the interdiffusion coefficients from figure 5 pertaining to the lowest and highest Al content of γ-TiAl investigated in [15] have been plotted as dashed lines. The upper line corresponds to practically the same composition investigated in our laboratory by the radiotracer technique.

The interdiffusion coefficient, $\tilde{D}$, is related to the tracer self-diffusion coefficients, D_A^* and D_B^* of the components of a homogenous A-B alloy, through Manning's generalization of Darken's equation [25]

$$\tilde{D} = (X_A D_B^* + X_B D_A^*)\, \Phi\, r\,. \tag{3}$$

Here X_A and X_B denote molar fractions of the components, Φ is the thermodynamic factor, and r is the so-called vacancy wind factor which usually is of the order of unity. Using a classical result from thermodynamics of binary alloys the thermodynamic factor can be written as

$$\Phi = \frac{X_A X_B}{RT}\,\frac{\mathrm{d}^2 G}{\mathrm{d}X_A^2}\,, \tag{4}$$

where G denotes Gibbs free energy. The thermodynamic factor is larger than unity for phases with negative deviations from ideality ($\Delta G < 1$), and smaller than unity in the opposite case.

Unfortunately the thermodynamic factor for γ-TiAl is not known to us. However, thermodynamic factors in intermetallic compounds are often larger, sometimes even considerably larger than unity due to the attractive interaction between the constituents. As a consequence interdiffusion coefficients are often larger than tracer diffusivities and activation enthalpies of interdiffusion are often smaller than for tracer diffusion.

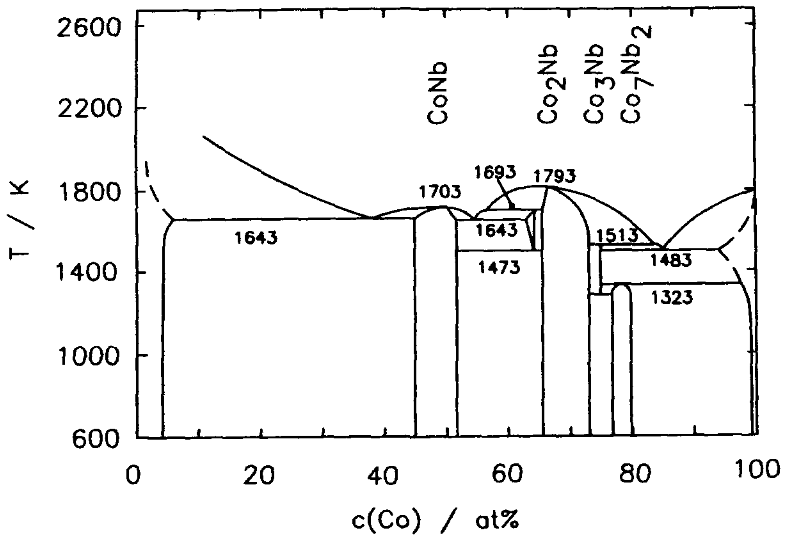

Figure 6: Phase diagram of the system Co-Nb according to [26]

In diffusion couples of pure Ti and γ-TiAl Kirkendall marker shifts towards the Ti-rich side of the couple have also been observed [15]. In a single-phase diffusion couple such an observation would indicate that Ti atoms diffuse faster than Al atoms. However, for multiphase diffusion couples such a conclusion is not justified. The behaviour of Kirkendall markers in multiphase diffusion couples is more complicated than in single-phase couples especially due to the influence of interfaces, which, e.g., can act as sources and sinks for vacancies.

3 Solid state diffusion reaction in the Co-Nb system

3.1 The Co-Nb system

A recent version of the phase diagram of the Co-Nb system according to [26] is shown in figure 6. Three intermetallic compounds exist in the Co-Nb system down to room temperature: an almost equiatomic phase CoNb with W_6Fe_7-structure (also denoted as μ-phase), a cubic phase denoted as Co_2Nb with Cu_2Mg-structure (cubic Laves phase), which, however, can accommodate several percent off-stoichiometry on the Co rich side, and an almost stoichiometric compound Co_7Nb_2.

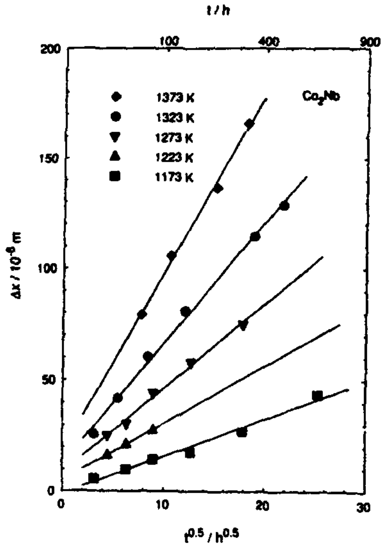

Figure 7: Growth kinetics of Co_2Nb in Co/Nb diffusion couples

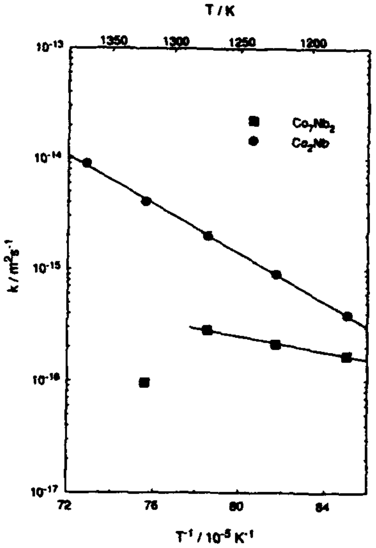

Figure 8: Growth constants for Co_2Nb- and Co_7Nb_2-layers in Co/Nb diffusion couples

3.2 Experimental procedure

Solid state diffusion reaction (multiphasc diffusion) has been studied in diffusion couples of pure cobalt and pure niobium in the temperature range 1173 K to 1473 K. After each diffusion anneal the samples were polished perpendicular to the diffusion zone. The surface was etched and the layer thicknesses of the intermetallic phases were measured with an optical microscope. The growth kinetics of those phases that grew fast enough, to be studied by optical means, were investigated for various temperatures. Concentration-depth profiles across the diffusion zones were determined using an electron microprobe analyzer operated in the point counting mode. Interdiffusion coefficients for the cubic Laves phase Co_2Nb have been evaluated using the Boltzmann-Matano- and Sauer-Freise methods. For further details about the experimental procedure and about results concerning the phase equilibria the reader is referred to a forthcoming paper [17].

3.3 Growth kinetics of intermetallic compounds in the Co-Nb system

In the diffusion zone of Co/Nb diffusion couples annealed below 1350 K in addidtion the two primary solid solutions three intermetallic phase layers CoNb, Co_2Nb, and Co_7Nb_2 separated by four interfaces are observed. In diffusion couples annealed above 1323 K only layers of CoNb and Co_2Nb and three interfaces are present. This observation is in agreement with the Co-Nb phase diagram shown in figure 6, but at variance with the phase diagram which can be found in [18]. Additionally the homogeneity range of the Co_2Nb phase broadens from 68.5–73 at% Co at 1173 K towards 67–77 at% Co (the maximum range) at 1413 K.

Figure 7 shows plots of the layer thickness Δx of the Co_2Nb phase versus the square root of diffusion time t according to

$$\Delta x^2 = 2 k_i t . \tag{5}$$

k_i denotes the growth constant of the phase i. Parabolic growth of the Co_2Nb phase without significant incubation time is indeed observed. Similar behaviour is found for Co_7Nb_2. Parabolic growth implies that the growth kinetics is diffusion controlled. Slow growth of the CoNb compound also occurs, however, the growth kinetics could not be investigated since the layer thickness never exceeded a few μm.

Figure 8 shows the temperature dependences for the growth constants of the Co_2Nb and Co_7Nb_2 layers. The growth constant of Co_2Nb increases with temperature, T, according to an Arrhenius law

$$k = 7.4 \cdot 10^{-7} \exp\left(\frac{-211\,\mathrm{kJmol^{-1}}}{RT}\right)\ \mathrm{m^2s^{-1}} , \tag{6}$$

where R denotes the gas constant. The growth constant of Co_7Nb_2 has a maximum near 1300 K. It is always smaller than the growth constant of Co_2Nb. As already mentioned at diffusion temperatures above 1323 K the Co_7Nb_2 phase diappears.

Kidson [27] has shown that growth constants for completely diffusion controlled growth have the following meaning

$$k_j = \left[\frac{(D\,K)_{kj} - (D\,K)_{jk}}{C^{eq}_{jk} - C^{eq}_{kj}}\right] - \left[\frac{(D\,K)_{ji} - (D\,K)_{ij}}{C^{eq}_{ij} - C^{eq}_{ji}}\right] . \tag{7}$$

C^{eq}_{ij} denotes the equilibrium composition on the i-side of an i/j interface, D_{ij} the interdiffusion coefficient in the i-phase near the i/j -interface, and K_{ij} is determined by the concentration gradient in the i-phase near the i/j-interface. In the derivation of equation (7) any influence of interface processes like phase nucleation, atomic transfer across the interface, and the creation and/or annihilation of point defects at the interfaces has been already disregarded, which is only justified for long enough diffusion times when the growth process is completely diffusion controlled [28, 29]. Even for this simple case growth constants have a complex meaning because they depend on diffusivities in all the layers present in the diffusion zone, on the concentration gradients on both sides of the interfaces, and on the (sometimes temperature dependent) solubility limits of the phases. If one deduces an activation enthalpy for the growth process, which in our case is possible for Co_2Nb, it still may have a complex meaning. Its value is usually not identical with

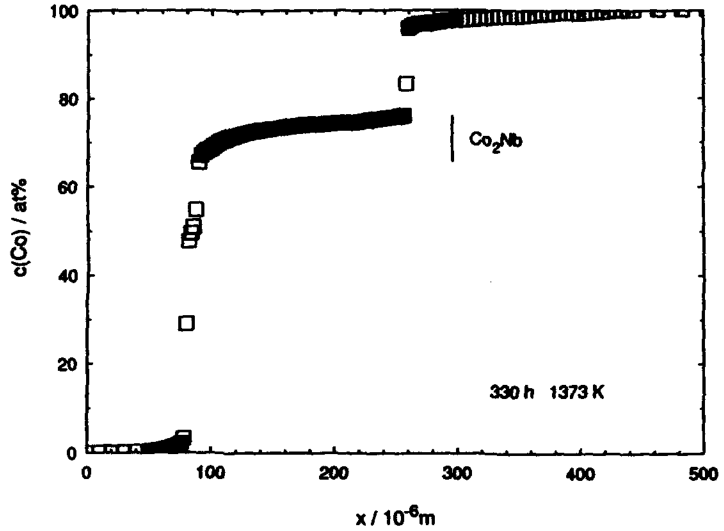

Figure 9: Concentration penetration plot for a Co/Nb couple annealed for 330 h at 1373 K

the activation enthalpy of interdiffusion in the pertaining layer. In the case of Co_7Nb_2 the temperature dependence of the growth constant cannot even be described by an Arrhenius relation.

3.4 Interdiffusion in the cubic Laves phase Co_2Nb

A typical concentration penetration plot obtained by electron probe microanalysis for a couple annealed at 1373 K for 330 h is shown in figure 9. The Co_2Nb layer with some stoichiometry range on the Co rich side between about 69 and 76 at.% Co is clearly observed. The CoNb phase is visible in optical micrographs (see [17]). However, its thickness is so small that it can be easily overlooked in electron microprobe analysis.

Boltzmann-Matano analysis has been used to evaluate interdiffusion coefficients for Co_2Nb as a function of composition from experimental concentration-depth profiles. If the variation of the molar volume with concentration reported in [30] is taken into account by applying the modification of the Boltzmann-Matano analysis introduced by Sauer and Freise and den Broeder [31, 32] very similar results are obtained [34].

Figure 10 shows the results using the molar fractions of Co as the concentration units for Matano's analysis. The interdiffusion coefficients have a significant compositional dependence with a maximum between 73 and 74 at.% Co. Arrhenius plots of the interdiffusion coefficients in the Co_2Nb-phase for various compositions are shown in figure 11. The activation enthalpy of interdiffusion decreases slightly with increasing Co concentration from 173 kJmol^{-1} for 70 at% Co to 157 kJmol^{-1} for 73 at% Co. The pre-exponential

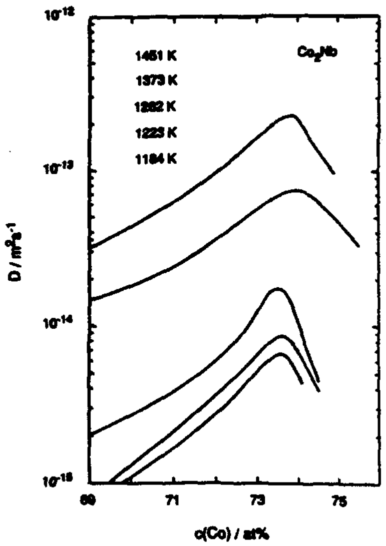

Figure 10: Concentration dependence of the interdiffusion coefficients in Co_2Nb

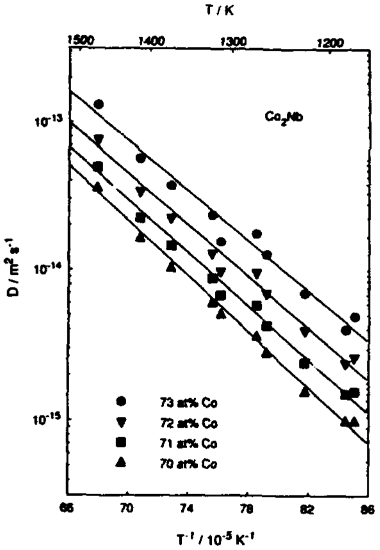

Figure 11: Interdiffusion coefficients in Co_2Nb-phase for various compositions

factor $4 \cdot 10^{-8}$ m^2s^{-1} is almost independent of composition. The activation enthalpy of interdiffusion is not much different from the activation enthalpy observed for the growth constant of the Co_2Nb phase indicating that the growth kinetics of this phase in Co/Nb diffusion couples is largely controlled by bulk diffusion through this phase.

3.5 Some remarks on diffusion and defect structure in Laves phases

Laves phase compounds crystallize with the cubic $MgCu_2$ (also denoted as C-15), the hexagonal $MgNi_2$ (C-36), and the hexagonal $MgZn_2$ (C-14) structures. The three structures are all densely packed with averaged coordination numbers larger than 12. Only atoms from one species are in contact to each other. At present there are only very few diffusion studies and even less defect studies, although - as already mentioned - Laves phases represent the largest group of intermetallic compounds.

According to our knowledge the data of figure 10 and 11 represent the first set of diffusion data for the cubic Laves phase Co_2Nb. As already mentioned in the previous section interdiffusion coefficients pertain to diffusion in a compound with a composition gradient. According to equation (3), apart from the component diffusivities of Co and Nb, the interdiffusion coefficient contains the thermodynamic factor of Co_2Nb. Presumably the maximum in the interdiffusion coefficient is due to a maximum in the thermodynamic factor.

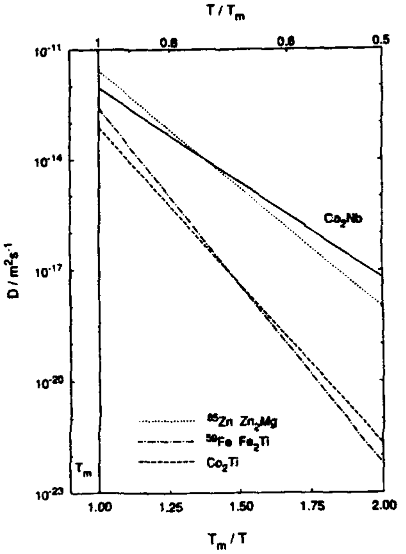

Figure 12: Diffusion processes in Co_2Nb and other Laves compounds in a homologous temperature scale

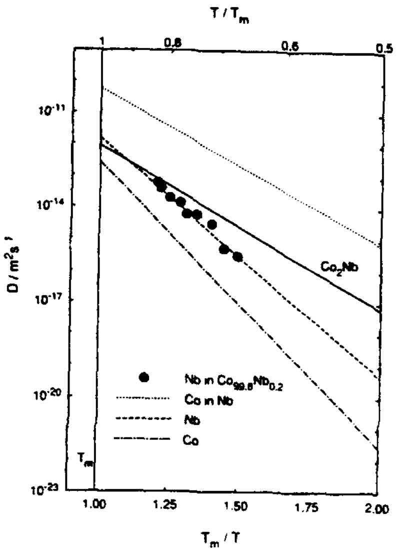

Figure 13: Diffusion processes in Co_2Nb and other materials in a homologous temperature scale

Saito and Beck [33] have performed a comparison of the X-ray density with gravimetrically measured densities for the Co-rich compounds of the Co-Nb system. Their measurements show that the variable stoichiometry of the Co_2Nb Laves phase is the result of the progressive occupation of Nb sites by Co atoms, and not the result of structural vacancies in the Nb sublattice. It is well-known that in intermetallic compounds with B2 order (CsCl stucture) of varying stoichiometry the diffusion coefficient shows a minimum near the stoichiometric composition because for off-stoichiometric compositions structural vacancies can act as additional diffusion vehicles [3]. In contrast to structural vacancies antisite atoms will not act as additional diffusion vehicles.

Figure 12 shows in a homologous temperature scale an Arrhenius diagram of all diffusion data for Laves phase compounds known to us. Günzel et al. [40] reported tracer diffusion of ^{65}Zn in Zn_2Mg, which is a hexagonal (C-14) Laves compound. Tracer diffusion of ^{59}Fe in Fe_2Ti – another hexagonal C-14 compound – was studied by Shinjaev [42]. Finally, interdiffusion coefficients in the Laves phase Co_2Ti from the work of van der Straten et al. [41] are displayed in figure 12. Obviously for homologeous temperatures the diffusion properties of the cubic Laves phase Co_2Nb and of the hexagonal Laves phase Zn_2Mg are similar.

Figure 13 shows a comparison of interdiffusion in Co_2Nb (composition 70 at.% Co) with self-diffusion processes in pure Co [4, 35] and pure Nb [4, 36]. Also shown in figure 13 as full circles are interdiffusion coefficients which originate from our concentration-depth profiles in the range of the very Co rich solid solution (see figure 9). These data essentially represent Nb diffusion in Co. Impurity diffusion of Co in Nb [37, 4] is a diffusion process which is clearly faster than diffusion in Co_2Nb. Very likely it occurs by an interstitial-substitutional exchange mechanism [38] where the exchange is mediated by vacancies similar to well-established cases of fast diffusing foreign atoms in germanium (see, e.g., [39]). Processes like self-diffusion in Nb and in fcc Co and Nb diffusion in Co, which occur by thermal vacancies, are somewhat slower than interdiffusion in Co_2Nb. However, one should keep in mind that interdiffusion coefficients in intermetallic compounds due to the influence of the thermodynamic factor (see equation (2)) are often larger than tracer diffusivities and activation enthalpies often smaller than in tracer diffusion experiments on the same material.

The already mentioned findings of Saito and Beck [33], the values of the pre-exponential factor and the activation enthalpy for interdiffusion as well as the similarity of the diffusion behaviour to materials where thermal vacancies are well-established vehicles of diffusion (see figure 13) plead for a thermal vacancy mechanism in Co_2Nb as well.

4 Summary and conclusions

Tracer diffusion studies in the Ti-Al system in our laboratory have been started with experiments of titanium diffusion in single-phase γ-TiAl. In the Co-Nb system phase equilibria, growth of intermetallic compounds, and interdiffusion in the cubic Laves phase Co_2Nb have been investigated. Our diffusion results are discussed together with information on diffusion and defect structure in γ-TiAl, on the Co-Nb system, and on other Laves phase compounds.

The salient points obtained for γ-TiAl are the following:

1. Titanium self-diffusion occurs via thermal vacancies.
2. The difference between our tracer diffusion data and interdiffusion data from literature [15] is largely attributed to the thermodynamic factor.
3. Deviations from stoichiometry are compensated by antisite atoms.
4. A significant contribution of structural vacancies to diffusion in off-stoichiometric material is unlikely.
5. Conclusions 1), 3), and 4) are strongly supported by positron annihilation studies [20, 21] and by density measurements [23].

The salient points obtained for Co-Nb are the following:

1. All intermetallic compounds (CoNb, Co_2Nb, and Co_7Nb_2) which could be expected on the basis of the 'Smithells' version [26] of the Co-Nb phase diagram are present in the diffusion zones of Co/Nb diffusion couples.

2. Parabolic growth was observed for Co_2Nb and Co_7Nb_2, whereas growth of CoNb was too slow to be determined by optical means.
3. The temperature dependence of the growth constant of Co_2Nb can be described by an activation enthalpy of 211 $kJmol^{-1}$. The growth constant of Co_7Nb_2 passes through a maximum near 1300 K.
4. Interdiffusion coefficients in the cubic Laves phase Co_2Nb show a maximum as a function of composition, which is tentatively attributed to the thermodynamic factor.
5. The interdiffusion coefficients obey Arrhenius laws for fixed compositions of Co_2Nb. The activation enthalpies vary from 173 $kJmol^{-1}$ to 157 $kJmol^{-1}$ for 70 at% Co to 73 at% Co. The pre-exponential factor is $4 \cdot 10^{-8}$ m^2s^{-1} almost independent of composition.
6. Deviations from stoichiometry according to density measurements are compensated by Co antisite atoms on the Nb sublattice [33].
7. Conclusion 6) together with similarities of the diffusion behaviour of Co_2Nb with well-established cases of thermal vacancy diffusion plead for thermal vacancies as dominating diffusion vehicles in Co_2Nb.

Acknowledgements

This work was partly supported by the Deutsche Forschungsgemeinschaft. We are grateful to Prof.Dr.H.E. Schaefer (Universität Stuttgart) for providing positron annihilation data prior to publication.

References

1) H.Bakker, *Tracer Diffusion in Intermetallic Compounds*, in: Diffusion in Metals and Alloys, Diffusion and Defect Monograph Series No.7 (1983) Trans Tech Publications, F.J.Kedves and D.L.Beke, eds.
2) H.Bakker, in: Diffusion in Crystalline Solids, G.E.Murch and A.S.Nowick, eds., (Academic Press, Inc., 1984, 189).
3) H.Wever, J.Hünecke, and G.Frohberg, *Diffusion in intermetallischen Phasen*, Z.Metallkde., 80(1989) 389-397.
4) H.Mehrer, ed., Diffusion in Solid Metals and Alloys, (Landolt-Börnstein, New Series, Vol. 26, Springer-Verlag, 1990).
5) H.Bakker and D.M.R. Lo Cascio, *Diffusion in Intermetallic Compounds: Underlying Aspects*, Defect and Diffusion Forum, in the press.
6) M.Koiwa, H.Yasuda, and H.Nakajima, *Diffusion in* $L1_2$*-type Intermetallic Compounds*, Defect and Diffusion Forum, in the press.

7) G.Sauthoff, *Intermetallic Phases as High-Temperature Materials*, Z.Metallkde., 77(1986) 654-683.

8) G.Sauthoff, *Intermetallic Alloys - Overwiew on New Materials Developments for Structural Applications in West-Germany*, Z.Metallkde., 81(1990) 855-861.

9) H.Wever, *Intermetallic Compounds*, Defect and Diffusion Forum, 83(1992) 55-72.

10) S.Naka, M.Thomas, and T.Khan, *Potential and Prospects of Some Intermetallic Compounds for Structural Applications*, Materials Science and Technology, 8(1992) 291-298.

11) M.Yamaguchi, *High Temperature Intermetallics - with particular Emphasis on TiAl*, Materials Science and Technology, 8(1992) 299-307.

12) G.Sauthoff, *Creep and Diffusion in Intermetallic Alloys*, this symposium.

13) J.D.Livingston, *Laves-Phase Superalloys?*, Phys. Stat. Sol. (a), 131(1992) 415-423.

14) S.Kroll, H.Mehrer, N.A. Stolwijk, C.Herzig, R.Rosenkranz, G.Frommeyer, *Titanium Self-diffusion in the Intermetallic Compound γ-TiAl*, Z.Metallkde., 83(1992) 591-595.

15) K.Hirano, Y.Iijima, in: Diffusion in Solids– Recent Developments, M.A.Dayananda and G.E.Murch, eds.(The Metallurgical Society of AIME (1984) 141).

16) J.Kucera, B.Million, *Diffusion of Platinum in the Fe-Pt System*, Phys. Stat. Sol. (a), 31(1975) 275 -282.

17) W.Sprengel, M.Denkinger, H.Mehrer, *Solid State Diffusion Reaction and Formation of Intermetallic Compounds in the Co-Nb System*, Defect and Diffusion Forum, in the press.

18) T.B. Massalski, ed., Binary Alloy Phase Diagrams, (ASM, Metals Park Ohio, 1986).

19) W.B Pearson, Handbook of Lattice Spacings and Structures of Metals, (Pergamon Press, 1958).

20) U.Brossmann, K.Badura, H.E.Schaefer, to be published.

21) Y.Shirai and M.Yamaguchi, *Studies of Vacancies and Dislocations in TiAl by Positron Annihilation*, Materials Science and Engineering, A152(1992) 173-181.

22) R.P.Elliot and W.Rostoker, *The Influence of Aluminium on the Occupation of Lattice Sites in the TiAl Phase*, Acta Metall., 2(1954) 884-885.

23) D.Vujic, Z.Li, S.H.Wang, *Effect of Rapid Solidification and Alloying Addition on Lattice Distortion and Atomic Ordering in $L1_0$ TiAl Alloys and their Ternary Alloys*, Metall.Trans., A19(1988) 2445-2455.

24) A.Seeger, *Investigation of Point Defects in Equilibrium Concentration with particular Reference to Positron Annihilation Techniques*, J.Phys.F: Metal Phys., 3(1973) 248-294.

25) J.Philibert, Atom Movements - Diffusion and Mass Transport in Solids, (Les Editions de Physique, 1991)

26) E.A.Brandes, ed., Smithells Metals Reference Book, 6th Ed. (Butterworths, London, 1983).

27) G.V.Kidson, *Some Aspects of the Growth of Diffusion Layers in Binary Systems*, J. Nucl. Mater., 3(1961) 21-29.

28) J.Philibert, *Reactive Diffusion*, Defect and Diffusion Forum, 66-69(1989) 995-1014.

29) U.Gösele, in: Alloying, J.L.Walter, M.Jackson, Ch.Sims, eds. (ASM International,

1988, 489-519).

30) A.Raman, *X-Ray Investigation in the Nb-Co System*, Z.Metallkde., 57(1966) 301-305.

31) F.Sauer, V.Freise, *Diffusion in binären Gemischen mit Volumenänderung*, Z. Elektrochemie, 66(1962) 353-363.

32) F.J.A. den Broeder, *A General Simplification and Improvement of the Boltzmann-Matano Method in the Determination of the Interdiffusion Coefficients in Binary Systems*, Scripta Metall., 3(1969) 321-326.

33) S.Saito, P.A.Beck, *Co-rich Intermediate Phases in the Nb-Co System*, Trans. Metall. Soc. AIME, 218(1960) 670-674.

34) W.Sprengel, H.Mehrer, to be published.

35) W.Bussmann, C.Herzig, W.Rempp, K.Maier, H.Mehrer, *Isotope Effect and Self-diffusion in Face-Centered Cubic Cobalt*, Phys. Stat. Sol. (a), 56(1979) 87-97.

36) R.E.Einziger, J.N.Mundy, H.A.Hoff, *Niobium Self-Diffusion*, Phys. Rev. B, 17(1978) 440-448.

37) J.Pelleg, *Diffusion of* ^{60}*Co in Niobium Single Crystals*, Phil. Mag., 33(1976) 165-172.

38) F.Wenwer, N.A.Stolwijk, H.Mehrer, *Two-stage Diffusion Profiles of Co in Nb: Evidence for the Dissociative Mechanism*, Z.Metallkde., 80(1989) 205-212.

39) N.A.Stolwijk, *Atomic Transport in Semiconductors: Diffusion Mechanisms and Chemical Trends*, Defect and Diffusion Forum, in the press.

40) R.Günzel, P.Paufler, G.E.R. Schulze, in: Diffusion in metallischen Werkstoffen, (VEB Deutscher Verlag für Grundstoffindustrie, Leipzig, 1970 183-189).

41) P.J.M. van der Straten, G.F.Bastin, F.J.J. van Loo, G.D.Rieck, *Phase Equilibria and Interdiffusion in the Cobalt-Titanium System*, Z.Metallkde., 67(1976) 152-157.

42) I.Shinjaev, *Diffuzionnye Processij v Splavakh*, (Nauka, Moskwa, 1975).

Measuring the Diffusivity of B2 Nickel Aluminide Alloys Containing Chromium Using the Square Root Diffusivity Analysis

William D. Hopfe[*], *Yoon-Ho Son*[+], *J. E. Morral*[*], *and A. D. Romig, Jr.*[++]

[*] Department of Metallurgy and Institute of Materials Science
University of Connecticut, U-136, Room 111,
97 N. Eagleville Road, Storrs, Connecticut 06269-3136 USA

[+] Korea Academy of Industrial Technology
472, Kajwa-4Dong, Seo-Ku
Inchon 404-254, Korea

[++] Materials and Process Sciences, Organization 1800
Sandia National Laboratories, Albuquerque, New Mexico 87185 USA

Abstract

The diffusivities of two off-stoichiometric NiAl alloys containing chromium have been measured by a diffusion couple technique that employs concentration differences of a few atomic percent. The concentration profiles were measured by EPMA and then evaluated using the square root diffusivity analysis. When substituting the diffusivities into error function solutions, concentration profiles were obtained that were within ±0.2 at% of EPMA data. It was found that adding chromium to $Ni_{1.28}Al_{.72}$ had the effect of decreasing D_{AlAl} and increasing D_{AlCr}, D_{CrAl}, and D_{CrCr}. The decrease in D_{AlAl} was about one fifth of that obtained when adding the same amount of aluminum.

Diffusion in Ordered Alloys
Edited by B. Fultz, R.W. Cahn, and D. Gupta
The Minerals, Metals & Materials Society, 1993

I. Introduction

The B2 nickel aluminide (NiAl) is an intermetallic compound that is important as a high temperature coating and potentially as a high temperature structural material. In order to model its interdiffusion behavior at high temperatures, it is necessary to know the diffusivity for a range of compositions.

Since the diffusivity of intermetallic compounds is subject to large variations with composition, its measurement on multicomponent alloys poses special problems. The Boltzmann-Matano analysis is not affected by the variations, but it has other limitations. For ternary alloys it cannot give the diffusivity for a predetermined composition; and for quaternary and higher order alloys it does not apply (1).

An alternative to the Boltzmann-Matano analysis is one of several analyses that were derived by assuming that the diffusivity is constant (2,3), a useful approximation when concentration differences are small. Recent work (4) has shown that one analysis, the "square root diffusivity analysis," has validity even when the diffusivity varies linearly with concentration. In the present work it was applied to measuring the diffusivity of NiAl alloys that contain less than the stoichiometric amount of Al, approximately 36%Al, and up to 7.5 at% Cr. The effect of Cr on diffusion was then compared with previous work on binary NiAl alloys.

II. Background

Shankar and Seigle (5) showed that the diffusivity of binary NiAl varies by several orders of magnitude across the single phase beta field of the phase diagram. In a plot of diffusivity vs. Al concentration the diffusivity has a deep minimum at 48-49 at% Al ($D \approx 1 \times 10^{-10}$ cm^2/sec). Presumably the formation of vacancies in alloys with more than stoichiometric Al (6) and a reduction in long range order in alloys containing less than the stoichiometric amount are primarily responsible for these changes.

The "square root diffusivity analysis" has been applied already to measuring the diffusivity of gamma phase, Ni-Cr-Al (7) and Ni-Cr-Al-Mo (8) alloys. For ternary alloys the results were within 10% of those obtained by the Boltzmann-Matano analysis (i.e. they were within the experimental error). The current work is the first time the square root diffusivity analysis has been applied to an intermetallic compound.

The analysis yields the "square root diffusivity" which is a kinetic property matrix, [r], that is related to the diffusivity matrix [D] by the relationship (9):

$$[D] = [r][r] \qquad (1)$$

The basis for the analysis applied to ternary alloys is the equation (10):

$$S_i = -\sqrt{\frac{t}{\pi}}(r_{i1}\Delta C_1^0 + r_{i2}\Delta C_2^0) \tag{2}$$

in which t is time, S_i is the amount of solute i crossing the initial interface from left to right, r_{ij} is an element of the square root diffusivity matrix, and ΔC_i^0 is the initial concentration difference between alloys on the right and the left sides of the given diffusion couple:

$$\Delta C_i^0 = C_i^R - C_i^L \tag{3}$$

Two diffusion couples are required to solve Eq. [2] for the r_{ij}'s. The diffusion couples must have the same average composition and the diffusivity obtained is for an alloy with the average composition. Additional details of the analysis method are given in several recent publications (1,7,8).

III. Experimental Procedure

The diffusivity of two aluminide alloys were obtained by making measurements on four diffusion couples. To make the couples, six alloys which differed by relatively small concentration differences were prepared from high purity Ni(99.99%), Cr(99.99%) and Al(99.99%) starting materials by repeated arc melting in a high purity argon atmosphere. The composition of each alloy prior to arc melting is given in Table 1. Arc melted buttons were drop cast into a 6 mm diameter cylindrical mold. The alloy rods were then homogenized by sealing them in nickel tubes and then annealing for 50 hours at 1200°C. The rods were then machined to 5 mm diameter rods and sectioned into 2.5 mm thick disks and polished. Because of the nature of NiAl, the alloys were brittle and individual grains often dropped out of the disks, especially in alloys that contained the smallest amount of Cr.

Table I. Composition of Alloys Prior to Arc Melting

Alloy #	Ni	Cr atomic %	Al
1	56.0	10.0	34.0
2	56.0	8.0	36.0
3	60.0	8.0	32.0
4	60.0	6.0	34.0
5	60.0	4.0	36.0
6	64.0	2.0	34.0

The diffusion couples were made by assembling a series of disks in stainless steel holders. For example, one series contained the alloys: 1/4/5/3/2/6. The holders applied hydrostatic stress to the alloys and protected them from oxidation. The holder was protected from excessive oxidation by vacuum encapsulating in quartz tubing. The assemblies were heated for 40 hours at 1200°C±2°C. Then the quartz tube was removed from the furnace and quenched in ice brine. The diffusion couple assembly was sectioned longitudinally by a diamond-impregnated saw to expose faces perpendicular to the initial interfaces of the diffusion couples. The samples were then ground and polished.

Composition profiles were measured from the diffusion couples by electron probe microanalysis (EPMA). A Cameca MBX electron probe microanalyzer was used, operating at 15 kV and a beam current of about 20 nA. The analytical spatial resolution was approximately 1 μm and the takeoff angle of the X-rays was 40 deg. Measurements were made at distance increments of 10 μm. The X-rays that were collected were automatically corrected for atomic number effects, absorption, and fluorescence by an ZAF correction program and then were converted into composition data. The composition values are accurate to better than ±2 pct relative, as determined by X-ray counting statistics.

IV. Results

Five measurements were made on each profile in order to determine [r]. These were the initial alloy concentrations, C_i^L and C_i^R; the location of the interface at the average composition, $\bar{x}_i$; and the change in solute on each side of $\bar{x}_i$, S_i^L and S_i^R. The values of $\bar{x}_i$ differed somewhat for Cr and Al due to experimental scatter (7,8).

The initial alloy concentrations were measured by averaging 25 points outside the reaction zone. These values and the standard deviations are summarized in Table II.

Table II. EPMA Measurements of the Initial Concentrations of Diffusion Couple Alloys

Alloy #	Couple	at% Cr	at% Al
1	4/1	9.5 ± 0.2	33.5 ± 0.7
2	2/6	7.0	34.7
	3/2	7.5	36.0
3	3/2	7.2	32.2
4	4/1	5.7	33.5
	5/4	5.7	33.5
5	5/4	3.7	35.5
6	2/6	1.9	34.4

The position of the interface at the average composition $(C_i^R+C_i^L)/2$ was then determined graphically from the concentration profiles.

The amount of solute $\bar{S}_i$ was taken as an average of the two areas determined graphically on each side of $\bar{x}_i$ (7,8), while the ΔC_i^o's were determined from the initial alloy compositions by Eq. [3]. In couple 2/6 the Al profile does not have a clear C_{Al}^R because of problems with the sample homogeneity. In this case $\bar{S}_{Al}$ was taken as S_i^L, the amount of solute entering alloy 2. The average concentration was taken as the average of the extrema concentrations. A similar procedure was used for the Cr profile of Couple 3/2. The $\bar{S}_i$ and ΔC_i^o for each profile of each diffusion couple are listed in Table III.

Table III. Measurements from Concentration Profiles

Couple#	ΔC^o_{Cr} at%	ΔC^o_{Al} at%	$\bar{S}_{Cr}$ at%μm	$\bar{S}_{Al}$ at%μm
2/6	-5.1	-0.3	621	337
3/2	0.4	3.8	-131	-463
4/1	3.8	-0.1	-492	-239
5/4	2.0	-2.0	-219	270

From Eq. [2] four equations can be written for each of two diffusion couples that had the same average composition (i.e. 4/1 and 3/2 as well as 2/6 and 4/5). By solving these equations simultaneously [r] was obtained for an alloy having the average composition. Finally, [D] was obtained from Eq. [1]. Both the r_{ij} coefficients and the D_{ij} coefficients are listed in Table IV.

Table IV. Square Root Diffusivity and Diffusivity Coefficients

Average Composition		CrCr	CrAl	AlCr	AlAl
4.8 at% Cr	r_{ij}	5.6	5.6	2.5	8.7
34.6 at% Al	D_{ij}	33	8.0	37	77
7.5 at% Cr	r_{ij}	6.1	1.7	3.0	7.7
33.5 at% Al	D_{ij}	42	23	42	64

Units: r_{ij}: 10^{-5} cm·sec$^{-1/2}$: D_{ij} : 10^{-10} cm^2·sec^{-1}

V. Discussion

In order to test the validity of the measured diffusivities, they were substituted into error function solutions used to calculate concentration profiles for diffusion couples. The calculations were made by software named PROFILER (available from one of the authors, JEM). The calculated profiles along with the EPMA data are shown for each diffusion couple in Fig. 1. The standard deviation between the data and the error function profiles is on the order of ±0.1 at% for Cr and ±0.2 at% for Al. The agreement here suggests that any constant diffusivity analysis could have been used to obtain a reasonable diffusivity matrix and that higher order systems could have been treated, too.

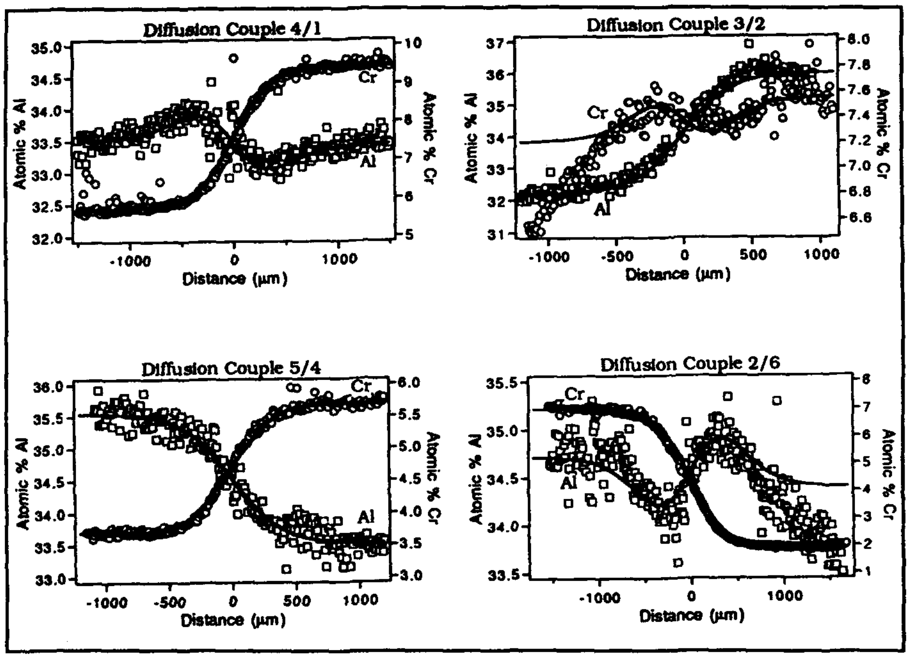

Figure 1: Concentration profiles in the four diffusion couples. Markers are EPMA data while lines were calculated by substituting the measured diffusivities into the error function solution of the diffusion equation.

The effect of adding Cr to $Ni_{1.28}Al_{.72}$ is compared in Fig. 2 to that of adding Al to the same alloy. From the data of Shankar and Seigle (5) it can be seen that adding 7.5 at% Al has the effect of reducing D_{AlAl} by nearly a factor of ten while a similar addition of Cr reduces D_{AlAl} by a factor of two. The decrease caused by adding Al is likely due to an increase in long range order, however the decrease caused by adding Cr was likely due to other reasons, for example, changes in the thermodynamic factor (11).

Adding Cr to $Ni_{1.28}Al_{.72}$ not only decreases D_{AlAl} but also increases D_{AlCr}, D_{CrAl}, and D_{CrCr} as shown in Fig. 3. The increase in D_{CrAl} is required by theory because D_{CrAl}must

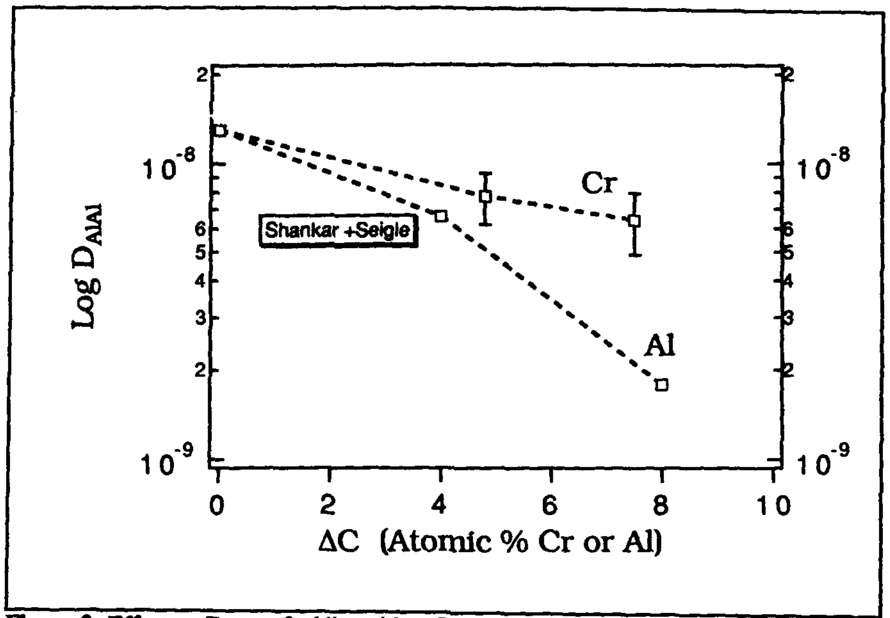

Figure 2: Effect on D_{AlAl} of adding either Cr or Al to an $Ni_{1.28}Al_{.72}$ alloy. ΔC refers to the amount of Cr or Al that is added.

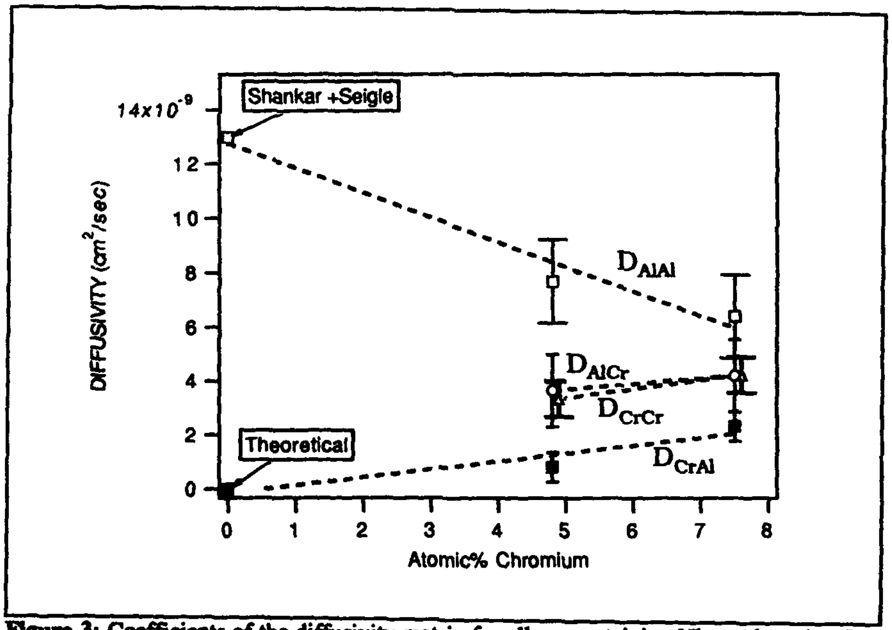

Figure 3: Coefficients of the diffusivity matrix for alloys containing $Ni_{1.28}Al_{.72}$ plus Cr.

approach zero as the concentration of Cr approaches zero (12). Otherwise a flux of Cr would be predicted by the flux equation when there is no Cr in the system.

VI. Conclusions

It has been shown that the square root diffusivity analysis can be applied to measuring the diffusivity of multicomponent intermetallic compounds. Even though it was applied here to ternary alloys, the results suggest that it could be applied to quaternary and higher order alloys. For the case of NiAl that contains less than the stoichiometric amount of Al, it was shown that adding Cr tends to reduce D_{AlAl}. Adding Al has a similar, but larger effect.

Acknowledgements

This work was supported by the National Science Foundation under grant number DMR-9025122. Also, the portion of this work performed at Sandia National laboratories was supported by the United States Department of Energy under contract No. DE-AC04-76DDP00789.

References

1. J. E. Morral, Yoon-Ho Son and M. S. Thompson, "Measuring the diffusivity of ternary, quaternary and higher order alloys," Fundamentals and Applications of Ternary Diffusion, G. R. Purdy,ed.,(New York, NY: Pergamon Press, 1990), 119-126.
2. J. S. Krishtal, A. P. Mokrov, A. V. Akimov and P. N. Zakharov, "Some ways of determining diffusion coefficients in multicomponent systems," Fiz. Metal. Metalloved., 35 (1973), 1234-1240.
3. M. S. Thompson, and J. E. Morral, "The square-root diffusivity," Acta Metall., 34(1986), 2201-2203.
4. Yoon-Ho Son, Diffusivity and Intrinsic Diffusivity Measurements on Multicomponent Alloys, Ph.D Thesis (Storrs, CT: University of Connecticut, 1992).
5. S. Shankar and L.L. Siegle, "Interdiffusion and Intrinsic Diffusion in the NiAl Phase of the Al-Ni System," Metal. Trans. A, 9A (1978), 1467-1476.
6. A. J. Bradley and A. Taylor, "An x-ray analysis of the nickel-aluminum system," Proc. Royal Soc., A159 (1937), 56-72.
7. M. S. Thompson, J. E. Morral and A. D. Romig, Jr., "Applications of the square root diffusivity to diffusion in Ni-Al-Cr alloys," Metall. Trans. A. 21A (1990), 2679-2685.
8. M. K. Stalker, J. E. Morral and A. D. Romig, Jr., "Application of the square root diffusivity to diffusion in Ni-Cr-Al-Mo alloys," (Metall. Trans. A., in Press for Jan 1993 issue).
9. J. E. Morral, "Rate constants for interdiffusion," Scripta Metall., 18 (1984), 1251-1256.
10. M. S. Thompson, and J. E. Morral. "The effect of composition on interdiffusion in ternary alloys," Acta Metall., 34 (1986), 339-346.
11. L.S. Darken, "Diffusion, mobility and their interrelation through free energy in binary metallic systems", Trans. Am. Inst. Min. Engrs., 175 (1948), 184-194.
12. J.S. Kirkaldy and D.J. Young, Diffusion in the Condensed State, (London: The Institute of Metals, 1987),158-159.

ORDER-DISORDER TRANSFORMATIONS

Phase Stability of the $L1_0$ Ordered Phase under Thermal Cycling Studied by PPM

T. Mohri and T. Ikegami

Department of Metallurgical Engineering
Hokkaido University
Sapporo, 060 Japan

Abstract

The Path Probability Method is employed to study ordering kinetics and phase stability under thermal cycles for $L1_0$ ordered phase of a spin system at 1:1 stoichiometry. Characteristic features of two types of ordering mechanism, Nucleation-Growth ordering and Spinodal ordering, are examined from the kinetic point of view. It is confirmed that an infinitesimal amount of fluctuation drives the Spinodal ordering while a critical amount of fluctuation is necessary for the Nucleation-Growth ordering. A steady state kinetic path under cyclic temperature variation is obtained in a thermodynamic configuration space. The steady state path deviates significantly from the equilibrium path in the high temperature region, which is explained based on the topological feature of the free energy contour surface. The extension of the present study of a spin system to an alloy system with the vacancy mechanism is discussed.

Diffusion in Ordered Alloys
Edited by B. Fultz, R.W. Cahn, and D. Gupta
The Minerals, Metals & Materials Society, 1993

I. Introduction

The Cluster Variation Method (hereafter CVM) [1] of statistical mechanics has been widely employed to study alloy thermodynamics. The advantage of the CVM is the fact that a wide range of atomic correlations, which play a crucial role in the phase transition, are explicitly incorporated in the free energy functional. Thereby accurate information about relevant thermodynamic quantities can be derived. Recently, by including electronic structure calculations, a first-principles approach to alloy thermodynamics has been carried out for various alloy systems [2,3].

Although equilibrium thermodynamics is a fundamental tool for understanding phase stability of a given alloy system, less information can be derived for kinetic aspects, which are particularly important in understanding the behavior of a metastable state brought about by various non-equilibrium processes. In fact, fascinating features of functional properties, owing in many cases to metastable properties and time dependent phase stability, is the central concern in designing an advanced material. Development of a reliable kinetic theory is an urgent goal in materials science.

Kikuchi's Path Probability Method (hereafter PPM) [4,5,6], which was proposed about a decade after CVM was devised, is the natural extension of the CVM to time domain, therefore various useful features are inherited from the CVM. An advantage of the PPM is that a calculated quantity in the long time limit correctly converges to the equilibrium one independently obtained by the CVM. Hence, the combination of the CVM and PPM enables one to perform a systematic study in synthesizing equilibrium and non-equilibrium aspects of the phase stability of a given material. The major stumbling block against a wide applicability of the PPM, however, is the fact that the PPM generally demands an enormous amount of variational parameters. Although the tetrahedron approximation is the common practice for the CVM study on an fcc-based alloy system, the formulation as well as the computation of the PPM within this approximation is quite complicated [7,8]. Most of the PPM studies have been limited to the bcc-based alloy system for which the pair approximation provides fairly accurate results [9].

In the description of an equilibrium state, both spin and alloy systems are equivalent. However, the essential difference between the two should be noted for the description of kinetics. The spin system is characterized by a flipping mechanism which does not necessarily conserve the concentration of up (and down) spins. While the exchange mechanism, either direct or through a vacancy, for an alloy system strictly conserves the composition. It has been recognized that the spin flipping mechanism for both the formulation and computation of the PPM demands less labor due to the restricted freedom of the evolution path, which makes the tetrahedron approximation tractable. In order to study the kinetic behavior of an fcc-based system by the PPM, the spin kinetics has been adopted by the author's group. Also, these studies are limited to 1:1 stoichiometric composition for which the composition is conserved without additional constraints. Thereby, the conserved nature of an alloy system is simulated to some extent. In the present report, two examples of the PPM studies performed by the authors' group [10,11,12], for an fcc-based $L1_0$ ordered phase are demonstrated. These are (1) ordering kinetics [10,11] and (2) phase stability under cyclic temperature variation [12].

It has been well known that the ordering reaction is driven by either Nucleation-Growth (hereafter NG) or Spinodal ordering (hereafter SP) [13,14] mechanisms. Most of the kinetic studies are, however, centred around the former mechanism. We attempted to clarify the kinetic features of the SP by examining both reactions based on the PPM calculations. In fact, one prominent feature of the PPM is that the time evolution of short range order parameters in addition to a long range order parameter are systematically derived, which is expected to provide more detailed information on the ordering kinetics. Such is the purpose of the first example, i.e., the study of ordering kinetics.

The main emphasis of the present report is placed on the second example which is motivated by the following observation. The phase stability of an intermetallic compound has been attracting broad attention. And the major theoretical efforts have been directed towards a better understanding of the stability at both the ground state and finite temperatures. The former is well investigated by electronic structure calculations, while the latter is investigated by a statistical mechanics method such as CVM or Monte Carlo method. However, the stability of the intermetallic ordered phase is not fully characterized by these two aspects only. For instance, the stability under cyclic temperature variation which is an indispensable component in designing a heat resistant intermetallic compound is basically a subject of kinetics. Such dynamical stability is controlled by various kinetic factors. Among them, the most prominent one is the diffusivity of component elements. The interplay between diffusion which drives a system towards the equilibrium state and external cooling (and heating) rates eventually induces a steady state which may be well characterized by a kinetic path traced in a thermodynamic configuration space. Since the PPM provides the time evolution of various configuration variables it is expected that the steady state behavior is well clarified by the PPM.

The organization of the present report is as follows. In the next section, a brief outline of the theoretical background of the PPM is described. The major results are demonstrated and discussed in the third section. As was described above, the present report is devoted to a spin system. The discussion of the alloy kinetics requires a detailed picture of the atomistic exchange mechanism. Such an effort has been recently initiated [7,8]. In the final section, a brief discussion of the extension of the present study to an alloy system is provided.

II. Theoretical background of the PPM

Phase equilibria and stability analyzed by the CVM

Within the tetrahedron approximation of the CVM, four independent variables (correlation functions) are sufficient to describe a disordered phase. For the $L1_0$ ordered phase, on the other hand, the number of the independent variables increases to eight due to the removal of the degeneracy among sublattices by a breaking of symmetry. Shown in Fig. 1 is the disorder-$L1_0$ phase diagram in the vicinity of 50 at.%. The transition temperature determined in the present study at 1:1 stoichiometry is $k_BT/v_{2.1} = 1.89$ where $v_{2.1}$ is the nearest neighbor pair interaction energy. Note that the temperature is, hereafter, normalized by the nearest neighbor pair interaction energy.

The broken line in the phase diagram is the Spinodal ordering (SP) temperature. Mathematically, the SP temperature is defined as the temperature at which the second order derivative of the free energy matrix with respect to the correlation functions vanishes [14]. Since the second order derivative of the free energy provides a measure of the stability of a system, the SP temperature can be regarded as a stability locus. It should be noted that unlike the case of spinodal decomposition in which concentration fluctuations lead to the

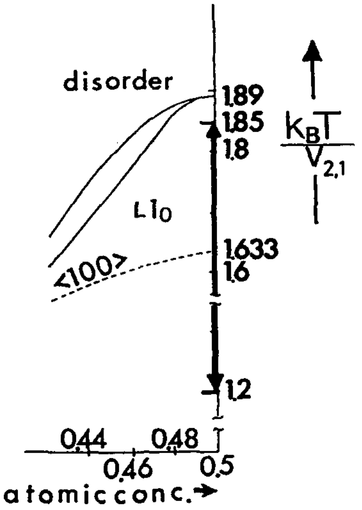

Figure 1: Disorder-$L1_0$ phase diagram in the vicinity of 1:1 stoichiometry. The broken line indicates the $\langle 100 \rangle$ Spinodal ordering locus. The temperature axis is normalized by the nearest neighbor pair interaction energy $v_{2,1}$. The arrow indicates the range of the cyclic variation of the temperature.

decomposition reaction, SP is driven by the fluctuations of order parameters. Below the SP temperature, ordering fluctuations trigger the transition which is a barrierless phase transition, whereas the Nucleation-Growth (NG) mechanism is expected above the SP temperature. The SP temperature determined in the present calculation at 1:1 stoichiometry is 1.63.

Although, as was described above, the number of the independent variables needed to describe the $L1_0$ ordered phase within the tetrahedron approximation is eight, only five of them are independent for a fixed composition at 1:1 stoichiometry due to the symmetry. These are the point correlation ξ_1^α (=-ξ_1^β), the pair correlations $\xi_2^{\alpha\alpha}$ (=$\xi_2^{\beta\beta}$) and $\xi_2^{\alpha\beta}$, the triangle correlation $\xi_3^{\alpha\alpha\beta}$ (=-$\xi_3^{\alpha\beta\beta}$) and the tetrahedron correlation $\xi_4^{\alpha\alpha\beta\beta}$,where α and β denote sublattices. Among these, ξ_1^α (=-ξ_1^β) describes the long range order which is related to C_A^α, the concentration of up spins (or A atoms) on the α-sublattice, by $C_A^\alpha = \frac{1}{2}(1 - \xi_1^\alpha)$, whereas the rest of the variables are short range order parameters. Shown in Fig. 2 [11] are the free energy contour lines at 1:1 stoichiometry in temperature-ξ_1^α space. This is obtained by minimizing the free energy functional for a fixed value of ξ_1^α with respect to the remaining variables at each temperature. Hence, this is regarded as a constrained phase equilibrium. The vanishing of the long range order parameter (ξ_1^α=0) indicates the disordered phase while a finite value corresponds to an ordered state. One can confirm that the free energy of the disordered phase and ordered phase becomes equivalent at around 1.89, which indicates the order-disorder transition. Also an inflection point of the free energy curve vanishes at around 1.63, which indicates the SP temperature.

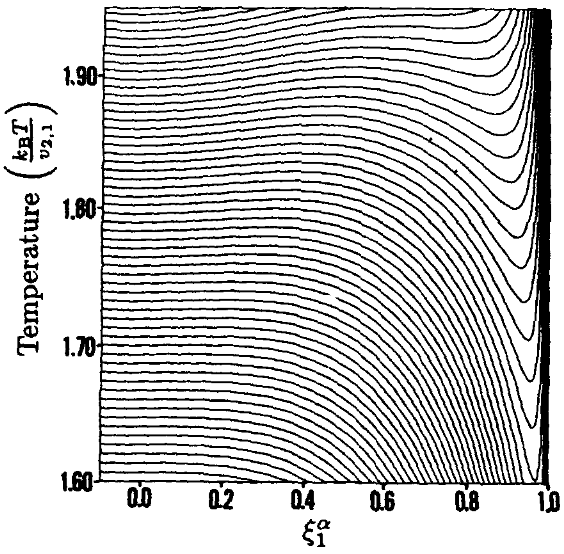

Figure 2: Free energy contour at 1:1 stoichiometric composition. The vertical axis is the temperature and the horizontal axis is ξ_1^α.

Path Probability Method

Most of the existing kinetic theories describe processes starting with the state variable and their time derivatives. On the contrary, the variational parameters appearing in the PPM are path variables which describe transitions among state variables. The main feature of the PPM may be well grasped by comparing with the CVM as follows.

In the CVM, the central quantity is the free energy functional which is described in terms of a set of correlation functions or cluster probabilities. An equilibrium state is defined as a minimum of the free energy functional with respect to the correlation functions. The counterpart of the grand potential of the CVM is the Path Probability Function, $P(t; t+\Delta t)$ (hereafter PPF), which is an explicit function of time. Likewise, corresponding to the cluster probabilities are the path variables by which the PPF is maximized to yield the most probable path of time evolution of a given system. The PPF P is written as the product of the following three terms.

$$P_1 = (\theta\Delta t)^{N(X_{1,2}+X_{2,1})}(1-\theta\Delta t)^{N(X_{1,1}+X_{2,2})} , \tag{1}$$

$$P_2 = \exp\left(-\frac{\Delta E}{2k_BT}\right) , \tag{2}$$

and

$$P_3 = \frac{\left(\prod_{ij,kl} NY_{ij,kl}!\right)^6 (N!)}{\left(\prod_{ijkl,mnop} NW_{ijkl,mnop}!\right)^2 \left(\prod_{i,j} NX_{i,j}!\right)^5}, \tag{3}$$

where N is the total number of lattice points, θ is the spin flip probability per unit time, $X_{i,j}$, $Y_{ij,kl}$ and $W_{ijkl,mnop}$ are the path variables for the flipping from one spin configuration to another designated by subscript (up spin or down spin) before and after the comma sign, on a point, pair and tetrahedron cluster, respectively, ΔE is the change of the internal energy before and after a flipping event. The first term P_1 describes a statistical average of non-correlated spin flip events over the entire lattice, and the second term P_2 is the conventional thermal activation factor. Hence, the product of P_1 and P_2 corresponds to the Boltzmann factor in the free energy and specifies the probability that one of the paths specified by a set of cluster probabilities occurs. The third term P_3 characterizes the PPM. One may see the similarity with the configurational entropy term of the CVM, which gives the multiplicity, i.e., the number of equivalent states. In a similar sense, P_3 can be viewed as the number of equivalent paths, i.e., the degrees of freedom of the microscopic evolution from one state to another.

Then, by maximizing the PPF, P, with respect to the path variables for each time step Δt, an optimized set of the path variables is obtained. Since a set of path variables relates cluster probabilities at time t and $t + \Delta t$, the repetition of this procedure yields the time evolution of the cluster probabilities for a specified set of initial cluster probabilities.

III. Results and Discussions

Kinetics of ordering transition

As is demonstrated in the previous section, two types of ordering transitions, NG and SP, are predicted by the stability analysis. However, conventional stability analyses including the one described above are based on the perturbation analysis. It is, therefore, anticipated that the time evolution of a system from a state that is far from equilibrium is not properly analyzed. An ordering process is the subject of kinetics. In order to reveal the distinction between the two ordering processes from the kinetic point of view, the PPM is employed to study the time evolution behavior of the system at isothermal aging temperatures 1.70 and 1.60, which are above and below the SP temperature, respectively. In each case, the system is initially maintained at temperature 2.5 which is in the disordered state.

Shown in Fig. 3a [10,11] are the time evolution of C_A^α and C_A^β which serve as long range order parameters and the free energy of the system during the isothermal aging process at temperature 1.7. Note that the time axis throughout this study is normalized by the spin flip probability θ and is in a logarithmic scale. In order to trigger the transition, the fluctuation of the long range order parameters is imposed at temperature 2.5, which is indicated by the initial separation of C_A^α and C_A^β. One can see that the fluctuation is amplified and C_A^α and C_A^β eventually reach steady state values which are confirmed to be the equilibrium ones for the $L1_0$ ordered phase at temperature 1.7 independently calculated by the CVM. However, for the small fluctuation shown in Fig. 3b [10,11], the imposed fluctuation fades away and eventually the system returns to the disordered state. These

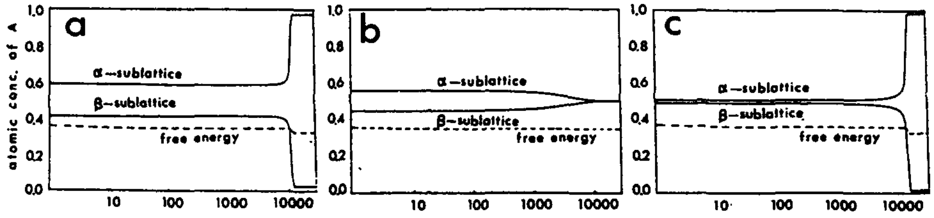

Figure 3: Time evolution of C_A^α, C_A^β and free energy at isothermal aging temperatures 1.70 (Figs. 3a and 3b) and 1.60 (Fig. 3c). The horizontal axis is the logarithmic time axis normalized by spin flip probability θ.

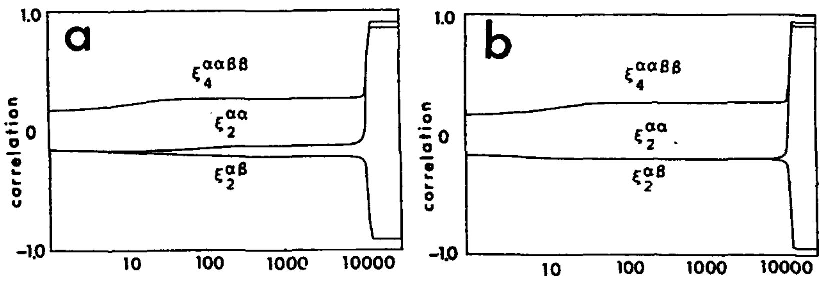

Figure 4: Time evolution of pair correlations $\xi_2^{\alpha\alpha}$ and $\xi_2^{\alpha\beta}$ and tetrahedron correlation $\xi_4^{\alpha\alpha\beta\beta}$ at isothermal aging temperatures 1.70 (Fig. 4a) and 1.60 (Fig. 4b).

two results clearly indicate that there exists a critical amount of fluctuation necessary to drive the transition, which is indicative of the NG ordering.

At temperature 1.60, below the SP temperature, a small amount of fluctuation is amplified to yield the $L1_0$ ordered phase, as is shown in Fig. 3c [10,11]. It was confirmed that even an infinitesimally small fluctuation could be amplified although the time required to complete the transition was prolonged. Such a barrierless transition is indicative of the SP reaction. It should be noted that in all cases, the free energy decreases monotonically.

An advantageous feature of the PPM is the fact that the PPM provides the time evolution of the short range order parameters, which facilitates detailed analysis of the transition behavior. The time evolution of two types of correlation functions, $\xi_2^{\alpha\alpha}$ and $\xi_2^{\alpha\beta}$, and the tetrahedron correlation, $\xi_4^{\alpha\alpha\beta\beta}$, are calculated for both temperatures and are plotted in Fig. 4a and 4b [10,11]. In both cases, the relaxations of these correlation functions precede the relaxation of long range order parameter (Figs. 3a, b and c), which is commonly observed in experimental situations. However the noticeable difference between

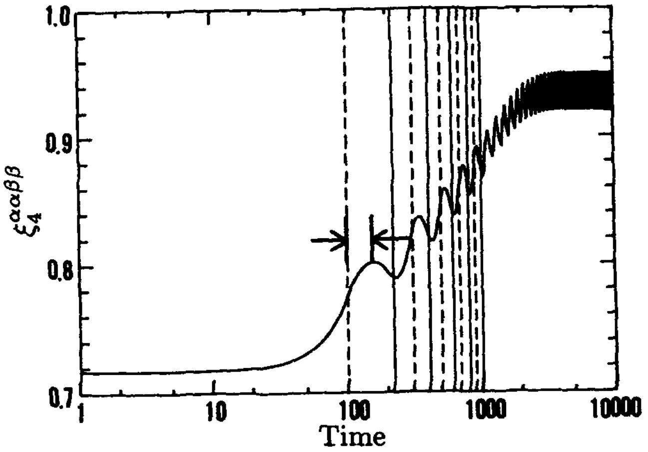

Figure 5: Time evolution of tetrahedron correlation function $\xi_4^{\alpha\alpha\beta\beta}$ under thermal cycling between T_{max}=1.85 and T_{min}=1.20 for t_Q=100 and θ=0.001. The broken and solid vertical lines indicate the times at which temperatures T_{min} and T_{max} are attained, respectively.

NG and SP is observed in the behavior of the two types of pair correlations. The two pair correlation functions start to deviate at an earlier time for the NG, an indication of the decoupling of the original lattice into two sublattices. Whereas for the SP, the single-lattice state is relatively long lived. The analysis of the kinetic path in the thermodynamic configuration space is expected to provide more detailed information. This is under way.

Dynamical stability under thermal cycling

As was mentioned in the introduction, steady state behavior under cyclic variation of temperature is another important subject in the discussion of the phase stability of an ordered compound. In the present study, the PPM is employed to analyze the time evolution and steady state behavior of the short range order and long range order parameters under a cyclic variation of the temperature between T_{max}=1.85 and T_{min}=1.20 (see Fig. 1). In order to characterize the external cooling (and heating) rate, the cooling (and heating) time, t_Q, is defined as the time required to travel from T_{max} (T_{min}) to T_{min} (T_{max}). Hence, a quick (slow) temperature variation is implied by a small (large) t_Q.

The time evolution of the tetrahedron correlation function, $\xi_4^{\alpha\alpha\beta\beta}$, for t_Q=100 and θ=0.001 is shown in Fig. 5. The broken and solid vertical lines indicate the times at which T_{min} and T_{max} are attained, respectively. One can see that the extremum values of the tetrahedron correlation function are not necessarily reached at T_{max} or T_{min} but some time lag is observed. One can also confirm that the steady state, which is characterized by the constant amplitude oscillation, is attained after around t=3000. It should be noted that the maximum and minimum values of $\xi_4^{\alpha\alpha\beta\beta}$ in the steady state are different from the equilibrium values for T_{max} and T_{min}, respectively.

In order to examine the steady state behavior, the kinetic path is traced in the free energy contour spanned by the temperature and ξ_1^{α} for a given t_Q and θ. The dependence on θ is demonstrated in Figs. 6a (θ=0.03) [12] and 6b (θ=0.003) [12] for a fixed value of

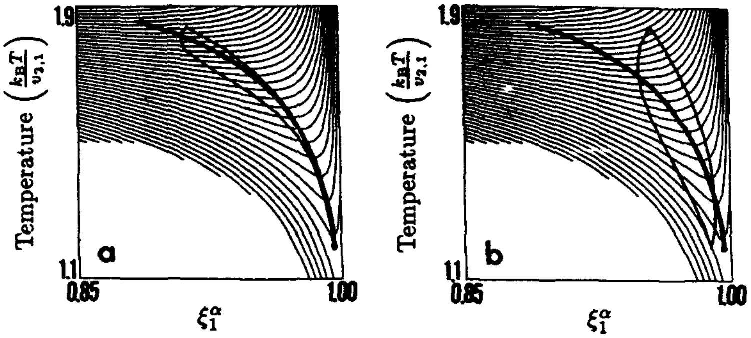

Figure 6: Steady state kinetic path (thin loop) during cyclic temperature variation between T_{max}=1.85 and T_{min}=1.20 for θ=0.03 (Fig. 6a) and θ=0.003 (Fig. 6b) at a fixed value of t_Q=1000 plotted with the free energy contour lines. The vertical axis is the temperature and the horizontal axis is the point correlation function, ξ_1^α, which is the long range order parameter. The thick line is the locus of the equilibrium ξ_1^α as a function of temperature.

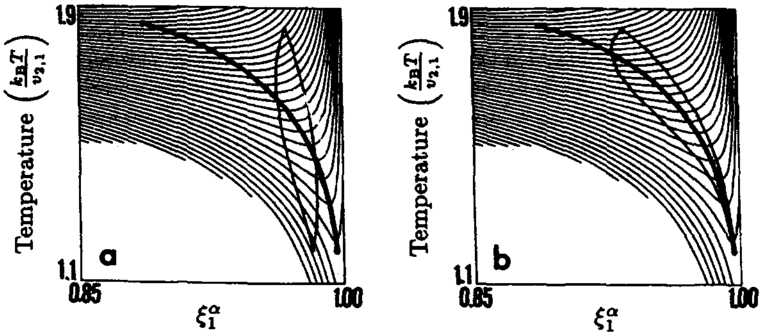

Figure 7: Steady state kinetic path (thin loop) under cyclic temperature variation for t_Q=100 (Fig. 7a) and t_Q=1000 (Fig. 7b) at a fixed θ=0.01. The thick line is the equilibrium locus.

t_Q=1000, while shown in Figs. 7a (t_Q=100) [12] and 7b (t_Q=1000) [12] are the dependence on t_Q for a fixed value of θ=0.01. The thick line in each figure represents the locus of the equilibrium ξ_1^α as a function of temperature. It is clearly seen that a loop is formed in the steady state and the loop deviates significantly from the equilibrium locus for smaller values of θ and t_Q. These results suggest that the steady state kinetics is controlled by the balance between the spin flip probability θ and the cooling (heating) rate t_Q. When the spin flip rate is insufficient to adapt to the external temperature change, deviation from the equilibrium path is pronounced.

Interestingly, one observes that the deviation of the loop from the equilibrium path is pronounced not in the low temperature but in the high temperature region. This intriguing behavior is understood based on the topological feature of the free energy contour lines. The gradient of the free energy contour is steeper in the horizontal direction (along ξ_1^α axis) for the lowtemperature region and in the vertical direction (along temperature) for the high temperature region. Hence, the deviation from the equilibrium ξ_1^α is limited by

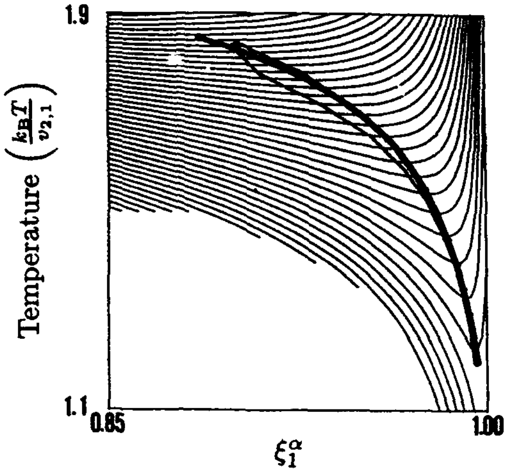

Figure 8: Steady state kinetic path during cyclic temperature variation between $T_{\max}$=1.85 and $T_{\min}$=1.20 for t_Q=1000. Thermal activation process of the spin flip event is explicitly considered through Eq. (4).

the bigger free energy change in the low temperature region, which keeps the path close to the equilibrium locus. While in the high temperature region, a horizontal shift of the path is attained without requiring a large increase in the free energy. Consequently, the path is trapped close to the equilibrium locus in the low temperature region and the entire shape is adjusted by shifting in the high temperature region.

The spin flip probability θ corresponds to an atomic mobility of an alloy system, which is discussed in the following section. In analogy with the alloy system, temperature dependence is introduced in the spin flip probability through

$$\theta = \nu \exp\left(-\frac{U}{k_B T}\right), \tag{4}$$

where U is the saddle point energy and ν is the frequency factor. An example of the calculated result for t_Q=1000 is demonstrated in Fig. 8 [12]. In this calculation, 0.645 and 5.0 are assigned to ν and U, respectively, which yields θ=0.01 at T_{min} and θ=0.043 at T_{max}. By comparing with Fig. 7b, for which temperature independent θ=0.01 is assumed, one may observe that the steady state loop more closely approaches the equilibrium locus. This is understood as the thermally activated enhancement of the spin flipping event in the high temperature region.

IV. Kinetics of an alloy system

The present study is devoted to an fcc spin system. In this final section, we briefly discuss the extension to an alloy system [7,8]. As was discussed in the previous section, the PPF is made of three factors. The product of the first two factors corresponds to the Boltzmann factor of free energy in equilibrium thermodynamics, while the third term is the counterpart of the entropy term. The introduction of the vacancy mechanism introduces a great variety of microscopic paths of atomic jump processes, which complicates the computational procedure. However, the extension of the P_3 term to an alloy system is quite straightforward once the path variables are properly defined. The essential difference introduced by the vacancy mechanism may be well understood through the formulation of the P_1 and P_2 terms, which are described below.

The central quantities in the pair interaction model are the pair path variables. In contrast to the spin system for which single type of pair path variable is defined, two types of pair path variables can be distinguished for the alloy system. One is $Y_0(m0;0m)$ ($Y_0(0m;m0)$) and the other is $Y(mj:0j)$, where m and j denote either an A or a B atom while 0 represents a vacancy. The former describes the direct exchange between an atom and an adjacent vacancy, while the latter indicates the jumping of the species m into an adjacent vacant site by breaking the chemical bond with species j.

With these pair path variables, the P_1 and P_2 terms are given as

$$P_1 = (\theta \exp(-\beta U)\Delta t)^{C_1 \sum_{m\neq 0}\{Y_0(m0;0m)+Y_0(0m;m0)\}} \tag{5}$$

and

$$P_2 = \exp\left[-C_2\beta\left\{\sum_{m\neq 0}\sum_{j\neq 0}\sum_{h=1}^{4}\sum_{direction}^{g_h} \epsilon(m,j)Y_h(mj;0j)\right\}\right] , \tag{6}$$

where C_1 and C_2 are constant terms uniquely related to the coordination number, θ is the attempt frequency, β is defined as $1/k_BT$, U is the saddle point energy and $\epsilon(m,j)$ is the pair interaction energy between species m and j. Hence, the P_1 term describes the probability of jump events occuring over the entire system. From the symmetry, the jumping-in sites of an atom after breaking the chemical bond are classified into four groups which are specified by h and the number of equivalent sites for each group is denoted by g_h in Eq. (6). Then, the exponent in Eq. (6) is the activation energy to break the chemical bond and, therefore, the P_2 term describes the probability of breaking the chemical bonds in the system.

The incorporation of the realistic energy terms U and $\epsilon(mj:0j)$ is the key to simulating an alloy system. A particular difficulty which is anticipated is the evaluation of the saddle point energy, U, which is sensitively dependent on the local atomic configuration. We believe that an accurate estimation of U is key to the success of alloy kinetics by the PPM.

Acknowldgements

One of the authors (TM) acknowledges support from a Grant for International Research Project from NEDO, Japan.

References

[1] R. Kikuchi, Phys. Rev. **81**, 998 (1951).
[2] T. Mohri, K. Terakura, T. Oguchi and K. Watanabe, Acta metall. **36**, 547 (1987).
[3] T. Mohri, K. Terakura, S. Takizawa and J. M. Sanchez, Acta metall. **39**, 493 (1991).
[4] R. Kikuchi, Prog. Theoret. Phys. Kyoto Suppl. **35**, 1(1966).
[5] T. Mohri, Acta metall. **38**, 2445 (1990).
[6] F. Ducastelle, Prog. Theoret. Phys. Kyoto in print.
[7] R. Kikuchi, Report to NIST.
[8] T. Mohri, to be published.
[9] H. Sato and R. Kikuchi, Acta metall. **24**, 797 (1976).
[10] T. Mohri, Proc. of NATO ASI in Rhodes (1992), Plenum, in print.
[11] T. Mohri, Proc. 15th Taniguchi Symp., Shima, Japan (1992), Springer, in print.
[12] T. Mohri and T. Ikegami, Proc. of International Conf. Diffusion in Materials, DIMAT-92, Kyoto (1992), Trans. Tech. Publications Ltd., in print.
[13] D. de Fontaine, Acta metall. **23**, 553 (1975).
[14] T. Mohri, J. M. Sanchez and D. de Fontaine, Acta metall. **33**, 1463 (1985).

Monte Carlo Simulations of Ordering Kinetics

T. F. Lindsey and B. Fultz

W. M. Keck Laboratory of Engineering Materials 138-78
California Institute of Technology
Pasadena, California 91125 USA

Abstract

We show how Monte Carlo methods can be used to study the thermodynamics or kinetics of ordering in metallic alloys. Algorithms for Monte Carlo simulations are described, and we review some results from studies of ordering with the vacancy mechanism. We describe an extension of the Monte Carlo method that introduces the concept of a force, and we use the method to study ordering in alloys with vacancy-solute interactions. We show examples of how the kinetic paths for ordering are modified by vacancy-solute interactions.

Diffusion in Ordered Alloys
Edited by B. Fultz, R.W. Cahn, and D. Gupta
The Minerals, Metals & Materials Society, 1993

I. Introduction

The kinetics of ordering is far more complicated than the thermodynamics of ordering. A first principles approach to ordering kinetics requires a detailed treatment of both interatomic interactions and atom movements. A full treatment would provide both the vibrational displacements and atom-vacancy exchanges. Today's computers are fast enough to perform a dynamical simulation for a small number of vacancy jumps. However, since ordering transformations involve a large number of vacancy-atom exchanges, a first-principles approach to ordering kinetics in a metallic alloy at low temperatures is out-of-reach today, and will remain so for decades. We expect that computer speed must improve by a factor of a trillion before it is feasible to attempt first-principles calculations of ordering kinetics. Even then there will remain the problem of interpreting the results in terms of their underlying physical phenomena.

While a dynamical simulation of ordering is not yet feasible, ordering kinetics can be studied by activated state rate theory. In this approach, the rate for vacancy-atom exchange is a function of the local environment surrounding the vacancy-atom pairs. The complexity of the atomic vibrational motion is replaced by configuration-dependent rate equations. Activated state rate theory can be implemented with two different approaches: analytical theories or Monte Carlo simulations. Analytical theories predict the time evolution of a set of state variables; the rates of change of different local atomic environments are calculated as functions of time. A useful aspect of this approach is that the state variables of the kinetic theory can also be used to calculate the free energy of the alloy. The rate equations also provide direct insights into how ordering is affected by changes in chemical bond strengths or activation barrier heights. Analytical theories such as Path Probability Method (PPM) [1-4] and Master Equation Method (MEM) [5-8] are approximate methods, however. Analytical theories do not provide a good treatment of larger heterogeneities such as antiphase domain boundaries, or local variations in short-range order. In principle, a better treatment of heterogeneities is achieved as larger clusters are used for the state variables, but a convergence of the kinetic behavior with larger cluster size has yet to be demonstrated.

A Monte Carlo simulation is not a theoretical calculation based on mathematical equations, but is a machine experiment. The term "Monte Carlo" refers to a class of computer algorithms that are based on random sampling. There is no one Monte Carlo method; Monte Carlo methods are applicable to a wide range of problems. They have been used, for example, by mathematicians to solve definite integrals and by materials scientists to calculate electron transmission through solids. Likewise, Monte Carlo methods can be used for a variety of different topics relating to diffusion and ordering. Unlike analytical theories that predict average values of the state variables, a Monte Carlo simulation of ordering provides an exact implementation of activated state rate theory for a crystal of finite size. Monte Carlo simulations include, for example, the random fluctuations and heterogeneities that are present in alloys. Furthermore, as described recently [9,10] cluster statistics obtained from a Monte Carlo simulation together with the cluster variation method can be used to obtain a free energy of an alloy.

The organization of this chapter is a follows. Previous work is reviewed in section II. In section III we describe activated state rate theory. It provides the foundation for the analytic methods such as the PPM and MEM, and our Monte Carlo simulations of kinetics. Section IV is a discussion of Monte Carlo algorithms. The Metropolis algorithm (which is applicable for equilibrium but not kinetic simulations) is presented first, followed by an exposition of the kinetic algorithm which is based on activated state rate theory using a vacancy-atom exchange mechanism. In section V we describe our current effort to build up a software environment for simulations of material properties A new result which we have obtained recently is the inclusion of vacancy-solute interactions, and this method is described in section VI. The results of the modified Monte Carlo simulations for a ternary alloy are discussed in section VII.

II. Review of Previous Work

Many Monte Carlo simulations of phase transformations have been performed (e.g., [11-13]), but most of these simulations used a direct interchange of the constituent atoms [13]. Diffusion of a lattice gas has also been studied [14,15]. Relatively few simulations have used a vacancy mechanism, although it was used in studies of steady-state diffusion kinetics in ordered alloys [16-19]. Flinn and McManus [20] performed the first computer simulations of the kinetics of an ordering transformation with a vacancy mechanism. However, their method was physically unrealistic since it assumed thermodynamic equilibrium for each exchange pair. This approach ensured an equilibrium detailed balance between forward and reverse jumps, but neglected the role of the vacancy-atom exchange activation barrier.

The Flinn-MacManus algorithm was used by Beeler and Delaney [21,22] in computer simulations of ordering transformations in binary bcc and fcc alloys. In simulations of ordering with a vacancy mechanism, Beeler found a "contraction" of the range of the vacancy random walk. More recent studies [23-27] showed that during ordering the vacancy occasionally becomes "trapped" in a local region of the crystal. As the vacancy moves, it encounters different local environments. Some of these local environments will cause the vacancy to go back and forth between two sites. This pair trapping may continue for many vacancy jumps, thus restricting the range of vacancy travel. After the early stages of short range ordering are complete and ordered domains are present, antiphase domain boundaries (APDB's) may serve as potent traps for vacancies. Vacancies spend a disproportionate amount of time traveling along antiphase domain boundaries, and spend much less time inside the ordered domains. This vacancy trapping behavior scales with the chemical strength, $V_{AA} - V_{AB}$ or $V_{BB} - V_{AB}$, whichever is largest. (See section VI for the definitions of V_{AA} and V_{AB}.) The atomic diffusion coefficients are suppressed strongly by this correlated motion of the vacancy, and unlike analytical calculations in the pair approximation [28], the vacancy correlation becomes even stronger at lower temperatures [25].

The probabilities and strengths of traps depend on the lattice coordination number, z, and connectivity of the lattice. For a given set of chemical interaction strengths, the traps increase in strength linearly with lattice coordination number, z, but decrease in density with z. Because the critical temperature for ordering corresponds to larger chemical interaction strengths for lattices with smaller z, with respect to the critical temperature vacancy trapping is most significant on a lattice with small z [26]. Vacancy trapping at APDB's was shown to affect the quality of order within a domain. When ordered microstructures formed with the atom interchange mechanism were compared to microstructures formed with the vacancy mechanism, many more antisite defects were found in the microstructure formed with the vacancy mechanism [24]. This is a consequence of the vacancy becoming trapped at APDB's, and being unable to spend enough time inside the domains to eliminate antisite defects.

The microstructure of an alloy undergoing short-range ordering has been studied microscopically and macroscopically by Monte Carlo simulations [29-31]. When several order parameters are available to characterize the state of the alloy (such as Warren-Cowley short-range order parameters for different nearest-neighbor shells), it is possible to ask if the alloy follows different trajectories through the state-space spanned by these different order parameters. We term these trajectories through state-space as "kinetic paths". Monte Carlo simulations by Gahn and Pitsch [29,30] showed that an alloy takes different kinetic paths when different mechanisms of atom movements are used. The observed differences in kinetic paths were not large, however, because their short-range order parameters were not fully independent variables. Gahn and Pitsch also studied the heterogeneity of vacancy motion in an alloy [31].

Monte Carlo simulations were also used to study vacancy percolation in an alloy when there were no chemical interactions between atoms, but when the two species of atoms had different activation barrier energies for interchange with an adjacent vacancy [27]. When one of the species is given a very large activation barrier, it is immobilized, and the usual concentration threshold for percolation in a bcc lattice (24.3%) was found for the mobile species. When the less mobile species has a finite activation barrier, however, there remains a distinct change in vacancy diffusion near the percolation threshold. The change reflects the strong difference between the activation barrier energies of the two atomic species. It seems that a good way to identify a percolation threshold in a diffusion experiment is to measure the temperature dependence of the diffusion coefficients above and below the percolation thresholds. The activation energy below the percolation threshold should be dominated by the activation energy of the less mobile species, but above the percolation threshold this will change abruptly to the activation energy of the mobile species.

III. Activated State Rate Theory

There are many physical phenomena involved in the kinetics of ordering, and to date only some of them have been included in analytical theories such as the path probability method [1-4], or master equation method [5-8]. A full treatment of ordering kinetics would follow the details of atom movements during diffusion. This includes the vibrational dynamic movements of the moving atom and its neighbors, and how the movements of these atoms are influenced by the interatomic potentials and the elastic distortions. For an approach more akin to thermodynamics, however, we average over many such details. We seek the probability of occurrence of a fluctuation in the alloy that permits an atom movement. There is a free energy cost for such a fluctuation. If we examine only those fluctuations that are attempts at an atom movement, it is reasonable to separate the total free energy of the alloy into a local contribution from the region around the candidate moving atom, and an uninteresting contribution from the rest of the alloy. For the region including the moving atom, the difference between the free energy of the fluctuation (superscript *) and the free energy of the initial state (subscript i), ΔF, is:

$$\Delta F = (E^{*}-E_i) - T(S^{*}-S_i) \tag{1}$$

The probability of success for an attempt at an atom movement, P, will be:

$$P = \kappa \exp\left(\frac{E_i - E^{*}}{k_B T}\right) \exp\left(\frac{S^{*} - S_i}{k_B}\right) \tag{2}$$

The entropy factor, which originates from changes in vibrational modes during atom movement, is typically ignored or absorbed into the attempt frequency for an atom movement. The movement occurs with frequency Γ:

$$\Gamma = \nu \exp\left(\frac{E_i - E^{*}}{k_B T}\right) \tag{3}$$

Equation 3 is used by analytical theories of ordering such as the PPM and MEM, and is also used as the basis for the Monte Carlo simulations described here. The implementation of Eqn. 3 requires a model for how the chemical environment around an atom sets E_i. Different models for atom movements have been attempted. While it is often true that these different implementations of activated state rate theory may lead to the same state of *thermodynamic* equilibrium, these different mechanisms do not predict the same kinetics.

IV. Monte Carlo Algorithms

A Monte Carlo algorithm requires a method for calculating the probabilities of candidate transitions, and a procedure for selecting one of them. We first review the popular "Metropolis algorithm", which provides the thermodynamic state of an alloy. A different approach is required for following the kinetics of a phase transformation. An importance difference between thermodynamic and kinetic simulations is that a thermodynamic calculation yields only the equilibrium state whereas a kinetic simulation produces the path leading to equilibrium. This path is defined by the time evolution of the set of LRO and SRO parameters. Since these variables may assume different combinations of values, many different kinetic paths are possible. A thermodynamic calculation is not intended for predicting the kinetic path, but only the end state of the path. After discussing the vacancy algorithm in this section, in sections VI and VII we show how vacancy-solute interactions can modify the kinetic paths of ordering in ternary alloys.

A. Metropolis Algorithm

The venerable Metropolis algorithm works as follows [32]. For each candidate kinetic event, there is an energy difference, ΔE, between the final state and the initial state of an alloy:

$$\Delta E = E_f - E_i \quad . \tag{4}$$

In the Metropolis algorithm, a transition from the initial to the final state occurs with one of the two probabilities:

i.) 1 if $\Delta E < 0$ (i.e., if the transition is energetically downhill)
ii.) $\exp(-\Delta E/k_BT)$ if $\Delta E > 0$ (i.e., if the transition is energetically uphill)

These two transition probabilities, while asymmetric, are a good choice because they always lead to thermodynamic equilibrium. Suppose, for example, that the final state is of lower energy than the initial state. The transition rate from the initial to the final state, $\Gamma_{i\rightarrow f}$, will be:

$$\Gamma_{i\rightarrow f} \propto 1 \quad . \tag{5}$$

On the other hand, the reverse transition from the final state to the initial state, $\Gamma_{f\rightarrow i}$, will be:

$$\Gamma_{f\rightarrow i} \propto \exp\left(-\frac{-\Delta E}{k_BT}\right) = \frac{\exp\left(\frac{-E_i}{k_BT}\right)}{\exp\left(\frac{-E_f}{k_BT}\right)} \quad . \tag{6}$$

To relate these transition probabilities to the state of thermodynamic equilibrium, we need two facts about Markovian processes [33]. First, it can be proved that the system will eventually reach a steady-state when the probability distribution of the states is static. It can also be proved that after sufficient time, the probability, p, of finding a system in a particular state is proportional to the lifetime of the state (i.e., it is more likely to find the system in long-lived states). For our two states, i and f, their relative lifetimes will be related inversely to the transition rates:

$$p_i \propto \frac{1}{\Gamma_{i\rightarrow f}} \quad , \tag{7}$$

$$p_f \propto \frac{1}{\Gamma_{f\rightarrow i}} \quad . \tag{8}$$

In steady state we therefore expect the probabilities of our initial and final states to be in the ratio:

$$\frac{p_i}{p_f} = \frac{\exp\left(\frac{-E_i}{k_BT}\right)}{\exp\left(\frac{-E_f}{k_BT}\right)} \quad . \tag{9}$$

The Metropolis algorithm leads to probabilities of microstates that are in the ratios of the Boltzmann factors of the states. This is just what we expect for thermodynamic equilibrium of a microcanonical ensemble. The transition probabilities of the Metropolis algorithm are not the only ones for which the thermodynamic state is recovered, however.

To calculate thermodynamic averages with microcanonical ensembles, we need to know the number of microstates with a specific energy. In Monte Carlo simulations of an alloy, information on the distribution of microstates is contained in the structure of the crystal, since the computer keeps track of the positions of all atoms and their mutual arrangements. A concept such as entropy is not needed, nor is it conveniently available.

So far we have said nothing about the choice of the initial and final states, or the allowed transitions between them. Provided the mechanism of atom movement allows all states of atom arrangements to be reached in an unbiased way, we could have moved atoms in groups or individually, over short distances or long distances, and the arguments leading to Eqn. 9 would still hold true. A key assumption of statistical mechanics is that the details of mechanism do not affect the equilibrium properties. Hence, for a equilibrium calculation one does not need to take into account the mechanisms of the system motion. It is necessary, however, to assume that the system is ergodic. The Metropolis algorithm satisfies this condition since candidate transitions which enter into Eq. 4 are selected randomly.

B. Vacancy Algorithm

The fundamental difference between statistical mechanics and statistical kinetics is that a kinetic theory must include the mechanisms for atom movements, and must do so correctly. Kinetic theories based on different types of elementary kinetic events should all lead to the same state of equilibrium, but their paths to equilibrium can be quite different. In particular, the Metropolis algorithm is inappropriate for studies of the kinetics of phase transformations, except perhaps magnetic ones. It provides a path to equilibrium, of course, but this path must be considered a convergence path, and not a real kinetic path.

For most metallic alloys at low temperatures, atom movements occur when an atom interchanges sites with a neighboring vacancy. Consider a vacancy that is surrounded by z atoms, which are candidates for the next kinetic event. A realistic Monte Carlo simulation of ordering kinetics must contain an algorithm to decide which one of these z atoms will interchange sites with the vacancy, and how much time is required for this elementary kinetic event. After the atom vacancy interchange has occurred, the algorithm is again applied to the new environment of the vacancy.

Suppose the characteristic rate for an interchange of the vacancy and the jth atom is proportional to ω_j. The jth atom is competing with the other $z-1$ neighbors of the vacancy to exchange sites with it, so the probability for the movement of the jth atom is:

$$p_j = \frac{\omega_j}{\sum_{i=0}^{z} \omega_i} \quad . \tag{10}$$

Here p_j is the probability that the jth atom will jump into the vacancy. A random number between 0 and 1, r, is then used to select one of these z candidate jumps:

```
if $r < p_1$, jump of atom 1
else, if $r < p_1 + p_2$, jump of atom 2
else, if $r < p_1 + p_2 + p_3$, jump of atom 3
        .
        .
else, jump of atom $z$
```

Using this algorithm a vacancy jump will occur for every Monte Carlo step. This is different from the Metropolis algorithm where each candidate transition will either occur or not occur. Hence, the kinetic algorithm is efficient in that every Monte Carlo step produces a vacancy jump.

To calculate the characteristic transition rates, $\{\omega_j\}$, we need to consider the physical process of the atom-vacancy interchange. We use the same mechanism that has been used in analytical studies with the PPM [1-4] and MEM [5-8]. To interchange sites with a vacancy, the candidate atom must surmount a barrier of height E^*. The energy required to surmount this barrier is the difference between E^* and E_i, the energy of the atom in its initial state. All chemistry in the problem is contained in the $\{E_i\}$. In the simplest approach, we determine E_i with only the first nearest neighbor (1nn) environment of the candidate atom. If the candidate atom is of type "A", for example:

$$E_i = N_{AA}V_{AA} + N_{AB}V_{AB} \quad , \tag{11}$$

leading to a characteristic jump frequency of:

$$\omega_j \propto \exp\left(-\frac{(E^* - E_i)}{k_B T}\right) \tag{12}$$

Our candidate A-atom has N_{AA} A-atoms in its 1nn shell, and N_{AB} B-atom neighbors. The difference in strength of these two types of bonds is $V_{AA} - V_{AB}$. If this difference in bond energy is positive, Eqn. 3 shows that with more A-atom neighbors, the A-atom will be more likely to jump. It should be noted that the energy for re-creating the the atom-atom bonds after the jump does not enter into Eqn. 3 or 11. It is still possible to prove that this vacancy mechanism will lead to a steady state that is a state of thermodynamic equilibrium. To do so, we note that all initial states of the vacancy-atom interchange are in thermodynamic equilibrium with the activated state for the interchange. If the initial states are in thermodynamic equilibrium with the states at the activation barrier, the initial states must be in equilibrium with each other, and the alloy will be in a state of thermodynamic equilibrium.

The average time required for the vacancy-atom interchange is controlled by the total transition rate, i.e.:

$$\Delta t = \frac{1}{\sum_{i=0}^{z} \omega_i} \tag{13}$$

The time scale for the Monte Carlo simulation is provided by a running sum of the times for the individual jumps, and the units of the time are the prefactor of the exponential jump probability of Eqn. 3. The units could be in "attempts" at surmounting the barrier, for example [34].

V. Software Environment for Materials Simulations

The Monte Carlo methods described here require only modest computer resources. At present we are using a DECstation 3100 engineering workstation. A typical simulation involves 262,143 atoms and one vacancy, and the vacancy jump rate is approximately 6 kHz. In about one day the alloy will typically evolve from an initially disordered state to a state close to thermodynamic equilibrium.

A Monte Carlo calculation can be used as a module in a larger software environment. Given the positions of all the atoms in the alloy, the results of other experiments, such as x-ray diffractometry and Mössbauer spectrometry, are simulated. This is an advantage over analytical calculations because the experimental measurables may not depend in a simple way on the state variables of analytical theory. At present we are trying to understand the kinetics of disorder→order transformations in bcc Fe alloys by using activated state rate theory of vacancy motion. Given a set of interatomic interactions from either first principles calculations or from ad-hoc assumptions, a disordered alloy is allowed to develop order with the Monte Carlo algorithm described in section III.B. At various stages of ordering, the Monte Carlo simulation is paused, and "simulated experimental measurements" are performed on the Monte Carlo alloy. The x-ray diffraction intensities are efficiently computed using a standard fast Fourier transform (FFT) routine. Likewise, Mössbauer spectra can be calculated using a magnetic response model of the hyperfine magnetic fields in ferromagnetic bcc iron alloys [35]. This combination of techniques is one way to obtain information on both the short- and long-range order of an alloy. These results from simulations can then be compared to experiment to test the predictions of analytical kinetic theories.

It is difficult to know the relationship between the time scales of the simulations and the real experiments, or even if it is a linear relationship. However, when more than one microstructural variable is measured, there are often other interesting features which may be observed. A good example of this is the "kinetic path" through the space spanned by the different state variables. A kink in the kinetic path through short- and long-range ordering was found in the disorder→B2 order transformation in FeCo [36]. This kink could be an example of a long-lived "pseudostable state" that occurs at a saddle point of a free energy function [37,38].

VI. Models for Vacancy-Solute Interactions

Vacancy-solute interactions have long been believed to influence the kinetics of diffusion [39,40]. Renewed interest in this problem has followed a set of measurements by Rockosch [41]. These experiments showed a correlation between the strength of vacancy-solute interactions and the dependence of the alloy lattice parameter on solute concentration. This suggests that much of the vacancy-solute interaction originates from a first-order elastic effect [42,43], although electronic contributions may also be significant [44]. Vacancy-solute interactions are strong. Energies of a few tenths of an electron volt are associated with the attraction or repulsion between vacancies and solute atoms. Such energies are larger than typical interatomic pair potentials involved in order-disorder transformations. Although vacancy concentrations are too low to affect the thermodynamics of ordering, they may have condiserable influence on the kinetics. To study how the kinetics or ordering are affected by vacancy-solute interactions, we must modify the vacancy algorithm described in section II.B.

We see two ways to model vacancy-solute interactions in Monte Carlo simulations. In the first, we could use the vacancy-solute interactions to shift the initial energy of the vacancy before the jump. This is much like the chemical interactions described in section II.B. For example, if there were a negative energy for a 1nn vacancy-solute bond, the vacancy-solute interaction would tend to retard the separation of vacancy-solute pairs. The interaction would not, however, provide a force to pull the vacancy towards the solute atom. This interaction takes effect only when the vacancy and solute are already neighbors. There is no bias for the vacancies to move near solutes, only a delay in having a vacancy move away. In Monte Carlo simulations we find that the time scale for ordering can be changed significantly by vacancy-solute interactions of this first kind, but there can be no change in the sequence of states followed by the alloy during ordering*. This remains true when the vacancy-solute interactions are of greater range than first nearest neighbors; vacancies are not pulled towards attractive solutes, but are delayed in leaving their vicinity.

For vacancy-solute interactions to work as attractions and repulsions, we need the concept of a force. Our second method for treating vacancy-solute interactions examines the change in the vacancy-solute interaction potential over a short distance. Physically, this provides an effective force which could arise from a short-ranged elastic strain field. The vacancy will be drawn to sites with the lowest elastic energy. To have such a force for vacancy-atom interactions, both the initial *and final* energies of the vacancy must influence the jump rate. To implement this idea, in the present work we used the following formula to compute the atom-vacancy exchange rate:

$$\omega_j \propto \exp\left(-\frac{(E^* - E_i)}{k_B T}\right)\exp\left(-\frac{(e_f - e_i)}{k_B T}\right) \tag{14}$$

The first factor in Eqn. 14 is the same as Eqn. 12. The second factor takes vacancy-solute interactions into account. It is the Boltzmann factor for the difference in energy between the final and initial state energies for the vacancy. As a first approximation, we assume that e_f and e_i can be calculated with a short range vacancy-atom bond model. For example, restricting the calculation to the first shell, for a binary alloy these energies are:

$$e_f - e_i = (N^{f}_{\mathrm{VA}} - N^{i}_{\mathrm{VA}})\, E_{\mathrm{VA}} + (N^{f}_{\mathrm{VB}} - N^{i}_{\mathrm{VB}})\, E_{\mathrm{VB}} \tag{15}$$

---

* It is interesting that the superposition principle used in analytical theories causes this first model of vacancy-solute interactions to alter kinetic paths, however [45].

where, for example, N^{f}_{VA} is the number of V-A bonds in the final state (after the interchange, and N^{i}_{VA} is the number of V-A bonds in the initial state. The energy of each bond is E_{VA} . With Eqns. 14 and 15, the vacancy is pulled towards or pushed away from specific solute atoms. This affects not only the time required for a vacancy-solute interchange, but also the types of interchanges that occur. These vacancy-solute interactions will affect the kinetic path of the alloy, as we show in the next section.

VII. Results of Simulations with Vacancy-Solute Interactions

Here we present results of Monte Carlo simulations that show how kinetic paths are influenced by vacancy-solute interactions. The thermodynamics and kinetics of ordering are influenced only be the ratio of the interatomic interaction energies and the temperature, so we set the temperature equal to unity and vary the energy parameters*. The ternary alloy used in these simulations had the composition 45% A, 50% B, 5% C, with one vacancy. The results of the simulations are presented in Figures 1-3. These figures are "kinetic paths", which are trajectories of the alloy through short-range order parameters. The short range order parameters that we choose are p_{AA} and p_{CC}, which are the probabilities that a pair of atoms, separated by a first nearest neighbor distance, are either both A-atoms or both C-atoms, respectively. In equilibrium there is a fixed relationship between p_{AA} and p_{CC}, which is located towards the lower left corner of the three figures. The alloys began as disordered solid solutions, and this state is towards the upper right corner. We found that many different kinetic paths can be produced by varying the strengths of the vacancy-solute interactions (E_{VA}, E_{VB}, E_{VC}), activation barrier heights (E^*_A, E^*_B, E^*_C), and interatomic interaction potentials (V_{AA}, V_{BB}, V_{CC}, V_{AB}, V_{AC}, V_{BC}). Changes in

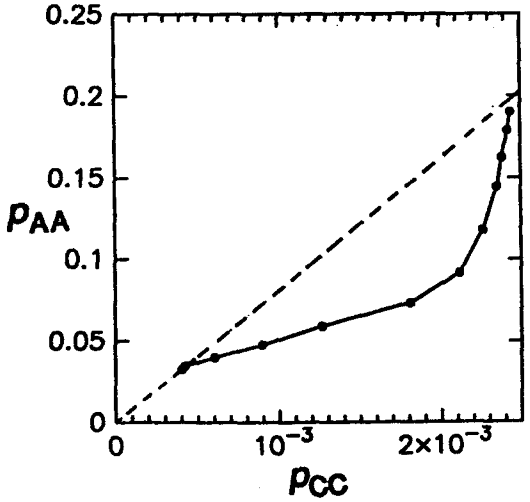

Figure 1. Kinetic paths of alloys without (dashed line) and with (solid line) vacancy-solute interactions. For the dashed curve, E_{VC} = 0.0. For the solid curve, E_{VC} = 1.5. For both alloys: $E^*_A = E^*_B = E^*_C = 10.0$, $V_{AA} = V_{BB} = V_{CC} = V_{AC} = 1.0$, $V_{AB} = V_{BC} = 0.0$, $E_{VA} = E_{VB} = 0.0$. (Energy in units of kT)

---

* The interaction energies are therefore in units of k_BT.

strength of the interatomic interactions can affect the end state of thermodynamic equilibrium, however, so the three cases presented here are comparisons of kinetic paths where the interatomic interactions are held constant, but the vacancy solute interactions or the activation barrier heights were varied.

Our first example (results presented in Figure 1) is an alloy where the A and C atoms are chemically identical, with unfavorable bonds to either A or C atoms. The B-atoms had a similar positive potential for having B-atom neighbors. Thermodynamically, the alloy is a simple binary. The initial state of disorder (upper right) is consistent with values of the pair variables p_{AA} and p_{CC} for a random alloy, i.e., $p_{AA} = c_A^2 = 0.45^2 = 0.2025$, and $p_{AA} = c_C^2 = 0.05^2 = 0.0025$. The state of thermodynamic equilibrium (lower left) is consistent with that of a binary alloy in which the C-atoms and A-atoms are identical, i.e., the ratio of p_{AA} and p_{CC} is: $p_{AA}/p_{CC} = c_A^2/c_C^2 = 1/81$. For a true binary alloy, the kinetic path in Figure 1 is a straight line passing through the origin with a slope of 1/81. In the absence of vacancy-solute interactions, therefore, the relationship between p_{AA} and p_{CC} is linear (dashed line). This changes when vacancy-solute interactions are active (solid line). When interactions between the vacancy and the C-atoms are repulsive, the mobility of the C atoms decreases. This causes the initial part of the kinetic path to move away from the straight dashed line in Figure 1. As the system approaches equilibrium, however, the A-atoms are not so strongly driven to change their positions. All state variables involving the A-atoms change more slowly, including p_{AA}. The kinetic path therefore bends, and the final approach to equilibrium involves a more rapid relative change of p_{CC}.

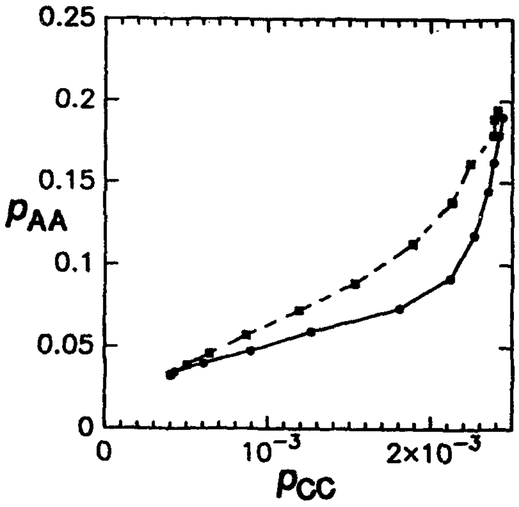

Figure 2. Kinetic paths of alloys with vacancy-solute interactions (solid line, as in Figure 1) and with vacancy-solute interactions plus a compensating activation barrier height difference.

For the solid curve, $E_{VC} = 1.5$ and $E_C^* = 10.0$.

For the dashed curve, $E_{VC} = 1.5$ and $E_C^* = 4.0$.

For both alloys, the other parameters were the same as for Figure 1: $E_A^* = E_B^* = 10.0$, $V_{AA} = V_{BB} = V_{CC} = V_{AC} = 1.0$, $V_{AB} = V_{BC} = 0.0$, $E_{VA} = E_{VB} = 0.0$. (Energy in units of kT)

In our second example, we tried to counteract the effect of the vacancy-solute interaction by a judicious choice of activation barrier height differences. In this example, the activation barrier height for the C-atoms is lower than for the A and B-atoms. The lowering of the C-atom activation barrier height makes the C atoms more mobile, thus increasing the rate of change of C-

C pairs. On the other hand, the repulsive interaction between the C-atoms and the vacancies has the opposite effect. This competition between kinetic effects is illustrated by the kinetic paths presented in Figure 2. The solid curve in Figure 2 is the same curve as presented in Figure 1 for the alloy with vacancy-solute interactions. The dashed curve was obtained for an alloy similar in all parameters, except for a lower activation barrier height for the C atoms. Figure 2 shows that the curvature of the kinetic path decreases, and the kinetic path moves towards the straight (dashed) line. The effect of the vacancy-solute interaction and the effect of the activation barrier height difference nearly compensate each other.

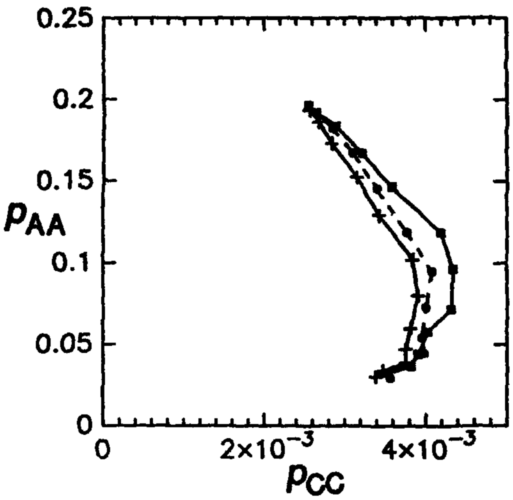

Figure 3. Kinetic paths for alloys with atoms having asymmetrical interatomic interactions, and C-atoms with different activation barrier heights and vacancy-C-atom interactions.

For all alloys, $E^*_A = E^*_B = 10.0$, $V_{AA} = 0.8$, $V_{BB} = 1.2$, $V_{CC} = -1.0$, $V_{AC} = 1.0$, $V_{AB} = V_{BC} = 0.0$, $E_{VA} = E_{VB} = 0.0$.

For the dashed curve and circles, $E_{VC} = 0$ and $E^*_C = 10.0$.

For the solid curve and squares, $E_{VC} = 0$ and $E^*_C = 6.0$.

For the solid curve and crosses, $E_{VC} = 1.0$ and $E^*_C = 6.0$.

(Energy in units of kT)

In our third example we show the complexity that comes with asymmetries in the interatomic potentials. In this example V_{CC} is attractive, not repulsive. In the simplest alloy (dashed curve) we set the activation barrier height to be the same for all the atoms, and there are no vacancy-solute interactions. In the kinetic path of the alloy, p_{CC} initially increases, and then decreases. This sign reversal of $d(p_{CC})/dt$ occurs because the C-C interactions are attractive, but the A-C interactions are repulsive. In the early stages, before long-range order is strong, the number of C-C pairs can grow independently of the A-C pairs. As the system orders further and there is a distinct formation of domains, however, the more numerous, but unfavorable A-C pairs cause the C-atoms to take more B-atom neighbors, and p_{CC} decreases. Similar overshooting phenomena have been reported previously in ternary alloys studied with analytical theories [5,31]. When the activation barrier height for the C atoms is lowered (solid curve with squares), Figure 3 shows that the kinetic path is shifted to the right. This occurs because the C atoms are more mobile. However, this effect can be compensated by a repulsive vacancy-solute interaction involving the C-atoms. The repulsive vacancy-C-atom interaction slows the rate of change of C-C pairs, thus shifting the kinetic path the left. We note that this kinetic path (solid curve with crosses) is similar to the kinetic path (dashed curve) for an alloy without either vacancy-solute interactions or differences in activation barrier heights.

In our model of ordering, the kinetic paths depend on three types of interactions: 1) atom-atom interatomic potentials $\{V_{XY}\}$, 2) activation barrier height variations $\{E^*_X\}$, and 3) vacancy-solute interactions $\{E_{VX}\}$. To some extent, the effects from these three types of interactions can be arranged to augment or cancel each other. This is especially true for the activation barrier heights and the vacancy-solute interactions because they do not depend strongly on the state of order in the alloy. The state variables involving vacancies relax quickly from their initially random distribution to values appropriate for the vacancy-solute interaction strengths. As order evolves in the alloy, we might expect that the numbers of different vacancy-atom pairs would change. In all cases we have examined to date, however, the changes in the numbers of the different vacancy-atom pairs are not large. The distribution of vacancy-atom pairs remains more-or-less constant as order evolves in the alloy. The activation barrier heights are modeled as being independent of the state of order in the alloy. It is therefore possible for the effects of activation barrier heights on the kinetics to accurately compensate for the effects of the vacancy-solute interactions. This compensation is not possible for the interatomic interaction strengths, however. The kinetic effects of the interatomic interactions depend strongly on the state of order in the alloy. As shown previously [°], it is not possible for the interatomic interaction strengths to compensate accurately for the etfects of differences in activation barrier heights, at least not over the full length of the kinetic path. Likewise it will not be possible for the interatomic interaction strengths to compensate accurately for the effects of vacancy-solute interactions.

We close as we began, by emphasizing that the kinetics of ordering is a larger problem than the thermodynamics of ordering. The state of thermodynamic order in the alloy is determined solely by the interatomic interactions. Atom-vacancy interactions and activation barrier heights will affect kinetics, but not thermodynamics. Atom-vacancy interactions and activation barrier heights affect both the rate of ordering and the kinetic path, but they do so differently for different mechanisms of atom movements. The connections between the microstates of an alloy are important in problems in kinetics, even for predictions of macroscopic behavior. Calculations of kinetic behavior therefore require physically reasonable mechanisms for atom movements. It is important that thermodynamic thinking not be transferred too directly to problems of kinetics.

VIII. Conclusions

In this chapter we show how Monte Carlo simulations can be used to study the kinetics of ordering. The vacancy-atom interchange is the elementary kinetic event in the simulations, and the rates of these interchanges are calculated with activated state rate theory. We include in the problem the interatomic chemical interactions, differences in activation barrier heights. By including a short-range force, we can also study the effects of vacancy-solute interactions. Only the interatomic interactions affect the thermodynamic state of order in the alloy, but the kinetics is affected by the interatomic interactions, activation barrier heights, and vacancy-solute interactions.

We found the activation barrier heights and vacancy-solute interactions had significant effects on the kinetic paths of a ternary alloy. We found that the activation barrier heights can be used to compensate for the kinetic effects of vacancy-solute interactions, and the observed kinetic paths depends on the relative signs and strengths of the barrier heights and vacancy-solute interactions. Changes in the interatomic interactions also affect the kinetic paths, but they cannot compensate precisely for the effects of the other interactions because the kinetic effects of the interatomic interactions depend on the state of order in the alloy.

IX. Acknowledgments

We acknowledge valuable conversations with L. Anthony, T. Mohri, and R. Kikuchi. This work was supported by a Grant for International Research from NEDO, Japan, and the U. S. Department of Energy under contract DE-FG03-86ER45270.

X. References

1. R. Kikuchi and H. Sato, J. Chem. Phys. 51, 161 (1969). *ibid* 57, 4962 (1972).
2. H. Sato and R. Kikuchi, Acta Metall. 24, 797 (1976).
3. H. Sato, K. Gschwend, and R. Kikuchi, J. de Physique C7, 357 (1977).
4. K. Gschwend, H. Sato, and R. Kikuchi, J. Chem. Phys. 69, 5006 (1978).
5. B. Fultz, Acta Metall. 37, 823 (1989).
6. L. Anthony and B. Fultz, J. Mater. Res. 4, 1132 (1989).
7. B. Fultz, J. Mater. Res. 5, 1419 (1990).
8. B. Fultz, J. Mater. Res. 7, 946 (1992).
9. A. G. Schlijper, A.R.D. van Bergen, and B. Smit, Phys. Rev. A 41, 1175 (1990).
10. L. Anthony and B. Fultz, these Proceedings.
11. K. Binder and M. H. Kalos in Monte Carlo Methods in Statistical Physics, K. Binder, ed., Topics Current Phys. vol. 7, (1979) Chapter 6.
12. L. D. Fosdick, Phys. Rev. 116, 565 (1959).
13. L. Guttman, J. Chem. Phys. 34, 1024 (1961).
14. G. E. Murch and R. J. Thorn, Philos. Mag. A, 36, 529 (1977). *ibid*, 37, 85 (1978).
15. G. E. Murch and R. J. Thorn, Philos. Mag. A, 40, 477 (1979).
16. H. J. de Bruin, G. E. Murch, H. Bakker, and L. P. van der Mey, Thin Solid Films 25, 47 (1975).
17. G. E. Murch and S. J. Rothman, Philos. Mag. A, 43, 229 (1981).
18. H. J. de Bruin, H. Bakker, and L. P. van der Mey, Phys. Stat. Solidi (b) 82, 581 (1977).
19. N. A. Stolwijk, H. Bakker, and M. van Gend, J. Phys. C: Solid St. Phys. 13, 5207 (1980).
20. P. A. Flinn and G. M. McManus, Phys. Rev. 124, 54 (1961).
21. J. R. Beeler, Jr., and J. A. Delaney, Phys. Rev. 130 (1963) 962.
22. J. R. Beeler, Jr., Phys. Rev. 138A (1965) 1259.
23. B. Fultz, J. Chem. Phys. 87, 1604 (1987).
24. B. Fultz, J. Chem. Phys. 88, 3227 (1988).
25. B. Fultz and L. Anthony in Diffusion in High Technology Materials 1988, D. Gupta, A. D. Romig, Jr. and M. A. Dayananda, eds., Trans Tech, Aedermannsdorf, Switzerland, (1988) pp. 253-260.

26. B. Fultz and L. Anthony, Phil. Mag. Lett. 59, 237 (1989).
27. H. Ouyang and B. Fultz, J. Appl. Phys. 66, 4752 (1989).
28. H. Bakker, Philos. Mag. A 40, 525 (1979).
29. U. Gahn and W. Pitsch, Z. Metallk. 78, 324 (1987).
30. U. Gahn and W. Pitsch, Acta Metall. 37, 2455 (1989).
31. U. Gahn and W. Pitsch, Acta Metall. 38, 1863 (1990).
32. N. Metropolis, A. W. Rosenbluth, M. N. Rosenbluth, A. H. Teller, and E. Teller, J. Chem. Phys. 21, 1087 (1953).
33. W. Feller, An Introduction to Probability Theory and its Applications Vol. I, (J. Wiley, New York, 1957) Chapter 15.
34. Y. Limoge and J. L. Bocquet, Acta Metall. 36, 1717 (1988).
35. B. Fultz, "Chemical Systematics of Iron-57 Hyperfine Magnetic Field Distributions in Iron Alloys", Chapter 1 in Mössbauer Spectroscopy Applied to Magnetism and Materials Science, G. J. Long and F. Grandjean, eds., (Plenum Press, New York) in press.
36. B. Fultz, Phys. Rev. B 44, 9805 (1991).
37. R. Kikuchi, T. Mohri, and B. Fultz, Mater. Res. Soc. Symp. Proc. 205 (MRS, 1992) pp. 387-392.
38. B. Fultz, "Pseudostable States", Philos. Mag., in press.
39. A. Lidiard, Phil. Mag. 46, 1218 (1955).
40. A. D. LeClaire, J. Nucl. Matl. 69,70 (1978).
41. H-J. Rockosch, Ph.D. Dissertaion, Univ. of Münster (1983).
42. N. H. March, Solid State Commun. 63, 1075 (1987).
43. R. Benedek, J. Phys F 17, 569 (1987)
44. U. Klemradt, B. Drittler, T. Hoshino, R. Zeller, P.H. Dederichs, and N. Stefanou, Phys. Rev. B 43, 9487 (1991).
45. B. Fultz, "Effects of Vacancy-Solute Interactions on the Kinetics of Ordering" in Kinetics of Ordering Transformations in Metals, H. Chen and V. K. Vasudevan, eds. (TMS, Warrendale, 1992) pp. 121-130.

CVM-Based Free Energy Estimates in Monte Carlo Simulations

L. Anthony and B. Fultz

W. M. Keck Laboratory of Engineering Materials 138-78
California Institute of Technology
Pasadena, California 91125 USA

Abstract

A method for estimating the configurational entropy and free energy in Monte Carlo simulations is proposed and implemented. This method is inspired by the cluster variation method. By choosing an appropriate set of base clusters of increasing size, a sequence of increasingly accurate estimates of the configuration entropy can be obtained. We demonstrate the method by calculating the time evolution of the free energy during the formation of chemical order on bcc lattices. Particular emphasis is placed on the time-dependence of the free energy during the transient appearance of pseudostable states.

Diffusion in Ordered Alloys
Edited by B. Fultz, R.W. Cahn, and D. Gupta
The Minerals, Metals & Materials Society, 1993

I. Introduction

An earlier chapter of these proceedings [1] reviewed Monte Carlo studies of order-disorder transformations in alloys. In this chapter, we present a novel technique for calculating free energies of alloys during Monte Carlo simulations. In particular, we are interested in the changes of the free energy during the evolution of chemical order. It has always been possible to keep track of the free energy in kinetic studies using the path probability method (PPM) [2,3]—the present method confers a similar capability upon kinetic Monte Carlo simulations.

To calculate the free energy during a Monte Carlo simulation, we borrow ideas from the cluster variation method (CVM) [4,5]. In practice, the Monte Carlo simulations are carried out in the usual manner. In addition, however, the simulated crystal lattice is periodically sampled for the probabilities of various cluster types. These cluster probabilities are used directly in the CVM formulae for the configurational entropy and free energy. This simple but powerful idea combines the best of both worlds—the relationship between free energy and kinetics (such as provided by PPM) and the accuracy of Monte Carlo simulations.

After this idea of using CVM entropy and free energy expressions in Monte Carlo simulations was developed and implemented, we were made aware of similar exploratory work by Schlijper [6,7] and others [8]. Schlijper et al. [6,7] demonstrated a CVM–Monte Carlo method for the estimation of free energies in the two- and three-dimensional Ising models and the three-dimensional three-state Potts model. In addition to the CVM entropy expressions, their method used an alternative Markovian estimate for the entropy. In this way, they were able to obtain upper and lower bounds on their entropy estimates. Bichara et al. [8] then applied the CVM–Monte Carlo portion of Schlijper's technique to the study of Fe–Al alloys in the tetrahedron approximation. However, these efforts were directed at equilibrium systems. To the best of our knowledge, the present work is the first application of such hybrid CVM–Monte Carlo techniques to the study of non-equilibrium systems.

II. Cluster Variation Method

The statistical mechanical basis of the CVM has been treated at great length in the many papers by Kikuchi and his coworkers [4,5]. Many workers have also attempted to clarify or reformulate its mathematical machinery [9–13]. The reader is referred to these papers for details. Suffice it to say that given a specification of base (or maximal) cluster(s) of the parent crystal lattice, the CVM formalism provides an explicit albeit approximate expression for the configurational entropy and free energy of the system in terms of cluster probabilities of the base cluster(s) and its subclusters. In general, the equilibrium free energy is obtained by minimizing the free energy expression with respect to these cluster probabilities subject to one or more constraints, such as composition, long-range order (LRO), short-range order (SRO), etc.

Although the CVM was originally developed to deal with equilibrium structures, the CVM free energy expression remains a useful quantity in the consideration of non-equilibrium systems as well. In fact, in the PPM (the extension of the CVM to time-dependent processes), the (non-equilibrium) free energy is obtained as a by-product of maximizing the path probability. Some may question the applicability of the free energy concept to non-equilibrium systems in general and kinetic Monte Carlo simulations in particular. Consider the familiar expression for the Helmholtz free energy [14],

$$F = E - TS_{\text{config}}, \tag{1}$$

as it applies to Monte Carlo kinetics. In the canonical Monte Carlo simulations employed here, the temperature, T, is always a well-defined quantity. In a pair interaction model, the internal energy, E, can, at any time, be obtained by simply examining all the atom pairs in the Monte Carlo crystal and summing their interaction energies. Whereas the configurational entropy, S_{config}, is proportional to the logarithm of, in principle, at least, a purely combinatorial term—one that is divorced from considerations of whether the system is in equilibrium. So we can conclude that both S_{config} and F are well-defined quantities in our Monte Carlo simulations. It remains, however, to demonstrate that they are useful for understanding the kinetic evolution of an alloy.

It should be pointed out that the CVM formalism does not prescribe the choice of base cluster(s) to be used. Traditionally, the critical temperature, T_c, predicted by a particular choice of base cluster(s) has been used as one of the measures of that method's accuracy. By this yardstick, it has been found that employing larger base clusters generally gives better approximations [11,15–17]. Exceptions abound however—for instance, it is well known that in fcc systems that the double-tetrahedron approximation gives a less accurate value for T_c than the (single) tetrahedron approximation in spite of the larger base cluster of the former [11]. For the purpose of the present work, we employed the entropy and free energy expressions corresponding to a variety of base cluster sets on the bcc lattice. In order of increasing accuracy, these are the: a) point, b) pair, c) tetrahedron, d) octahedron, and e) octahedron–cube approximations (see Fig. 1).

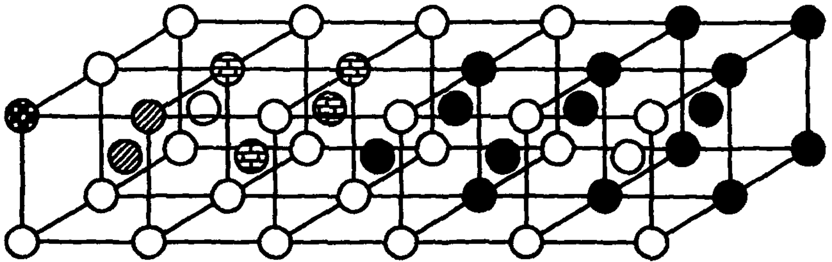

Figure 1: A portion of the bcc lattice showing (from left to right) the a) point ◍, b) pair ▨, c) tetrahedron ▦, d) octahedron ●, and e) cube ● clusters.

III. Monte Carlo Simulations

The algorithm for our Monte Carlo simulations has been described in detail elsewhere (see Ref. [1] and the references therein). For the present work we used a bcc lattice of 64 × 64 × 64

× 2 = 524 288 atoms, unless stated otherwise. The crystal lattice was initially randomly seeded with A and B atoms in a 1:1 ratio (AB stoichiometry) with one of the sites left vacant. This latter vacancy served as the agent of the mechanism of ordering. In our vacancy mechanism of ordering, the eight first-nearest neighbors of the vacancy had Boltzmann probabilities for exchanging sites with the vacancy. A pair interaction model using first- (1nn) and second-nearest-neighbor (2nn) pair interactions was used for obtaining the Boltzmann factors, which were used as weights in the random selection of an atom-vacancy interchange. B2 and/or B32 order was allowed to develop in the initially disordered crystal lattice by annealing at a fixed finite temperature below the critical temperature for ordering. During the Monte Carlo simulations, we kept track of the SRO and LRO parameters. The Warren-Cowley SRO parameters were obtained by counting the A–A, B–B, and A–B pairs for each near-neighbor shell and applying the usual formulae. The LRO parameters were obtained from the diffraction pattern of the crystal lattice, calculated by obtaining the three-dimensional Fourier transform of our alloy. The intensities of the $(\frac{1}{2}\frac{1}{2}\frac{1}{2})$ and (100) superlattice diffraction peaks were normalized by that of the (110) fundamental peak and used as measures of the B32 and B2 LRO parameters, respectively.

In addition, we periodically computed the configurational entropy and free energy of the crystal. This was done by counting the frequencies of the various cluster types that enter into the well-known CVM formulae [11] for the entropy. Knowing the value of S in the various cluster approximations, we computed E by summing the energies of the various 1nn and 2nn pairs, and then used Eq. 1 to obtain the corresponding approximations for F. In principle, the statistical accuracy of F is limited by the size of the Monte Carlo crystal being studied. In the present study, we chose to maximize the accuracy by counting all the clusters of a given cluster type in the crystal lattice. This was possible as there were only about half a million atoms in the Monte Carlo crystal. (The number of clusters of any given cluster type is equal to a small integral multiple of the number of atoms.) We had no problems with statistical accuracy or reproducibility, but problems could arise with larger base clusters. The larger the cluster type, the smaller (on average) the individual cluster probabilities for that cluster type, and the more susceptible these are to statistical fluctuations. It could therefore become necessary to use as large a crystal lattice as possible, or to perform ensemble averaging in order to maximize the precision of the estimated S and F.

IV. Results and Discussion

Using this new computational tool to monitor the free energy in our Monte Carlo simulations, we followed the change in the free energy density as an initially disordered alloy developed order. Figure 2 shows the change in the (100) superlattice intensity as a function of Monte Carlo step for an equiatomic binary alloy with $V_{AA}{}^1 = V_{BB}{}^1 = 1.00$. The interatomic interaction potentials are in units of kT, and this particular choice corresponds to a temperature of 0.315 T_c. The (100) superlattice intensity increases monotonically until it reaches an approximate plateau at about 250 Monte Carlo steps. This increase of the (100) intensity reflects the growth of B2 order, which is the equilibrium phase for this particular choice of pair interactions. At this point (at ~250 Monte Carlo steps) the alloy has reached equilibrium and consists of a single well-ordered B2 domain. (The additional very slight increase in the (100) intensity after 250 Monte

Carlo steps is due to the "annealing out" of some of the single-site defects in the alloy [18].) Also shown in Fig. 2 are the point (solid line), tetrahedron (dotted line), octahedron (dashed line), and octahedron–cube (dotted dashed line) approximations to the free energy density (in units of kT). These exhibit the same general trend of a monotonic decrease in F until about 250 Monte Carlo steps, from which point on there is only a barely perceptible additional decrease and the alloy is essentially at equilibrium.

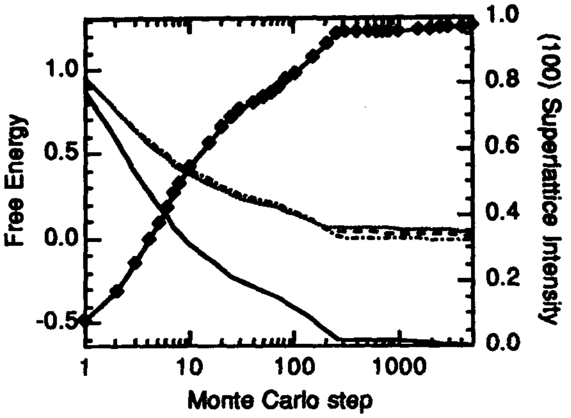

Figure 2: Graph showing the growth of the (100) superlattice diffraction intensity (◆) as a function of Monte Carlo step for an initially disordered equiatomic binary alloy with $V_{AA}^1 = V_{BB}^1 = 1.00$ (in units of kT). Also shown, on the same horizontal axis, are the point (solid line), tetrahedron (dotted line), octahedron (dashed line), and octahedron–cube (dotted dashed line) approximations to the free energy density (in units of kT).

It is interesting to compare the results for the different approximations of F (Fig. 2). Initially (at 0 Monte Carlo steps), the configurational entropy density is ln 2 for all levels of approximation. This is because the initial random configuration corresponds to $T = \infty$; and all CVM configurational entropy and free energy expressions are exact in the high-temperature limit [11]. As order evolves in the alloy, however, the free energy curves from the various approximations begin to deviate from each other, although all four curves show the same qualitative trends. In the point-approximation, the free energy density is just the internal energy density offset by ln 2. The free energy densities from the tetrahedron, octahedron, and octahedron–cube approximations are similar to each other, suggesting that they are probably close to the exact value. The deviation among these three curves gives a rough estimate of the error resulting from truncating the approximation at the octahedron–cube level. Another estimate can be obtained from the absolute value of F at equilibrium—for the exact case corresponding to Fig. 2, we must have $F \approx 0$ for nearly perfect B2 order because $E \approx 0$ (very few 1nn A–A and B–B bonds) and $S \approx 0$ (nearly perfect order).

The above approximations for F obtained using our hybrid CVM–Monte Carlo technique are in principle quite different from the corresponding approximations obtained using conventional CVM and PPM. This is because while both approaches employ the same level of approximation in obtaining the configurational entropy S, the same is not true of the internal energy E. The internal energy in the hybrid CVM–Monte Carlo method is essentially exact for the large crystal lattices used here, irrespective of the level of cluster approximation used to calculate the configurational entropy. In contrast, the internal energy in conventional CVM and PPM is limited by the same level of approximation as used in calculating the configurational entropy.

Figure 3 shows the variation of the $(\frac{1}{2}\frac{1}{2}\frac{1}{2})$ and (100) superlattice diffraction intensities as functions of Monte Carlo step for an equiatomic binary alloy with $V_{AA}^1 = V_{BB}^1 = 1.00$; $V_{AA}^2 = V_{BB}^2 = 0.70$ (in units of *kT*). For this particular choice of pair interaction the equilibrium state is one of B32 order. The $(\frac{1}{2}\frac{1}{2}\frac{1}{2})$ superlattice intensity, which represents B32 order, increases monotonically until it reaches its equilibrium plateau after about 1500 Monte Carlo steps. (The sharp increase in the $(\frac{1}{2}\frac{1}{2}\frac{1}{2})$ superlattice intensity at about 1000 Monte Carlo steps, just before equilibrium is reached, is due to the annihilation of antiphase domain boundaries.) Meanwhile, the (100) superlattice intensity, which represents B2 order, increases initially until it reaches its maximum value at about 10 Monte Carlo steps. After that, it begins to decrease monotonically until it has practically vanished by the time equilibrium is reached. Also shown in Fig. 3, on the same horizontal axis, is the octahedron–cube (dotted dashed line) approximation to the free energy density, which decreases monotonically until it reaches its equilibrium value of approximately 1.97 (in units of *kT*) after about 1000 Monte Carlo steps. For the exact case corresponding to Fig. 3, we would have $F \approx 2.0$ for nearly perfect B32 order because $E \approx 2.0$ (approximately one 1nn A–A bond and one 1nn B–B bond per atom) and $S \approx 0$ (nearly perfect order).

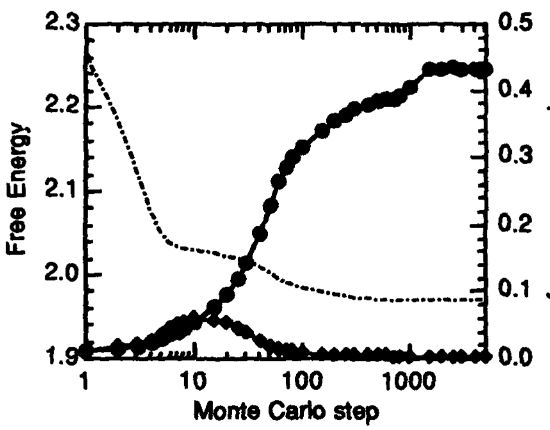

Figure 3: Graph showing the variation of the $(\frac{1}{2}\frac{1}{2}\frac{1}{2})$ (●) and (100) (◆) superlattice diffraction intensities as a function of Monte Carlo step for an initially disordered equiatomic binary alloy with $V_{AA}^1 = V_{BB}^1 = 1.00$; $V_{AA}^2 = V_{BB}^2 = 0.70$ (in units of *kT*). Also shown, on the same horizontal axis, is the octahedron–cube (dotted dashed line) approximation to the free energy density (in units of *kT*).

The transient appearance of B2 order in this simulation has analogs in similar studies of disorder→order transformations carried out using analytical techniques such as the master equation method and PPM [19–22]. Such transient states have been termed "pseudostable" elsewhere in the literature [20,21]. In the earlier analytical work, such transient or pseudostable states have been shown to be associated with a stationary point or saddle point in the free energy surface [21]. Based on the approximation to the free energy shown in Fig. 3, a similar association appears to exist here. As expected, the free energy density decreases monotonically with Monte Carlo step. However, there appears to be an approximate plateau in *F* where the (100) superlattice intensity reaches its maximum. This is not unlike the behavior of the free energy density reported in Ref. [20]. The often long-lived nature of those transient states was attributed to the vanishing of the free energy gradient, and hence the thermodynamic driving force, in the vicinity of the stationary point in the free energy surface [20,21].

The above results can also be explained heuristically as follows. The phase boundary between B2 and B32 in the ground state ($T = 0$) occurs at $V_2/V_1 = \frac{2}{3}$ [23]. This is close to the value of V_2/V_1 used in the simulation of Fig. 3. We therefore expect the thermodynamic driving forces for the formation of the two types of order, B2 and B32, to be very similar for the conditions of this simulation. The alloy in its initial random configuration is in a highly non-equilibrium state. Its free energy is very much higher than what it would eventually be in the equilibrium B32-ordered state. It can begin to dispose of this excess free energy by forming domains of not only B32 order but B2 order as well. Some local regions in a random alloy are B2-like, and can form B2-type order more expediently than B32. (Although the B2 domains in this simulation may have a higher free energy density than the B32 domains, it is still much less than that of the initial disordered state.) This accounts for the large drop in F in the early stages of the simulation (from 1 to about 10 Monte Carlo steps). In fact, examination of the simulated microstructure of the transient state (at ~10 Monte Carlo steps) showed it to consist of small domains of B2 and B32 order of a few lattice constants in diameter. However, once the initial disordered state has been replaced by these microdomains of B2 and B32 order, any further decrease in the free energy can only be achieved by the growth of the B32 domains at the expense of the B2 domains. This is indeed what occurs in the next stage of the simulation (from ~10 Monte Carlo steps onwards). As expected, the resulting additional drop in F is much less than that in the first stage because of the presumably much smaller free energy difference between B2 and B32 order.

We repeated the simulation of Fig. 3 using a crystal lattice $\frac{1}{8}$ the previous size but performed 8 times with 8 different random number seeds. The resulting aggregate superlattice diffraction intensities and free energy densities thus obtained were essentially identical to those obtained previously. This suggests the feasibility of using ensemble averaging in concert with the methods described above to increase the precision of our free energy estimates. This should be a particularly useful capability when extending our scheme to larger base clusters.

V. Conclusions

We have developed and implemented a technique for extracting configurational entropies and free energies from kinetic Monte Carlo simulations. We were able to obtain a range of approximations to the free energy depending on the choice of base clusters used. Using the best of these (the octahedron–cube approximation), we were able to verify that the free energy density decreased monotonically with time as order evolved in an initially disordered alloy. We were also able to show that the free energy versus time curve approximated a plateau in the neighborhood of certain transient or pseudostable states.

VI. Acknowledgments

We acknowledge stimulating conversations with R. Kikuchi, J. Sanchez, T. Mohri, and T. Lindsey. This work was supported by a Grant for International Research from the Ministry of Trade and Industry, Japan, and the U. S. Department of Energy under contract DE–FG03–86ER45270.

VII. References

1. T. Lindsey and B. Fultz, these proceedings.
2. R. Kikuchi, Annals of Phys. **10**, 127 (1960).
3. R. Kikuchi, Suppl. Prog. Theor. Phys. **35**, 1 (1966).
4. R. Kikuchi, Phys. Rev. **81**, 988 (1951).
5. M. Kurata, R. Kikuchi, and T. Watari, J. Chem. Phys. **21**, 434 (1953).
6. A. G. Schlijper and B. Smit, J. Stat. Phys. **56**, 247 (1989).
7. A. G. Schlijper, A. R. D. van Bergen, and B. Smit, Phys. Rev. A **41**, 1175 (1990).
8. C. Bichara and G. Inden, "Gibbs energies and chemical potentials of solid solution phases—a combined Monte Carlo and cluster variation approach," to be published.
9. J. A. Barker, Proc. Roy. Soc. A **216**, 45 (1953).
10. T. Morita, J. Math. Phys. **13**, 115 (1972).
11. J. M. Sanchez and D. de Fontaine, Phys. Rev. B **17**, 2926 (1978).
12. J. M. Sanchez, F. Ducastelle, and D. Gratias, Physica A **128**, 334 (1984).
13. F. Ducastelle, *Order and phase stability in alloys*, (North-Holland, Amsterdam, The Netherlands, 1991), Sec. 4.3.
14. The present Monte Carlo simulations employ a rigid crystal lattice. Consequently, the Helmholtz and Gibbs free energies only differ by a fixed constant, *PV*.
15. A. G. Schlijper, J. Stat. Phys **40**, 1 (1985).
16. A. Finel, Thèse de Doctorat d'Etat, Université Paris (1987).
17. R. Kikuchi, "CVM entropy algebra," to be published.
18. B. Fultz, J. Chem. Phys. **88**, 3227 (1988).
19. L. Anthony and B. Fultz, J. Mater. Res. **4**, 1132 (1989).
20. R. Kikuchi, T. Mohri, and B. Fultz, Mater. Res. Soc. Symp. Proc. **205**, 387 (Materials Research Society, Pittsburgh, 1992).
21. B. Fultz, "Pseudostable States," Philos. Mag. B, in press.
22. L. Anthony and B. Fultz, "Kinetics of B2, $D0_3$, and B32 ordering: Results from pair approximation calculations and Monte Carlo simulations," submitted to J. Mater. Res.
23. M. J. Richards and J. W. Cahn, Acta Metall. **19**, 1263 (1971).

Order–Disorder Transitions in Driven Compounds

P. Bellon, F. Soisson, and G. Martin

CEREM / SRMP, CE Saclay
F91191 Gif-sur-Yvette, France

Abstract

We consider the case of a driven alloy where atomic diffusion takes place by two mechanisms acting in parallel (as it is the case for an alloy under irradiation) : thermally activated jumps and forced jumps. (e.g. due to nuclear collisions). Order-disorder reactions are followed in a binary A_cB_{1-c} alloy on a body centred cubic lattice. Possible steady-state for such an open system are identified by a deterministic treatment of the above kinetic model under mean-field approximation. On increasing the external forcing intensity (the irradiation flux), the nature of the A2-B2 transition is shifted from 1st to 2nd kind, beyond a tricritical line. Stochastic descriptions, which incorporate fluctuations, are required to study the relative stability of these steady-states. Furthermore, time- and space-correlations of forced jumps (cascade effects) can then be considered : they are shown to modify significantly the stability of the system.

Diffusion in Ordered Alloys
Edited by B. Fultz, R.W. Cahn, and D. Gupta
The Minerals, Metals & Materials Society, 1993

Introduction

In previous works, we addressed the question of phase stability under irradiation from the point of view of dynamical systems [1-6]. Indeed in simple cases, an alloy under irradiation can be seen as a system where two dynamics are acting in parallel : the thermally activated jumps and the ballistic jumps, due to nuclear collisions. Kinetics and steady-state properties of such a dissipative system cannot be obtained from standard equilibrium thermodynamics. However, starting from a mesoscopic kinetic description, using the formalism introduced by Kubo et al [7], in some specific cases stochastic potentials governing the probability distribution of states can be built analytically. From these potentials, dynamical equilibrium phase diagrams are obtained, providing a map of the most stable steady-state for any given set of irradiation conditions. By the use of deterministic numerical simulations, more complex cases, e.g. heterogeneous systems, can be studied [6] : ordered precipitates can become unstable after the introduction of an anti-phase boundary. Because of the lack of fluctuations in the above simulations, information on the relative stability of competing steady-states cannot be obtained, and bursts of ballistic jumps in displacement cascades during heavy-ion or neutron irradiation cannot be taken into account.

After recalling in the first section the diffusion model, we introduce a deterministic kinetic model in the second section. In the third section, stochastic treatments are presented and solved by the use of numerical simulations, emphasizing cascade effect on phase stability.

I. Diffusion model

As an example, we consider a binary A_cB_{1-c} alloy on a B.C.C. lattice and focus on the B2-A2 order-disorder transition. We model atomic diffusion by permuting two nearest-neighbour atoms, belonging thus to distinct sublattices, according to two mechanisms operating in parallel :

- forced (ballistic) jumps induced by the external forcing at a frequency Γ_b which is independent of the state of order of the system and of its temperature.;

- thermally activated jumps. According to rate theory the activation energy $E^{act}_{\alpha\beta}$ (respectively $E^{act}_{\beta\alpha}$) is the energy necessary to extract an $A_\alpha B_\beta$ pair (respectively $A_\beta B_\alpha$) from its environment, where its energy is $E_{\alpha\beta}$ (respectively $E_{\beta\alpha}$) and to bring it into a saddle point position where its energy is E_s. For simplicity, the extraction energy is computed in the broken bound model and E_s is assumed to be independent on the surrounding of the AB pair.

The exchange of an A atom on a site i of sublattice α with a B atom on a site j of sublattice β occurs at the frequency :

$$\Gamma^{ij}_{\alpha\beta} = \Gamma^{th\,ij}_{\alpha\beta} + \Gamma_b = \nu \exp\left(-\frac{E^{ij}_{\alpha\beta}}{kT}\right) + \Gamma_b \qquad (1)$$

It is easy to show that the first dynamics entering in equation (1) (the thermally activated one) fulfils the detailed balance condition. Notice that for this dynamics, the system knows which state it is leaving but ignores the state it is moving to, beyond the saddle point (the same dynamics was already proposed by Fultz [8]). It is sometimes assumed that the activation energy is a half of the energy difference between final and initial states : this would only affect the kinetics of a thermal system ($\Gamma_b=0$), but would modify the steady-states of a driven one ($\Gamma_b\neq0$). Our choice is more appropriate to far from equilibrium systems.

In the following, we will consider a Bragg-Williams mean-field approximation (BW), which is appropriate for B2 ordering. Decomposing the B.C.C. lattice into two sublattices, the state of order, in a homogeneous model, is described by the A atomic concentrations C_1 and C_2 on both sublattices, or by the concentration C and the degree of order $S=C_1-C_2$. We restrict to nearest neighbour interactions : with V_{ij} the energy of a pair of i-j atoms, we define $V=(V_{aa}+V_{bb}-2V_{ab})/2$ (where $V>0$ for ordering systems). For the sake of simplicity, we choose $V_{aa}=V_{bb}$. We will also consider one- and two-dimensional heterogeneous models : a local concentration on the i^{th} site of the sublattice α is defined by C_α^i, this concentration corresponding to averaging performed over atomic planes or rows, respectively. Under this approximation, the activation energy for thermally activated jumps writes :

$$E_{12}^{ij}=E_s-\sum_{p}^{nn(i)}\{C_2^pV_{aa}+(1-C_2^p)V_{ab}\}-\sum_{q}^{nn(j)}\{C_1^qV_{ab}+(1-C_1^q)V_{bb}\} \tag{2}$$

where the summations in equation (2) are restricted to nearest-neighbour of sites i and j (nn(i) and nn(j) respectively).

II. Deterministic treatment

Applying the above diffusion model to the case of a heterogeneous system in the BW approximation, the rate of change of concentration at site i on sublattice 1 is given by :

$$\frac{dC_1^i}{dt}=\sum_{j}^{nn(i)}\left\{-(\Gamma_{12}^{ij}+\Gamma_b)C_1^i(1-C_2^j)+(\Gamma_{21}^{ji}+\Gamma_b)C_2^j(1-C_1^i)\right\} \tag{3}$$

A similar expression for dC_2^i/dt is obtained by interchanging subscripts 1 and 2 in equation (3). For thermal systems ($\Gamma_b=0$), the above kinetic equation drives the system to an equilibrium state which is precisely the one obtained by minimizing the mean-field free energy, computed in the same Bragg-Williams approximation [2,3,6].

As can be seen from eq.(1-2), the control parameters are: the reduced temperature T/T_c ($T_c=zV/2k_b$), the average composition C and the reduced forced frequency :

$$\gamma_b=(\Gamma_b/\nu)\times\exp\left\{\frac{(E_s-8K)}{k_bT}\right\} \tag{4}$$

where $K=(V_{aa}+V_{bb}+2V_{ab})/2$. The deterministic evolution of the system as well as its steady-states are obtained by numerical integration of eq.(3), using periodic boundary conditions, for different sets of initial conditions $\{C_1^i(t=0),C_2^i(t=0)\}$ with a fourth-order Runge-Kutta method with an adaptive step-size [6]. The relative error on the concentration is kept less than 10^{-6} during each integration step, and steady-state is assumed to be reached when all derivatives have absolute values smaller than 10^{-8}.

In previous work [2,5,6], we have shown that beyond a threshold value in the forcing intensity, γ_b, the A2-B2 order-disorder transition which is of second kind at equilibrium may become first kind. As a result, steady-state two-phase systems are expected for non-stoechiometric composition. This was indeed observed [6] : from such steady-state profiles, the dynamical equilibrium phase diagram of figure 1 can be built. In most of the two-phase field, the system can be in three locally stable states : homogeneously ordered, homogeneously disordered, and two-phased. Since fluctuations are absent from the above description, the relative stability of these metastable states cannot be studied. Let us mention that in the case of a kinetic Ising model with two dynamics in parallel (a metropolis one and an infinite temperature dynamics one), Gonzales-Miranda et al [9] also observed a shift from 1st to 2nd kind of the nature of the para-ferromagnetic transition.

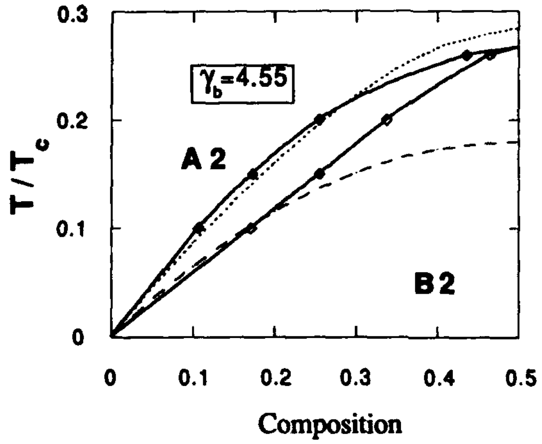

Figure 1 : Dynamical equilibrium phase diagram at fixed forcing intensity $\gamma_b = 4.55$, obtained from steady-state solutions of deterministic equations (3). The two-phase field is delimited by the solid lines ; the dotted (dashed) line is the line above (below) which any ordered (disordered) phase is unstable.

III. Stochastic treatments

Fluctuations are recovered in the above description if discrete variables are considered instead of the continuous C_1^i [10,11]. Let Ω be the number of lattice sites per plane : we will now describe the system by variables such as N_1^i, the number of A atoms on sublattice 1 in plane i . Note that in the limit $\Omega \to \infty$, $N_1^i/\Omega \to C_1^i$. We will now consider different cases, depending on the correlations of the forced jumps.

Uncorrelated ballistic jumps

Let us assume in this paragraph that ballistic jumps concern only one atomic pair at once : with the same diffusion model as above, the transition rates for the exchange of any given A-B pair of nearest-neighbours are given by :

$$W_{12}^{ij} = \Omega \ [\frac{N_1^i}{\Omega} \frac{\Omega - N_2^j}{\Omega} \Gamma_{12}^{ij} + \frac{N_1^i}{\Omega} \frac{\Omega - N_2^j}{\Omega} \Gamma_b] \qquad (5)$$

where Γ_{12}^{ij} is function of N_m^k/Ω instead of C_m^k (k=i,j ; m=1,2). Transition probabilities are given by :

$$w^{ij}_{12} = W^{ij}_{12}/\Omega \qquad (6)$$

The system is now characterized by the probability P(s,t) to find it in a state s at the time t, the state s being the list of the A atom numbers on all lattice sites. The time evolution of such a probability distribution follows a Master Equation :

$$\partial P(s,t)/\partial t = \sum_{s'} - W_{s,s'} P(s,t) + W_{s',s} P(s',t) \qquad (7)$$

Contrary to the case of homogeneous models [1-3,5,7], no analytical solution is known for equation (7)in the case of a heterogeneous system, even under steady-state conditions.

However, it is possible to perform a numerical integration of this ME, by sampling a trajectory of the system which is consistent with the transition rates defined by equation (6). We present now the algorithm for a one-dimensional system, but it is easily generalized to two dimensions.

Let us define the sum of these transition probabilities over all possible exchanges in the system :

$$\sigma = \sum_{\text{all possible exchanges}} w^{ij}_{12} \qquad (8)$$

A trajectory is numerically built from the above stochastic description as follows [10,11]. Starting from an initial configuration for the $\Omega \times N$ atoms, the next exchange to occur is obtained by sampling one event among all possible pair exchanges which would modify the current configuration. This sampling is performed by adding all the transition probabilities, thus building a segment of length σ, and by pulling at random a first number on this segment . The location of the random number in the segment determines the exchange which has occurred. The probability distribution for the residence time of the system in its current state decays exponentially with time, the time constant being σ^{-1}. By pulling a second random number, the time spent by the system in the configuration before the realization of the jump is obtained from this exponential decay. Physical time can therefore be measured in such simulations, and time-average quantities can be computed. This algorithm is similar to the Monte Carlo one proposed by Bortz et al [12] for atomistic simulations.

In a practical way, $\Omega = 100$ was large enough so as to reproduce with a very good accuracy the composition limits of the two phase field in figure 1. Compositions are obtained by time-averaging the compositions of the ordered and disordered phases, once a two-phase state is reached. We chose the normal to atomic planes to be [100] : in this simple case, all the sites in any atomic plane belong to the same sublattice and one variable per plane is thus sufficient for the description.

The relative stability of the three locally stable states is obtained by measuring the mean first passage times from one metastable state to another : we only observed transitions from homogeneous states (either ordered or disordered) toward the two-phase state, and this for all the runs performed, even for very long time. Figure 2 displays such a transition from a homogeneously ordered state to the two-phase state. The local composition X_i and the local degree of order S_i are plotted as function of the plane index i. They are given by :

$$X_i = \frac{2N_i + N_{i+1} + N_{i-1}}{4\Omega} \quad \text{and} \quad S_i = \frac{\left| 2N_i - N_{i+1} - N_{i-1} \right|}{2\Omega} \tag{7}$$

The system remains in its initial state for some time (figure 2a), but then a fluctuation starts to build-up (figure 2b) ; this fluctuation consists in a small disordered region but without any modification of the local atomic composition ; then composition decreases in this disordered region (figure 2c), and finally the two-phase state is obtained after the growth of the disordered region (figure 2d) It is thus concluded that the two-phase state is indeed the most stable state of the system, in agreement with results obtained from analytic stochastic description [5].

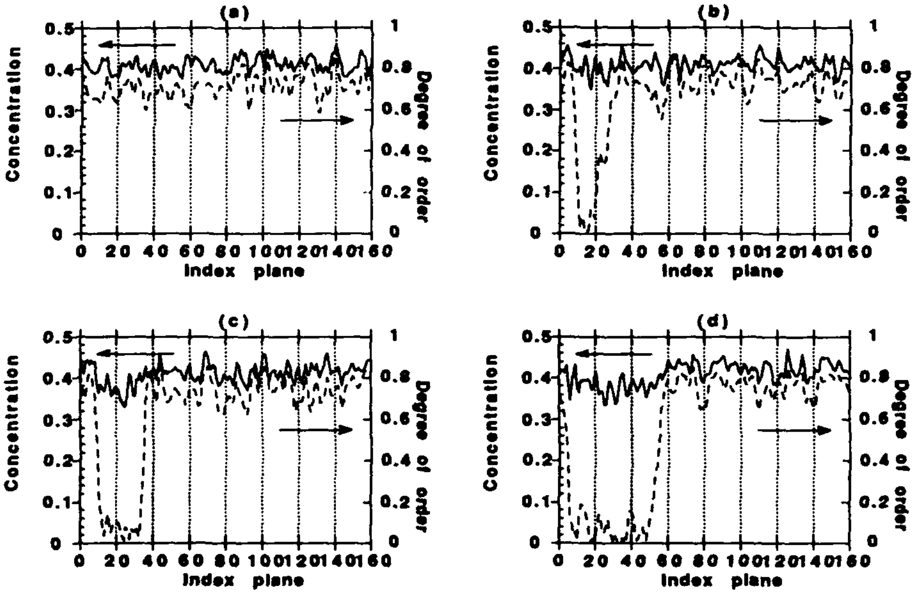

Figure 2 : Transition from an homogeneous ordered state toward a two-phase state at $T/T_c = 0.25$, $\gamma_b = 4.55$, at an average composition of 0.41, and for isolated ballistic jumps (b = 1). (a), (b), (c) and (d) are instantaneous configurations obtained after 4.6×10^6, 4.9×10^6, 5.5×10^6, and 7×10^6 pair exchanges respectively (the system contains 160×100 atoms).

Time- and space-correlated ballistic jumps

Up to now we have considered that ballistic jumps were uncorrelated. However, in a displacement cascade, ballistic jumps are strongly correlated both in time and space. These correlations are expected to alter the phase diagram built in figure 1 [2]. Although we start from a Bragg-Williams approximation, time and space correlations are present in the heterogeneous description. The correlations in the ballistic jumps can be implemented in the above scheme as follows. We assume the number of atom pairs undergoing forced exchanges by one collision is

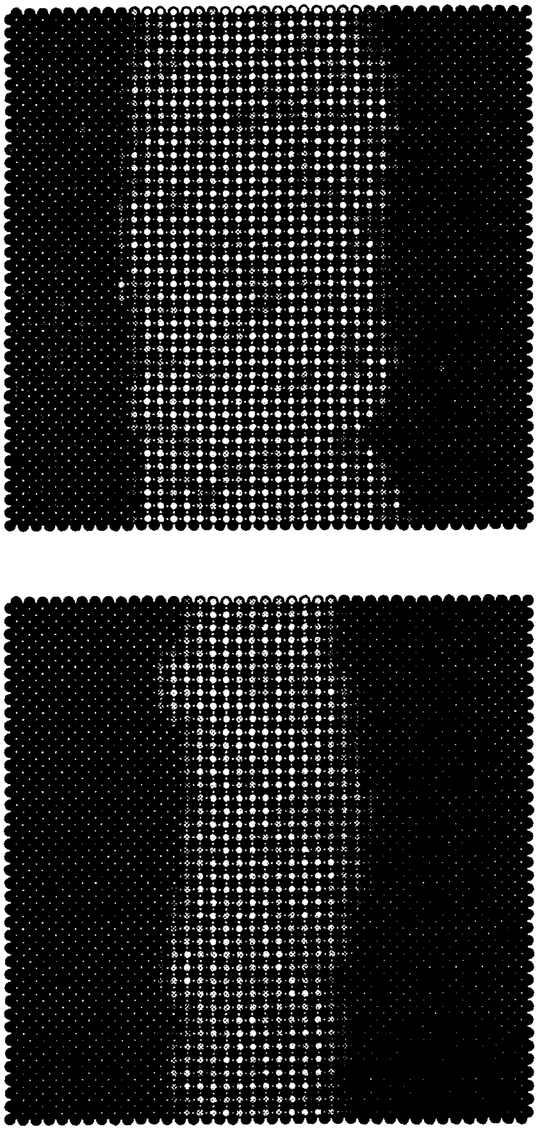

Figure 3 : Influence of the cascade density on the limit of the two-phase field : for the same geometry of the cascade, the number of ballistic jumps is increased from 20 (top) to 60 (bottom). The configurations are obtained by numerical integration of ME for 40×40 BCC cell system in the (001) plane, for a reduced irradiation temperature of 0.20, a ballistic jump frequency of 4.55 and for an average composition of 0.30.

the same for all cascades ; this number is denoted by b. Since Γ_b is the number of forced exchanges per atom per unit time, the number of cascade per atom and unit time is therefore :

$$\Gamma_c = \Gamma_b / b \qquad (8)$$

This cascade frequency, Γ_c, replaces now the second term in the right hand side of equation 1. During the selection of the next event to occur, if the first random number is located on a segment corresponding to Γ_c, then a cascade is occurring : let us consider for simplicity that all cascades are centro-symmetric and have the same 'geometry', i.e. that the number of planes affected by forced exchanges of nearest neighbours and the numbers of forced exchanges between these planes are fixed. Then, starting from the actual distribution of A and B atoms among these affected planes, 2b numbers are pulled at random so as to choose which atoms are affected by the cascade. The atomic configuration is then updated by performing exchanges between the selected atoms. This procedure avoids the tedious analytic calculations of transition probabilities connecting the actual configuration to any configuration which can be reached after a cascade. The only restriction is that all cascades are included in our approach, while only the cascades which actually modify the state of the system have to enter in the computation of σ. For the cases considered below, where alloys not are too dilute and with sufficiently large enough number of replacements in a cascade, the relative number of cascades improperly taken into account (less than 10^{-4}) is too small to be significant.

We have studied the effect of cascade on the phase diagram of figure 1, here at an average composition of 0.30 (with a two-dimensional system, made of 40×40 BCC unit cells, each colon containing Ω=100 atoms) : keeping constant the number of replacements per atom per unit time, $\Gamma_b = 4.55$, on increasing the number of atoms in a cascade, different behaviours are observed (Figure 3). Here the size of the cascade is kept constant (mixing up to 3rd nearest-neighbours), and b the number of ballistic jumps in a cascade is the sum of b_1 forced exchanges between central site and nearest neighbours and b_2 between 1st and 2nd, and 2nd and 3rd nearest neighbours ($b=4\times b_1+12\times b_2$). For simplicity we choose $b_1=2\times b_2$. For a very dilute cascade, b=20, (fig. 3a), the most stable-steady state of the system coïncides with the one obtain in the mean-field approximation (fig. 1) ; for b=60, the ordered phase has a lower volume fraction (fig. 3b), indicating that the two-phase field has been shifted toward the stoechiometric composition ; for very dense cascade, b=200, a hundred forced exchanges are performed at once : the system is now disordered, with some ordered regions, but having a very short life-time.

In the case of dense cascade, b=200 above, we lower the temperature of the system to T/T_c=0.15. Starting either from an initially fully ordered state or from an initially disordered state (fig. 4), the system evolves toward a state where disordered zones coexist with ordered ones : however it is not guarantied that coarsening will occur in this case ; although further simulations are required, a characteristic length for the spatial distribution of precipitates seems to be reached ; this characteristic length would depend one the cascade density, as well as on the cascade size (which was kept constant here). According to this picture, on a macroscopic scale, for an alloy at a steochiometric composition one would observe a continuous increase of the superlattice reflections in a diffraction experiment on decreasing the temperature, this transition presenting some similarities with a 2nd order transition. Further calculations are in progress to address this point.

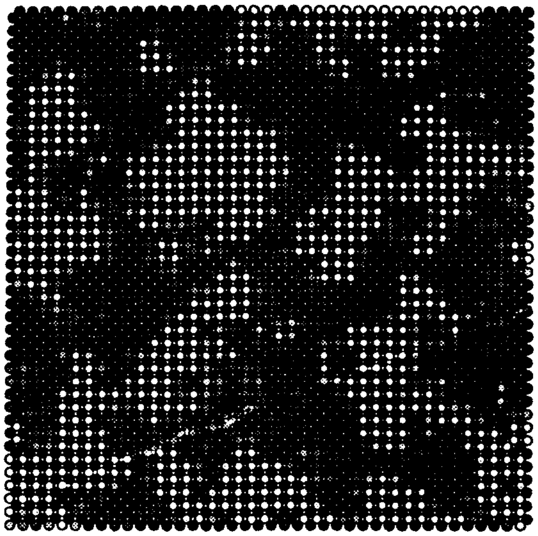

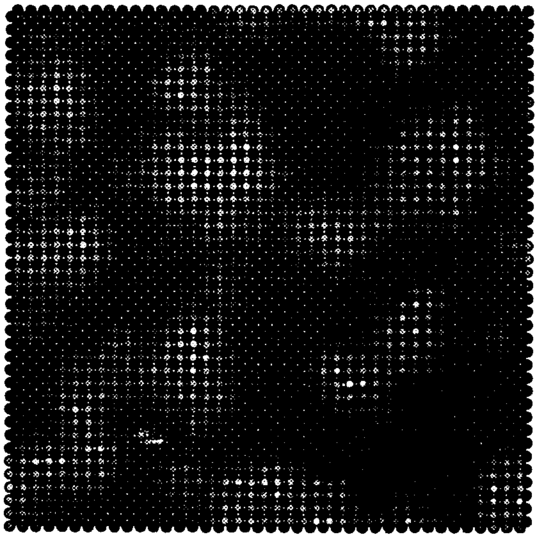

Figure 4 : Instantaneous (top) and time-averaged (bottom) configurations obtained by numerical integration of ME for 40×40 BCC cell system in the (001) plane at an average composition of 0.30, initially in a fully disordered state. The reduced irradiation temperature and ballistic jump frequency are 0.15 and 4.55. Here dense cascades (b=200) are producing a dynamical coexistence of disordered and ordered zones, after 3.15×10^6 thermal exchanges and 9.7×10^6 ballistic exchanges

Conclusion

Phase stability and kinetic paths in ordered alloys under irradiation are studied by deterministic or stochastic numerical simulations. Dynamical equilibrium phase diagrams can be computed, which are shown to be very sensitive on the existence of displacement cascades. Further work is in progress for introducing point defects in a consistent way and for improving the statistical approximation.

References

1) Bellon P. and Martin G. : Phys. Rev. B , 1988, 38, 2570.
2) Bellon P. and Martin G. : Phys. Rev. B , 1989, 39, 2403.
3) Haider F., Bellon P., and Martin G. : Phys. Rev. B , 1990, 42, 8274.
4) Salomons E., Bellon P., Soisson F., and Martin G. : Phys. Rev.B, 1992, 45, 4582.
5) Bellon P. : Phys. Rev. B, 1992, 45, 7517.
6) Soisson F., Bellon P., and Martin G. : Phys. Rev. B, in the press.
7) R. Kubo, K. Matsuo and K. Kitahara, J. Stat. Phys., 1973, 9, 51.
8) B. Fultz,J. Mater. Res., 1990 , 5, 1419.
9) J. M. Gonzalez-Miranda, P. L. Garrido, J. Marro and J. L. Lebowitz, Phys. Rev. Lett., 1987, 59, 1934.
10) Gillespie D. T. : Physica, 1979, 95A, 69.
11) Haider F.: in *Ordering and Disordering in Materials*, Ed. Yavari (North-Holland, 1992) p. 215.
12) Bortz A. B. , Kalos M. H., and Lebowitz J. L. : J. Comp. Phys., 1975, 17, 10.

Ordering and Disordering Mechanisms — An Overview

Robert W. Cahn

Department of Materials Science and Metallurgy
Cambridge University
Pembroke Street, Cambridge CB2 3QZ, England

Abstract

A distinction is drawn between homogeneous and heterogeneous ordering; the latter can be akin to cellular decomposition and involve grain boundary migration, or other types of localized nucleation site may operate. The use of diffraction as well as microscopy to distinguish between these mechanisms is instanced. Attempts to interpret ordering kinetics in terms of diffusion and ordering energy have mostly been restricted to homogeneous ordering; special emphasis has been placed on the determination of activation energies. Some empirical studies on the relation between ordering *kinetics* and *self-diffusivity in* $L1_2$ *compounds*, and that between the activation energy for self-diffusion and ordering energy, are summarised. Recent experiments on the mechanically–induced disordering of 'permanently' ordered intermetallic compounds will be outlined, with emphasis on Ni_3Al. The subsequent reordering of such materials takes place readily, but they do not necessarily return to a state of perfect order.

Diffusion in Ordered Alloys
Edited by B. Fultz, R.W. Cahn, and D. Gupta
The Minerals, Metals & Materials Society, 1993

Introduction

Since ordering or disordering of any alloy phase is usually a diffusive process, the kinetics of either process is linked to the diffusion of the constituent species in the alloy phase. It is thus rather surprising that so little attention has been paid to the linkage between ordering (or disordering) and diffusivity. There are at once three complications: it is not clear whether the fastest or the slowest diffusing species (in a binary phase) will be rate-determining; diffusivities are likely to be different in the ordered and disordered forms of an alloy phase and in all intermediate states; and the magnitude of the 'driving force', determined by the ordering energy and by the temperature, will necessarily affect the relationship between kinetics and diffusivity. A distinction has also to be made between long-range and short-range order, which have quite different kinetics and driving forces; this overview is concerned only with long-range order, but Lücke and Yu, also Mohri and Ikegami, at this Symposium, are discussing short-range ordering in depth.

In attempting to interpret the kinetics of ordering or disordering quantitatively, it is necessary to assume that the process is homogeneous. If, say, the rate and mechanism of ordering varies drastically from point to point... i.e., if the process is heterogeneous... it will be altogether too complicated for effective analysis.

The purpose of this short paper is merely to outline what is known about the following aspects of the general problem: (1) the circumstances under which ordering or disordering are homogeneous or heterogeneous processes; (2) approaches which have been used for measuring the kinetics; (3) the relationship of ordering kinetics and diffusivities in orderable compounds to the ordering energy. All of the foregoing refers to alloys which have a critical ordering temperature well below the melting-point, so that the alloy can be disordered by quenching from above T_c. To complement this, (4) I outline recent work on the mechanical disordering of an ordered phase which cannot be disordered thermally (i.e., one which has a high ordering energy) and on subsequent reordering of the mechanically disordered phase. — The broader objective of this paper is to interest the 'diffusion community' in the problem of ordering and disordering kinetics.

Homogeneous or Heterogeneous?

Following the discovery of antiphase domains (APDs) in Cu_3Au in the 1930s, it was generally assumed that any orderable alloy phase behaves like Cu_3Au, i.e., that a "foam", in W.L. Bragg's words, of ordered APDs is nucleated at different points in the disordered crystal and that these grow until they touch, followed by progressive coarsening. Meanwhile, the degree of order, S, in the domains approaches the equilibrium value for the temperature in question; it has never been quite clear whether, under any circumstances, the equilibrium degree of order can be achieved while the domains are still quite small (or have not even yet joined up), or whether the value of S is to some degree determined by the domain size. Another perennial issue is whether an alloy with an equilibrium S less than unity has randomly distributed 'wrong' atoms or whether these atoms are clustered in some way. This kind of issue was discussed over quarter of a century ago in an earlier TMS symposium [1]. Irrespective of how the wrong atoms are distributed, this form of ordering can be regarded as 'homogeneous' and its kinetics can sensibly be analysed in terms of diffusivities.

Another kind of ordering reaction was discovered later, notably by Tanner [2] who examined Ni_2V, which orders with a change of symmetry, to orthorhombic. (Tanner calls such transformations "neostructural"). In different temperature ranges, this phase orders either homogeneously or by a process of domain nucleation at grain boundaries. Most commonly, the two processes combine: domains first nucleate at the boundaries and then, progressively, the residual intragranular material orders homogeneously. The heterogeneous grain-boundary reaction is coarse and can often be observed by optical microscopy (e.g., in Ni_4Mo, by Brooks and Sanganeria [3]). The heterogeneous process in this alloy and in others such as Ni_2Cr, Ni_3V and Ni_4Mo was thoroughly reviewed by Tanner and Leamy [4] in a survey which is of lasting value. The process is not restricted to neostructural ordering transformations: for instance, it has more recently been observed in FeCo [5,6]; here again, either the heterogeneous or the homogeneous process predominates according to temperature. Fig. 1 shows an optical micrograph of predominantly heterogeneous ordering in FeCo at 400°C. The process is akin to "cellular" phase transformations, familiar in physical metallurgy.

Fig. 1. FeCo, quenched from 800°C, 2 hours 400°C. Heterogeneous ordering. [6]

Fig. 2. Thermally polished CuPt, annealed for 85 hours at 550°C, observed by polarised light, showing ordered domains growing from grain boundaries, pores and a scratch. [7]

Another alloy which orders heterogeneously at relatively low temperatures is CuPt, which changes from f.c.c. to rhombohedral on ordering and can therefore be conveniently examined by polarised light (Fig. 2). Here, ordered domains can nucleate at various kinds of surface defects, as seen in the figure [7]. X-ray diffraction can also distinguish between homogeneous and heterogeneous ordering provided ordering is accompanied by a reduction of symmetry (as in Ni_2V or CuPt); a single fundamental diffraction line then splits into a pair, and one can determine whether both disordered and ordered phases coexist and, if so, whether the ordered phase has yet reached its equilibrium degree of order (because the angular split varies with the value of S). This approach was successfully used with both Ni_2V [4] and CuPt [7]. Such studies can also serve to indicate whether, as is apt to happen, the intragranular material begins to order homogeneously while domains nucleated at the grain boundaries have still penetrated only a small way into each grain [7].

It must be reiterated here that when an alloy undergoes heterogeneous ordering (which has been presented here in simplified terms for lack of space), there is not much hope of interpreting the kinetics of the process in terms of diffusivities... though at least one investigator has tried!

Disordering

Disordering mechanisms above T_c have been studied much less than ordering mechanisms. There have been intermittent reports that just above the critical temperature, the disordering process begins at antiphase domain boundaries, which are known to be locally disordered. A few years ago, this was shown clearly by TEM of ternary alloys based on Ni_3Al + Fe, in which thick disordered regions were seen at APD boundaries [8]. Such heterogeneous nucleation of disordering has recently been studied in great detail by a Franco-Belgian group [9,10], who used both TEM and HREM. They heated ordered $Co_{30}Pt_{70}$ and Cu-17at% Pd alloys, which have the $L1_2$ (Cu_3Au-type) structure, and found thickening of APD boundaries as much as 40° below the critical temperature; the process is akin to progressive melting at free surfaces in pure metals some way below the thermodynamic melting temperature. Above T_c, the boundaries thicken rapidly as the disordered phase grows. This work has recently been reviewed [11]. — It is to be presumed, but has not been carefully examined, that an alloy rapidly heated to a temperature well above T_c will disorder homogeneously.

Measurement of Ordering Kinetics

With those alloys which can readily be obtained in a metastable disordered form by quenching from above the critical temperature, such as Cu_3Au, FeCo, Ni_3Fe, it is quite straightforward to follow (homogeneous) ordering kinetics either by diffraction or by measurement of a physical property sensitive to the state of order; the electrical resisitivity has been preferred, though some excellent work was done many years ago by measurement of elastic modulus. Real-time dilatometry would be a good method, because of the change of lattice parameter with change of S, but this has not in fact been done. At temperatures at which ordering is very fast, until recently there has been no available method, but now real-time millisecond diffraction has become possible by use of synchrotron radiation sources and this has been applied to the problem by Ludwig et al [12]; the instrumentation was treated in another paper [13]. At the other extreme, there are problems with alloys with a low T_c, only slightly above ambient temperature such as NiFe, Cu_3Zn and Cu_3Al. With such alloys, indirect approaches relying on scanning calorimetry have been used, and in the case of NiFe, ordering was accelerated by concomitant neutron irradiation[14] If that is done, however, normal diffusivities become irrelevant to the analysis of the ordering kinetics!

One other problem can arise is if T_c is so high (though still below the melting-point) that it is not feasible to quench in disorder at all: a notable example of this problem is Ti_3Al, which always proves to be ordered, however rapidly it is quenched from the disordered state. Without a disordered starting material, the measurement of ordering kinetics becomes more difficult (though not impossible). An alternative approach is to try rapid solidification (e.g., melt-spinning). This does not appear to have been tried with Ti_3Al, though it has been tried many times with Ni_3Al without success. (However, a ternary Ni_3Al + Fe alloy has been disordered by melt-spinning into an unusually thin ribbon [15]). Condensation from the vapor works better... it is an effectively very fast method indeed and can work even for the very firmly ordered 'permanent' intermetallics, i.e., those which remain ordered up to the melting-point. Harris et al. [16], also West and Aziz [17], have succeeded in depositing disordered Ni_3Al in this way. The general problem of "disorder trapping" during melt-quenching, which is of course linked with atomic mobilities in the solid state, has been treated in an important paper by Boettinger and Aziz [18], and for some specific refractory intermetallics, critical speeds for an advancing solid interface have been calculated: 60 cm/s for TiAl – in which disorder has been successfully trapped – and 200 cm/s for Al_3Nb, in which this has not yet proved possible.

A surprising member of the class of ordering alloys in which disorder cannot be trapped is β–CuZn, with B2 structure. This alloy, which undergoes an almost ideal second-order transition, remains stubbornly ordered however fast it is quenched in the solid state from above T_c (≈460°C). It is not known whether this is due to the rather high diffusivity or to the second-order nature of the ordering transition. Melt-quenching does not appear to have been tried.

There is no space here to list the many studies of ordering kinetics that have been published during the past 40 years. The results of a number of these have been assembled in an earlier overview by the author [19]. In that overview, a distinction was made between d–o and o–o measurements: the former refers to an initially disordered alloy, the latter, to one in a state of partial order which then changes to a state of higher (or lower) order when the temperature is changed. Few o–o studies have been published for those alloy phases in which disorder is readily trapped, but recently it has been shown that ordering kinetics can even be studied in phases which cannot readily be obtained in disordered form (or only in geometrically unfavourable thin layers). Such an o–o experiment has been done with Ni_3Al [20], using electrical resistivity measured at the annealing temperature. Here, the order parameter, S , is always quite close to 1 and changes by a few per cent only, and no attempt was made to convert the changes in resistivity (Fig. 3) into the corresponding changes in S . The absolute resistance changes are very small, and great precision is required. It will be noticed that the *sign* of the resistance change inverts at a particular temperature; this phenomenon can be explained in terms of a well-established model due to Rossiter [21]. Partly because of this difficulty in establishing how S changes with time when some other property is measured, the few studies of this kind, including the cited one on Ni_3Al, only concern themselves with the activation energy of the ordering process, and not with absolute rates. The objective then is to compare the activation energies so concerned with those measured for diffusion, and this is discussed below.

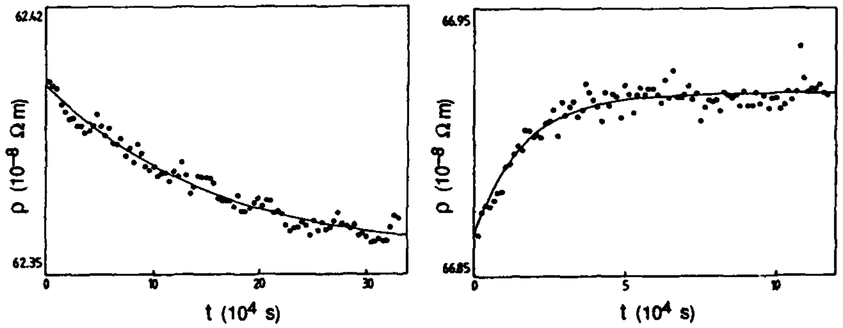

Fig. 3. Isothermal time dependence of the electrical resistivity of Ni_3Al after rapid cooling from 1173 K to (left) 880 K and (right) 973 K. The solid curves were fitted by assuming a single relaxation time, τ, in an $\exp(-t/\tau)$ expression. [19]

A similar strategy was followed by Tanner in the early paper already cited [2] on Ni_2V. Using x-ray diffraction measurements, and assuming that the heterogeneously nucleated ordered regions growing from the grain boundaries were perfectly ordered and that the intragranular regions were still wholly disordered, he obtained the ordering kinetic diagram reproduced in Fig. 4. The ordering activation energy below 550°C is close to the measured one for volume diffusion, and Tanner assumed that the lower energy above 550°C was to be associated with grain boundary diffusion. Since the ordering process here is governed by grain-boundary motion, Tanner was at a loss to interpret the low-temperature activation energy (though he made some valiant guesses). This example shows how quixotic an enterprise it is to attempt the interpretation of heterogeneous ordering reactions in terms of diffusivities.

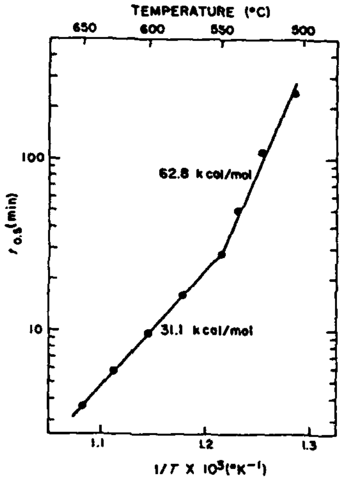

Fig. 4. Plot of time needed for 50% transformation in Ni_2V during isothermal ordering. [2]

Another form of o–o experimentation has been developed by H. Bakker's group in Amsterdam. They have studied permanently ordered intermetallics, particularly CoGa and a range of A15 superconducting phases. When CoGa is quenched from a high temperature in the solid state, a large number of antisite defects (i.e., wrongly placed atoms) remains in the alloy; the lattice parameter changes and so does the magnetic behavior. The change in S due to quenching is small. Restoration of the lost order is possible by annealing and the kinetics of restoration can be related to diffusion rates. The same thing was done by measuring changes in the superconducting transition temperature, T_t, of phases such as Nb_3Au following high-temperature quenching and also after progressive annealing. There is an accepted single relationship between T_t and S, valid for all A15 phases:

$$(T_t(S)/T_{t(max)}) = 0.17 + 0.83 \exp[-7.78(1 - S)], \tag{1}$$

and therefore this approach offers a particularly direct way of measuring small changes in S and the kinetics of those changes. Early examples of this approach were studies of V_3Ga and $Ca_3Rh_4Sn_{13}$ and a concise summary of some of this research, with references, can be found in a recent review by Bakker et al. [22].

The Relationship of Diffusivity and Ordering Kinetics to Ordering Energy

As we have seen in the last section, most measurements of ordering kinetics give essentially only one useful piece of information, and that is an activation energy (sometimes more than one in different temperature ranges) based on a fit for a single relaxation time. This activation energy is generally assumed to be identical to the activation energy for the dominant diffusion process (whatever that may be in each case). A valuable survey based on many experiments, a number from their own group, has recently been published by Cadeville et al. [23]. All the alloys surveyed in this paper have the $L1_2$ structure. For this related group, it is found that the activation energy deduced from ordering kinetics at various temperatures, E_A, is closely related to the critical temperature for ordering, T_c. This is shown in Fig. 5. Since the ordering energy is approximately proportional to T_c, as has been known ever since W.L. Bragg first analysed the ordering process, Fig. 5 tells us that the activation energy for ordering in an $L1_2$ superlattice rises as the ordering energy increases. This is not necessarily related in any simple way to the activation energy for diffusion.

The same group also examined E_A for $Fe_{1-x}Al_x$ alloys, with results as shown in Fig. 6, below. This work is described fully in a recent paper [24]. The striking feature of this plot is the very low activation energy for B2-type substoichiometric FeAl. The vacancy formation energy is known, from positron annihilation measurements, to be normal, so the migration energy is deduced to be extremely low (0.2–0.3 eV). There is at present a lively debate about the possible jump mechanisms in the FeAl phase that would account for the low migration energy, involving linked jumps of the components of a "triple defect". The matter is complicated by evidence that this phase has unusually high vacancy concentrations (presumably, constitutional, not thermal, vacancies). This rather complicated debate is outlined in a recent paper by Vogl et al. [25].

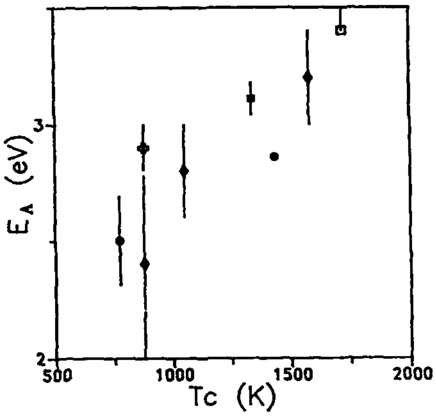

Ni_3Al (□), Ni_3Mn (○),
$Ni_{75}Al_{25-x}Fe_x$ (◆ and +),
$Ni_{74}Al_{21}Cr_5$ (■) and $Ni_{75}Al_{20}Mn_5$ (●).

Fig. 5. Activation energies for ordering versus the critical ordering temperature for a number of $L1_2$ alloys. [23]

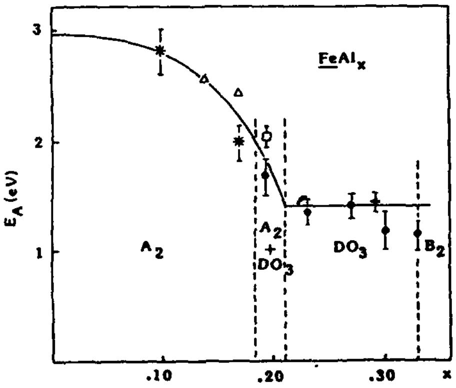

Fig. 6. Activation energies for ordering versus x in $Fe_{1-x}Al_x$. * refers to resistometry at 4K, ● refers to in-situ resistometry. The other symbols refer to other methods of measurement. [23], [24]

It is not surprising that the activation energy for diffusion – or, to be pedantic, the part of it that corresponds to the activation energy for vacancy migration – increases as compounds become more strongly ordered, since then the energy cost of moving an atom from a "right" to a "wrong" position increases also. This effect of the ordering energy would be expected to be much more pronounced in B2 compounds such as CuZn or NiAl, since in these all atoms have unlike neighbors (whereas in $L1_2$, a proportion of the majority atoms have like neighbors). Unfortunately, no correlation like that in Fig. 5 seems to have been attempted for B2 compounds; that is probably because many of these are permanently ordered, i.e., are ordered up to the melting point. Nevertheless, o–o ordering kinetics would offer a means to obtain data like those in Fig. 5.

In this connection, it is interesting to examine the relationship between activation energies for diffusion of the same phase in the ordered and disordered conditions. In B2 β–brass, where the comparison can be readily made, it has long been known [26] that E_A is much higher in the ordered condition. Fig. 7 reproduces their famous graph. "O" and "D" have been inserted to denote the ordered and disordered temperature domains. By contrast, Fig. 8 reproduces a graph from my earlier study [19], relating entirely to $L1_2$ phases. There are no straightforward comparisons available between the same phase in ordered and disordered conditions, because phases like Cu_3Au have T_c values so low that diffusivities cannot be effectively measured below T_c, and there are no phases with high T_c values still below the melting temperature. The lines drawn thick in Fig. 8 refer to the interdiffusion coefficient in ordered and disordered forms of Ni_3Al; the latter line is derived from measurements made in Japan on primary disordered Ni–Al alloys containing up to 18 at.% of Al; the plots of the interdiffusion coefficient for several temperatures as a function of Al content were straight lines and were extrapolated to 25 at.% Al, representing an imaginary disordered version of Ni_3Al. It can be seen that here, ordering does not change the activation energy for diffusion at all, in spite of the fact that the ordering energy is much greater than in CuZn! There has been no proper theoretical analysis of diffusion in $L1_2$ phases, unlike the mass of theory published for B2 phases, because the problem is much more difficult. All that can be said is that the presence of a number of *like* nearest-neighbor bonds clearly reduces drastically the effect of order on diffusivity. This topic is overripe for attention by theorists.

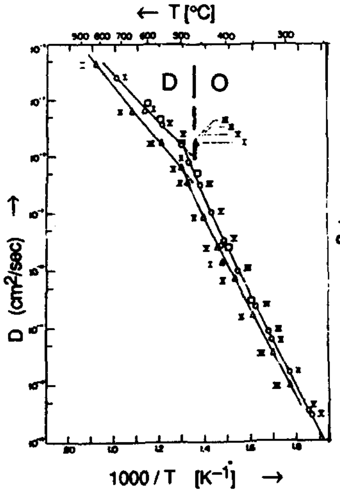

Fig. 7. Diffusion coefficients of Cu (triangles), Zn (circles) and Sb (squares) in (B2) β–CuZn of several near-stoichiometric compositions. [26]

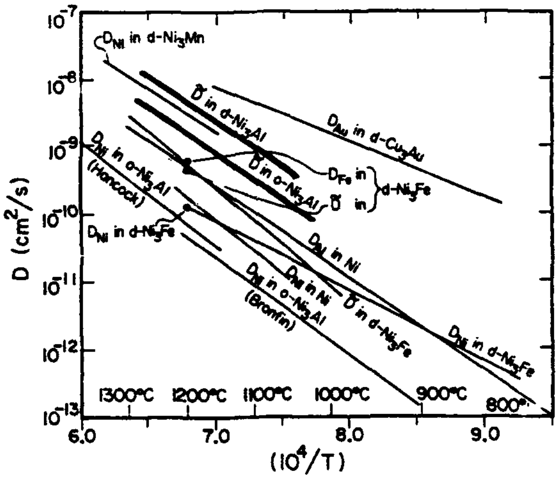

Fig. 8. Diffusivities in a range of $L1_2$ phases, derived from many sources. (For details see ref. [19])

For Ni_3Al, the o–o ordering kinetics examined by Kozubski and Cadeville [20] yielded an activation energy of 3 – 3.4 eV (the higher end of this range is included in Fig. 5), in satisfactory agreement with experimental values for chemical and inter-diffusion in this phase (2.7 – 3.4 eV). However, a recent detailed analysis [27] of the kinetics of reordering of Ni_3Al disordered by mechanical milling (see below) revealed a lower activation energy, rising from 1.2 to 1.6

eV as reordering progressed (the change was attributed to progressive vacancy trapping by impurities). All that this can confidently be said to show is that the activation energy for ordering is not simply related to that for any diffusion process. In the case of B2 phases, interpretation of any future ordering kinetics studies will be complicated by the fact that in such phases, the activation energy for diffusion changes drastically as order is progressively established.

Absolute Ordering Rates in Relation to Diffusivities and Ordering Energy

In the foregoing discussion, emphasis has been largely on activation energies, and nothing was said about the analysis of absolute rates of ordering. This matter has received little attention, yet it is of great intrinsic interest. The central issue is this: Clearly the diffusivity in the reordering phase plays a major part in determining the ordering rate, but by no means exclusively so. The diffusional correlation factor must play an important role as well; this factor, which varies considerably between different superlattices, can in a sense be regarded as a measure of the "efficiency" of diffusion, for it determines how many jumps are necessary on average to increase the number of correctly situated atoms by one. But that efficiency would also be expected to be be influenced by the "driving force" for ordering, which is simply the ordering energy .

Some years ago, I attempted [19] to grapple with this issue in a preliminary way, by comparing absolute ordering rates for different $L1_2$ phases, bringing together numerous published values for both ordering kinetics and diffusivities relating to Ni_3Fe, Ni_3Mn, Cu_3Au and Ni_3Al. I then picked, by interpolation, the temperature for each of these phases at which the relaxation time, τ, was 100 minutes, and obtained from published data the slower of the chemical diffusion rates of the constituent elements (where both had been measured), or simply the one known chemical diffusion rate in other cases. For the first three phases listed above, which have critical temperatures in the range 660 to 790 K and hence rather similar ordering energies, the diffusivity for $\tau = 100$ min is in the rather narrow range $7 \times 10^{-22} - 6 \times 10^{-20}$ m^2/s; the highest D was for Cu_3Au, which has the lowest ordering energy. However, for Ni_3Al, which has the high (virtual) critical ordering temperature, above the melting point, of ≈ 1680 K [28], the corresponding diffusivity for $\tau = 100$ min is only 1.5×10^{-26} m^2/s.

What this tells us is that to achieve ordering at the same rate, starting in each case from disordered material (in the case of Ni_3Al, this referred to an old study on material disordered by filing; recent studies [20,27] were not yet available), much *slower* diffusion will suffice if the driving force, represented by the ordering energy, is very *high* . A different way of wording this is to say that diffusion is more efficient, or more "focused" on the task of enhancing order, if the driving force is high. To turn this indication into a proper analysis will require more theoretical expertise than I possess!

Permanently Ordered Alloys Disordered by Mechanical Means

Repeated reference has been made in the foregoing to Ni_3Al disordered by mechanical milling, and to a reordering study made on material disordered in this way. Here I shall very briefly outline this work. In fact, the bulk of the work has already been reviewed in a paper presented earlier this year [29] to a symposium organized by the ASM on Kinetics of Ordering Transformations. Since the connection of this research with diffusion is highly indirect, this discussion will be kept very brief.

This research had several distinct purposes: to obtain the fully disordered alloy (so that properties such as the lattice parameter could be measured as a function of order over the entire range$0 < S < 1$ [29] [30]); to measure the stages of disordering, as evidenced by heat release, lattice parameter change and changes in diffraction pattern; to examine whether amorphisation follows on disordering on continued milling; to study the reordering of the disordered alloy. Ball-milling is a much more efficient disordering process than filing, which was used many years ago to disorder Ni_3Al partially. Now that disordered Ni_3Al can also be deposited from the vapor [16,17], it will be particularly interesting to compare reordering kinetics for the dislocation-free alloy (made by vapor-deposition) and the intensely cold-worked material; this has not been attempted yet.

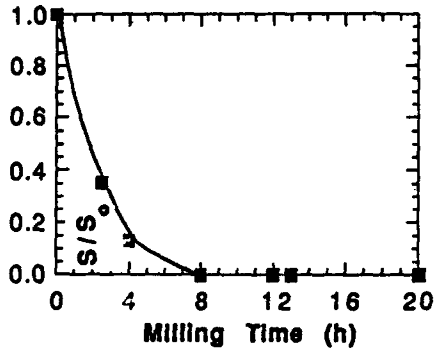

Fig. 9. Variation of the long-range order parameter as a function of the milling time for Ni_3Al–based powder. [29]

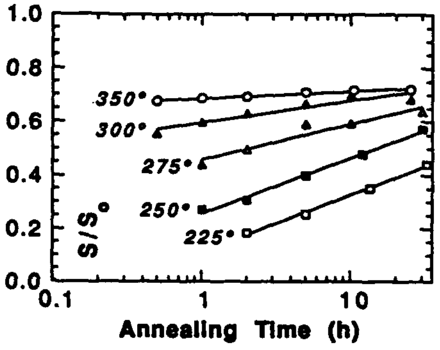

Fig. 10. Variation of the relative LRO parameter,S , of initially disordered Ni_3Al–based alloy during isothermal anneals at temperatures cited. [29]

To exemplify the kind of information that has flowed from this kind of research, I show here two figures, taken from ref. [29]. Fig. 9 shows the stages of disordering of Ni_3Al during ball-milling and Fig. 10 shows the rates of reordering, following complete disordering, at various temperatures. As can be seen in Fig. 10, mechanically disordered material cannot return to a state of perfect order; it is probable (but not yet known) that this would require a temperature high enough to ensure recrystallization. Subject to this kind of difference between mechanically disordered material and that disordered by very rapid quenching or vapor condensation, this approach to disordering permanently (very strongly ordered) alloys is likely to prove valuable for a range of other alloys apart from Ni_3Al. The approach has indeed already been used to study mechanical disordering (and amorphisation) of Zr_3Al, as described in ref. [29] and in [31] and [32].

In connection with the special concerns of this Symposium, the technique will be of interest because it will permit ordering kinetics to be measured, and related to measured diffusivities, for very strongly ordered alloy phases. Such research is reviewed in the context of our understanding of the ordering reaction and its consequences, in a forthcoming book chapter [33].

Acknowledgment

I am grateful for the financial support received from the European Community, 1990–92, that made possible some of the research reported here, and was the occasion of my renewed interest in the ordering reaction and its relation to other parameters, such as diffusion.

References

[1] J.B. Cohen and J.E. Hilliard, eds., Local Atomic Arrangements Studied by X-ray Diffraction (New York, Gordeon and Breach 1966).

[2] L.E. Tanner, "The Ordering Transformation in Ni_2V," Acta Metall. 20 (1972), 1197–1228.

[3] C.R. Brooks and M. Sanganeria, "Intergranular Fracture Along Migrated Boundaries in Ordered Ni_4Mo," Scripta Metall. 22 (1988) 1683–1688.

[4] L.E. Tanner and H.J. Leamy, "The Microstructure of Order-Disorder Transitions," in H. Warlimont, ed., Order-Disorder Transformations in Alloys (Heidelberg, Springer, 1974), 180–239.

[5] R.A. Buckley, "Ordering and Recrystallization in Fe-50Co-0.4% Cr," Metal Science 13 (1979) 67–72.

[6] M. Rajkovic and R.A. Buckley, "Ordering Transformations in Fe-50Co Based Alloys," Metal Science 15 (1981) 21–30.

[7] R.S. Irani and R.W. Cahn, "The Mechanism of Crystallographic Ordering in CuPt," J. Mater. Sci. 8 (1973) 1453–1472.

[8] R.W. Cahn, P.A. Siemers and E.L. Hall, "The Order-Disorder Transformation in Ni_3Al and Ni_3Al-Fe Alloys – II. Phase Transformations and Microstructures," Acta Metall. 35 (1987) 2735-2764.

[9] C. Leroux, A. Loiseau, M.C. Cadeville, D. Broddin and G. van Tendeloo, J. Phys: Condens. Matt. 2 (1990) 3479.

[10] A. Finel, V. Mazauric and F. Ducastelle, "Theoretical Study of Antiphase Boundaries in Fcc Alloys," Phys. Rev. Lett. *65 (1990) 1016–1019.*

[11] G. van Tendeloo, D. Schryvers, L.E. Tanner, D. Broddin, C. Ricolleau and A. Loiseau, "Structural Phase Transformations in Alloys: An Electron Microscopy Study," in J.L. Morán-Lopez, F. Mejía-Lira and J.M. Sanchez. eds., Structural and Phase Stability of Alloys (New York, Plenum, 1992), 219–230.

[12] K.F. Ludwig, Jr., G.B. Stephenson, J.L. Jordan-Sweet, J. Mainville, Y.S. Yang and M. Sutton, "Nucleated and Continuous Ordering in Cu_3Au," Phys. Rev. Lett. 61 (1988) 1859–1862.

[13] G.B. Stephenson, K.F. Ludwig, Jr., J.L. Jordan-Sweet, J. Mainville, Y.S. Yang and M. Sutton, "Instrumentation for Millisecond-Resolution Scattering Studies," Rev. Sci. Instrum. 60 (1989) 1537–1540.

[14] J. Paulève, D. Dautreppe, J. Laugier and L. Néel, "Irradiation-assisted ordering of NiFe", Compt. Rend. Acad. Sci. (Paris) 254 (1962) 965–968.

[15] A.R. Yavari and B. Bochu, "$L1_2$ Ordering in Ni_3Al–Fe Disordered by Rapid Quenching," Phil. Mag. A 59 (1989) 697–705.

[16] S.R. Harris, D.H. Pearson, C.M. Garland and B. Fultz, "Chemically disordered Ni_3Al synthesized by high-vacuum evaporation," J. Mater. Res. 6 (1991) 2019–2021.

[17] *J.A. West and M.J. Aziz, "Kinetic Disordering of* Intermetallic Compounds through First– and Second–Order Transitions by Rapid Solidification," in A.R. Yavari, ed., Ordering and Disordering in Alloys (London, Elsevier Applied Science, 1992), 23–30.

[18] W.J. Boettinger and M.J. Aziz, "Theory for the Trapping of Disorder and Solute in Intermetallic Phases by Rapid Solidification," Acta Metall. 37 (1989) 3379–3391.

[19] R.W. Cahn, "Ordering Kinetics and Diffusion in Some $L1_2$ Alloys," in G. Slade Cargill

III, F. Spaepen and K.-N. Tu, eds. Phase Transitions in Condensed Systems – Experiments and Theory, MRS Symp. Proc. 37 (1987), 385–404.

[20] R. Kozubski and M.C. Cadeville, "*In situ* Resistometric Investigation of Ordering Kinetics in Ni_3Al," J. Phys. F: Met. Phys. 18 (1988) 2569–2575.

[21] P.L. Rossiter, The Electrical Resistivity of Metals and Alloys (Cambridge University Press, 1987) 253–257.

[22] H. Bakker, D.M.R. Lo Cascio and L.M. Di, "Some Aspects of Diffusion in Intermetallic Compounds," in C.T. Liu, R.W. Cahn and G. Sauthoff, eds., Ordered Intermetallics – Physical Metallurgy and Mechanical Behaviour, (NATO ASI Series, Vol. 213, Dordrecht, Kluwer Academic, 1992) 433–448.

[23] M.C. Cadeville, V. Pierron-Bohnes and R. Kozubski, "Ordering Kinetics in Superalloy-Type Intermetallic Compounds in Relation with Diffusion Mechanisms", as ref. 17, 79-94.

[24] P. Vennégues, M.C. Cadeville, V. Pierron–Bohnes and M. Afyouni, "Strong Decrease of the Activation Energy as a Function of Al Content in $Fe_{1-x}Al_x$ Alloys Deduced from Kinetic Measurements of Ordering," Acta Metall. Mater. 38 (1990) 2199–2213.

[25] G. Vogl, Ch. Karner, O. Randl, B. Sepiol and D. Tuppinger, "Use of Atomistic Techniques to Study Diffusion in Intermetallics," as ref. 22, 497–509.

[26] A.B. Kuper, D. Lazarus, J.R. Manning and C.T. Tomizuka, "Diffusion in Beta Brass," Phys. Rev. 104 (1956) 1536.

[27] M.D. Baró, S. Suriñach, J. Malagelada, M.T. Clavaguera-Mora, S. Gialanella and R.W. Cahn, "Kinetics of Reordering of Ni_3Al Disordered by Ball-Milling," Acta Metall. Mater. 41 (1993), in press.

[28] R.W. Cahn, P.A. Siemers, J.E. Geiger and P. Bardhan, "The Order-Disorder Transformation in Ni_3Al and Ni_3Al–Fe Alloys. – I. Determination of the Transition Temperatures and their Relation to Ductility," Acta Metall. 35 (1987) 2737–2751.

[29] S. Gialanella, R.W. Cahn, J. Malagelada, S. Suriñach, M.D. Baró and A.R. Yavari, "Mechanical Disordering and Thermal Reordering Kinetics of Permanently Ordered $L1_2$ Compounds," in H. Chen and V.K. Vasudevan, eds., Kinetics of Ordering Transformations (Warrendale, TMS, 1992), 161–175.

[30] S. Gialanella, S. B. Newcomb and R.W. Cahn, "Order Parameter and Lattice Parameter of $L1_2$ Ordered Alloys, with Special Reference to Ni_3Al–based Alloys," as ref. 17, 67–78.

[31] S. Gialanella, A.R. Yavari and R.W. Cahn, "Metastable Phases of the Zr-Al System Obtained by Mechanical Attrition and Rapid Solidification," Scripta Metall. Mater. 26 (1992) 1233–1238.

[32] A.R. Yavari, S. Gialanella, T. BenAmeur, R.W. Cahn and B. Bochu, "On the Bcc, Hcp and Amorphous Polymorphs of Zr_3Al," J. Mater. Res. 7 (1992) in press..

[33] R.W. Cahn, "The Place of Atomic Order in the Physics of Solids and in Metallurgy," in F.E. Fujita, ed., Physics of New Materials (Heidelberg, Springer, 1993), in press.

Kinetics of $L1_0$ Ordering in CuAuPd Ternary Alloys

Syo Matsumura, Tatsuji Furuse, and Kensuke Oki*

Department of Materials Science and Technology
Graduate School of Engineering Sciences
Kyushu University 39, Kasuga-shi, Fukuoka 816, Japan

* Present address: Department of Nuclear Engineering
Kyushu University 36, Fukuoka 812, Japan

Abstract

An electron diffraction technique, IKL-ALCHEMI, was applied to a study on the kinetics of $L1_0$-type ordering in CuAuPd ternary alloys at 573 K. Au and Pd atoms have a tendency to share the same sublattice, while Cu atoms prefer the other one. In the alloys containing 50 at%Cu, LRO parameters of the three elements S_i's evolve monotonically with time, having the inequality $|S_{Au}|>|S_{Cu}|>|S_{Pd}|$ in the early stage, but $|S_{Pd}|\geq|S_{Cu}|\geq|S_{Au}|$ in the late stage. If the Cu content is less than 50 at%, S_{Au} is once raised, and then slightly attenuated by evolution of S_{Pd}. The kinetic behavior is explained in terms of the interatomic potentials and the diffusive mobilities of atoms.

Diffusion in Ordered Alloys
Edited by B. Fultz, R.W. Cahn, and D. Gupta
The Minerals, Metals & Materials Society, 1993

I. Introduction

Kinetics of ordering transformations in alloys has been attracting a great deal of attention with scientific and technological interests [1]. Many papers have been published on this problem so far [2-4]. Yet the investigations have largely been confined to binary systems, although most systems of technological interest consist of more than two components. We, of course, know that many studies have been conducted on ordering in ternary or multi-component alloys. But, the quantitative understanding is quite poor, parhaps owing to the limitations of conventional diffraction techniques of X rays, electrons or neutrons in determining quantities with respect to the atomic configuration, or order parameters, in ternary or multinary ordering alloys.

The long-range ordering in a crystalline alloy removes certain symmetry-elements from the symmetry group of the fundamental lattice [2,3]. If the number of components of the alloy is n, every removed symmetry-element yields n-1 long-range order (LRO) parameters characterizing the degree of order. It follows that the structure factor of a superlattice reflection must be given as a function of the n-1 LRO parameters. In the binary case where n=2, one LRO parameter is involved in the structure factor, and is determined explicitly from the diffracted intensity. The time-evolution of long-range order in a binary alloy is examined quantitatively through diffraction experiments. In contrast, the diffraction method cannot extract more than one LRO parameter from a ternary or multinary alloy with n>2 unless the scattering factors or the scattering lengths of elements are varied. Anomalous x-ray scattering near absorption edges or neutron scattering with isotopic substitution is usually employed to vary the scattering power [5-7]. The plural LRO parameters for n>2 are evaluated from a set of diffraction profiles as a function of x-ray wavelength or isotope content. These techniques are elegant in principle, but not suitable for routine work, since huge experimental facilities such as a synchrotron source or an atomic reactor are required in most of the cases. Mössbauer spectroscopy has been employed in the study of ordered atom-configuration in some ternary alloys [8-10]. The application of the latter technique, however, must be restricted to iron- and tin-base alloys in practice.

As an alternate diffraction technique to determine plural LRO parameters in multi-component alloys, the present authors [11] have recently proposed to utilize the intersecting Kikuchi-line (IKL) method [12] and the channeling enhanced x-ray microanalysis (ALCHEMI) [13] in the transmission electron microscopy. The new technique, which we call IKL-ALCHEMI, offers possibilities for routine analyses of multi-component ordered alloys at typical laboratories, because a transmission electron microscope equipped with an EDX spectrometer is used as the experimental apparatus. There exists, in principle, no limitation of the kind and the number of components.

Kinetics of ordering in alloys containing more than two components is particularly challenging, as an application of this new technique. If an LRO phase is being developed from a disordered state in a multi-component alloy, an interesting question arises: "How the alloy gets toward the equilibrium state of LRO in the n-1 dimensional space spanned by LRO parameters?". The course on which the alloy passes is called as "transformation path" or "kinetic path". Fultz, *et al.* recently studied the path problem for $B2$-type ordering in an FeCo-Mo alloy by Mössbauer spectroscopy [10]. To the authors' best knowledge, their result is, at present, an unique example of the path of ordering determined experimentally.

This paper reports our recent results of IKL-ALCHEMI study on the kinetics of ordering in a ternary system. Our examples are CuAuPd alloys, which form the $L1_0$-type structure with two-equivalent sublattices, as illustrated in Fig. 1. In this work, our attention is focused mainly on the kinetic behavior as a function of alloy-composition. In the following, we will review the principles of IKL-ALCHEMI, and then present the experimental results.

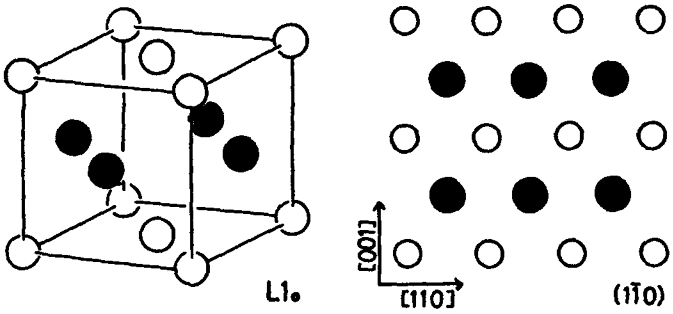

Figure 1 - $L1_0$ ordered structure and the (110) projection. Closed and open circles refer to α and β sublattices, respectively.

II. IKL-ALCHEMI

The occupation probabilities of Cu, Au or Pd on the two sublattices denoted by α and β are assumed to be

$$\Gamma_i(\alpha \text{ or } \beta) = x_i(1 \pm S_i), \qquad [i = \text{Cu, Au or Pd}], \tag{1}$$

where x_i and S_i are the atomic fraction and the LRO parameter of element i, respectively. The LRO parameters S_i are variable between -1 and +1. If $S_i = \pm 1$, i-atoms are located only on one of the two sublattices, while $S_i = 0$ characterizes equality in occupation on the two. Note that the number of independent variables included in eq. (1) is two for the ternary case at a given composition, owing to the conservation law,

$$\sum_i x_i S_i = 0. \tag{2}$$

The structure factor of a superlattice reflection $\boldsymbol{g}$ is given as

$$F(\boldsymbol{g}) = \sum_i f_i(\boldsymbol{g}) T_i(\boldsymbol{g}) x_i S_i \ , \tag{3}$$

where $f_i(\boldsymbol{g})$ and $T_i(\boldsymbol{g})$ are the atomic scattering factors of the elements and their temperature factors, respectively.

If electrons are illuminated on an area of a specimen in a transmission electron microscope, characteristic X rays are emitted from the constituent atoms. The intensity of X rays from an element i is given by

$$N_i = k_i x_i (1+S_i) I(\alpha) + k_i x_i (1-S_i) I(\beta) . \tag{4}$$

Here, k_i is the coefficient of fluorescent yield from the element i, $I(\alpha)$ and $I(\beta)$ are the mean flux of electrons at α and β sites, respectively. In ALCHEMI [13,14], we measure relative change in N_i's between two different conditions of electron diffraction. One of the two conditions is of dynamical excitation of a low-order superlattice reflection with a slight deviation from the exact Bragg position, and the other is a quasi-kinematical condition where no low-order reflections are strongly excited. The former condition makes $I(\alpha)$ and $I(\beta)$ different from each other, while the latter one almost equalizes them. Hence, N_i's depend on the diffraction condition. Let N_i^a and N_i^b be x-ray counts under the dynamical and the quasi-kinematical conditions, respectively. The proportion of N_i^a relative to N_i^b is denoted as $R_i (=N_i^a / N_i^b)$. If one obtains R_i's from an ALCHEMI pair of EDX spectra, the ratios of S_i's to S_j are determined to be

$$P(i,j) = \frac{S_i}{S_j} = 1 - \frac{R_i - R_j}{\sum_k x_k (R_k - R_j)} \tag{5}$$

Using $P(i,j)$ thus determined by ALCHEMI, we rewrite eq. (3) as

$$F(g) = \sum_i \{f_i(g)\, T_i(g)\, x_i\, P(i,j)\} S_j . \tag{6}$$

In eq.(6), S_j is an unique unknown parameter which can be evaluated by the diffraction experiment measuring the structure factor [15,16], *e.g.* the IKL method. A Kikuchi or Kossel line of a high-order reflection splits into two segments when the line crosses a strong Kikuchi band of a low-order reflection [12,16]. The separation between the two segments is directly proportional to the distance between two branches of the dispersion surface causing the strong band, that is to say, it is proportional to the structure factor of the low-order reflection. If we measure the separation due to a low-order superlattice reflection g, the value of $F(g)$ or S_j is determined from the separation through analyzing the many-beam dynamical electron diffraction. Thus all LRO parameters and the occupation probabilities of atoms on the sublattices given in eq.(1) are specified by the combination of IKL and ALCHEMI techniques.

III. Experimental Procedure

Four ingots of varying composition in the CuAuPd ternary system were prepared in an argon atmosphere in a high-frequency induction furnace. The compositions of the alloys are listed in Table I, and plotted in the isothermal section of phase diagram at 573 K [17], as shown in Fig. 2. The ingots were annealed at 873 K, quenched in iced brine, and then rolled into sheets. The sheets were kept at 873 K for 1.8 ks to remove strain and to obtain *fcc* disordered solid solutions, and were then annealed at 573 K in the $L1_0$ field for various durations. The annealed specimens were electrochemically thinned to electron transparency by twin-jet polishing in a solution of 35 g of Cr_2O_3, 200 ml of CH_3COOH and 100 ml of distilled water at room temperature. The electron microscope used was a JEOL JEM-2000FX with an EDX spectrometer at the HVEM Laboratory, Kyushu University. The specimens were cooled down to about 100 K by liquid nitrogen in the microscope. In ALCHEMI, the accelerating voltage was set to 160 kV, and EDX spectra were recorded under dynamical excitation of the (110) superlattice reflection and under a quasi-kinematical condition. In the IKL experiments, the acceleration voltage was raised up to 200 kV, and electrons were illuminated with sufficient convergence. The specimens were oriented so that (646) and (647) reflections simultaneously satisfied the exact Bragg condition. Under the above condition, Kikuchi-lines of the (646) and (647) reflections intersect with the (001) band within their CBED disks, splitting into segments. We measured the separation between the segments of the (646) reflection.

In the simulation of many-beam dynamical diffraction for analysis of the separation, 75 reflections, which are shown in Fig. 3 in a previous paper [11], were taken into account. The parameters used were obtained as explained in the previous paper.

Table I Compositions of the specimens

	x_{Cu} [at%]	x_{Au} [at%]	x_{Pd} [at%]
a	50	25	25
b	50	35	15
c	45	30	25
d	45	40	15

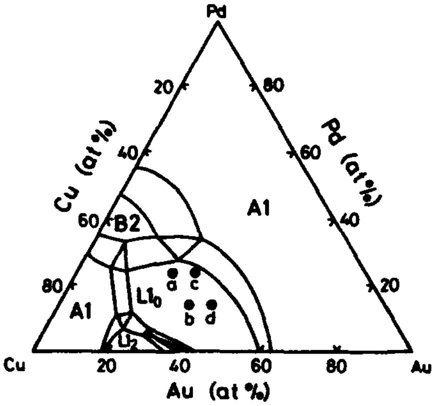

Figure 2 - Isothermal sections of the phase diagram of CuAuPd at 573 K. Closed circles a,b,c and d indicate compositions of the specimens.

IV. Results and Discussion

Final states in thermal equilibrium

Figure 3 shows an example of ALCHEMI pair of EDX spectra taken from $Cu_{50}Au_{25}Pd_{25}$ annealed at 573 K for 604.8 ks. The specimen is believed to have almost established thermal equilibrium. The full scale of the spectra is normalized to the Cu($K\alpha$) integrated intensity. It is seen in the ALCHEMI pair that the dynamical condition with a positive s_{110} attenuates the signals from Au and Pd. Here, s_{110} denotes the excitation error of (110) superlattice reflection, and the positive value expresses the reciprocal point of (110) reflection set inside the Ewald sphere. The values of R_{Au}=0.706, R_{Pd}=0.717 and R_{Cu}=1 for the ALCHEMI pair in Fig. 3 give P(Cu,Au)=-0.963 and P(Pd,Au)=0.926, following eq.(5). Similar ALCHEMI pairs were obtained from different regions in the same specimen, and the most probable values of P(Cu,Au) and P(Pd,Au) were determined. Table II summarizes the values thus determined. The negative values of P(Cu,Au) characterize the anti-site correlation between Cu and Au. In contrast, P(Pd,Au) takes positive values, indicating that Au and Pd atoms tend to share the same sublattice. The absolute values of the two parameters almost attain unity in the alloys containing 50 at%Cu, while they exceed unity in the alloys with Cu content less than 50 at%. The LRO parameters are expected to be $|S_{Cu}| \approx |S_{Au}| \approx |S_{Pd}|$ in the former cases, and $|S_{Cu}| \approx |S_{Pd}| > |S_{Au}|$ in the latter ones.

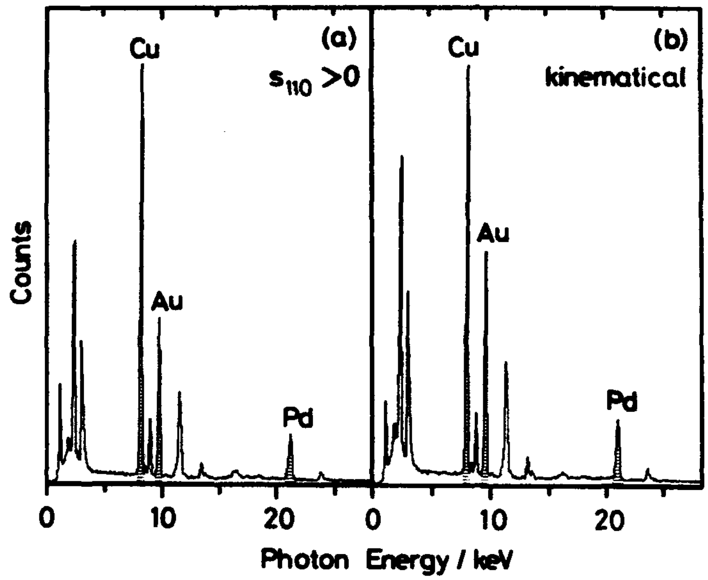

Figure 3 - ALCHEMI pair of EDX spectra obtained from $Cu_{50}Au_{25}Pd_{25}$ annealed at 573 K for 604.8 ks. (a) dynamical condition with $s_{110}>0$, (b) kinematical condition. The Cu(*K*α) intensity is equalized between (a) and (b).

Table II Parameters *P*(*i*,*j*) in the equilibrium states

	$Cu_{50}Au_{25}Pd_{25}$	$Cu_{50}Au_{35}Pd_{15}$	$Cu_{45}Au_{30}Pd_{25}$	$Cu_{45}Au_{40}Pd_{15}$
P(Cu,Au)	-1.05±0.05	-1.05±0.05	-1.49±0.21	-1.31±0.17
P(Pd,Au)	1.11±0.09	1.16±0.15	1.48±0.37	1.27±0.51

Figure 4 shows a CBED pattern of $Cu_{50}Au_{25}Pd_{25}$ equilibrated by aging for 604.8 ks. Here, a pair of white arrows indicate the separation of (646) Kikuchi-line due to dynamical diffraction of g=001. The splitting distances of equilibrated alloys are listed in Table III. The separation expands with increase in Au content at a given Cu content, while it narrows with deviation of Cu content from 50 at% at a constant x_{Pd}. The composition dependence of the separation seems reasonable, since the separation is, in principle, proportional to the structure factor of the (001) superlattice reflection.

Table IV gives the occupation probabilities of Cu, Au and Pd on the two sublattices as well as the LRO parameters in every specimen alloys with thermal equilibrium at 573 K, which have been determined through the combination of IKL and ALCHEMI. The occupation probabilities Γ_i have been obtained with accuracy about 2 at%. In the alloys with 50 at%Cu, most of Au and

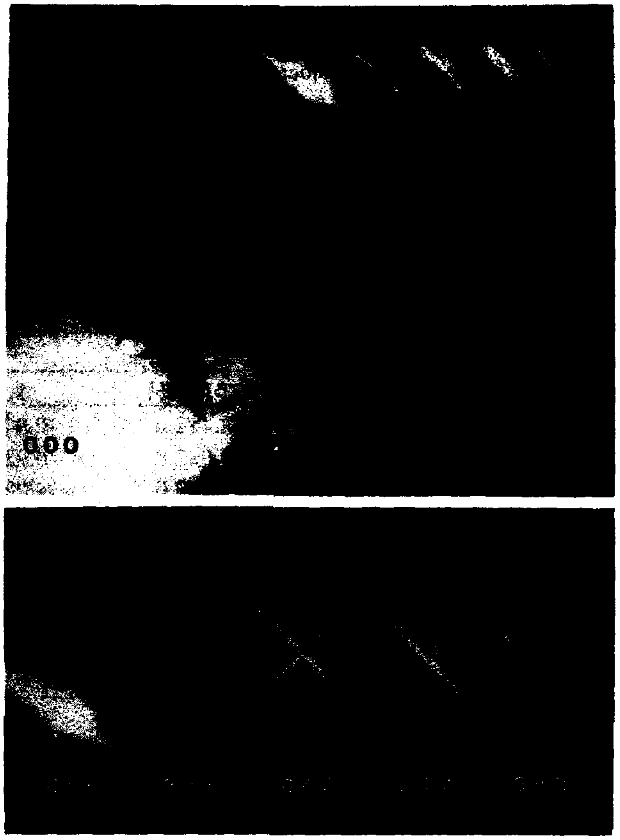

Figure 4 - CBED pattern of $Cu_{50}Au_{25}Pd_{25}$ annealed at 573 K for 604.8 ks. Whole pattern (upper) and enlarged one (lower). White arrows indicate the splitting of (646) Kikuchi-line due to (001) reflection.

Table III Separation of (646) Kikuchi-line in the equilibrium states [nm^{-1}]

$Cu_{50}Au_{25}Pd_{25}$	$Cu_{50}Au_{35}Pd_{15}$	$Cu_{45}Au_{30}Pd_{25}$	$Cu_{45}Au_{40}Pd_{15}$
0.384±0.005	0.486±0.005	0.379±0.005	0.452±0.005

Pd atoms reside on α sites, while most of Cu atoms are located on β. The LRO parameters of the three elements achieve almost unity in the absolute value. Hence, the compositions $Cu_{50}(Au_{1-y}Pd_y)_{50}$ can be regarded as stoichiometric for $L1_0$ ordering. If we assume the pairwise interactions between the first nearest neighboring atoms, V_{ij}, to be responsible for the formation of $L1_0$ type long-range order, the results for the stoichiometric alloys suggest that V_{CuAu} and V_{CuPd} are effective to the formation, but V_{AuPd} is not so significant. In the alloys with $(x_{Au}+x_{Pd})=0.55$, the LRO parameter of Au reduces considerably, while S_{Cu} and S_{Pd} remain high. These nonstoichiometric alloys contain 5 at% of excess Au and Pd atoms. Of the excess atoms, Au atoms are preferentially forced from α to β sites. Most Pd atoms remain on their preferential α sites, even in the nonstoichiometric case. Therefore, we conclude that the pairwise interactions should be $V_{CuPd}>V_{CuAu}>V_{AuPd}$ in our specimens of CuAuPd. This inequality of the pairwise interactions holds in dilute Pd alloys [11,18]. We have examined the equilibrium states of long-range order over a more broad range of composition in the $L1_0$ phase field seen in Fig. 2. From the results compared with the predictions by the cluster variation method [19] with a simple tetrahedron approximation [2,20], we have evaluated the interactions to be V_{CuPd}=1200 K, V_{CuAu}=663 K and V_{AuPd}=400 K [18].

Table IV Equilibrium states of $L1_0$ long-range order

		$\Gamma_i(\alpha)$ [at%]	$\Gamma_i(\beta)$ [at%]	S_i
$Cu_{50}Au_{25}Pd_{25}$	Cu	1.6±2.0	98.4±2.0	-0.97±0.04
	Au	48.0±2.0	2.0±2.0	0.92±0.08
	Pd	50.4±2.0	-0.4±2.0	1.02±0.08
$Cu_{50}Au_{35}Pd_{15}$	Cu	-1.0±1.8	101.0±1.8	-1.02±0.04
	Au	69.2±1.8	0.8±1.8	0.97±0.05
	Pd	31.8±1.8	-1.8±1.8	1.12±0.12
$Cu_{45}Au_{30}Pd_{25}$	Cu	3.4±2.6	86.6±2.6	-0.92±0.05
	Au	48.6±2.6	11.4±2.6	0.62±0.08
	Pd	48.0±2.6	2.0±2.6	0.92±0.10
$Cu_{45}Au_{40}Pd_{15}$	Cu	3.2±3.2	86.8±3.2	-0.93±0.07
	Au	68.4±3.2	11.6±3.2	0.71±0.08
	Pd	28.4±3.2	1.6±3.2	0.90±0.21

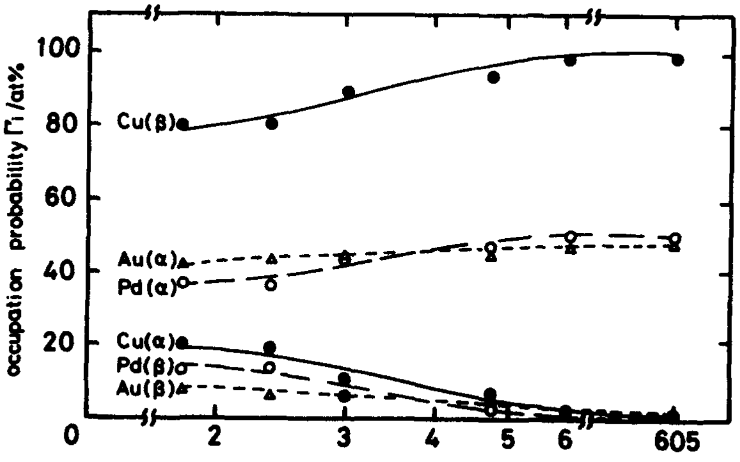

Figure 5 - Change in the values of Γ_i during ordering process in $Cu_{50}Au_{25}Pd_{25}$.

Kinetic behavior in $L1_0$ ordering

The transient states in the processes of $L1_0$ ordering at 573 K have been examined through the same procedure of IKL-ALCHEMI explained above. Figure 5 shows changes in the values of Γ_i in $Cu_{50}Au_{25}Pd_{25}$ during the process. The probabilities finding (Cu on β), (Au on α) and (Pd on α) continuously increases with annealing, while the anti-site atoms disappear. This simply indicates the development of $L1_0$-type long-range order in the alloy.

Figure 6 gives the LRO parameters in the alloys of $(x_{Au}+x_{Pd})=0.5$ as a function of annealing time. The absolute values of S_{Cu}, S_{Au} and S_{Pd} continuously increases with annealing time in the stoichiometric alloys, as shown in Fig. 6. In the early stage, the magnitude of the LRO parameters are in order of $|S_{Au}|>|S_{Cu}|>|S_{Pd}|$, but the inequality almost vanishes or changes into a weak one where $|S_{Pd}|>|S_{Cu}|>|S_{Au}|$ in the late stage. Figure 6 clearly reveals that the ordering rates are different among the three elements. The ordering rate of an element is considered to be proportional to product of the diffusive mobility and the driving force coming from the free energy [2,21]. The latter factor gives Pd atoms predominance in the ordering rate in the early stage, because the interaction parameter V_{CuPd} is stronger than V_{CuAu}. However, the magnitude of S_{Pd} increases more slowly than S_{Cu} and S_{Au}, as shown in Fig. 6. This result suggests that the diffusive mobility of Pd is significantly lower than those of Cu and Au in these alloys.

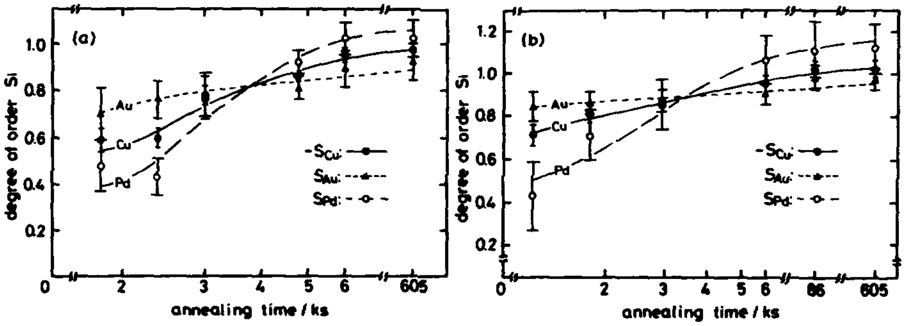

Figure 6 - LRO parameters S_i as a function of annealing time.
(a)$Cu_{50}Au_{25}Pd_{25}$, (b)$Cu_{50}Au_{35}Pd_{15}$.

Figure 7 shows variation of the LRO parameters during annealing in the alloys of $(x_{Au}+x_{Pd})=0.55$. The values of S_{Cu} and S_{Pd} gradually increase with time in both of the alloys. In contrast, the parameter S_{Au} decreases with annealing. Since Cu and Au atoms are more mobile than Pd atoms, the ordering reaction between Cu and Au would precede the ordering between Cu and Pd. The magnitude of S_{Cu} and S_{Au} would be rapidly enhanced in the earlier stage, at which the ordered domains are too small to measure the LRO parameters by the present method. In the following intermediate or late stage, the ordering between Cu and Pd becomes significant and increases S_{Cu} and S_{Pd} with time as shown in Fig. 7. As the sum total of Pd and Au atoms outnumbers α-sublattice sites and V_{CuPd} is larger than V_{CuAu}, the subsequent ordering reaction between Cu and Pd involves partial removal of Au atoms from α to β sites. The LRO parameter S_{Au} therefore decreases slightly with the evolution of order between Cu and Pd atoms, as can be seen in Fig. 7.

The change in Γ_i during the ordering process plotted in the Gibbs triangle gives the kinetic path. In Fig. 8, the paths for the alloys with 25 at%Pd are demonstrated. In the initial states of disordered phase, the values of Γ_i for the two sublattices are degenerate into the alloy composition indicated by closed symbol. As the ordering proceeds, $\Gamma_i(\alpha)$ and $\Gamma_i(\beta)$ move toward the Au-Pd rich and the Cu-rich sides in the triangle, respectively. In the early stage, the ordering reaction between Cu and Au atoms occurs dominantly, the paths being nearly parallel to the edge between Cu and Au corners. The subsequent ordering between Cu and Pd bends the paths in the intermediate or late stage. The difference in the ordering rate mentioned is responsible for the kinetic paths curved in the shape of inverse "S".

We are now simulating the kinetic behaviors of $L1_0$ ordering, using the master equation approach developed by Fultz [22]. The preliminary calculation has supported the conclusions drawn here.

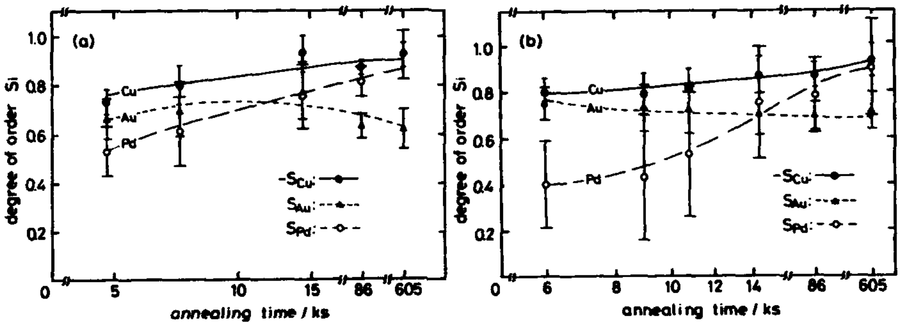

Figure 7 - LRO parameters S_i as a function of annealing time. (a)$Cu_{45}Au_{30}Pd_{25}$, (b)$Cu_{45}Au_{40}Pd_{15}$.

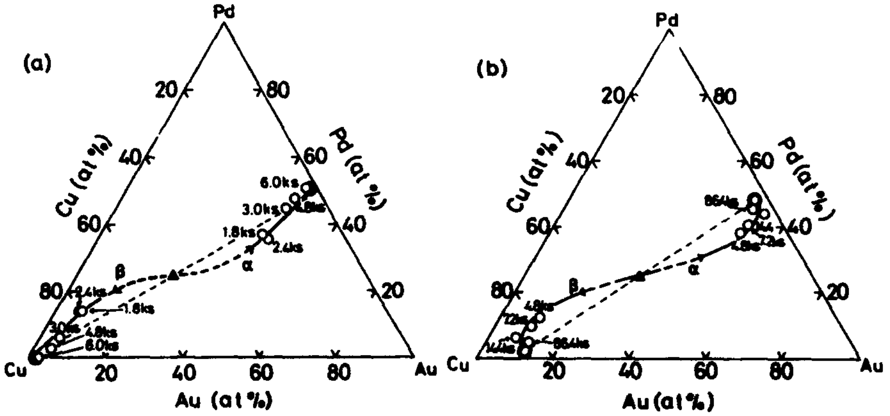

Figure 8 - Kinetic paths of $L1_0$ ordering in $Cu_{50}Au_{25}Pd_{25}$(a) and $Cu_{45}Au_{30}Pd_{25}$(b).

IV. Concluding Remarks

In this paper, we have reported an application of the combination of IKL and ALCHEMI techniques to study of kinetic behavior of $L1_0$ ordering in CuAuPd ternary alloys at a temperature of 573 K. The time-evolution of $L1_0$-type long-range order has been examined in the light of change in the occupation probabilities of the three elements on the two sublattices, Γ_i(α or β), as well as change in the long-range order parameters, S_i. In the $L1_0$ ordered structure, atoms of Au and Pd have a tendency to share the same sublattice, while Cu atoms prefer the other one. The long-range ordering is explained in principle by pairing interactions of Cu atoms with Au or Pd ones in the first nearest neighbors. In a case of $Cu_{0.5}(Au_{1-y}Pd_y)_{0.5}$, the absolute values of S_i for the three elements rise monotonically with annealing time. The magnitudes of the three S_i's are in order $|S_{Au}|>|S_{Cu}|>|S_{Pd}|$ in the early stage, but the inequality changes into $|S_{Pd}|\geq|S_{Cu}|\geq|S_{Au}|$ in the late stage. When the sum total of Au and Pd contents exceeds 50 at%, S_{Cu} and S_{Pd} increase with annealing in a similar way as in the case of $(x_{Au}+x_{Pd})=0.5$, but S_{Au} rises and then slightly decreases after reaching a maximum. In such a nonstoichiometric case, the final state contains a considerable number of anti-site atoms of Au. The kinetic behaviors of $L1_0$ ordering in CuAuPd are explained in terms of the pairwise interactions V_{ij} as

$$V_{CuPd}>V_{CuAu}>V_{AuPd}, \tag{7}$$

and the diffusive mobilities D_i as

$$D_{Au}, D_{Cu}>D_{Pd}. \tag{8}$$

The change in Γ_i during the ordering processes draws kinetic paths curved in the shape of an inverse "S" in the Gibbs triangle.

The present results have clearly proven the IKL-ALCHEMI method to be useful in studying kinetics of ordering in multi-component alloys. This technique can be used as routine work at an average-size laboratory, and is applicable to heterogeneous or decomposed alloys. One can, of course, obtain simultaneously informations on the microstructure by the usual imaging or diffraction mode of transmission electron microscopy. We believe that IKL-ALCHEMI will stimulate much experimental study of multi-component ordering alloys.

Acknowledgments

Help in the experiment by M. Takahashi is greatly acknowledged. One of the authors (S.M.) should like to express sincere thanks to Profs. B.Fultz, R.W.Cahn and Dr.D.Gupta for inviting him to present this report at the symposium on "Diffusion in Ordered Alloys and Intermetallics" and to contribute it to the proceedings. This work was supported in part by Grants-in-Aid for Scientific Research (B) under Contract No.03452247 (K.O.) and for Encouragement of Young Scientists No.03855141 (S.M.) from the Ministry of Education, Science and Culture, Japan.

Appendix: Note on limitation of IKL-ALCHEMI

It should be noted that IKL-ALCHEMI does not bring in any direct informations with regard to pair-correlations of atoms. In n-component systems, the pair-correlation functions are defined by $n(n-1)/2$ independent variables [23], or Wallen-Cowley parameters, while eq. (1) is given with n-1 independent variables of the LRO parameters. The numbers of independent variables in both functions are equal to each other in a binary case, but they become different if $n>2$. When $n=3$, the former and the latter functions include three and two independent variables, respectively. If the present study concerned the alloys of $(x_{\mathrm{Au}}+x_{\mathrm{Pd}})=0.55$ only, one could not judge which of the following situations is responsible for the selective removal of Au atoms to anti-sites: $V_{\mathrm{CuPd}}>V_{\mathrm{CuAu}}>V_{\mathrm{AuPd}}$ and $V_{\mathrm{CuPd}}, V_{\mathrm{AuPd}}>V_{\mathrm{CuAu}}$. We have concluded, from comparing the stable configurations of atoms when $(x_{\mathrm{Au}}+x_{\mathrm{Pd}})=0.5$ and 0.55, that the former situation, or eq. (7), is the case. The x-ray diffraction technique with anomalous scattering near absorption edges is preferable if one wishes to measure directly pair-correlations in a multi-component alloy of a given composition [7].

References

1. H. Chen, and V.K. Vasudevan, eds. Kinetics of Ordering Transformations in Metals (Warrendale, PA: TMS, 1992).
2. D. de Fontaine, "Configurational Thermodynamics of Solid Solutions," Solid State Physics, Vol.34, ed. H.Eherenreich, F.Seitz and D.Turnbull (New York, NY: Academic Press, 1979), 73-274.
3. A. Khachaturyan, Theory of Structural Transformations in Solids (New York, NY: John Wiley & Sons, 1983).
4. J.D. Gunton, M. San Miguel and P.S. Sahni, "The Dynamics of First-Order Phase Transitions," Phase Transitions and Critical Phenomena, Vol.8, ed. C.Domb and J.L. Lebowitz (London: Academic Press, 1983), 267-482.
5. P. Cenedese, F. Bley and S. Lefebvre, "Diffuse Scattering in Disordered Ternary Alloys: Neutron Measurements of Local Order in a Stainless Steel $Fe_{0.56}Cr_{0.21}Ni_{0.23}$," Acta Cryst., A40(1984), 228-240.
6. A. Marty *et al.*, "Determination of Long Range Order in Ni-Base Ternary Alloys by X-Ray Anomalous Diffraction Using Synchrotron Radiation," Acta metall. matter., 38(2)(1990), 345-350.
7. S. Hashimoto and H. Iwasaki, "Novel Use of Anomalous Scattering of Synchrotron Radiation for Local Atomic Order in a Disordered Ternary Alloy," Radiation Effects and Defects in Solids, 124(1992), 147-171.
8. V. Niculescu *et al.*, "Correlation of The Internal Fields, Magnetic Moments, and Site Preference in $Fe_{3-x}Mn_xSi$ Alloys," Phys. Rev. B, 13(1976), 3167-3134.
9. G. Athanassiadis *et al.*,"Study of Ternary Ordered Solid-Solutions Derived From Fe_3Al by Substitution" Phys. stat. sol. (a), 40(2)(1977), 425-435.
10. B. Fultz, H.H. Hamdeh and D.H. Pearson, "Kinetic Paths in Two Order Parameters: A Mössbauer Spectrometry Experiment with FeCo-Mo," Acta metall., 37(11)(1989), 2841-2847.

11. S. Matsumura, T. Morimura and K. Oki, "An Analytical Electron Diffraction Technique for the Determination of Long-Range Order Parameters in Multi-Component Ordered Alloys," Mater. Trans. JIM, 32(10)(1991) 905-910.
12. J. Gjønnes and R. Høier, "The Application of Non-Systematic Many-Beam Dynamic Effects to Structure-Factor Determination," Acta Cryst., A27(1971), 313-316.
13. J.C.H. Spence and J. Taftø, "ALCHEMI: A New Technique for Locating Atoms in Small Crystals," J. Microsc., 130(2)(1982), 147-154.
14. J.C.H. Spence, "Electron Channelling and Its Uses," Electron Diffraction Techniques, Vol.1 (Oxford: Oxford Univ. Pr., 1992), 465-532.
15. J. Gjønnes, A. Olsen and H. Matsuhata, "Progress Toward Structure Determination," J. Electron Microsc. Tech., 13(2)(1989), 98-110.
16. J.C.H. Spence, "Accurate Structure Factor Amplitude and Phase Determination," Electron Diffraction Techniques, Vol.1 (Oxford: Oxford Univ. Pr., 1992), 360-438.
17. E. Raub and G. Wörwag, "Über Gold-Palladium-Kupfer-Legielungen," Z. Metallkunde, 46(2)(1955), 119-128.
18. T. Morimura *et al.*, "An Analytical Electron Diffraction Study of $L1_0$-Type Atomic Long-Range Order Depending on Alloy-Composition in a Ternary System of CuAuPd," Electron Microscopy 92, Vol.2, ed. A.López-Galindo and M.I.Rodríguez-García (Granada: Universided de Granada, 1992), 301-302.
19. R. Kikuchi, "A Theory of Cooperative Phenomena," Phys. Rev., 81(6)(1951), 998-1003.
20. K. Udoh, K. Yasuda and H. Yamauchi, "Cu-Au-Pd Coherent Phase Diagram," (TMS Technical Paper A86-37, TMS, 1986).
21. D. de Fontaine, "An Analysis of Clustering and Ordering in Multicomponent Solid Solutions-II Fluctuations and Kinetics," J. Phys. Chem. Solids, 34(8)(1973), 1285-1304.
22. B. Fultz, "Kinetic Paths in Two Order Parameters: Theory," Acta metall., 37(3)(1989), 823-829.
23. D. de Fontaine, "The Number of Independent Pair-Correlation Functions in Multicomponent Systems," J. Appl. Cryst., 4(15)(1971), 15-19.

Local Atomic Structure in $Hg_{0.80}Cd_{0.20}Te$ and $Hg_{0.725}Cd_{0.275}Te$

J. P. Quintana and J. B. Cohen*

Department of Materials Science and Engineering
Robert R. McCormick School of Engineering and Applied Science
Northwestern University, Evanston, Illinois 60208 USA

* Present Address: DND-CAT Synchrotron Research Center
Robert R. McCormick School of Engineering and Applied Science
Northwestern University, Evanston, Illinois 60201 USA

Local atomic arrangements in $Hg_{0.80}Cd_{0.20}Te$ were investigated by measuring the diffuse x-ray scattering at two different energies near the Hg L_{III} absorption edge to yield intensity due only to Hg-Hg, Hg-Te, and Hg-Cd pair interactions. The data were separated into short range order and displacement intensities. Simulation revealed ordered regions with 3:1 Hg-Cd near neighbor configurations. The Hg-Te length is contracted. Similar measurements were made near the Mn K edge in $Cd_{0.725}Mn_{0.275}Te$, showing potential problems in the measurement of the diffuse x-ray intensity using anomalous dispersion techniques.

Diffusion in Ordered Alloys
Edited by B. Fultz, R.W. Cahn, and D. Gupta
The Minerals, Metals & Materials Society, 1993

I. Introduction

The state of local order and strain in the pseudobinary zincblende semiconductors ($A_{1-x}B_xC$) is known to affect electronic band structure and electronic properties such as carrier mobility [1-3]. However, only a limited number of studies have been performed on the state of local order and strain in these systems. $Ga_{1-x}In_xAs$ [4], $Cd_{1-x}Zn_xTe$ [5], and $Cd_{1-x}Mn_xTe$ [6] show that the A-C and B-C bond lengths are relatively constant throughout the entire composition range despite the change in lattice parameter. Recent EXAFS studies on $Hg_{1-x}Cd_xTe$ [7] also suggest this trend while previous EXAFS studies [8] led to inconclusive results or to suggestions that the near neighbor bond lengths are bimodal [9]. The A-A, A-B, and B-B distances in the studied systems are reported as being equal to those calculated from the average lattice parameter of the alloy. However, standing wave measurements on $Cd_{0.725}Mn_{0.275}Te$ [10] suggest the opposite effect: the A-A, B-B, and A-B distances are unequal. Studies on the state of local order are also conflicting. Previous x-ray diffuse scattering studies [11-13] as well as electroreflectance measurements in $Hg_{1-x}Cd_xTe$ [14] suggest Cd clustering, while Raman studies [15] and NMR studies [16, 17] suggest that a Hg:Cd 3:1 cluster around each Te atom is favored. This arrangement is indicative of local ordering rather than clustering. This study is motivated to resolve some of these discrepancies.

II. Experimental

The *diffuse* x-ray scattering is sensitive to the difference between the actual crystal and the average crystal described by the Bragg peaks. Consequently, local interatomic strains as well as local ordering and clustering affect the shape and intensity of the diffuse x-ray scattering. Borie and Sparks[18] as well as Georgopoulos and Cohen[19] have proposed methods for extracting real space information from the diffuse scattering by expanding the kinematic scattering equation out to second order in displacements and measuring the diffuse scattering in a volume of the crystal's reciprocal space. Quintana [20] has extended this formalism for pseudobinary zincblende $F\bar{4}3m$ structures with the result that the diffuse scattering at each point in reciprocal space is a sum of seventy linear terms involving the short range order parameters and moments of the interatomic displacement distribution. The coefficients of these terms involve the atomic scattering factors as well as the reciprocal space coordinates where the data are taken. By taking data at symmetry related points in reciprocal space, the terms involving the real space parameters can, in principle, be determined by a least squares technique since the scattering factors and reciprocal space coordinates are known [21]. The number of equations can be reduced in such an experiment by performing two experiments close to an absorption edge of one of the atoms on the mixed FCC sublattice [20, 22]. When the data are converted to electron units, the intensity resulting from the difference of the two measurements is dependent only on terms involving the atomic species that corresponds to the absorption edge. The number of remaining terms in the equation depends on the behavior of the scattering factors and the relative magnitude of the imaginary parts of the atomic scattering factors. Fifteen terms are left in the equation for $Hg_{0.80}Cd_{0.20}Te$ and forty seven terms are left for $Cd_{0.725}Mn_{0.275}Te$ [20].

A 15mm diameter n-type single crystal of $Hg_{0.80}Cd_{0.20}Te$ was purchased from Cominco Ltd. (Trail, British Columbia). Two measurements of the diffuse x-ray scattering in a volume of reciprocal space were performed on the MATRIX Beamline X18A at the National Synchrotron Light Source, Brookhaven National Laboratory. One measurement of

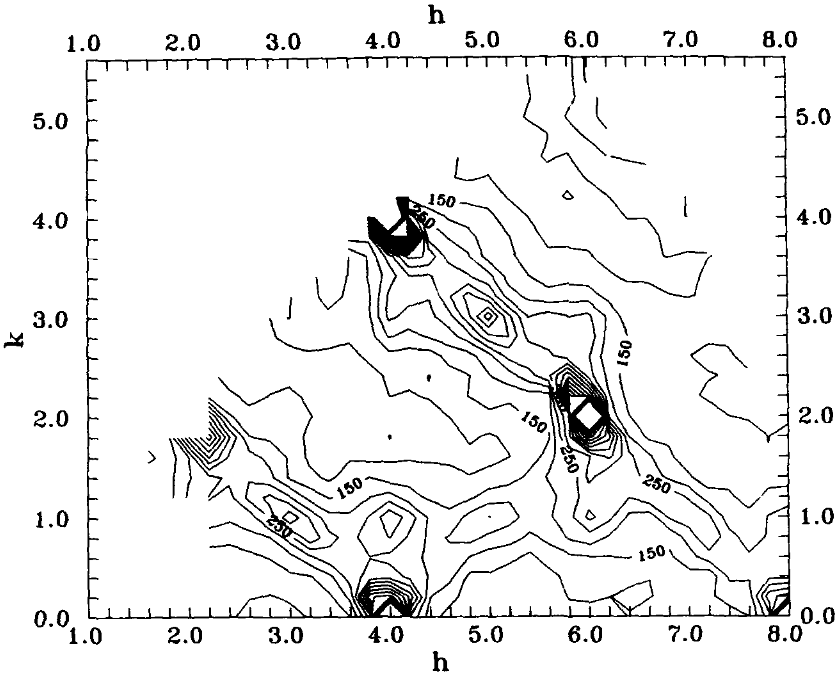

Figure 1: Plot of the difference x-ray diffuse scattering on the (hk0) reciprocal lattice plane from a commercial $Hg_{0.8}Cd_{0.2}Te$ single crystal. The difference is taken between measurements at *12086* eV and *12271* eV. *Contours are every* 50 e.u.

the x-ray diffuse scattering was performed at 12271 eV, near the Hg L_{III} edge, and a second measurement performed at 12086 eV. The diffuse scattering in a volume of reciprocal space from the single crystal of $Cd_{0.725}Mn_{0.275}Te$ grown by U. Debska (used in Durbin's standing wave study [10]) was measured near the Mn K edge at 6525 eV and also at 6405 eV. Measurements of the direct beam were made to convert the measured data to electron units. All measurements were made at room temperature at a spacing of $\Delta h = 0.2$ in reciprocal space with the sample underneath an evacuated Be dome to minimize background scattering. The data were collected with a Si(Li) solid state detector and corrected for deadtime [23]. In the $Hg_{0.80}Cd_{0.20}Te$ experiment, the Hg L_α and Mn K_α resonant Raman scattering was recorded simultaneously with the diffraction data so that the Hg L_β and Mn K_β resonant Raman scattering could be subtracted from the $Hg_{0.80}Cd_{0.20}Te$ and $Cd_{0.725}Mn_{0.275}Te$ data sets respectively. The real and imaginary parts of the Hg and Mn scattering factor's in the vicinity of their respective edges was also measured [24].

III. Results and Conclusion

Figure 1 shows the difference intensity in electron units between the measurements at 12271 eV and 12086 eV on the (hk0) plane. This difference intensity is due only to Hg-Hg, Hg-Cd and Hg-Te interactions. The intensity was corrected for second order thermal diffuse scattering and separated using unbiased linear least squares techniques to yield the Warren-Cowley short range order parameters as well as the local displacements [25]. Only four short range order parameters and the first three intersublattice displacements are significant and these are given in Tables I, II, and III. The displacements are given as vector quantities of the average displacement from the ideal lattice of the Hg-Te and Cd-Te atom pairs for each interatomic vector $\mathbf{r}_{lmn}$ (e.g. $<\Delta_{lmn}^{HgTe}>$ and $<\Delta_{lmn}^{CdTe}>$ respectively). The Cd-Te displacements can not be determined directly since the difference intensity only contains information regarding interactions with Hg. However, the average Cd-Te displacements are related to the Hg-Te displacements through [26]:

$$x_{Hg} < \Delta_{lmn}^{HgTe} > - x_{Cd} < \Delta_{lmn}^{CdTe} > = 0 \qquad (1)$$

which comes from the existence of the average lattice. Here, x_{Cd} and x_{Hg} are the sublattice fractions of the respective components. The features at the forbidden Bragg reflections (e.g. (531) and (310)) are primarily due to second order strain effects on the multicomponent sublattice.

Table I Warren-Cowley short range order parameters for a commercial $Hg_{0.8}Cd_{0.2}Te$ crystal.

l	m	n	α_{lmn}
0.00	0.00	0.00	1.265 (71)
0.50	0.50	0.00	-0.050 (26)
1.00	0.00	0.00	0.118 (35)
2.00	2.00	0.00	-0.043 (25)

Table II First order Hg-Te displacements in a commercial $Hg_{0.8}Cd_{0.2}Te$ crystal. Displacements are in $10^2 a_0$.

l	m	n	$<x>_{lmn}$	$<y>_{lmn}$	$<z>_{lmn}$
0.25	0.25	0.25	-0.044 (4)	-0.044 (4)	-0.044 (4)
0.75	0.75	0.25	-0.021 (3)	-0.021 (3)	0.010 (5)
-0.75	-0.75	-0.75	0.016 (5)	0.016 (5)	0.016 (5)

Table III First order Cd-Te displacements in a commercial $Hg_{0.8}Cd_{0.2}Te$ crystal. Displacements are in $10^2 a_0$.

l	m	n	$<x>_{lmn}$	$<y>_{lmn}$	$<z>_{lmn}$
0.25	0.25	0.25	0.17 (2)	0.17 (2)	0.17 (2)
0.75	0.75	0.25	0.08 (1)	0.08 (1)	-0.04 (2)
-0.75	-0.75	-0.75	-0.06 (2)	-0.06 (2)	-0.06 (2)

Tables II and III clearly show that the near-neighbor Hg-Te and Cd-Te distances are not equal to the average distance calculated from the lattice parameter. This effect has been found in other pseudobinary zincblende systems amenable to EXAFS studies [4, 6, 7]. Based on this other work, the average distance of the Hg-Te bond is expected to either remain constant or increase slightly with x since the lattice parameter in the $Hg_{1-x}Cd_xTe$ system increases with x. The first neighbor Hg-Te distance corresponds to a displacement which is less than the near neighbor bond distance in pure HgTe by 0.0015 Å. While this may seem counterintuitive based on the trends seen in these EXAFS studies, a less than normal Hg-Te bond distance has been predicted by Sher et. al. [28] and Hass and Vanderbilt [29] and is thought to relate to chemical forces that result in charge-transfer effects between Cd^{2+} and Hg^{2+} ions. Based on EXAFS results, Mayanovic et. al. [7], suggest that the Hg-Te bond distance is not different from the Hg-Te distance in HgTe and that charge transfer does not occur since no shift is noted in the Hg L_{III} edge. Our strain results are in disagreement with the extension of previous EXAFS results to this system and support a displacement distribution assuming charge transfer. This may be due to the differences in the manner that EXAFS and diffuse scattering average the strain. EXAFS measures the average radial distance where diffuse scattering, being an interference effect, measures the vectorial deviation from the average lattice. (Also, the uncertainty in our measurements is 10% of the uncertainty in Mayanovic et. al.'s study [7].)

Using short range order parameters for the 1/2[110],[100] and [220] interatomic vectors, the local order on the Hg-Cd sublattice was simulated using a three dimensional 131072 atom modeling program [27]. A comparison of the number of configurations in the computer model along with the expected number for a random system shows that there is a large number of 3:1 Hg-Cd quadruplets in the actual alloy as compared to a random array in support of the Raman scattering study of Compaan et. al [15]. Further simulations were performed using different values of the 1/2[110], [100] and [220] short range order parameters within the uncertainties given in Table I. In all cases, the number of 3:1 Hg-Cd quadruplets was higher than that for a random alloy. Further inspection of the model revealed that the 3:1 Hg-Cd ratio appears to result from ordered (100) planes similar to Cu_3Au type local ordering [25].

Figure 2 shows the difference intensity between the measurements at 6525 eV and 6405 eV on the (hk0) plane in electron units. This difference intensity is due only to Mn-Mn, Mn-Cd and Mn-Te interactions. We found that the quality of the difference data was substantially less than the quality for the $Hg_{0.80}Cd_{0.20}Te$ experiment and no conclusions could be drawn from the data. In fact, whereas the bulk of the $Hg_{0.80}Cd_{0.20}Te$ data had a standard deviation which was 7% to 10% of the difference intensity, 94% of the difference data for $Cd_{0.725}Mn_{0.275}Te$ has a variance which is at least 25% of the difference intensity. As noted by Quintana [20], different components of the diffuse intensity can result in either a positive or negative contribution depending on which absorption edge is chosen for the experiment. For example, contributions due to short range order and second order displacements on the multicomponent sublattice (e.g. thermal diffuse scattering) will tend to counteract each other in the difference pattern when the experiment is performed near the atom with the smaller scattering factor. Since the Mn scattering factor is less than Cd, this was the situation in this case. An experiment performed near the Cd K (26719 eV) or Cd L_{III} (3538 eV) edges may have given more statistically meaningful data. However, at high energies, instrumental considerations reduce the available experimental resolution. At low energies, the radius of the Ewald sphere limits the number of measurable points.

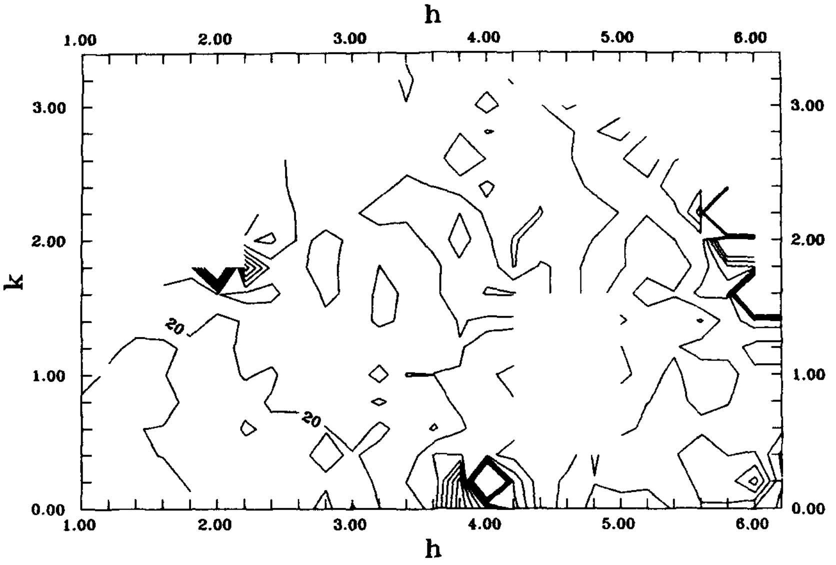

Figure 2: Plot of the difference x-ray diffuse scattering on the (hk0) reciprocal lattice plane from a $Cd_{0.725}Mn_{0.275}Te$ single crystal. The difference is taken between measurements at 6405 eV and 6525 eV. Contours are every 50 e.u.

IV. Acknowledgements

This work was supported by the National Science Foundation through grant no. DMR-8920567. This work made use of the MATRIX beamline at the National Synchrotron Light Source, Brookhaven National Laboratory and is sponsored by the US Department of Energy, Division of Chemical Sciences under contract no. DE-FG02-ER45183 as well as the Northwestern MRC X-ray Diffraction Facility supported in part by the National Science Foundation through the Northwestern University Materials Research Center, Grant No. DMR 8821571. We would also like to thank Prof. Steve Durbin from Purdue University for the CdMnTe crystal used in this study.

V. References

1. K.C. Hass, Phys. Rev. B. 27 2 1088 (1983)
2. J.J. Dubowski, Phys. Stat. Sol. (b) 85 663 (1978)
3. A. Compaan, B. Aggarwal, R.C. Bowman Jr., and D.E. Cooper, SPIE Proceedings Vol. 1055 67, (1989)
4. J.C Mikkelsen Jr. and J.B. Boyce, Physical Review B. 28 7130 (1983)
5. A. Motta, A. Balzarotti, P. Letardi, A. Kisiel, M.T. Czyzyk and M. Zimnal-Starnawska, J. Crystal Growth 72 205 (1985)
6. A. Balzarotti, N. Motta, A. Kisiel, and M. Zimnal-Starnawski. Physical Review B. 31 7526 (1985)
7. R.A. Mayanovic, W.-F. Pong, and B.A. Bunker. Physical Review B. 42 11174 (1990)
8. P. Letardi, N. Motta, and A. Balzarotti J. Phys. C. 20 2853 (1987)
9. A. Balzarotti. in *Ternary and Multinary Compounds*, edited by S. Deb and A. Zunger (Materials Research Society, Pittsburgh, 1987) p. 333
10. S.M. Durbin, J. Appl. Phys., 53 7637 (1982)
11. V.T. Bublik. Kristall und Technik 12 849 (1978)
12. V.T. Bublik, S.S. Gorelik, and M.D. Kapustina, Inorganic Materials 7 1335 (1971)
13. V.T. Bublik and A.A. Zaitsev. Phys. Stat. Sol. (a) 39 345 (1977)
14. S.P. Kozyrev, L.K. Vodopynaov and R. Triboulet. Solid State Communications 45 383 (1983)
15. A. Compaan, R.C. Bowman Jr., and D.E. Cooper. Semicond. Sci. Technol. 5 S73 (1990)
16. D.K. Zamir, K. Beshah, P. Becla, P.A. Wolff, R.G. Griffin, D. Zax, S.Vega and N. Yellin. J. Vac. Sci. Technol. A. 6 2612 (1988)
17. D.B. Zax, S. Vega, N. Yellin and D. Zamir. Chem. Phys. Lett. 138 105 (1987)
18. B. Borie and C.J. Sparks Jr., Acta Cryst., **A** 27, 198 (1971)
19. P. Georgopoulos and J.B. Cohen, J. de Physique, *C7*, *191* (1977)
20. J.P. Quintana. J. Appl. Cryst. In Press (1993)
21. L.H. Schwartz and J.B. Cohen *Diffraction From Materials*, (Springer-Verlag, Berlin, 1977)
22. P. Cenedese, F. Bley, and S. Lefebvre, Acta Cryst. **A40** 228 (1991)
23. J.P. Quintana, J. Appl. Cryst. **24** 261 (1991)
24. J.P. Quintana, B.D. Butler, and D.R. Haeffner, J. Appl. Cryst. **24** 184 (1991)
25. J.P. Quintana and J.B. Cohen, J. Mat. Res. In press (1993)
26. M. Hayakawa and J.B. Cohen, Acta. Cryst. **31**, 635 (1975)
27. P. Gehlen and J.B. Cohen. Physical Review, A139 844 (1966)
28. A. Sher, A.B. Chen, W.E. Spicer, and C.K. Shih. J. Vac. Sci. Tecnol. A. 3 105 (1985)
29. K.C. Hass and D. Vanderbilt. J. Vac. Sci. Technol. A. 5 3019 (1987)

DIFFUSION COUPLES

Formation of Periodic Layered Structures in Ternary Diffusion Couples

C. R. Kao and Y. A. Chang

University of Wisconsin-Madison
Madison, Wisconsin 53706 USA

Abstract

Periodic layered structures were found to form in numerous ternary diffusion couples of the type B_δ-C/A involving a displacement type of reaction. In all of these couples, A is the dominant diffusing species in comparison to B within the diffusion zone, whereas, C is essentially immobile. A thermodynamic argument was presented to rationalize the formation of the periodic layered structure. The mobilities of B and A in the reaction layers are the most important parameters in determining the relative stability of the simple layered structure versus the periodic layered structure. The periodic layered structure is favored if the mobility of B is substantially lower than that of A. On the other hand, if the mobility of A and B are comparable, the simple layered structure is favored.

Diffusion in Ordered Alloys
Edited by B. Fultz, R.W. Cahn, and D. Gupta
The Minerals, Metals & Materials Society, 1993

I. Introduction

During the last decade, a new class of morphologies exhibiting a periodic layered structure has been observed in some ternary diffusion couples involving a displacement type of reaction such as in Fe_3Si/Zn [1], Co_2Si/Zn [1,2], SiC/Ni [1,2], CoNi/Mg [3], SiC/Pt [4], and GaAs/Co [5]. In these ternary diffusion couples, two reaction product phases, $B_\delta C$ and $AB_{\delta'}$, form between the two end phases, $B_{\delta''}C$ and A, with the resulting morphology consisting of alternating layers, $B_\delta C/AB_{\delta'}/B_\delta C/AB_{\delta'}$ ...., perpendicular to the diffusion direction. The subscripts δ, δ', and δ'' are stoichiometric coefficients. The typical thickness of each alternating layer is 1-10 µm. The growth of the total reaction layers follows the parabolic relationship [1,2], indicating diffusion-controlled kinetics. The number of periodic layers increases as reaction proceeds and, in some cases, the number of layers also follows the parabolic relationship [1,2].

The objectives of the present study are to present thermodynamic arguments to rationalize the formation of the periodic layered structure and to report the results of a kinetic analysis on the relative stability of the simple layered structure versus the periodic layered structure in such ternary diffusion couples.

II. Thermodynamic Analysis

Fig. 1 shows the phase diagram of a hypothetical ternary system A-B-C at temperature T and pressure P. The A-B binary has an intermediate compound, AB, the B-C binary has two intermediate compounds, B_2C and BC_2, and the A-C binary does not have any intermediate compound. The ternary diffusion couple under consideration is B_2C/A, as indicated by a dashed line in Fig. 1. The ternary phase relationships for the couples Fe_3Si/Zn, Co_2Si/Zn, SiC/Ni, and SiC/Pt at the temperatures where experiments were performed are similar to those shown in Fig. 1. The common features of all systems studied are the components corresponding to A have high

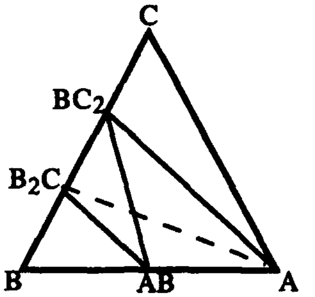

Fig. 1 - A hypothetical ternary phase diagram. The diffusion couple under consideration, B_2C/A, is connected by a dashed line.

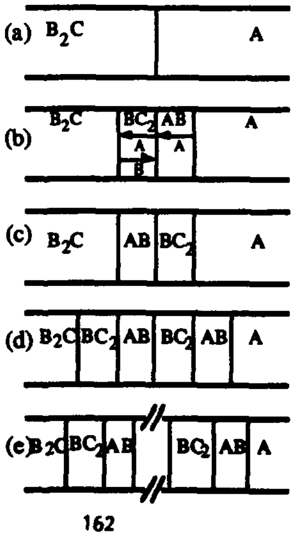

Fig. 2 - Sequence of the morphological evolution for the diffusion couple B_2C/A shown in Fig. 1. (a) The diffusion couple B_2C/A at time = 0. (b) and (c) Two possible arrangements for formation of the initial double layers. The arrangement in (b) is the favored one for the case when C is essentially immobile. (d) Formation of the second double layers BC_2/AB at some time later. (e) Eventual formation of periodic layered structure in the diffusion couple B_2C/A

mobilities in the diffusion zone and the components corresponding to C are essentially immobile.

When a diffusion couple B_2C/A is annealed at a sufficiently high temperature, reactions will occur at the interface resulting in the formation of AB and BC_2. Two layered structures are possible as shown in Fig. 2(b) and 2(c). They are $B_2C/BC_2/AB/A$ and $B_2C/AB/BC_2/A$. Under the assumptions that A has a high mobility and C is essentially immobile, the structure shown in Fig. 2 (b), $B_2C/BC_2/AB/A$ is the preferred one. Fig. 2 (e) shows the periodic layered structure observed in such ternary diffusion couples.

Since the driving force for diffusion is the chemical potential gradient or activity gradient of a particular component, it is necessary to know the activities of this component in the various heterogeneous mixtures. The stability diagrams in terms of the activity of A, a_A, and as a function of $n_C/(n_B+n_C)$, where n_B and n_C denote the numbers of moles of B and C, respectively, are shown in Figs. 3 and 4. These diagrams can be calculated from a knowledge of the Gibbs energies of formation of the compounds AB, BC_2, and B_2C. Fig. 3 is a simplified version of Fig. 4, where some ranges of homogeneity are allowed for all the intermediate phases and end phases. The activity of A is important in the present case since A is the dominant diffusing species in the diffusion zone.

As shown in Figs. 3 and 4, at values of a_A higher than a critical value, a_A^*, B_2C is thermodynamically unstable. The value of a_A^* corresponds to the activity of A in the three-phase mixture of $AB+B_2C+BC_2$. The value of a_A^* can be determined from the Gibbs energies of formation of AB, B_2C, and BC_2 by using the following three equations.

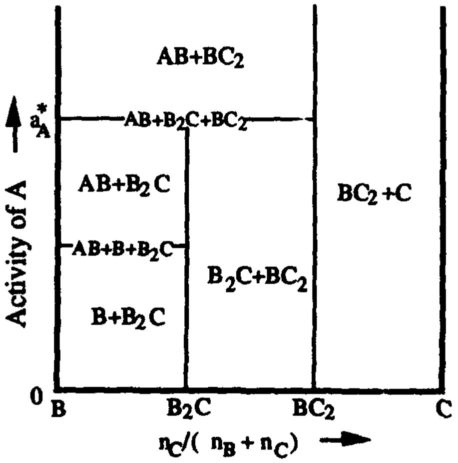

Fig. 3 - Stability diagram for the ternary phase diagram in Fig.1.

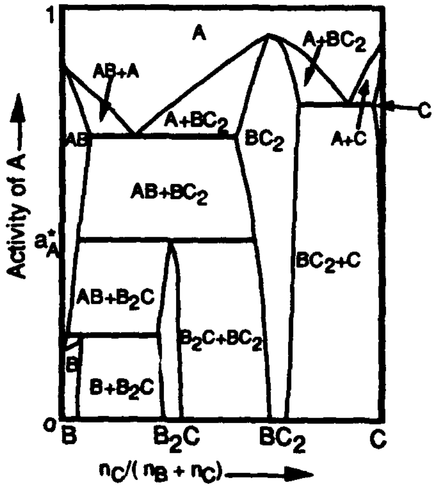

Fig. 4 - Stability diagram for the ternary phase diagram in Fig.1. Contrary to Fig. 3, some ranges of homogeneity are allowed for all the intermediate phases and end phases.

$$3A + 2B_2C = BC_2 + 3AB, \tag{1}$$

$$\Delta G^o = 3\Delta G^o{}_{AB} + \Delta G^o{}_{BC_2} - 2\,\Delta G^o{}_{B_2C}, \tag{2}$$

$$a_A{}^* = \exp(\,\Delta G^o/3RT). \tag{3}$$

where $\Delta G^o{}_{AB}$, $\Delta G^o{}_{BC_2}$, $\Delta G^o{}_{B_2C}$, and ΔG^o are Gibbs energies of formation for AB, BC_2, and B_2C and the Gibbs energy of reaction for Eq. (1), respectively; R is the gas constant.

It is evident from Figs. 3 and 4 that the B_2C+BC_2 two-phase mixture is thermodynamically stable only in the region of $0 < a_A < a_A{}^*$. For values of $a_A \geq a_A{}^*$, the AB phase will form at the B_2C/BC_2 interface provided nucleation is not a problem.

Let us now return to the diffusion couple B_2C/A. As shown schematically in Fig. 2 (b), the BC_2-AB double layer grows by diffusion of A through the AB layer to the BC_2/AB interface to react with B diffusing from the B_2C/BC_2 interface. The reaction at BC_2/AB interface is

$$A + B = AB. \tag{4}$$

The reaction at the B_2C/BC_2 interface is

$$2B_2C = BC_2 + 3B. \tag{5}$$

The overall reaction is equal to { 3 x Eq. (4) + Eq. (5) } which is the same as Eq. (1). The growth front for the AB phase is at the BC_2/AB interface and the growth front for BC_2 phase is at the B_2C/BC_2 interface.

As the reaction proceeds, due to the rapid diffusion of A over that of B within the diffusion zone the activity of A at the B_2C/BC_2 interface increases with time. When the activity of A becomes greater than $a_A{}^*$, the B_2C/BC_2 interface becomes thermodynamically unstable (see Figs. 3 or 4). At a critical value of $a_A > a_A{}^*$, the phase AB will nucleate and grow at the B_2C/BC_2 interface. This in turn leads to a depletion of B at the surface of B_2C. This depletion of B will cause the nucleation and growth of BC_2 between this newly formed AB layer and the B_2C layer. At this stage, there are two BC_2/AB double layers between B_2C and A as shown in Fig. 2(d). After the formation of the second double layer, the BC_2 phase in the first double layer will stop growing since no supply of C can reach the first double layer. The second double layer grows until the activity of A at the B_2C/BC_2 interface again becomes greater than $a_A{}^*$. The process of forming another double layer of BC_2/AB repeats itself, resulting in the formation of periodic layered structure in the diffusion zone of B_2C/A as shown in Fig. 2(e).

As shown in Fig. 2(e), when A diffuses from the end phase A to the other end phase B_2C, uphill diffusion of A in terms of concentration gradient occurs. However, the driving force for diffusion of A is its chemical potential (or its activity) which decreases in the diffusion couple B_2C/A from the end phase A to the end phase B_2C.

The above thermodynamic arguments are not limited to the specific type of phase diagram shown in Fig. 1. Let us take another example when there is one intermediate phase of equal atomic composition in all three binaries as shown in Fig. 5. Moreover, the three intermediate phases co-exist with one another. The corresponding stability diagram in terms of a_A and as a function of $n_C/(n_B+n_C)$ is given in Fig. 6. Only the simplified stability diagram is shown here. In this stability diagram, the relative positions of the activity of A for the invariant equilibria AB+B+BC and BC+C+AC depend on the Gibbs energies of formation of AB, BC, and AC but the values of a_A for both invariants have to be less than that of invariant AB+BC+AC. The phase diagram of GaAs/Co is similar to the one given in Fig. 5 although the actual phase equilibria are much more complicated in their details. The ternary diffusion couple under consideration is BC/A as indicated by a dashed line in Fig. 5. As before, A is assumed to have high mobility in the diffusion zone and C is immobile. The value of $a_A{}^*$ in Fig. 6 is determined by Eqs. (6)-(8)

$$2A + BC = AB + AC, \tag{6}$$

$$\Delta G^o = \Delta G^o{}_{AC} + \Delta G^o{}_{AB} - \Delta G^o{}_{BC}, \tag{7}$$

$$a_A{}^* = \exp(\Delta G^o/2RT). \tag{8}$$

The sequence of the morphological evolution for the diffusion couple BC/A is summarized in Fig. 7. The AC layer grows by the reaction of BC with A which diffuses from the AB/A interface to the BC/AC interface. The reaction at the BC/AC interface is

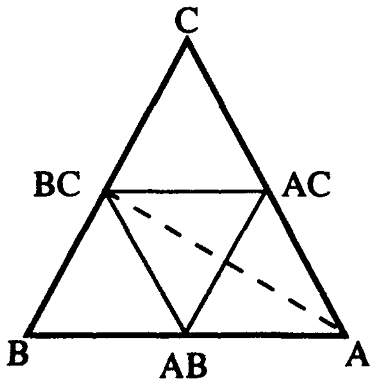

Fig. 5 - Another hypothetical ternary phase diagram A-B-C with three intermediate phases AB, BC, and AC. The diffusion couple under consideration, BC/A, is connected by a dashed line.

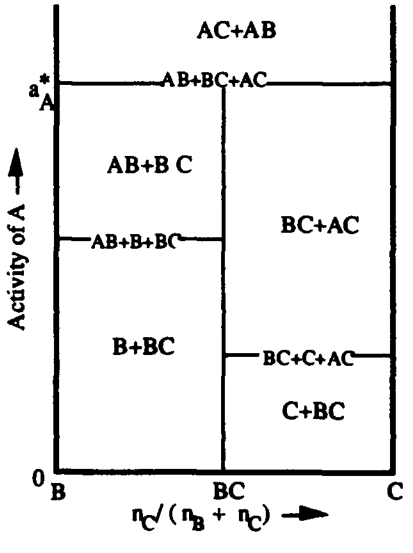

Fig. 6 - Stability diagram for the ternary phase diagram in Fig. 4.

$$A + BC = AC + B. \tag{9}$$

The AB layer grows by the reaction of A from the AB/A interface at the AC/AB interface with B released from Eq. (9). The reaction at the AC/AB interface is

$$A + B = AB. \tag{10}$$

The overall reaction is Eq. (6) which is just the sum of Eqs. (9) and (10). The AC layer always forms next to the BC layer because of the immobility of C.

The only potentially unstable interface against diffusion of A is BC/AC when a_A becomes greater than a_A^*. This instability against A diffusion may result in the formation of a periodic layered structure, similar to the case shown in Fig. 7 (d).

III. Discussion

A detailed kinetic analysis [6] on the formation of the periodic layered structure shows that the mobilities of B and A in the reaction layers are the most important parameters in determining the relative stability of the simple layered structure versus the periodic layered structure. The periodic layered structure is favored if the mobility of A is much higher than that of B. On the other hand, the simple layered structure is favored if the mobilities of A and B are on the same order of magnitude. This conclusion can also be reached with the following simple arguments without going into the detailed kinetic analysis.

Let's use the diffusion couple B_2C/A with the phase relationships shown in Fig. 1 as an example. The reactions in the couple can proceed with the simple layered structure or the periodic layered structure as illustrated in Fig. 8. In order for the reactions to proceed with the simple layered structure, both A and B have to diffuse a distance of typically a few hundred microns as illustrated in Fig. 8 (a). On the other hand, B only has to diffuse a distance of typically a few

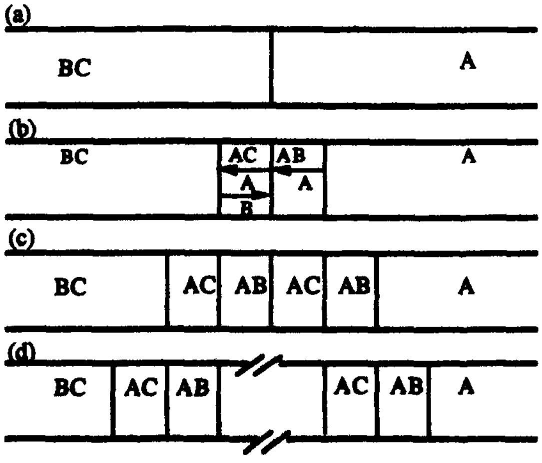

Fig. 7 - Sequence of the morphological evolution for the diffusion couple BC/A shown in Fig. 4. (a) The diffusion couple at time = 0. (b), (c), and (d) Morphological evolution for the formation of the periodic layered structure in the couple BC/A.

microns in order for the reactions to proceed with the periodic layered structure as illustrated in Fig. 8 (b). However, the periodic layered structure has the disadvantage of creating large amount of BC_2/AB interface. Therefore, if the mobility of B in the BC_2 phase is much smaller than that of A in the AB phase, the periodic layered structure is favored because this structure avoids the long-range diffusion of the slow-moving component. If the mobility of B in the BC_2 phase is comparable to that of A in the AB phase, the simple layered structure is favored because the diffusion distance of A is cut by one-half and the system does not pay the penalty of creating large amount of the AB/BC_2 interface.

If it is assumed for the purpose of discussion that *B is the dominant diffusion species in the* ternary diffusion couple B_2C/A, no periodic layered structure will form. This can be verified by constructing the stability diagram using the activity of B as a parameter and checking the stabilities of all the interfaces against the diffusion of B.

It is worth noting that perturbation at the BC_2/AB interface may lead to interfacial instability. This instability will result in the formation of an aggregate type of structure. However, in the present study we have assumed that planar interface is maintained at the BC_2/AB interface and considered only the relative stability of a simple layered structure versus that of a periodic layered structure.

IV. Conclusion

A thermodynamic argument was presented to rationalize the formation of periodic layered structure in some ternary diffusion couples of B_2C/A *with the phase relationships shown in* Fig. 1. This type of structure may also occur in other ternary diffusion couples of BC/A with the

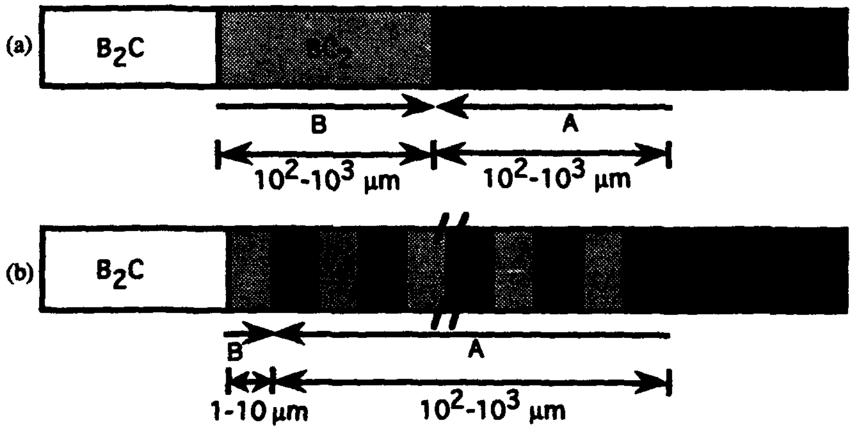

Fig. 8 - Two possible morphologies for a diffusion couple B_2C/A with the phase relationship shown in Fig. 1. (a) The simple layered structure. (b) The periodic layered structure.

phase relationships shown in Fig. 5.

The mobilities of B and A in the reaction layers are the most important parameters in determining the relative stability of the simple layered structure versus the periodic layered structure. The periodic layered structure is favored if the mobility of B is substantially lower than that of A. On the other hand, if the mobility of A and B are comparable, the simple layered structure is favored.

Acknowledgment

The authors wish to thank Dr. J.-C. Lin of Alcoa Laboratories, Alcoa Center, PA for first suggesting the possibility that the formation of the periodic layered structure in $B_{\delta''}C/A$ type diffusion couples is due to the relative mobilities of A and B in the phases formed in the diffusion couples. In fact, these qualitative arguments were used to rationalize the formation of the periodic layered structure in GaAs/Co diffusion couples as given in Ref. 5. The authors also wish to thank DARPA/ONR for partial financial support through Grant No. N-000-14-92-J-1863.

References

1. K. Osinski, A W. Vriend, G. F. Bastin, and F. J. J. van Loo, Z. Metallkde., 1982, vol. 73, p. 258.

2. F. J. J. van Loo and K. Osinski, in "Fundamentals and Applications of Ternary Diffusion" (Eds.: G. R. Purdy), Pregamon Press, NY, 1990, p. 109.

3. S. F. Dunaev and S. A. Zver'kov, J. Less-Common Met., 1989, vol. 153, p. 143.

4. T. C. Chou, J. Materials Research, 1990, vol. 5, p. 601.

5. F.-Y. Shiau, Y. A. Chang, and J.-C. Lin, Mats. Chem. Phys., 1992, vol. 32, p. 300.

6. C. R. Kao and Y. A. Chang, Acta Metall. Mater., 1992, under review.

Formation and Growth of Intermetallic Phases in Binary Diffusion Couples

C.-P. Chen and Y. A. Chang

University of Wisconsin-Madison

Madison, Wisconsin 53706 USA

Abstract

The growth rates of intermediate phases in a binary diffusion couple A/B were modeled numerically in terms of diffusion theory for several binary systems. The results showed that the growth rates of phases depend primarily on their interdiffusion coefficients (taken to be constant for all the phases) unless the range of homogeneity of a particular phase is extremely small. Numerical modeling was used to account for phenomena observed in Ti/Al and thin-film Co/Si couples. In the first case, $TiAl_3$ was the only phase observed by EPMA when a couple Ti/Al was annealed at 625 ^{o}C, but three other phases exist at this temperature in the Ti-Al phase diagram. This phenomenon is due to the fact that the interdiffusion coefficient of $TiAl_3$ is at least four orders of magnitude larger than those of the other phases. In the second case, in a thin-film Co/Si couple annealed at 545 ^{o}C, it was found experimentally that the initial growth rate of Co_2Si was the highest, followed by that of CoSi. $CoSi_2$ was not observed until sometime later, when the Co_2Si formed initially was consumed. These phenomena were also accounted for quantitatively, and were shown to be due not only to the interdiffusion coefficients of these phases, but also to the additional constraint of a limited initial supply of Co.

In addition to modeling the growth of phases with essentially composition-independent interdiffusion coefficients, we have also evaluated the growth rate of NiAl in a Ni/Al couple. For NiAl, a plot of $\log\tilde{D}$ vs. composition exhibits a V-shaped curve. The calculated composition profile within the NiAl single phase region of the Ni/Al diffusion zone is a sigmoidal curve. In fact, the existence of the sigmoidal concentration profile might have misled previous investigators to conclude incorrectly that new phases, not found on the phase diagram, appeared in the couples of Ni/Al.

Diffusion in Ordered Alloys
Edited by B. Fultz, R.W. Cahn, and D. Gupta
The Minerals, Metals & Materials Society, 1993

I. Introduction

The formation and growth of intermediate phases in a binary diffusion couple (denoted A/B) depend on the nucleation and growth of the phases. If nucleation of the phases does not pose any difficulty, all the phases which appear in the phase diagram should form and grow in a bulk A/B diffusion couple. Moreover, if we consider diffusion to be the only growth mechanism, the growth of these phases should follow a parabolic relationship with respect to time. Since the growth rate of a phase in an A/B couple depends on the interdiffusion coefficient and the range of homogeneity of the phase, as well as those of its neighboring phases, under certain conditions the rate of growth of a particular phase may be extremely small. In fact, the existence of such a phase may not be detected experimentally using techniques such as electron probe microanalysis (EPMA). The apparent absence of the phase is then due to its extremely slow growth, not its lack of nucleation.

As was shown by van Loo et al. [1], the only phase identifiable by electron probe microanalysis (EPMA) in an Al/Ti bulk diffusion couple annealed at 625 ^{o}C was $TiAl_3$. Yet according to the phase diagram, three other phases, i.e. $TiAl_2$, TiAl and Ti_3Al, should have formed in the couple [2]. On the other hand, when a $TiAl_3$/Ti couple was annealed at 800 ^{o}C, the three intermediate phases $TiAl_2$, TiAl and Ti_3Al did form. However, when a layer of pure Al was joined on the outside of the remaining $TiAl_3$ layer of the above couple and then annealed at 625 ^{o}C for a few hours, the intermediate phases $TiAl_2$, TiAl and Ti_3Al vanished completely. The resulting configuration of this couple became Al/$TiAl_3$/Ti.

The growth of intermediate phases in a thin-film diffusion couple is more complex, since the material supply in one of the end phases is limited. As was shown recently by Jan et al. [3], the three intermediate phases in Co-Si, i.e. Co_2Si, CoSi and $CoSi_2$, formed sequentially in a thin-film Co/Si diffusion couple.

Tarento and Blaise [4] have claimed the formation of new phases in Ni/Al couples, which do not exist in the Ni-Al phase diagram. However, according to the concentration profiles of several bulk diffusion couples of Ni/Al reported by Shankar and Seigle [5], abrupt concentration changes occur over a small distance within the NiAl single phase region of the diffusion zone. It is likely that the sharp concentration changes within the single-phase region in their couples might have misled Tarento and Blaise [4] to claim the formation of new phases.

The objectives of the present study are (i) to evaluate numerically the growth rates of intermediate phases in model binary bulk diffusion couples using the theory of diffusion in terms of the interdiffusion coefficients of these phases and (ii) to account quantitatively for some of the apparent anomalies reported in the literature of phase growth and formation in both bulk and thin-film diffusion couples.

II. Diffusion theory for the growth of intermediate phases in a binary diffusion couple

Figures 1 a,b show the concentration profiles, i.e. C-x curves, for the *growth of an n*-phase binary diffusion couple at constant temperature T and pressure P. The growth of the intermediate phases in such a couple is governed by three fundamental equations. They are Fick's first law, which relates the flux to the interdiffusion coefficient and concentration gradient, the equation of continuity, and the interface mass balance equation. These equations (referring to the symbols in Fig. 1) are

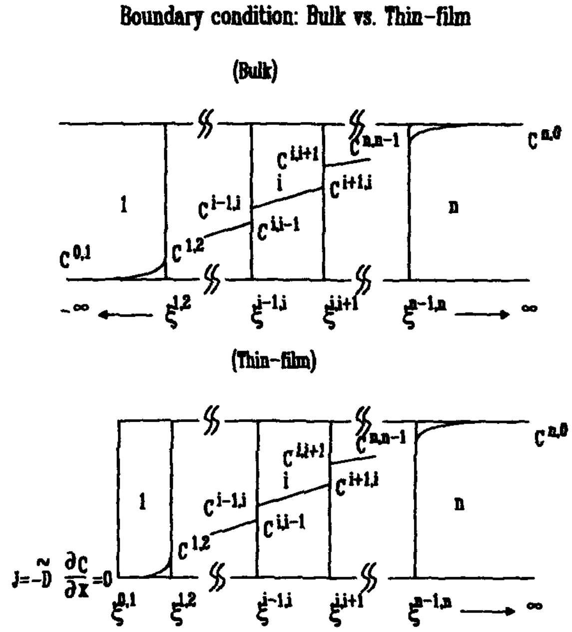
Boundary condition: Bulk vs. Thin-film

(Bulk)

(Thin-film)

Fig. 1 (a) The concentration profiles of a multiphase binary diffusion couple at constant temperature and pressure for the bulk case. The boundary conditions are $C^{0,1}$ = constant at $x = -\infty$, and $C^{n,0}$ = constant at $x = \infty$. (b) The concentration profiles of a multiphase binary diffusion couple at constant temperature and pressure for the thin-film case. The boundary conditions are $\left[\tilde{J}^i\right]_{x=\xi^{0,1}} = -\tilde{D}^i\left[\frac{\partial C^i}{\partial x}\right]_{x=\xi^{0,1}} = 0$ and $C^{n,0}$ = constant at $x = +\infty$.

$$\tilde{J}^{i} = -\tilde{D}^{i}\frac{\partial C^{i}}{\partial x} \qquad [1]$$

$$\frac{\partial C^{i}}{\partial t} + \frac{\partial \tilde{J}}{\partial x} = 0 \qquad [2]$$

$$(C^{i-1,i} - C^{i,i-1})\frac{d\xi^{i-1,i}}{dt} = \tilde{J}^{i-1,i} - \tilde{J}^{i,i-1} \qquad [3]$$

where $\tilde{J}^{i}$ is the interdiffusion flux, $\tilde{D}^{i}$ is the interdiffusion coefficient, C^i is the concentration of the ith phase, x is a distance coordinate, and $\xi^{i-1,i}$ is the position of the interface between the (i-1)th and ith phases. The superscript i,i-1 indicates that the quantities C and $\tilde{J}$ refer to the ith phase at the i/(i-1) interface while i-1,i refers to the (i-1)th phase at the i/(i-1) interface.

These equations are applicable to both bulk and thin-film couples, but the solutions to these equations are different in each case due to the different boundary conditions. While the supplies of the two end phases in the bulk case are unlimited, that for one of the end phases is finite for the thin-film case. The solutions for each of these cases are given below.

A. The Bulk (Semi-Infinite) Case

The boundary conditions for the bulk case are $C^{0,1}$ = constant at $x = -\infty$, and $C^{n,0}$ = constant at $x = +\infty$, as shown in Fig. 1a. For these boundary conditions and assuming constant interdiffusion coefficients, the position of the interface between the (i-1)th and ith phases, i.e. $\xi^{i-1,i}$ is [6-8]

$$\xi^{i-1,i} = Z^{i-1,i}\sqrt{t} \qquad [4A]$$

where

$$Z^{i-1,i} = 2\left[\frac{(\tilde{D}K)^{i,i-1} - (\tilde{D}K)^{i-1,i}}{C^{i-1,i} - C^{i,i-1}}\right] \qquad [4B]$$

$$K^{i,i-1} = \sqrt{t}\left[\frac{\partial C}{\partial x}\right]^{i,i-1} \qquad [5A]$$

$$K^{i-1,i} = \sqrt{t}\left[\frac{\partial C}{\partial x}\right]^{i-1,i} \qquad [5B]$$

$$C^{i} = A^{i} + B^{i}\,\mathrm{erf}\left(\frac{x}{2\sqrt{\tilde{D}^{i}t}}\right) \qquad [6]$$

Values of A^i and B^i can be obtained by substituting Eq. [6] into Eqs. [1] and [2].

The growth of the ith phase, ω^i can be obtained from $\xi^{i,i+1}$ and $\xi^{i-1,i}$ as given below:

$$\omega^{i} = \xi^{\,i,i+1} - \xi^{\,i-1,i} = W^{i}\sqrt{t} \qquad [7]$$

$$W^{i} = 2\left\{\left[\frac{(\tilde{D}K)^{\,i+1,i} - (\tilde{D}K)^{\,i,i+1}}{C^{i,i+1} - C^{i+1,i}}\right] - \left[\frac{(\tilde{D}K)^{\,i,i-1} - (\tilde{D}K)^{\,i-1,i}}{C^{i-1,i} - C^{i,i-1}}\right]\right\} \qquad [7A]$$

When the interdiffusion coefficients and the phase boundaries of all the phases at constant T and P are known in a bulk couple, Eq. [7] may be used to calculate the growth of the ith phase as a function of time.

B. The Thin-Film Case

B.1 Concentration-independent diffusivity

As shown in Fig. 1B, due to the limited supply of the end phase (designated as phase 1), one of the boundary conditions of the bulk case, i.e. C = constant at x = -∞ is no longer valid. The appropriate boundary condition for this case is zero flux at x = -∞,

$$\left[\tilde{J}^{\,i}\right]_{x=\xi^{0,1}} = -\,\tilde{D}^{\,i}\left[\frac{\partial C^{i}}{\partial x}\right]_{x=\xi^{0,1}} = 0 \qquad [8]$$

The other boundary condition, i.e. $C^{n,0}$ = constant at x = +∞, is still valid. Since a simple analytical solution to the diffusion equation does not exist for these boundary conditions, it is customary to solve the diffusion equations numerically. Hickl and Heckel [8] have successfully solved this problem numerically using the explicit finite difference form, in connection with their study on the kinetics of phase layer growth during aluminide coating of nickel. However, this approach is inefficient and takes an excessively long computing time to obtain the solutions, particularly when the number of intermediate phases increases beyond one. In the present study, the diffusion equations have been transformed into a finite difference form along the distance coordinate x for 20 nodal points in each phase. The partial differential equations now become a set of ordinary differential equations.

Since the interface position $\xi^{i-1,i}$ moves during the growth (or dissolution) of the phases, this is a moving boundary problem. The movement of these boundaries must be taken into account when solving such problems. Rearranging the equation of continuity Eq. [2], yields

$$\left[\frac{\partial C^i}{\partial t}\right]_x = -\frac{\partial \tilde{J}^i}{\partial x} = \tilde{D}^i \frac{\partial^2 C^i}{\partial x^2} \qquad [9]$$

since

$$\left[\frac{\partial C^i}{\partial t}\right]_\xi = -\frac{\partial C}{\partial x}\frac{dx}{dt} + \left[\frac{\partial C^i}{\partial t}\right]_x \qquad [9A]$$

$$\left[\frac{\partial C^i}{\partial t}\right]_\xi = -\frac{\partial C}{\partial x}\frac{dx}{dt} + \tilde{D}^i \frac{\partial^2 C^i}{\partial x^2} \qquad [10]$$

If uniform grid sizes are taken for each phase, then

$$\frac{dx}{dt} = \left(1-\frac{j-1}{n-1}\right)\frac{d\xi^{i-1,i}}{dt} + \left(\frac{j-1}{n-1}\right)\frac{d\xi^{i,i+1}}{dt} \qquad [11]$$

where j is the jth grid and n is the total number of nodal points in the *ith* phase. *Combining* Eqns. [10] and [11] yields the finite difference form of the equation of continuity:

$$\frac{\partial C_j^i}{\partial t} = \frac{\left(C^i_{j-1}-C^i_{j+1}\right)}{2\Delta x^i}\left[\left(1-\frac{j-1}{n-1}\right)\frac{d\xi^{i-1,i}}{dt} + \left(\frac{j-1}{n-1}\right)\frac{d\xi^{i,i+1}}{dt}\right]$$

$$+ \tilde{D}^i \frac{\left(C^i_{j+1}-2C^i_j+C^i_{j-1}\right)}{(\Delta x^i)^2} \qquad [12]$$

where Δx^i is the grid size of the ith phase. The finite difference form of the interface mass balance equation, i.e. Eq. [3], then becomes

$$\left(C_1^{i+1}-C_n^i\right)\frac{d\xi^{i,i+1}}{dt} = \tilde{D}^{i+1}\frac{\left(-C_3^{i+1}+4C_2^{i+1}-3C_1^{i+1}\right)}{2\Delta x^{i+1}}$$

$$-\tilde{D}^i\frac{\left(C^i_{n-2}-4C^i_{n-1}+3C^i_n\right)}{2\Delta x^i} \qquad [13]$$

By solving the proceeding equations simultaneously, the composition profile C^i in each phase and the interface position, $\xi^{i,i+1}$ may be obtained for different periods of time.

In order to use this model to solve the thin-film diffusion couple problem, an initial thickness must be assigned to each phase. In the present study, the semi-infinite boundary conditions are used in the initial stage of calculations. In other words, the thin-film couple is treated as a bulk couple before B atoms of the substrate completely penetrate the film and the end phase A is consumed. Accordingly, the initial thickness of each phase when performing the thin-film couple calculation is based on the thickness predicted for the bulk case.

B.2 Concentration-dependent diffusivity

For a system with concentration-dependent diffusivity, the boundary conditions are the same as in case B.1. The numerical technique for solving this kind of problem is also the same as that used in case B.1, except equations [9] through [13] need to be modified. Equation [9] becomes

$$\left[\frac{\partial C^i}{\partial t}\right]_x = -\frac{\partial \tilde{J}^i}{\partial x} = \tilde{D}^i \frac{\partial^2 C^i}{\partial x^2} + \frac{\partial \tilde{D}^i}{\partial x}\frac{\partial C^i}{\partial x} \qquad [14]$$

in which

$$\frac{\partial \tilde{D}^i}{\partial x}\frac{\partial C^i}{\partial x} = \frac{\partial \tilde{D}^i}{\partial C^i}\left(\frac{\partial C^i}{\partial x}\right)^2$$

$$\left[\frac{\partial C^i}{\partial t}\right]_\xi = -\frac{\partial C}{\partial x}\frac{dx}{dt} + \left[\frac{\partial C^i}{\partial t}\right]_x \qquad [9A]$$

$$\left[\frac{\partial C^i}{\partial t}\right]_\xi = -\frac{\partial C}{\partial x}\frac{dx}{dt} + \tilde{D}^i \frac{\partial^2 C^i}{\partial x^2} + \frac{\partial \tilde{D}^i}{\partial C^i}\left(\frac{\partial C^i}{\partial x}\right)^2 \qquad [15]$$

If uniform grid sizes are also taken for each phase, then the finite difference form of the equation of continuity can be generated by combining equations [11] and [15]:

$$\frac{\partial C^i_j}{\partial t} = \frac{\left(C^i_{j-1} - C^i_{j+1}\right)}{2\Delta x^i}\left[\left(1 - \frac{j-1}{n-1}\right)\frac{d\xi^{i-1,i}}{dt} + \left(\frac{j-1}{n-1}\right)\frac{d\xi^{i,i+1}}{dt}\right]$$

$$+ \tilde{D}^i(C^i_j)\frac{\left(C^i_{j+1} - 2C^i_j + C^i_{j-1}\right)}{(\Delta x^i)^2} + \frac{\left(\tilde{D}^i(C^i_{j+1}) - \tilde{D}^i(C^i_{j-1})\right)}{2\Delta C^i}\left(\frac{C^i_{j+1} - C^i_{j-1}}{2\Delta x^i}\right)^2 \qquad [16]$$

The finite different form of the interface mass balance equation then becomes

$$\left(C^{i+1}_1 - C^i_n\right)\frac{d\xi^{i,i+1}}{dt} = \tilde{D}^{i+1}(C^{i+1}_1)\frac{\left(-C^{i+1}_3 + 4C^{i+1}_2 - 3C^{i+1}_1\right)}{2\Delta x^{i+1}}$$

$$-\tilde{D}^i(C^i_n)\frac{\left(C^i_{n-2} - 4C^i_{n-1} + 3C^i_n\right)}{2\Delta x^i} \qquad [17]$$

By using the same numerical technique as that in case B.1, the composition profile C^i in each phase and the interface position, $\xi^{i,i+1}$, may be obtained for different periods of time.

III. Numerical evaluation of the growth of phases in model binary diffusion couples

Using the equations given in the previous section, we demonstrate numerically that the growth rates of intermediate phases in an A/B diffusion couple depend primarily on their interdiffusion coefficients (assumed to be constant for all the phases), unless the range of homogeneity of a particular phase becomes extremely small. For the purpose of illustration, we shall assume the binary system A-B has three intermediate phases, i.e. A_3B, AB and AB_3, with ranges of homogeneity of 2 at%. Values of the interdiffusion coefficients for the intermediate phases are taken to vary as much as four orders of magnitude, and the diffusional fluxes for the two end phases A and B are assumed to be negligible.

Fig. 2 shows the growth of the three intermediate phases, A_3B, AB and AB_3, as a function of the square root of time, with their three interdiffusion coefficients being 100, 10 and 1 $\mu m^2/hr$. As shown in the figure, the growth rate of A_3B is the highest and that of AB_3 is the smallest. The values of the interdiffusion coefficients clearly dominate the growth rates of these phases. Similar results are presented in Fig. 3. In this case, the interdiffusion coefficients of A_3B, AB and AB_3 are taken to be 200, 5 and 50 $\mu m^2/hr$, respectively. Since the interdiffusion coefficient of AB_3 is greater than that of AB in the second case, the growth rate of AB_3 is greater; as shown in Fig. 3, in contrast to the case shown in Fig. 2. These results also demonstrate that if the interdiffusion coefficient of AB_3 in the first case or that of AB in the second case is smaller than that of A_3B by two orders of magnitude, the amount of AB_3 or AB in the diffusion couple would be so small that it may not be determined by EPMA. Fig. 4 shows the results for a couple A/B when the interdiffusion coefficient of A_3B, AB and AB_3 are 100, 0.1 and 0.05 $\mu m^2/hr$, respectively. As shown in this figure, using the same scale as that in Fig. 2, we could conclude that AB and AB_3 do not form in this diffusion couple. In actuality, the amounts of these two phases formed are so small that their thicknesses are essentially zero, as shown in Fig. 4.

In all three cases discussed so far, growth of the phases in these couples follows the parabolic relationship. In other words, these phases grow linearly with the square root of time. However, this would not be the case for the growth of phases in a thin-film diffusion couple. Let us now examine the results of a thin-film A (5μm) / B diffusion couple with the interdiffusion coefficients of A_3B, AB and AB_3 again being 100, 10 and 1 $\mu m^2/hr$, respectively. The ranges of homogeneity are again taken to be 2 at%. As shown in Fig. 5, the thicknesses of the phases A_3B, AB and AB_3 increase linearly with the square root of time initially, similar to the results shown in Fig. 2, until the end phase A is completely consumed. Subsequently, the thickness of A_3B decreases with the square root of time while those of AB and AB_3 increase with the square root of time but with increases in their slopes. This may seem strange at first. However, when we analyze the situation, this is exactly the result we should expect.

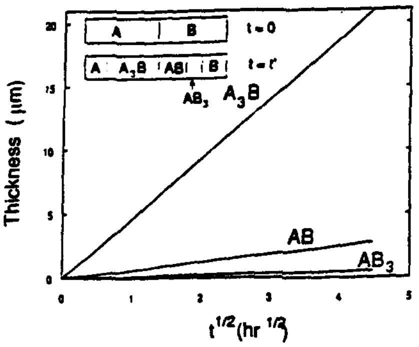

Fig. 2 Growth of phases in an A/B bulk diffusion couple. The interdiffusion coefficients of A_3B, AB and AB_3 are 100, 10, and 1 μm^2/hr, respectively; all of these phases have a homogeneity range of 2 at%. The solubilities of A in B and of B in A are negligible.

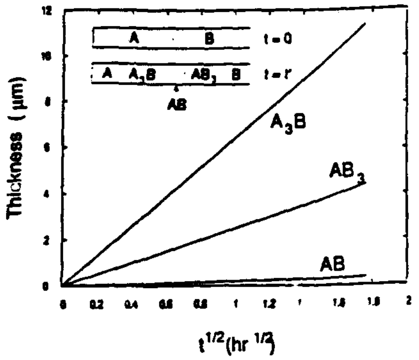

Fig. 3 Growth of phases in an A/B bulk diffusion couple. The interdiffusion coefficients of A_3B, AB and AB_3 are 200, 5, and 50 μm^2/hr, respectively; all of these phases have a homogeneity range of 2 at%. The solubilities of A in B and of B in A are negligible.

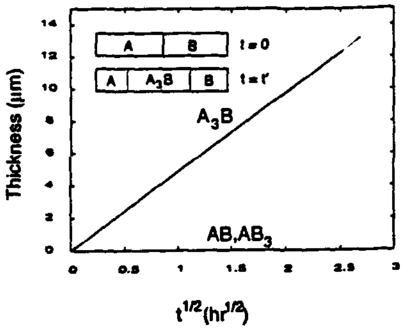

Fig. 4 Growth of phases in an A/B bulk diffusion couple. The interdiffusion coefficients of A_3B, AB and AB_3 are 100, 0.1, and 0.05 μm^2/hr, respectively; all of these phases have a homogeneity range of 2 at%. The solubilities of A in B and of B in A are negligible.

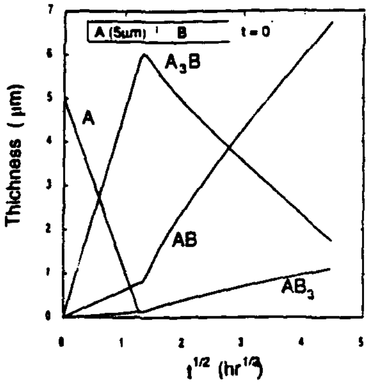

Fig. 5 Growth of phases in a thin-film A(5μm)/B diffusion couple. The interdiffusion coefficients of A_3B, AB and AB_3 are 100, 10, and 1 μm^2/hr, respectively; all of these phases have a homogeneity range of 2 at%. The solubilities of A in B and of B in A are negligible.

Initially, we have an A/B diffusion couple with the growth of A_3B, AB and AB_3 following those shown in Fig. 2. However, when A is completely consumed, we then have an A_3B/B diffusion couple. Even though the interdiffusion coefficient of A_3B is the highest, its thickness must decrease with time, since the end member A has been consumed; there is no longer any supply of A. The thicknesses of AB and AB_3 increase accordingly. In the present case, the interdiffusion coefficient of AB_3 is only two orders of magnitude smaller than that of A_3B. If it were more than two orders of magnitude smaller, we might not even observe the formation of AB_3 until A_3B was completely consumed.

Let us next exmaine the results when a thin-film A_3B (5μm) / B diffusion couple is annealed at a sufficiently high temperature. For this example, the interdiffusion coefficients of A_3B, AB and AB_3 are taken to be 4000, 10 and 1 μm²/hr, respectively, and the ranges of homogeneity for these phases are 2 at%. As shown in Fig. 6, the thickness of A_3B decreases with time, while those of AB and AB_3 increase with time, with the growth rate of AB being considerably higher than that of AB_3. After 10 hours of annealing (i.e. $t^{1/2} \cong 3.16$ hr $^{1/2}$), a layer of A is joined to the outside surface of A_3B. The couple, now with the configuration

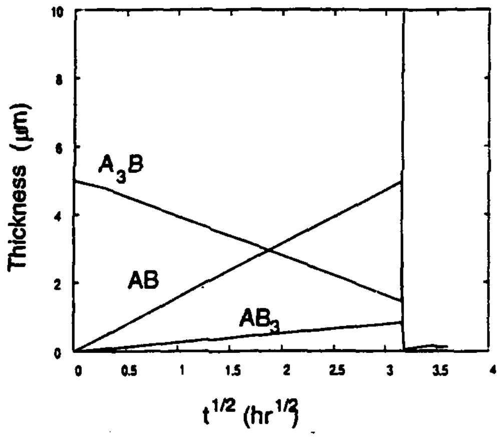

Fig. 6 Growth of the phases AB and AB_3 in a thin-film A_3B (5 μm) / B diffusion couple for about 10 hours and the subsequent growth of phases in this couple when a layer of A is joined to the outside of the remaining A_3B layer. The interdiffusion coefficients of A_3B, AB and AB_3 are 4000, 10 and 1 μm²/hr, respectively; all of these phases have a homogeneity range of 2 at% .The solubility of A in B and that of B in A are negligible.

$A/A_3B/AB/AB_3/B$ is again annealed at the same temperature. The thicknesses of AB and AB_3 drop to nearly nothing, while that of A_3B increases suddenly to a very high value. The resulting configuration in essence becomes $A/A_3B/B$, since the thicknesses of AB and AB_3 are so small that they are not detectable. As long as there is supply of A in the end member, A_3B grows rapidly, due to its high interdiffusion coefficient. However, when the supply of A in the end member is not available, growth of AB and AB_3 takes place in the diffusion couple.

The five examples demonstrate the importance of the interdiffusion coefficient on the growth rates of phases in a binary diffusion couple. The results clearly show that we may not be able to detect the existence of a particular phase by techniques such as EPMA when the interdiffusion coefficient is extremely small, even if nucleation of this phase does not pose any difficulty. In the following, we will use the equations given in section II to account quantatively for the actual behavior of several diffusion couples reported in the literature.

IV. Application of numerical modeling to actual cases and discussion

A. Ti-Al

Van Loo et al. [1] carried out diffusion couple experiments of Ti/Al at 625 °C. Even though four intermetallic phases, i.e. Ti_3Al, TiAl, $TiAl_2$ and $TiAl_3$, exist in the Ti-Al system at this temperature [2], the only phase detected by EPMA was $TiAl_3$. They also obtained the interdiffusion coefficient for $TiAl_3$ from their experiments. Moreover, when they annealed $Ti/TiAl_3$ couples at 800 °C, they found the formation of Ti_3Al, TiAl and $TiAl_2$, clearly indicating nucleation of these phases was not the problem. Furthermore, when they joined a layer of Al onto the $TiAl_3$ layer of the $TiAl_3/TiAl_2/TiAl/Ti_3Al/Ti$ couple annealed at 800 °C and subsequently annealed it at 625 °C, the phases Ti_3Al, TiAl and $TiAl_2$ disappeared rapidly, resulting in the configuation $Al/TiAl_3/Ti$. However, van Loo et al. did not attempt to evaluate the interdiffusion coefficients of Ti_3Al, TiAl and $TiAl_2$ from their experiments.

The behavior of phase growth in the Al/Ti, $TiAl_3/Ti$ and $Al/TiAl_3/TiAl_2/TiAl/Ti_3Al/Ti$ couples is similar to that of the model example given in Fig. 6. In fact, using the interdiffusion coefficient of $TiAl_3$ obtained by van Loo et al. [1], those of Ti, TiAl and Ti_3Al obtained by Ouchi et al. [9], and that of $TiAl_2$ estimated by us, the calculated thicknesses of the phases in an Al/Ti couple at 625 °C are shown in Fig. 7. The interdiffusion coefficients for $TiAl_3$, $TiAl_2$, TiAl, Ti_3Al and Ti at 625 °C used are 8597, 0.1634, 0.02284, 0.02545 and 0.038224 $\mu m^2/hr$, respectively. The interdiffusion coefficient of $TiAl_2$ was estimated using the diffusion couple data reported by van Loo et al. [1]. As shown in the figure, the only detectable phase is $TiAl_3$; its interdiffusion coefficient is at least five orders magnitude larger than those of the other phases.

Figure 8 shows the growth of phases in a thin-film $TiAl_3$ (5μm) / Ti couple at 800 °C for 10 hrs(i.e. $t^{1/2} \cong 3.16\ hr^{1/2}$). The thickness of $TiAl_3$ decreases with time, while those of $TiAl_2$, TiAl and Ti_3Al increase with time. At $t \cong 10$ hrs, a layer of Al is joined to the couple annealed at 800 °C for 10 hrs, and the diffusion couple of Al/$TiAl_3$/$TiAl_2$/TiAl/Ti_3Al/Ti is subsequently annealed at 625 °C. As shown in Fig. 8, the thickness of Ti_3Al increases suddenly to a very high value while the thickness of the other phases decrease precipitously to nearly zero. These calculated results are consistent with the results found experimentally by van Loo et al. [1].

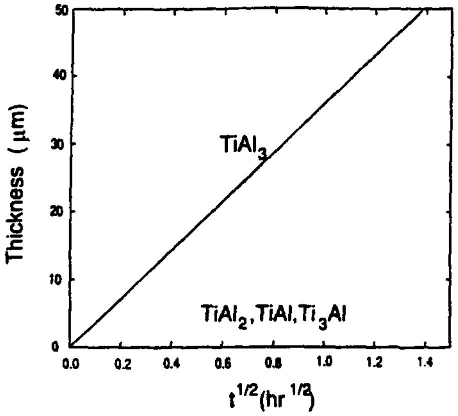

Fig. 7 Growth of phases in a Ti/Al bulk diffusion couple at 625 °C. The interdiffusion coefficient of the $TiAl_3$, $TiAl_2$, TiAl, Ti_3Al and Ti phases are 8.597, 0.16344, 0.02284, 0.02545 and 0.038224 μm^2/hr, respectively.

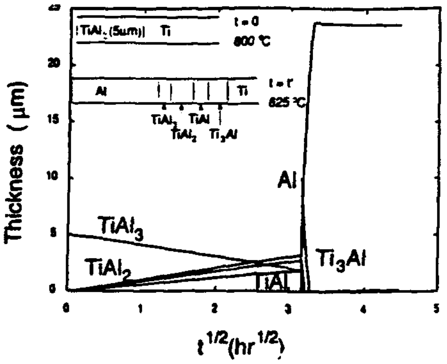

Fig. 8 Growth of $TiAl_2$, TiAl and Ti_3Al in a thin-film $TiAl_3$ (5 μm) / Ti diffusion couple annealed at 800 °C for 3 hours, as well as the subsequent phase growth at 625 °C when 25 μm of Al is joined to the $TiAl_3$ end of the $TiAl_3$/Ti couple annealed at 800 °C for three hours. The interdiffusion coefficients at 625 °C are given in the caption of Fig. 7. The values at 800 °C are 68.461, 35.5, 0.54, 0.5648 and 0.541 μm^2/hr, respectively, for $TiAl_3$, $TiAl_2$, TiAl and Ti_3Al.

B. Co-Si

A number of investigators have studied the growth of phases in thin-film Co/Si diffusion couples, as recently analyzed and summarized by Jan et al. [3]. It was found that in such a thin-film couple, the phases formed and grew sequentially. Here we present the calculated growth rates of the Co-Si intermediate phases in several thin-film couples. The calculated results can account quantitatively for the experimental data reported in the literature. As shown in Fig. 9, the calculated thicknesses of Co_2Si, CoSi and $CoSi_2$ in a 450 nm Co/Si diffusion couple at 545 °C are in quantitative agreement with the experimental data of van Gurp and Langereis [10]. The interdiffusion coefficients of Co_2Si, CoSi and $CoSi_2$ were taken from Jan et al. [3]. The growth rate of $CoSi_2$ is extremely small before Co is completely consumed, and becomes appreciable after Co is consumed. The small growth rate initially is due primarily to its small interdiffusion coefficient.

Tu et al. [11] measured the growth (as well as dissolution) of phases in a thin-film couple with the following configuration: 250 nm Co/235 nm CoSi/ bulk Si at 430 °C. Fig. 10 shows the predicted thicknesses of Co, Co_2Si, CoSi, and $CoSi_2$ as a function of the square root of time. The thicknesses of Co and CoSi decrease initially, with a corresponding increase in the thickness of Co_2Si. The predicted values of Co, Co_2Si, and CoSi at $t = 0.5$ hr ($t^{1/2} = 0.707$ $hr^{1/2}$) are in good agreement with the experimental data of Tu et al. [11].

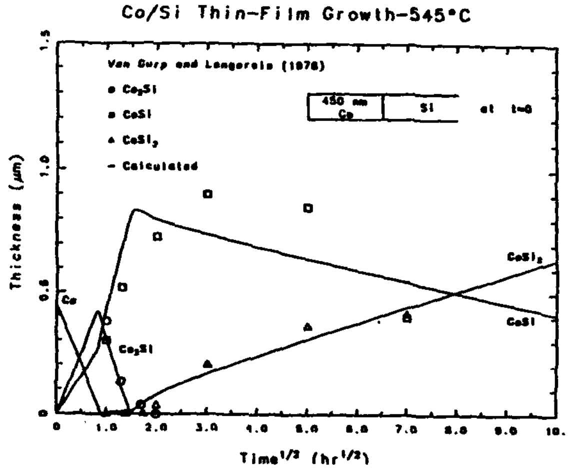

Fig. 9 Growth of phases in a 450 nm Co/Si couple at 545 °C: comparison between the predicted values and experimental data of van Gurp and Langereis. [9]

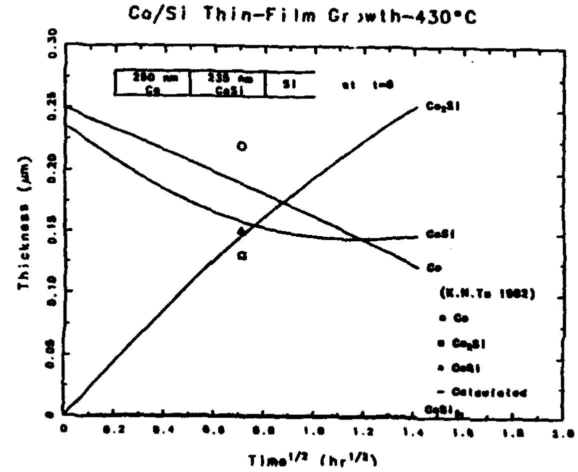

Fig. 10 Growth (and dissolution) of phases in a 250 nm Co/ 235 nm CoSi/ Si couple at 430 °C: comparison between the predicted values and experimental data of Tu et al. [9]

C. Ni-Al

In all of the calculations so far, we have assumed the interdiffusion coefficients of phases to be composition-independent. This clearly is not the case even for some of the Ti-Al intermetallic phases. However, since the interdiffusion coefficients for these phases do not change appreciably with composition, the assumption of constant diffusion coefficients does not cause serious errors in the calculated concentration profile across a diffusion couple. However, for the intermetallic compound NiAl with the B2 (CsCl) structure in the Ni-Al system, the assumption of a constant diffusion coefficient will lead to serious errors in the calculated concentration profile of NiAl within a Ni/Al diffusion couple. For the NiAl phase, the diffusion coefficient in the vicinity of the stoichiometric composition is a minimum, and it increases by several orders of magnitude as deviations from stoichiometry occur [5]. In the following, the Ni-Al system is used to demonstrate the significant effect of concentration-dependent diffusivity on the concentration profile.

Figure 11 shows the calculated concentration profile for a specimen with a fixed surface concentration of NiAl at 1000 °C. The boundary condition of this calculation is based on the experiment performed by Shankar and Seigle [5]. According to the Ni-Al phase diagram [12], at 1000 °C for Ni concentrations higher than ~ 43 at% Ni, the equilibrium phases are NiAl, Ni_3Al (ζ) and Ni. The interdiffusion coefficients used in the calculations are taken from Shankar and Seigle [5]. As shown in this figure there is an abrupt change in the Ni concentration within the single phase NiAl over a small distance within the diffusion zone. The calculated results are in agreement with the experimental data of Shankar and Seigle [5]. The apparently anomalous behavior of this concentration profile within the NiAl phase is due to the sharp change in its interdiffusion coefficient with deviations from stoichiometry. In fact, it is most likely this phenomenon that led Tarento and Blaise to conclude that new phases formed in their diffusion couples.

A qualitative rationalization of the results shown in Fig. 11 is given in Fig. 12. In the top portion of Fig. 12, log $\tilde{D}$ is plotted as a function of x_B for an ordered phase AB. Let us now perform a thought experiment. As shown in the top portion of Fig. 12, a diffusion couple with 11 diffusion members is annealed. As was determined in the numerical evalution of the growth of phases given in section III, the phase with the highest interdiffusion coefficient grows the fastest, while that with lowest coefficient grows the slowest. Under such conditions, it is evident that the elements with high interdiffusion coefficients grow, while those with low coefficients shrink. Eventually, we have under steady-state conditions a sigmodial concentration profile, as shown in the lower portion of Fig. 12.

It is worth noting that this phenomenon has been discussed by d'Heurle and Ghez [13].

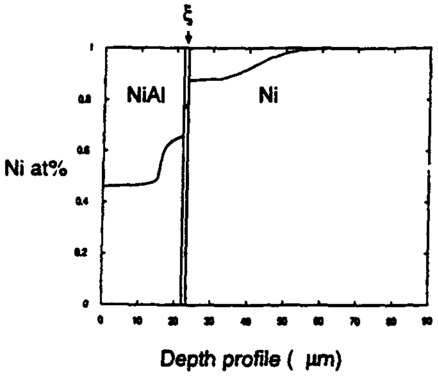

Fig. 11 Calculated concentration profiles of a pack-aluminized nickel and NiAl sample at 1000 °C.

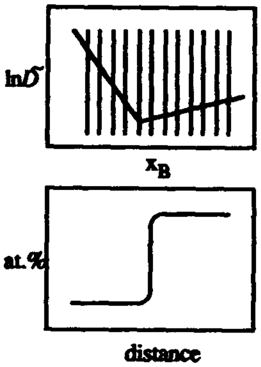

Fig. 12 Top: Plot of concentration-dependent diffusivity $\ln\tilde{D}$ vs. x_B within a single phase region, which is divided into 11 small elements. Bottom: The resulting concentration profile at steady-state from the diffusivity of top figure.

V. Conclusion

The growth rates of intermediate phases in a binary A/B diffusion couple were calculated with diffusion theory for several model systems. It was found that the growth rates of these phases depend primarily on their interdiffusion coefficients (assumed to be composition-independent for all the phases), unless the range of homogeneity of a particular phase is extremely small. When the interdiffusion coefficient of a specific phase is orders of magnitude smaller than that of the other phases, its growth rate is so small in comparison that its existence may not be detected by analytical techniques such as electron probe microanalysis (EPMA). On the other hand, when the interdiffusion coefficient of a specific phase is orders of magnitude greater than those of the other phases, this phase may be the only one detected experimently by EPMA. The growth rates of phases in the thin-film diffusion couples have the additional constraint that the material supply for one of the end phases is limited.

The calculations for several model binary systems were applied successfully to two actual cases Ti/Al, and thin-film Co/Si. Using interdiffusion coefficients of $TiAl_3$, $TiAl_2$, TiAl and Ti_3Al in Ti-Al, the calculations showed that in a diffusion couple of Ti/Al annealed at 625 °C, the only phase found was $TiAl_3$, in agreement with the experimental findings of van Loo et al. [1]. The thicknesses of the other three intermediate phases were on the order of one micron. This is due to the fact that the interdiffusion coefficient of $TiAl_3$ is at least five order magnitude larger than those of the other phases. When thin-film Co/Si couples were annealed, the phases Co_2Si, CoSi and $CoSi_2$ formed sequentially [10]. Using the interdiffusion coefficients of Co_2Si, CoSi and $CoSi_2$ [3], the experimental data reported in the literature [10, 11] for the growth of the intermediate phases were reproduced by calculation.

In addition to the phenomena observed in Ti/Al and thin-film Co/Si couples, the concentration profile in single-phase NiAl within the diffusion zone of Ni/Al was also reproduced in our calculations. The unusual concentration profile is that of an sigmoidal curve of the Ni (or Al) concentrations in the diffusion zone. This existence of the sigmoidal curve is due to the existence of a V-shaped curve of a $\log\tilde{D}$-vs-composition plot for the NiAl phase, a highly ordered intermetallic compound.

VI. Acknowledgment

The authors wish to thank D. Swenson, S. Mohney and C.R. Kao of our research group for reviewing the manuscript and the Department of Energy for financial support through Grant No. DEFG 02-86 ER 452754.

VII. References

1. F.J.J. van Loo and G.D. Rieck, 21, 61 (1973).
2. U.R. Kattner, J.-C. Lin and Y.A. Chang, Metall. Trans., 23A, 2081 (1992).
3. C.-H. Jan, C.-P. Chen, and Y.A. Chang, J. Appl. Phys. 73, 1168 (1993).
4. R.J. Tarento and G. Blaise, Acta. Metall. 37, 2305 (1989).
5. S. Shankar and L.L. Seigle, Metall. Trans., 9A, 1467 (1978).
6. G. V. Kidson, J. Nucl. Mater. 3, 21 (1961).
7. A solution was provided by C. Wagner as given in W. Jost, Diffusion in Solids, Liquids and Gases, 2nd Ed., Academic Press, New York, 68 (1960).
8. A. J. Hickel and R. W. Heckel, Metall. Trans. 6A, 431 (1975).
9. K. Ouchi, Y. Iijima and K. Suzuki, " Interndiffusion in Ti-Al System", p. 559-568 in Titanium '80 Science and Technology, H. Kimura and O. Izumi ed., AIME, New York, N.Y., 1980.
10. G. J. van Gurp and C. Langereis, J. Appl. Phys., 46, 4301 (1975).
11. K. N. Tu, G. Ottaviani, R. D. Thompson and J. W. Mayer, J. App. Phys. 53, 4406 (1982).
12. T.B. Massalski, J.L. Murray, L.H. Bennett and H. Baker, Binary Phase Diagram, vol 1, Am. Soc. for Metal, Metal Park, Ohio, 1986.
13. F.M. d'Heurle and R. Ghez, Thin Solid Films, 215, 19 (1992).

Modalities of Ordered Phase Formation via Chemical Interactions

F. M. d'Heurle

IBM Research Center
P. O. Box 218, Yorktown Heights, New York 10562 USA
and
FTE, KTH-Electrum
P. O. Box 1298, 164 28 Kista, Sweden

To Prof. Paul Gordon, my thesis adviser, to celebrate his being selected for the Albert Eaton White Distinguished Teacher Award by the American Society for Metals International. Chicago, Nov. 1992.

Abstract

We consider the mathematics of phase growth according to diffusion equations, and examine the implications for actual physical systems. In fact, reaction kinetics are more likely to be linear-parabolic than simply parabolic. In binary intermetallic compounds with unequal concentrations of the two components the majority atoms tend to diffuse more rapidly than the minority atoms. This has been formulated as the "ordered Cu_3Au" rule. Corollaries of this rule can be used to understand the order of phase formations, and have definite predictive value. Exceptions to the rule and its derivatives point out specific characteristics of the systems. Although conceived in terms of vacancy diffusion on the lattice, the ordered Cu_3Au rule is valid for reactions occurring at low temperatures where grain boundary diffusion processes should be dominating. This implies that in ordered compounds, probably even more so than in pure metals, the mechanisms of grain boundary diffusion are closely related to those of lattice diffusion.

Diffusion in Ordered Alloys
Edited by B. Fultz, R.W. Cahn, and D. Gupta
The Minerals, Metals & Materials Society, 1993

Introduction

The reaction of two adjacent phases, leading to the formation of one or several new phases, is of such general importance that one would expect it to be the object of numerous studies. In fact this is not the case. In only one book [1] is the question discussed in its generality. Initially one finds in the literature two articles [2,3] that treat from a purely mathematical point of view the diffusive growth of several phases simultaneously. In the last fifteen years there appeared a number of publications [4-14] that shall be briefly analyzed here. One may also consult a survey [14] of the reactions of Al with transition metals, and two articles [15,16] where reactive phase formation is discussed in general terms but focused on Al-Ni. The formation of amorphous phases has been the object of much attention [17-20]. Amorphous phases [21] form (by reaction) when the difference in mobilities between the components of a binary phase is large, so that the high mobility of a component allows the phase to grow, whereas the low mobility of the other prevents it from crystallizing; typical of such reactions is the formation of amorphous SiO_2, where the difference in mobilities between Si and O_2 is *astronomical*. The subject is probably more complex: it will not be discussed here. Reference shall be made, however, to a discussion [22] of the nucleation of such phases. Presumed differences between thin film and "bulk" reactions are trivial [13] and hardly deserve discussion. A beautiful study [23] of bulk reaction in the Ag-Zn system shall be mentioned, as well as a study [24] by the same authors of a specific aspect of growth instability. Reaction in ternary systems will not be discussed; readers may consult the literature [9,25,26]. Stresses [27-29] and nucleation[8,22] shall be discussed briefly.

Mathematical Considerations and Consequences

The mathematics of diffusion-controlled growth

The mathematics [2,3] for the simultaneous growths of several layers is complicated. Here, we consider only two layers growing between two elements totally insoluble into each other. Moreover, it shall be assumed that only one, and the same, element is mobile in both of the growing layers; such is the case [30,31] almost precisely during the growth of Ni_2Si and NiSi between Ni and Si at temperatures between 200°C and 400°C. The geometry is shown as in Fig. 1. In the mathematics of diffusion, both phases should start to grow simultaneously at time zero. With A alone moving the reactions would be, for the formation of A_2B, at the A_2B/AB interface:

$$AB + A = A_2B \tag{1}$$

with driving force ΔF_1. For the formation of AB, again at the A_2B/AB interface:

$$A_2B - A = AB \tag{2a}$$

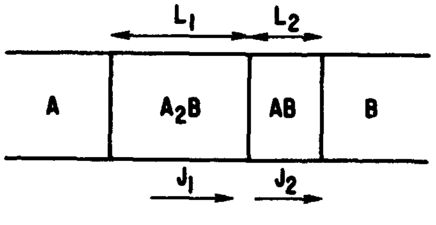

Figure 1 - Schematic representation of the growths of two phases A_2B and AB between the elements A and B.

and at the AB/B interface:

$$B + A = AB \tag{2b}$$

The sum of 2a and 2b gives:

$$A_2B + B = 2AB \tag{2}$$

with driving force ΔF_2. In the examples given the driving forces correspond to the motion of single A atoms. However, one should be careful; this need not be the case for all possible reactions. The fluxes (j_i's) of A atoms in the two phases, written in term of the Nernst-Einstein equation, are:

$$j_i = c_i \times D_i/kT \times \Delta F_i/L_i \tag{3}$$

where c_i is the concentration of A atoms in the respective phases, D_i their diffusion coefficients, and L_i the lengths of the two phases. One should use the exact potential gradient for the moving species inside the respective phases, from one interface to the other, but this is often not available. One should also consider that the D's in Eq. 3 are averaged over the whole composition range for each phase, regardless of how narrow the composition limits might be. For heuristic purposes, the driving forces as defined here can be used, although this is not strictly correct [see 13]. For the lengths, it is clear that the rate of growth of phase 1 should be proportional to j_1 minus j_2 since for every A atom moving through 1 one forms one molecule of A_2B, but for every A atom moving through 2 one destroys one molecule of A_2B. One may then write:

$$dL_1/dt = \alpha/L_1 - \beta/L_2 \tag{4}$$

and

$$dL_2/dt = 2\beta/L_2 - \alpha/L_1 \tag{5}$$

Except for some geometrical factors, α and β are given by Eq. 3. Starting from zero, L_1, L_2 and their sum L will grow as $\sqrt{t}$. According to pure diffusion, phases cannot disappear since if any phase L_i becomes sufficiently small the corresponding dL_i/dt becomes infinitely large. If one were to prepare samples with arbitrary values of L_1 and L_2, Eqs. 4 and 5 define the behavior of the two respective lengths, since they define the respective values of the L_i's for which the phases may grow or not. According to [7] one may represent the situation as described in Fig. 2, where the field defined by L_1 and L_2 is divided into three different areas, M, N and O; these are separated by lines 1 and 2 corresponding respectively to the conditions where dL_2/dt and dL_1/dt are equal to zero. Only in the middle region N would both phases grow simultaneously. In either one of the extreme fields, M and O, one phase would decrease in size (without ever disappearing) while the other would grow. Let us assume that one starts with a sample consisting of A (semiinfinite), A_2B, AB and B (semiinfinite), with the lengths of the two intermediate phases given by point P in domain O (Fig. 2). Phase 1 is sufficiently thick that Eq. 4 is negative; consequently it will shrink, while phase 2 grows. The behavior is described by the curved line with an arrow. As the trajectory crosses into domain N (at Q), the curve becomes vertical since on line 2 dL_1/dt, which may be written as $(dL_1/dL_2) \times (dL_2/dt)$, is equal to zero. From then on the trajectory will tend asymptotically towards line 3. A parallel situation occurs for a sample defined initially by a point in domain M. Starting from the origin, with L_1 and L_2 both equal to zero, the growths of the two phases would occur simultaneously, their ratio would be a constant described by line 3. Because D_1 and D_2 will generally have different activation energies, the behavior may change by simply changing the temperature. Regardless of the starting configuration the respective thickness will evolve towards an asymptotic value shown in Fig. 2 by the dotted line 3:

$$L_1/L_2 = (\alpha - \beta + \sqrt{(\alpha - \beta)^2 + 8\alpha\beta}\,)/2\beta \qquad (6)$$

which tends towards α/β when α is much larger than β.

Setting both Eqs. 4 and 5 greater than zero defines the limits required for the simultaneous growths of the two phases:

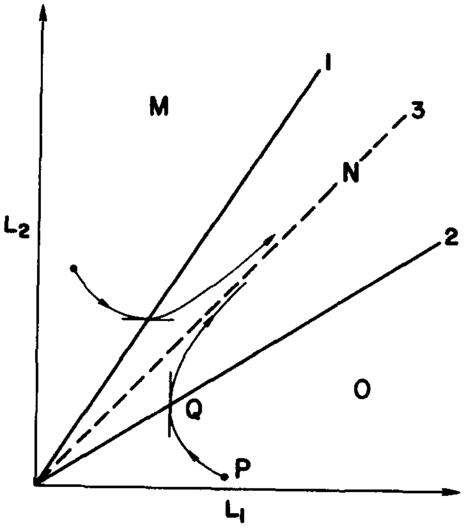

Figure 2 - Plot of the respective thicknesses L_1 and L_2 of phases 1 and 2 growing according to pure diffusion kinetics, from [7].

$$\alpha/L_1 > \beta/L_2 > \alpha/2L_1 \qquad (7)$$

Since generally the geometrical factors and free energy terms that enter into α and β vary little from phase to phase in comparison with the diffusion coefficients, they can be neglected. Then by rearranging the terms, the relations in 7 can be written as:

$$L_2/L_1 > D_2/D_1 > L_2/2L_1 \qquad (8)$$

The lengths of the different layers scale linearly with their respective diffusion coefficients and not, as could be anticipated given the relationships as $\sqrt{t}$, as the square root of these coefficients. As a consequence if D_1 and D_2 are in the ratio of 1000/1, when the one layer would have grown to 100 nm, the other would remain below 0.1 nm, in practice it would not exist. Until phase 2 (AB) begins to be physically present, phase 1 (A_2B) would not have grown as in Eq. 1 but as:

$$0.5B + A = 0.5A_2B \qquad (9)$$

with a corresponding free energy change per mobile A atom of $\Delta F_1'$, greater than ΔF_1. Mathematically as a first approximation, D_1 would remain the same; physically things could be quite different since to the change being considered would correspond a change in concentration limits, which could greatly affect the diffusion coefficient. Thus in multiple phase growth, the initial growth of the first phase should be especially fast, not only because in Eq. 4 the negative term is absent, but also because an increase in the driving force leads to a high value of α. When the square of the measured thickness is plotted as a function of t, a straight line drawn through the data points intercepts the time axis at a positive value (the so-called incubation time), which reveals that phenomena other than diffusion control the initial period of growth.

Experimental evidence

In order to illustrate the above formalism, one may chose the rather extreme example of the formations of W_5Si_3 and WSi_2. In thin film experiments [32,33] at temperatures below 1000°C, and reactions [34,35] carried out at higher temperatures, one observes only WSi_2, not W_5Si_3. The respective activation energies [34,35] are 3.7 eV and 2.1 eV. Assuming equal preexponential factors, at about 1225°C the ratio of thicknesses for W_5Si_3 and WSi_2 would be 10^{-5}, i.e. when WSi_2 would be 10 μm thick, W_5Si_3 would remain of the order of 0.1 nm, and that ratio would be even smaller at lower temperatures. The same observations would apply for $MoSi_2$, Mo_5Si_3, and Mo_3Si, with respective activation energies reported [34,35] as 2.2 eV, 3.7 eV and 3.4 eV. The disilicides only should be observed in thin film experiments with metal thickness less than 100 nm and low temperatures. In "bulk" experiments several phases will be observed only at very high temperatures, if the experiments are conducted for long periods of times, and if the techniques for detecting the minor phases are more sensitive than those employed for measuring the growth of the major phases. Detection sensitivity is a major cause of alleged differences between thin film and bulk experiments. It may be a problem the whole family of reactions of V, Nb, Ta and Cr with Si, where only the disilicides are usually observed.

Self Regulation

One aspect of phase formation, perhaps unexpected, that follows from Eqs. 8 is the self-regulatory character of multiple phase growth. Since the lengths are inversely proportional to the diffusion coefficients, the gradients of free energy $\Delta F_i/L_i$'s will be inversely proportional to D_i's, and consequently the j_i's nearly equal to each other. This is physically mandated by the requirement that for phase growth to occur, as dictated by the overall decrease in free energy of the system, atoms leaving from either one of the two sources, A or B, must in some way reach the other. The situation is clearer in the case of a single phase with a diffusion coefficient that varies with composition. Then the flux must be constant from one end of the phase to the other, since there cannot be any creation of new lattice sites except at the interfaces. Thus, with j equal to the product D dc/dx being constant, in regions where D is small the gradient will be big, which is obtained by the relatively slow growth of the corresponding physical regions [see 19]. Multiple phase growth behaves in a similar fashion.

First phase formed, a theoretical point.

The free energy of formation of phases from reaction between elements is usually high enough so that nucleation is easy and does not contribute to a rate controlling factor. This should be reconsidered for ordered phases with low critical temperatures. To this observation one should add that when several phases are possible, their free energies of formation from the elements do not vary much from phase to phase; factors of 10 are certainly quite rare. On the other hand, diffusion coefficients are expected to vary widely. Thus in the competition between several phases, as defined by Eqs. 3 and 9, it is anticipated that the first phase formed should be the one with the highest diffusion coefficient. The choice is determined by kinetic factors rather than thermodynamic ones.

Competitive growth, Nernst-Einstein's versus Fick's law.

An interesting analysis [24] of instabilities is based entirely on diffusion kinetics. In Fig. 3, phase 1 has grown to a length L'_1 according to a relation such as in Eq. 9. At that time phase 2 starts forming, most likely locally and not as a continuous layer as considered up to now. Its thickness must be some minimum L_2 or it would be subcritical and dissolve. There are now two different conditions at the two interfaces with B.

a) The interface A_2B/B will move as:

$$dL'_1/dt = \alpha'/L'_1 \tag{10}$$

where α'_1 corresponds to ΔF_1 (Eq. 9, greater than ΔF_1 from Eq. 1).

b) The motion of the interface AB/B will be given by the sum of Eqs. 4 and 5, namely:

$$dL/dt = dL_1/dt + dL_2/dt = \beta/L_2 \tag{11}$$

Comparison of Eqs. 10 and 11 shows that there will exist conditions such that the interface A_2B/B will move faster than the interface AB/B. Consequently the nascent AB phase embryos would become buried into A_2B and are therefore unstable. Thus, otherwise simple diffusion kinetics may lead to different results depending on whether the layers are continuous or not.

All diffusion equations above are written according to the Nernst-Einstein equation rather than according the more universally accepted Fick's law. There are several advantages to such a procedure. Let us remark here that when writing the equations for multiple phase growth using Fick's law, one ends up with the factors Δc_i, corresponding to the limits of concentrations for the various phases. Consequently the literature contains numerous statements to the effect

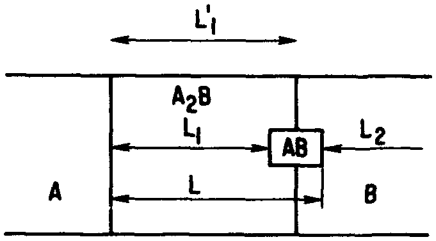

Figure 3 - Sketch illustrating the first stage of formation of the new phase AB at the interface A_2B/B.

that phases with broad concentration limits should grow fast. This is wrong! The driving forces for diffusion are the respective chemical potentials; these do not vary in proportion to the concentration limits.

Interface Reaction Rates and Critical Phase Lengths

Diffusion equations predict infinitely fast rates for thin layers. Physically this is impossible. Indeed, careful plotting of growth data [e.g. Ru_2Si_3, 36] reveals that the initial rate of phase growth is smaller than what ensues from a $t^{1/2}$ dependence. One may assume, that at the beginning growth occurs as $K \times t^1$, and call K the interface reaction rate, even if one does not have a precise idea of what the term implies [as pointed out in 13,19]. This leads to linear-parabolic kinetics initially defined by Evans [37], expressed as:

$$L^2 + A \times L = B \times t \tag{12}$$

from which one extracts the values of K equal to B/A, and "α" equal to B, the reaction and diffusion rate constants.

The consequences of linear-parabolic kinetics on sequential phase formations have been the object of several analyses [4,5,11,12]. For small values of L_2, j_2 cannot become infinite but must be limited to a finite value, proportional to K_2. Equation 5 then becomes:

$$dL_2/dt = 2K_2 - \alpha/L_1 \tag{13}$$

For this term to be positive, namely for phase 2 to start growing, L_1 must exceed a value L_{1c} given by:

$$L_{1c} > \alpha/2K_2 \tag{14}$$

If the reaction rate K_2 is extremely rapid, L_{1c} will tend towards zero, so that phase 2 will start growing immediately, as given by pure diffusion kinetics. Reference to Eq. 13 explains why L_{1c} should be proportional to ΔF_1 and D_1 (α); because after (and at) the birth of phase 2, phase 1 consumes phase 2. Equation 13 is valid only for small values of L_2. The general formulation [13,16] for Eqs. 4 and 5 becomes:

$$dL_1/dt = \alpha/(L_1 + \alpha/K_1) - \beta/(L_2 + \beta/K_2) \tag{15}$$

and

$$dL_2/dt = 2\beta/(L_2 + \beta/K_2) - \alpha/(L_1 + \alpha/K_1) \tag{16}$$

The authors of Ref. 10 emphasized that Eqs. 15 and 16 are equivalent to Eqs. 4 and 5, simply with a translation of the origin for L_1 and L_2. This allows one to plot L_1 and L_2, as in Fig. 2, but with the configuration found in Fig. 4. Depending on the values of the different parameters there are three possible cases, a) the one shown in Fig. 4, b) one in which the origin would be found between lines 1 and 2, and c) by symmetry with a, one in which both lines 1 and 2 would intercept the vertical axis. With cases a (Fig. 4) and c, and starting with phases of arbitrary thickness, there exist conditions where one of the phases would actually disappear, which is illustrated by the cross-hatched region in Fig. 4. The discussion on the trajectory for phases of arbitrary thickness in Fig. 2 remains essentially valid here. Starting from the intersection of line 1 with the L_1 axis (at R) and working backwards (decreasing L_1), one can follow a trajectory that must be tangent at the point of intersection and go up for smaller values of L_1 and larger ones (positive) for L_2. That circumscribes the hatched domain within which

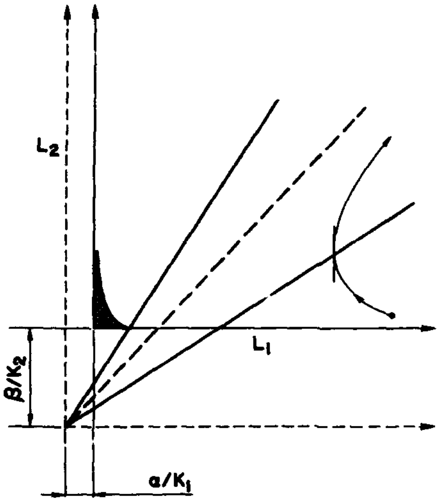

Figure 4 - Plot of the respective thicknesses L_1 and L_2 of phases 1 and 2 growing according to linear-parabolic kinetics (with finite reaction rates, K_1 and K_2), from [10].

phase 2 would actually disappear. Starting from the origin, with L_1 and L_2 equal to zero, phase 1 alone would grow until the critical length L_{1c} is reached, at which point phase 2 also would start growing; the trajectory should move towards the dotted line from then on. Under the conditions described here a phase might actually disappear, which is in contradistinction with what can happen with pure *diffusion kinetics; then phases may be reduced in size* but not actually cease to exist. As one might have expected, phase disappearance would occur only for relatively thin layers. Physically, such disappearance would be enhanced by the fact that sufficiently thin layers are thermodynamically unstable [8]. For thick layers and long times, the kinetics become indistinguishable from pure diffusion: the respective phase lengths approach the values given by the dotted line in Fig. 4. The existence of critical values, L_{ic}, dictates that phases should appear sequentially (equally in "bulk" and thin film experiments).

Is there much experimental evidence for such behaviors? The answer to this question should remain ambiguous, because the concept of interface reaction is poorly defined. Here, a the definition has been eluded, simply by saying that diffusion fluxes cannot become infinitely fast even for infinitely small layers. Observations of the initial stages of phase growth remain poor. In the one well documented case [38] of linear-parabolic growth, that of SiO_2, precise measurements show that the initial growth [39,40] does not actually fit on the curve. Undoubtedly many cases of initial "incubation" times are not due to limited reaction rates, but to impurities, oxide or other substance, at the original interface. An argument based on this idea loses weight, however, when referring not to the first phase formed, but to the subsequent ones, when impurities at the original interface should play an increasingly minor role. New ideas and observations [22,41] about the beginning of phase growth remain to be generalized, and incorporated into overall kinetic equations. It is this author's opinion that interface reaction plays a significant role in phase growth. The evidence seems overwhelming. 1) To begin with, the argument about the impossibility of infinitely fast diffusion appears logically incontrovertible. 2) One encounters accounts of phase disappearance. In order to be meaningful the examples must be such that the sources (for elements A and B) have not been exhausted. 3) In thin film experiments, the various phases appear one at a time, since quite often at least one of the two reactants is present in amounts so small that obtaining phases of thickness equal to or greater than L_{1c} is impossible. (Scant transmission electron microscopy in cross section, now available with atomic level resolution, fails to reveal the presence of embryonic "missing" phases at interfaces). 4) There are several examples of sequential phase formation reported in "bulk" experiments when the observations are made with sufficient care, namely: a) Fe-Zn [42] where phases of increasing Fe content form at intervals with remarkable regularity. b) For Ag-Zn, the proper kinetic equations reported in [23] show that the phases do not start to grow simultaneously. c) Sequential phase growth was reported quite long ago in the formation [43] of complex oxides from the reaction of simple oxides. 5) As already noted, the initial stage of phase growth usually proceeds at a rate smaller than dictated by diffusion alone, namely with an exponent of t greater than 0.5 [36].

The presentation of the problem here, using only one moving species and only two intermediate phases, and reducing the question of interface reaction to a lower limit for diffusion fluxes, is an oversimplification. A greatly more detailed study is available in [12]. What is the actual magnitude of L_{ic}? It will vary of course from system to system, and for a given system it will change with temperature. From Eq. 14 we note that L_{ic} varies as the corresponding D_i, and therefore as the activation energy for this term. However, in the absence of any proper physical understanding of K and of its potential activation energy, it is impossible to estimate how L_c should vary as a function of temperature. Consider some experimental examples: a) In Ni-Si reactions for the transition from Ni_2Si to NiSi, L_{1c} is undoubtedly greater than 400 nm in the usual range of reaction temperatures 300°C - 400°C [44,45]. It has been shown [46] to be as big as 25 μm at 600°C in lateral diffusion experiments. The corresponding critical length, however, is certainly quite smaller in the similar transition between Co_2Si and CoSi. Thus, while it is relatively easy to form by metal-silicon reaction a film of pure Ni_2Si, it is rather difficult to form one of pure Co_2Si free of the presence of CoSi. b) Again, in lateral diffusion samples [47], at 280°C about 5 μm of Cu_3Si have to form before $Cu_{15}Si_4$ becomes detectible. c) For Fe-Zn reactions at 385°C, the photographs published in [42] yield values of L_c of the order of some 600 nm for the different phases. Thus, while the initial stage of phase formation remains to be properly explored, the available experimental evidence points to the existence of initially slow growth, modulated by some process akin to interface reaction. Multiple phases appear sequentially. Before leaving this topic, let us note that during the initial stages of growth when reaction rates play a significant role in the kinetics, the concentration limits of the various phases are reduced to values within those reported in equilibrium diagrams.

Dominant moving species.

A common question asked about the formation of a new phase is: Which is the dominant moving species? In "bulk" experiments, and with phases with sufficiently broad composition limits, it is possible with care to use classical evaluations including the determination of the Matano interface and its motion. Examples are found in [23] for Ag-Zn reactions, and [48] on Al-Ni. In thin films such precise analysis is impossible; one must content oneself with an overall measurement of the motion of deposited or implanted markers [see 8,44,49]. Marker displacement shows that one component of the intermetallic compound diffuses at a rate that is at least ten to twenty times greater than the other, but do not provide any estimate of the upper limit. A better evaluation of the difference has been obtained [8] with bilayers of similar elements: e.g. Mo and W on Si. The isomorphous disilicides are formed as usual at about 600°C-700°C, but after formation the two silicides remain quite distinct. Mixing of the metal atoms requires temperatures in excess of 1000°C, that shows at once that the silicides are formed by Si motion, and that the metals are greatly less mobile than Si. The same procedure can be used with oxides [21] where oxygen is the dominant moving species.

Attempts have been made to use kinetic data to decide whether growth occurs via grain boundary or lattice diffusion [50-52]. Unfortunately, it has been shown [53,54] that it is nearly impossible to differentiate these mechanisms except in the case of SiO_2 [55]. To distinguish between the modes of diffusion, one needs to study "bulk" samples and compare the growth data. In the case of Ni_2Si, it has been possible to attribute growth to grain boundary diffusion [56]. Space limitations prevent one to go into further detail; relevent information can be found in [57-61]

The Ordered Cu_3Au Rule and its Corollaries

The rule, respective mobilities of majority and minority atoms in compounds.

Except for SiO_2 and other such inordinately opened structures, and for interstitial [62] compounds, and Hägg [63] phases, diffusion in intermetallic compounds results almost always from vacancy [58,64] mechanisms. In compounds such as A_mB_n, with m/n greater than 1, the A atoms should diffuse faster than B's if there exists a continuous network of A lattice sites on which "A" vacancies can be propagated without disturbing the overall crystal structure. On the contrary, if there exists no such network for the B atoms, their diffusion will require either the local destruction of the ordered structure or the coincidence of two vacancies (on the A and B sublattices); this will also require some additional activation energy as compared to the diffusion of A. The excess should be commensurate with the formation energy of the compound. This is found for $AlNi_3$ [16,65]. Therein, the activation energies for the diffusion of Co and Cr (which diffuse on the Ni sublattice), are 325 kJ/mol and 366 kJ/mol, respectively; however, for Ti (which substitutes for Al) the value is 468 kJ/mol. The difference is comparable to the heat of formation [66] of $AlNi_3$, 150 kJ/mol of Al (or $AlNi_3$). The ensuing Cu_3Au rule (after the well known $L1_2$ structure), states [8] that in intermetallic compounds, the majority atoms A diffuse faster than those of the minority component. The reliability of the rule will vary as m/n differs from 1. It is probably always valid for m/n equal to, or greater than 3. For m/n equal to 2 the situation becomes ambiguous already. In structures [67] such as those going from $TiSi_2$ to WSi_2, all the metal atoms are totally isolated from each other; consequently, growth always occurs via Si atom motion [8,49]. In order to achieve similar mobilities for the metal atoms, much higher temperatures are required. However, in [68] structures such as Al_2Cu, Mg_2Cu, and Mg_2Ni, where continuous chains [69] of Cu and Ni atoms exist, both species are found to be mobile during growth from metal-metal interaction. In equiatomic compounds, of type AB, one does not expect the diffusion of either species to be favored. As a matter of fact as compared to compound of the type A_mB_n, diffusion in AB compounds should be relatively difficult(barring the effects of constitutional defects as encountered in ALNi and CoGa). In general the Cu_3Au rule depends only on local atomic environment, and as such applies independently of crystal symmetry. Thus, in the quasicrystals[72,73] Al_4Mn and Al_4Fe, Al atoms constitute the fast diffusing species. For a recent compilation of data on diffusion in intermetallic compounds consult[70]. Since the activation energy for the motion of the minority atoms should be equal to that corresponding to the majority atoms plus a fraction of the heat of formation of the compound, the rule should become less and less valid as the interaction between elements becomes weaker, and as the heat of ordering becomes smaller. It ceases to have any validity when the phases are not ordered, as is apparently the case in the Cu-Ge system for the phase most rich in Cu (besides the terminal solid solution), an hexagonal phase that forms [71] by the joint motion of the two elements.

Corollaries, order of phase formation.

In compounds where elements of the majority atoms form a continuous network, the diffusion of these atoms should have characteristics approaching those of the pure elments. In Ni_3Al , for example, diffusion of Ni has nearly the same activation energy [58,70,74] as in pure Ni, about 300 kJ mol^{-1}. Consider now reactions between elements A and B in which A has a significantly lower melting point than B. Given that the first phase formed should be one with the highest diffusion coefficient, that phase is likely to be the one with the highest content in A. There are many examples to confirm this. We have already mentioned the Fe-Zn [42] reactions. There are numerous reactions [14] between Al and transition metals; the first phases formed are such as $NiAl_3$, Co_2Al_9, Cr_2Al_{13}, $TiAl_3$, $MoAl_{12}$, $NbAl_3$ [75], $ZrAl_3$, WAl_{12}, $TaAl_3$, and $HfAl_3$. To these one may add [76,77] $CuAl_2$ and Ir_2Al_9. Experimental evidence implies that $NiAl_3$ forms from the very beginning on an atomic scale[78]. In Cu-Mg [79] reactions, Mg_2Cu forms before $MgCu_2$, as in Ni-Mg [69] Mg_2Ni. Other examples of first phase formed include $AuGa_2$ [80,81], $PtHg_4$ [82], $AgIn_2$ [83], $PdSn_4$ [84], Ni_3Sn_4 [85], $NiCd_5$ [86], $PdCu_3$ and $PtCu_3$ [87], and probably $FeSn_2$ [88], or in Ag-Hg the γ phase with a composition close to Ag_2Hg_3 [89]. In a series of reactions [90] between Au and transition metals, the first phases formed were those with the highest Au content. However, in Au-Pb reactions [91] the first phase formed is Pb_2Au; in Pb-Pt reactions [91], it is Pb_2Pt.

There follow some corollaries to the ordered Cu_3Au rule and its applications to the prediction of the first phase formed. 1) In general, the majority atoms will constitute the dominant moving species in the first phase formed. This is not a matter of cause and effect, as sometimes implied. Rather, the structural similarity between element A and compounds rich in A dictates that, if A has a low melting point, atoms of A will have high diffusion coefficients in A-rich compounds, decreasingly from phase to phase with decreasing concentrations of A. 2) Although changes in structure may effect diffusion coefficients unpredictably, we expect that compounds of the form A_mB_n will form in order of decreasing m/n ratios. A beautiful example of such a sequence is the Fe-Zn [42] reaction where the phase ζ with 7 at% Fe forms first, followed by δ and Γ with 8-13 at% and 23 at% Fe, respectively. Moreover, Kirkendall voids [92] reveal that growth occurs via the motion of Zn atoms. Reference [93] states "the first compound is formed directly from the starting metals, the second is formed by the reaction of the first compound with the excess of the high-melting metal, and the third by the reaction of the second compound with the excess of the high-melting metal". This is in agreement with the analysis presented here.

Exceptions to the Cu_3Au rule and its corollaries.

Exceptions to these rules are interesting for they suggest importance of other physical phenomena. An exception to the Cu_3Au rule is encountered in the formations of the isomorphous $NiSi_2$ and $CoSi_2$, CaF_2 structure, where the metal atoms have been found [94,95] to be more mobile than the majority Si atoms. Failure of the rule here is related to the open structure, with coordination number 4 for Si, and to the absence of metal atoms in 4 of the 8 lattice sites available in the unit cell; thus the diffusion process is not likely to be a simple vacancy mechanism.

A striking exception, in Au-Al [96] interactions, is the initial formation of Au_2Al rather than the aluminum-rich compound $AuAl_2$. We expect this related to anomalously high melting temperature of $AuAl_2$, 1060°C. Another exception is Al-Fe, where the first phase to form would be anticipated to be the aluminum-rich Al_3Fe, although some other phase is usually observed [13,73]. The aluminum-rich compounds formed with transition elements of the fourth period exhibit a curious regularity: Al_2Cu, Al_3Ni, $Al_{4.5}Co$, Al_3Fe, Al_6Mn, Al_7Cr, and $Al_{10.5}V$. Clearly, Al_3Fe does not fit in the series. Several stable compounds richer in Al than Al_3Fe, such as Al_6Mn of Mn structure, or the quasicrystal Al_4Fe have high mobilities of Al atoms which is in full agreement with Cu_3Au rule. On the other hand, there are also Al atom deficient stable compounds, such as $Al_{2.5}Fe$[97] which show large atomic mobilities due to a different reason namely the presence of high density(16%) of constitutional vacancies on the Al sublattice. However, stable phases have relatively close compositions, minor structural details can affect considerably the respective mobilities. In such cases, the corollaries to the Cu_3Au rule (although not the rule itself) should fail quite frequently. Impurities can affect the order of phase formation and cause apparent failure of the rules formulated here. Sometimes that can be attributed to gross modifications of thermodynamic factors, specially where the activity of one of the reactants is particularly liable to be lowered by impurities: such are Al and Si in the presence of oxygen [16].

Lattice and grain boundary diffusion in intermetallic compounds, mechanisms.

The ordered Cu_3Au rule is conceived in terms of vacancy diffusion on crystalline lattices. It is remarkable that it seems to apply to solid interactions regardless of temperature, especially since many of the observations on first phase formation are made with thin films after reactions at quite low temperatures where one expects grain boundary diffusion to be dominant. Unfortunately while data on lattice diffusion in intermetallic compounds are beginning to accumulate, precise information about grain boundary diffusion in these compounds is hardly existent. So one is limited to generalizations based on phenomenological observations. The presently noted validity of the Cu_3Au rule and its corollaries in low temperature reactions implies that the processes of grain boundary diffusion are not too different from those in the lattice. A case in point is the similarity of diffusion profiles in Al-Ni, regardless of whether the reactions are carried out at temperatures [48] above 1000°C, or at much lower temperatures [98] 220°C. In particular the very curious and characteristic profiles of the NiAl phase are the same [analyzed in detail in 15], although through this large temperature range the relative contributions of lattice and grain boundary migrations should vary considerably. Indeed, the similarities of the complex profiles implies that the lattice and grain boundary diffusion coefficients for NiAl vary in the same way as a function of composition. In many pure metals it is now known [99] that both transports, in the lattice and along grain boundaries, occur via vacancy mechanisms. The extension of this observation to intermetallic compounds justifies the ordered Cu_3Au rule even where grain boundary diffusion predominates. In a Zr matrix, Co and Fe atoms diffuse [100] via interstitial mechanisms both in the lattice and in grain boundaries. In matrices where lattice diffusion involves anomalously fast processes, the same is observed [105] for the grain boundaries. In NiO [101], Ni is a faster diffuser than oxygen both in the lattice and along grain boundaries; the respective diffusion coefficients vary in the same way as a function of O_2 pressure. In Cr_2O_3 it [103] on the contrary, oxygen diffuses faster than Cr, both in the lattice and along the grain boundaries; diffusion does not depend on the O_2 pressure. Oxygen diffusion in the lattice and in the grain boundaries of $Cu_{2-x}O$ proceeds via the same interstitial mechanism [104]. In general it seems, grain boundary diffusion follows approximately the same modalities as lattice diffusion. In ordered compounds this effect should be even more pronounced since grain boundaries must necessarily adopt a configuration close to that of the lattice, for were it not so the grain boundary energies would become enormous.

Nucleation

When A reacts with B to form some A_mB_n the free energy change ΔF is usually sufficiently big that as a first approximation one may ignore nucleation effects. However, the subsequent formation of new phases, let us say richer in B, occurs by the reaction of A_mB_n with B. The process can go on until one reaches some A_rB_s where ΔF changes sign, then A_rB_s ceases to be stable, and under normal circumstances will not form at all. However, the formation of the preceding phase A_pB_q, will be accompanied by a ΔF of the right sign (negative), but its magnitude may be very small. A decreasing ΔF with increasing amounts of either A or B, is a fundamental feature of chemical systems. Then, because for small thickness of A_pB_q the overall gain in free energy is smaller than the energy required to create an extra interface, nucleation can be extremely difficult and become rate controlling. Examination of the activation energy for nucleation, of the form $\Delta\sigma^3/\Delta F^2$ (where $\Delta\sigma$ is the increase in surface energy) makes this immediately clear. The modalities of such phase formation have been explored in a series [8,105] of publications. For the first one or two phases to grow this behavior is usually not found, which justifies one's neglect of nucleation effects. The situation, however, may not be so simple. There is evidence [41] that interface reactions may often begin with the nucleation of some metastable, amorphous phase (because the interface energies would be smaller for amorphous phases than for crystalline ones). A recent analysis [22] reveals that such initial nucleation would not fundamentally affect the order of phase growth proposed above. Diffusion rather than nucleation is the dominating factor. Stresses [see 27-29,106] should affect the kinetics of phase formation, either by modification of the chemical potential terms in the Nernst-Einstein equation, and perhaps more fundamentally by changing the equilibrium conditions between stable and metastable phases. Calculations of stresses during phase growth are complex and are unfortunately marred by a totally erroneous discussion of nucleation in the literature. The truly detailed analysis of the relationship between stress and phase growth are essentially limited to SiO_2 [29,107,108-110] but its discussion is beyond the scope of this article. Interested readers may consult a few other publications [111-113]

Conclusions and Summary

1) Analysis of diffusion equations provides the relations between thickness, diffusion coefficients, and free energy changes that govern the "mathematical" growths of several phases: a) If one starts from zero, all phases should grow in proportion to $\sqrt{t}$. b) The ratios of the various thickness should remain constant. The exact function is complicated but surprisingly the ratios should vary nearly as the respective diffusion coefficients rather than their square roots. c) According to diffusion equations alone, phases of arbitrary thickness can decrease in thickness but should never disappear (mathematically! Physically things may behave differently since sufficiently thin layers cease to exist).

2) Introducing the simple physical condition that a phase does not really exist before its thickness reaches several Å, immediately complicates the kinetics for the other phases. Thus: a) a small modification of "pure" diffusion conditions introduces the notion of sequential phase formation, and b) since the rate of growth of a phase should decrease as the number of "existing" phases increases, the absence of experimental observations revealing initially (at time $t = 0$) rapid growth implies that factors other than diffusion control the very first stage of phase formation.

3) Even simple diffusion kinetics may lead to unstable conditions if some of the growing layers are not continuous.

4) With the introduction of interface reaction rates, the simple $\sqrt{t}$ kinetics become modified to linear-parabolic.

5) When growth is controlled initially by interface reaction rates, new phases appear only after other phases have reached a critical thickness. This results in the sequential phase formation which is usually observed when experiments are conducted with sufficient care. Contrary to what follows from pure diffusion kinetics, when growth becomes a function of interface reaction rates thin phases of arbitrary thickness may actually disappear for purely kinetic reasons.

6) Although the values of the critical thickness that must be reached by one phase before another one can appear will vary from system to system, physical examples of values equal to or greater than 500 nm are found.

7) According to the ordered Cu_3Au rule, in binary compounds the atoms of the majority elements should diffuse faster than those of the minority. This will be generally true when the ratio of concentrations is greater than 3 to 1, but may be valid also for ratios of 2 to 1.

8) Where several phases may form, the order of phase formation is likely to be dictated by kinetic rather than thermodynamic factors. According to the ordered Cu_3Au rule and its corollaries, when two metals with different melting points react with each other, the first phase formed should contain the maximum concentration of the metal with the lowest melting point. Ipso facto in that phase, atoms of the low melting metal should constitute the dominant diffusing species. Both statements are usually valid. One may want to go further and consider the sequence of phases that grow consecutively: they should contain increasing amounts of the metal with the high melting point (e.g. in Fe-Zn reactions).

9) Exceptions to rules 7 and 8, deserve attention. They may be due to anomalously high melting points (Al_2Au), to special structural details (Mg_2Cu, Mg_2Ni, or $NiSi_2$ and $CoSi_2$), or to the presence of constitutional defects (e.g. $FeAl_3$ and $FeAl_{2.5}$).

10) When the free energy change upon the formation of a new phase becomes small (of the order of 50 cal/cm^3) nucleation becomes difficult, and at low temperature may prevent the formation of such phases. This is usually not important for the first few phases to form. However, should one want to penetrate the intricacies of initial phase formation, other more subtle nucleation effects might be important.

11) Stresses should play a role in reaction kinetics. Except for the thermal oxidation of silicon, there appears to be little of a quantitative nature to report.

Acknowledgements

Part of this publication was presented at a summer school on thin films in Hämenlinna, Finland, June, 1992. The author is greatly indebted to coworkers in the field of interface reactions, V. I. Dybkov, P. Gas, D. Gupta, C. S. Petersson, J. Philibert, L. Stolt, O. Thomas, Shi-Li Zhang, and many others.

References

1. H. Schmalzried, *Solid State Reactions*, Verlag Chemie, Weinheim, 1981.
2. G. V. Kidson, J. Nucl. Materials 1961, 3, 21.

3. C. Wagner, Acta Metall., 1969, **17**, 99.
4. U. Gösele and K. N. Tu, J. Appl. Phys., 1982, **53**, 3552. 3552.
5. F. M. d'Heurle and P. Gas, J. Mater. Res., 1986, **1**, 205.
6. U. Gösele, in *Alloying*, (Edited by J. L. Walters, M. R. Jackson, and C. T. Sims), ASM International, Metals Park, Ohio, 1988, p. 489.
7. W. C. Johnson and G. Martin, Solid State Phenomena, 1988, **3**(4), 247.
8. F. M. d'Heurle, J. Mater. Res., 1988, **3**, 167.
9. F. J. J. van Loo, Prog. Solid St. Chem., 1990, **20**, 47.
10. W. C. Johnson and G. Martin, J. Appl. Phys., 1990, **68**, 1252.
11. J. Philibert, *Atom Movements: Diffusion and Mass Transport in Solids*, Les Editions de Physique, Les Ullis, 1991, see p. 421 and ff..
12. V. I. Dybkov, J. Phys. Chem. Solids, 1992, **53**, 703.
13. F. M. d'Heurle, IBM Research Report, 1992, RC 18152.
14. E. Colgan, Mater. Sci. Rep., 1990, **5(1)**, 1.
15. F. M. d'Heurle and R. Ghez, Thin Solid Films, 1992, **215**, 19.
16. F. M. d'Heurle and R. Ghez, Thin Solid Films, 1992, **215**, 26.
17. K. Samwer, Physics Reports (Review Section of Physics Letters), 1988, **161(1)**, 1.
18. See *Phase Transformation Kinetics in Thin Films*, M. Chen, M. Thompson, R. Schwartz, and M. Libera, eds., (MRS Symp. Proc., vol. 230), Mater. Res. Soc., Pittsburgh, 1992.
19. A. M. Gusak and K. P. Gurov, Solid State Phenomena, 1992, **23&24**, 117.
20. P. J. Desré and A. R. Yavari, J. Alloys Compounds, 1992, **188**, in print.
21. O. Thomas, F. M. d'Heurle, and A. Charai, Philos. Mag., 1988, **B 58**, 529.
22. C. V. Thompson, J. Mater. Res., 1992, **7**, 367.
23. D. S. Williams, R. A. Rapp, and J. P. Hirth, Metal. Trans., 1981, **A 12**, 639.
24. D. S. Williams, R. A. Rapp, and J. P. Hirth, Thin Solid Films, 1986, **142**, 47.
25. J. A. van Beek, P. M. T. de Kok, and F. J. J. van Loo, Oxid. Metal., 1984, **22**, 147.
26. F. J. van Loo, J. van Beek, G. Bastin, and R. Metselaar, Oxid. Metal., 1984, **22**, 161.
27. e.g. W. Nix, J. Bravman, E. Arzt, and L. Freund, eds., *Thin Films: Stresses and Mechanical Properties III*, (MRS Symp. Proc., vol. 239) Mater. Res. Soc., Pittsburgh, 1992.
28. D. L. Beke, L. Koćky, I. Gödény, and F. J. Kedves, Defects and Diffusion Forum, 1989, **66-69**, 1357.
29. J. K. Srivastava and E. A. Irene, J. Electrochem. Soc., 1985, **132**, 2815.
30. W. K. Chu, H. Kräutle, J. W. Mayer, H. Müller, M.-A. Nicolet, and K. N. Tu, Appl. Phys. Lett. 1974, **25**, 454.
31. T. G. Finstad, phys. stat. solidi, 1981, **a 63**, 223.
32. A. Sinha and T. Smith, J. Appl. Phys., 1973, **44**, 3465.
33. L. D. Locker and C. D. Capio, J. Appl. Phys., 1973, **44**, 4366.
34. P. R. Gage and R. W. Bartlett, Trans. Metall. Soc. AIME, 1965, **233**, 832.
35. R. W. Bartlett, P. R. Gage, and P. A. Larssen, Trans. Metall. Soc. AIME, 1964, **230**, 1528.
36. C. S. Petersson, J. E. Baglin, J. J. Dempsey, F. M. d'Heurle, and S. J. LaPlaca, J. Appl. Phys., 1982, **53**, 4866.
37. C. J. Evans, *The Corrosion and Oxidation of Metals: Scientific Principles and Practical Applications*, Edward Arnold, London, 1960, p. 826.
38. B. E. Deal and A. S. Grove, J. Appl. Phys., 1965, **36**, 3770.
39. A. S. Grove, *Physics and Technology of Semiconductor Devices*, John Wiley, New York, 1967, p. 31.
40. H. Massoud, J. D. Plummer, and E. A. Irene, J. Electrochem. Soc., 1985, **132**, 2685.
41. L. A. Clevenger and C. V. Thompson, J. Appl. Phys., 1990, **67**, 1325.
42. D. I. Harvey and G. J. Cameron, J. Australian Inst. Met., 1969, **14**, 255.
43. P. P. Budnikov and A. M. Ginstling, *Principles of Solid State Chemistry*, MacLaren and

Sons, London, 1968. p. 144.
44. K. N. Tu and J. W. Mayer, in *Thin Films: Interdiffusion and Reactions*, J. M. Poate, K. N. Tu, and J. W. Mayer, eds., John Wiley, New York, 1978, p. 359.
45. F. M. d'Heurle, C. S. Petersson, J. E. E. Baglin, S. J. LaPlaca, and C. Y. Wong, J. Appl. Phys., 1984, **55**, 4208.
46. R. Zheng, L. S. Hung, and J. W. Mayer, J. Vac. Sci. Technol., 1983, **A 1**, 758.
47. S. Q. Hong, C. M. Comrie, S. W. Russell, and J. Mayer, J. Appl. Phys., 1991, **70**, 3655.
48. S. Shankar and L. L. Siegle, Metall. Trans., 1978, **9 A**, 1467.
49. M.-A. Nicolet and S. S. Lau, in *VLSI Electronics, Microstructure Science, vol. 6*, N. G. Einspruch and G. B. Larrabee, eds., Academic Press, New York, 1983, p. 330.
50. J. P. Stark, Acta Metall., 1983, **31**, 2083.
51. El-Saied M. Aly and J. P. Stark, Acta Metall., 1984, **32**, 907.
52. B. S. Lim and J. P. Stark, Acta Metall., 1984, **32**, 915.
53. P. Gas, C. Zarin, B. Swensson, M. Östling, C. S. Petersson, and F. M. d'Heurle. J. Appl. Phys., 1990, **67**, 2390.
54. S.-L. Zhang, F. M. d'Heurle, and P. Gas, Appl. Surf. Sci., 1990, **53**, 103.
55. E. Rosencher, A. Straboni, S. Rigo, and G. Amsel, Appl. Phys. Lett., 1979, **34**, 254.
56. J. C. Ciccariello, S. Poize, and P. Gas, J. Appl. Phys., 1990, **67**, 3315.
57. A. Atkinson and R. I. Taylor, Philos. Mag., 1979, **A 39**, 581.
68. H. Bakker, in *Diffusion in Crystalline Solids*, G. E. Murch and A. S. Novick, eds., Academic Press, New York, 1984, p. 189.
59. N. L. Peterson, in *Grain Boundary Structure and Kinetics*, American Society for Metals, Metals Park, Ohio, 1980, p. 209.
60. T. G. Finstad, Thin Solid Films, 1978, **51**, 223.
61. M. M. P. Janssen, Met. Trans., 1973, **4**, 1623.
62. H. J. Goldschmidt, *Interstitial Alloys*, Plenum Press, New York, 1967.
63. G. Hägg, Z. phys. Chem., 1929, **B 6**, 221.
64. H. Bakker, Materials Science Forum, 1987, **15-18**, 1155.
65. Y. Minamino, S. B. Jung, and K. Hirao, Met. Trans. A, 1992, **23**, 2783.
66. *Selected Values of the Thermodynamic Properties of Binary Alloys*, R. Hultgren, P. Desai, D. Hawkins, M. Gleiser, and K. Kelley, eds., ASM, Metals Park, Ohio, 1973, p. 163.
67. F. M. d'Heurle, in *VLSI Science and Technology/1982*, C. Dell'Oca and W. M. Bullis, eds., The Electrochemical Society, Pennington, New Jersey, 1982, p. 194.
68. Q. Z. Hong and F. M. d'Heurle, J. Appl. Phys., 1992, **72**, 4036.
69. K. Schubert, *Kristallstrukturen zweikomponentiger Phasen*, Springer Verlag, Berlin, 1961, pp. 288, 289.
70. H. Bakker, in *Landolt-Börnstein*, New Series III/26, 1990, chapt. 4, p. 213.
71. F. M. d'Heurle and J. Gupta, IBM Research Report RC 18152, Yorktown Heights, New York, 1992. 72. P. B. Barna, A. Csanády, G. Radnoczi, K. Urban, and U. Timmer, Thin
Solid Films, 1990,
193/194, 1.
73. A. Csanády, J. R. Günther, P. B. Barna, and J. Mayer, Thin Solid Films, 1988, **167**, 203.
74. G. F. Hancock, phys. stat. solid., 1971, **a 7**, 735.
75. K. Barmak, K. R. Coffey, D. A. Rudman, and S. Foner, J. Appl. Phys., 1990, **67**, 7313.
76. T. G. Hentzell, R. Thompson, and K. N. Tu, J. Appl. Phys., 1983, **54**, 6923.
77. K. M. Axler, E. M. Foltyn, D. E. Petersson, and W. B. Hutchinson, J. Less-Common Met., 1989, **156**, 213.
78. M. W. Ruckman, L. Jiang, and M. Strongin, J. Vac. Sci. Technol., 1990, **A 8**, 134.
79. B. Arcot, C. Cabral, J. M. E. Harper, and S. P. Murarka, Mater. Res. Soc. Symp. Proc., 1991, **225**, 231.

80. V. Simic and Z. Marinkovic, Thin Solid Films, 1976, **34**, 179.
81. J. E. E. Baglin and J. M. Poate, in *Thin Films: Interdiffusion and Reactions*, J. M. Poate, K. N. Tu, and J. W. Mayer, eds., John Wiley, New York, 1978, p. 305.
82. S. K. Lahiri and D. Gupta, J. Appl. Phys., 1980, **51**, 555.
83. Rita Roy and S. K. Sen, Thin Solid Films, 1991, **197**, 303.
84. S. Nakahara and R. J. McCoy, Thin Solid Films, 1982, **89**, 285.
85. W. J. Tomlinson and H. G. Rhodes, J. Mater. Sci., 1987, **22**, 1769.
86. V. V. Bogdanov and L. N. Paritzkaya, presented at Conference on Diffusion and Defects in Solids, DD-91, Moscow, July 1991.
87. Jian Li, J. W. Strane, S. W. Russelll, S. Q. Hong, J. W. Mayer, T. K. Marais, C. C. Theron, and R. Pretorius, J. Appl. Phys., 1992, **72**, 2810.
88. R. C. Krutenat, in *Encyclopedia of Chemical Technology*, John Wiley, New York, 1981, vol. 15, p. 244.
89. G. C. Paffenbarger and N. W. Rupp, in *Encyclopedia of Chemical Technology*, John Wiley, New York, 1981, vol. 7, p. 483.
90. E. G. Colgan and J. W. Mayer, J. Mater. Res., 1987, **2**, 28.
91. K. N. Tu and R. Rosenberg, Jpn. J. Appl. Phys. Suppl. 2, 1974, p. 633.
92. M. Onishi, Y. Wakamatsu, and H. Miura, Trans. Jpn. Inst. Met., 1974, **15**, 331.
93. Z. Marinkovic and V. Simic, Thin Solid Films, 1992, **217**, 26.
94. F. M. d'Heurle, C. S. Petersson, L. Stolt, and B. Strizker, J. Appl. Phys., 1982, **53**, 5678.
95. F. M. d'Heurle and C. S. Petersson, Thin Solid Films, 1985, **128**, 283.
96. S. Campisano, G. Foti, E. Rimini, S. S. Lau, and J. Mayer, Philos. Mag., 1975, **31**, 903.
97. K. Schubert, *Kristallstrukturen zweicomponentiger Phasen*, Springer, Berlin, 1964, p. 296.
98. R. J. Tarento and G. Blaise, Acta Metall., 1989, **37**, 2305.
99. R. W. Baluffi, in *Diffusion in Crystalline Solids*, G. E. Murdoch and A. S. Nowick, eds., Academic Press, New York, 1984, p. 320.
100. K. Vieregge, R. Willecke, and Ch. Herzig, J. de Phys., Colloque C-1, 1990, **51**, C1-691.
101. J. Bernardini, S. Bennis, and G. Moya, Defects and Diffusion Data, 1989, **66-69**, 805.
102. A. Atkinson, and R. I. Taylor, Philos. Mag., 1981, **A 43**, 979.
103. A. C. S. Sabioni, A. M. Huntz, F. Millot, and C. Monty, Philos. Mag., 1992, **A 66**, 361.
104. E. Perinet, J. Le Duigou, and C. Monty, in *Non-Stoichiometric Compounds, Surfaces, Grain Boundaries and Structural Defects*, J. Nowotny and W. Weppner, eds., Kluwer Academic Publishers, Norwell, MA, 1989, p. 387.
105. F. M. d'Heurle, J. de Phys., Colloque C1, 1990, **51**, C1-803.
106. H. E. Hexner, G. Plüger, and W. Gerling, Z. Metallk., 1992, **83**, 487.
107. D.-B. Kao, J. McWitte, W. Nix, and K. Saraswat, IEEE Trans. Electr. Dev., 1988, **ED-35**, 25.
108. C. H. Bjorkmann and G. Lucovsky, Mater. Res. Soc. Symp. Proc., 1992, **239**, 81.
109. L. O. Wilson and R. B. Marcus, J. Electrochem. Soc., 1987, **134**, 481.
110. G. Ghibaudo, Philos. Mag., 1987, **B 55**, 147.
111. Per Kofstad, *High Temperature Corrosion*, Elsevier, London, 1988.
112. S.-L. Zhang and F. M. d'Heurle, Thin Solid Films, 1992, **213**, 34.
113. D. J. Strolovitz, and T. A. Ramanarayanan, Oxidation Metals, 1984, **22**, 133.

DIFFUSION AND PROPERTIES

Creep and Diffusion in Intermetallic Alloys

G. Sauthoff

Max-Planck-Institut für Eisenforschung GmBH.
D-4000 Düsseldorf, Germany

Abstract

Intermetallics for structural applications at high temperatures must show a sufficient high temperature strength which is controlled by creep processes. In the first section the creep behaviour of single-phase intermetallic alloys is overviewed with respect to stress and temperature dependence and effects of composition and microstructure. It is shown in particular that creep deformation is controlled by diffusion. The second section refers to multiphase intermetallic alloys, and both particulate and non-particulate alloys are regarded. Data are presented for single-phase and multiphase alloys based on B2 phases and less-common phases and the consequences of diffusion control for alloy design are discussed.

Diffusion in Ordered Alloys
Edited by B. Fultz, R.W. Cahn, and D. Gupta
The Minerals, Metals & Materials Society, 1993

1. Introduction

Intermetallic phases form because of a strong predominantly metallic bonding between unlike metal atoms. From this not only particular ordered crystal structures and physical properties result, but also comparatively high strengths at low and high temperatures and low ductilities at low temperatures. Strength and deformability are controlled by various different mechanisms depending on stress, temperature and microstructure. A quick overview on the prevailing deformation mechanisms is given by the deformation mechanism map for a given material [1].

Fig. 1 - Deformation map with curves of constant shear strain rate as a function of normalized shear stress and temperature (μ = shear modulus, T_m = melting temperature) for Cr with 0.1 mm grain size (a) and ZrC with 0.01 mm grain size (b) [1].

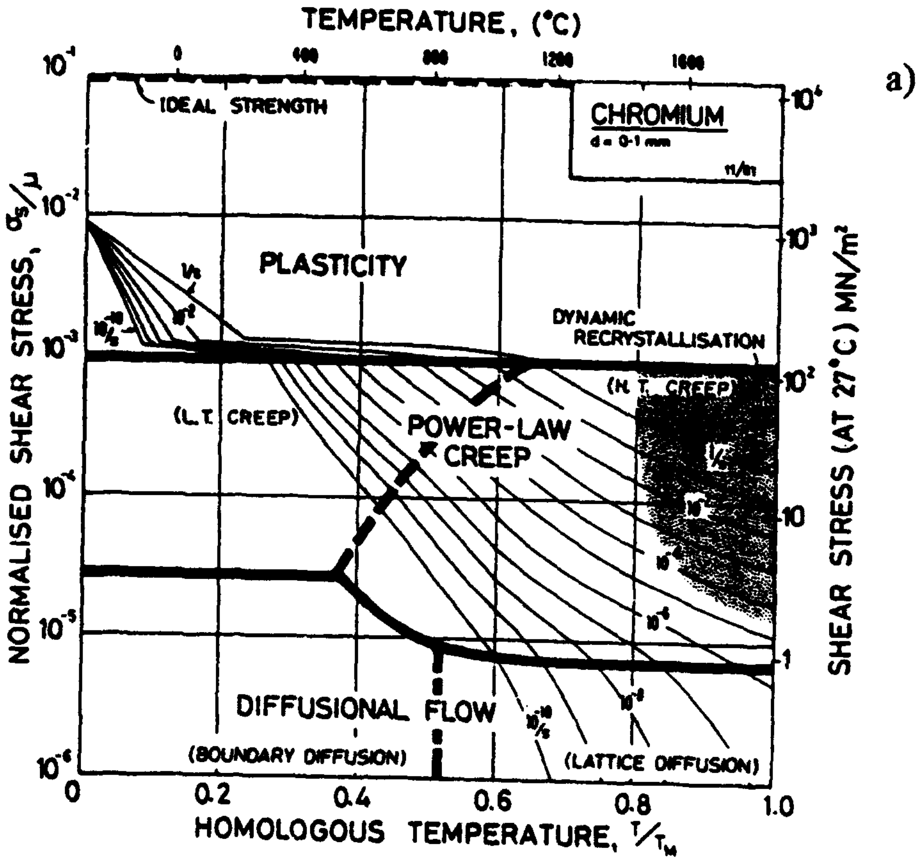

Complete deformation maps are available for many metals and alloys as well as for some non-metallic materials [1], but not yet for intermetallic phases. The comparison of a map for a pure metal, e.g. the transition metal Cr with cubic A2 structure - Fig. 1a -, and a map for an only partially metallic interstitial compound, e.g. the refractory carbide ZrC with cubic B1 structure - Fig. 1b -, shows that these maps which refer to normalized scales do not differ too much for these dissimilar materials in spite of the differences in atom bonding and crystal structure. Figure 2 [2] shows the high-temperature part of the deformation map for the ternary intermetallic phase $(Ni_{0.8}Fe_{0.2})Al$ with cubic B2 structure which is known as $L2_0$ structure, too, and results from the A2 structure by atomic ordering. Again the behaviour of the intermetallic does not differ too

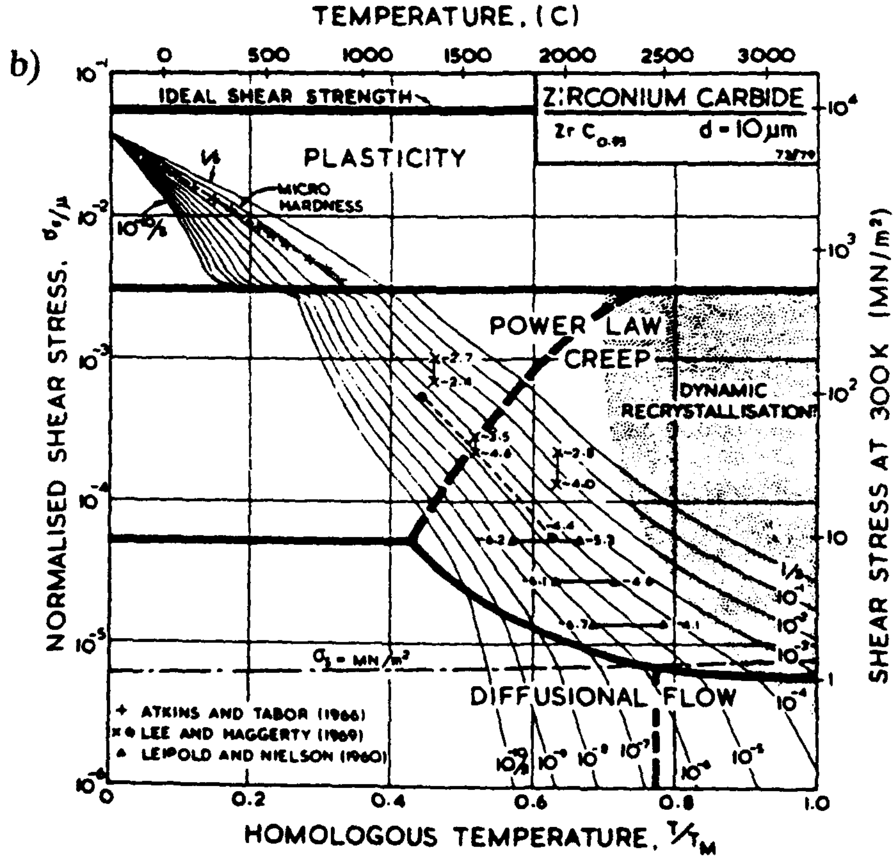

much from that of the other two examples. Obviously the normalization of applied stress by the respective shear modulus and temperature by the respective melting temperature is sufficient for a unifying description of the global deformation behaviour of various materials including intermetallics.

In view of the shown deformation maps the transition from low-temperature deformation which is controlled by the conservative motion of dislocations, to high-temperature deformation which is controlled by thermally activated creep processes is supposed to occur in the temperature range 0.3 T_m - 0.5 T_m for intermetallics, too, where T_m is the melting temperature. This means that the mechanical properties of intermetallic phases at high temperatures are determined by creep processes and depend sensitively on temperature and deformation rate. In the following this is discussed in some more detail on the basis of earlier reports [4-10]. The temperature dependence of creep resistance is regarded, and the effects of stoichiometry, solutes, grain boundaries and second phases are shown. The examples for the following discussion are taken from the work of the author's group which is centered on B2 phases, NiAl-base alloys and less-common phases.

2. Creep of Single-phase Intermetallic Alloys

The creep behaviour of intermetallic phases is exemplified by that of the ternary B2 phase (Ni,Fe)Al which was studied in detail as a function of stress, temperature, composition, and grain size [2,3,11,12]. The B2 crystal structure of this phase results from atom ordering in the bcc lattice, and with stoichiometric composition - 50 at.% Al - the phase is completely ordered up to the melting point. The Ni and Fe atoms substitute each other in one of two sublattices of the B2 structure, i.e., (Ni,Fe)Al may be regarded as an intermetallic alloy of the binary phases NiAl and FeAl - both with B2 structure - with complete mutual miscibility.

2.1. Stress Dependence

At high temperatures - e.g. 60 % of the melting temperature or higher - the secondary creep at rates between about $10^{-8}\,s^{-1}$ and $10^{-6}\,s^{-1}$ shows power law behaviour, i.e., the observed secondary creep rates are described by the familiar Dorn equation for dislocation creep [1]:

$$\dot{\varepsilon} = A(DGb/kT)(\sigma/G)^n \tag{1}$$

where $\dot{\varepsilon}$ = secondary strain rate, A = dimensionless factor, D = effective diffusion coefficient, G = shear modulus, b = Burgers vector, k = Boltzmann's constant, T = temperature, σ = applied stress, and the exponent n is between 3 and 5.

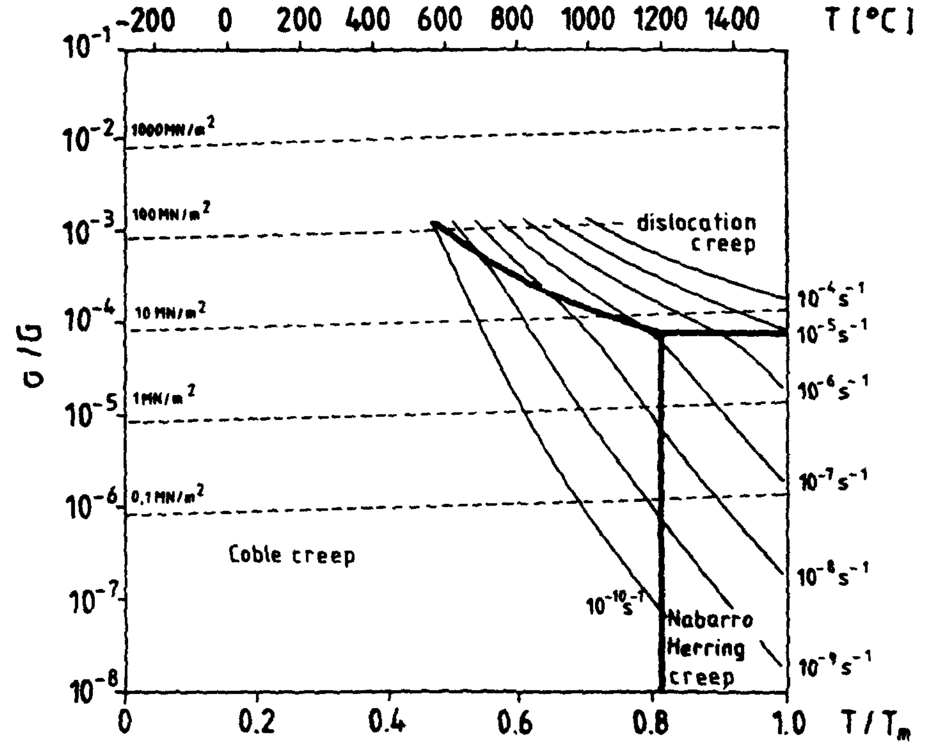

Fig. 2 - High-temperature deformation map with curves of constant compressive strain rate as a function of normalized compressive stress and temperature (G = shear modulus, T_m = melting temperature) for $(Ni_{0.8}Fe_{0.2})Al$ with 0.1 mm grain size [2,3].

Dislocation creep of conventional disordered alloys is produced by gliding and climbing dislocations. If climb is the slower step as in pure metals, the creep rate is controlled by dislocation climb which gives rise to a well-defined subgrain structure, and the stress exponent is 4 or 5. This is characteristic for the so-called class-II alloys. Otherwise viscous dislocation glide is rate controlling which leads to dislocation tangles without subgrain formation and a stress exponent 3 as characteristics of the class-I alloys [13].

The secondary creep behaviour of (Fe,Ni)Al shows analogous characteristics. In the Ni-rich phases and in the binary NiAl a well-defined substructure is found after creep. The subgrain size is of the order of 10 μm, and the dislocation density within the subgrains is about 10^7 cm^{-2} In agreement with this, stress exponents between 4 and 4.5 have been found for the Ni-rich phases, i.e., these phases behave like class-II alloys with dislocation climb controlling the creep. In the Fe-rich phases and in FeAl, however, no subgrain formation has been observed even after long creep times. The dislocation density *remains high* - about 10^{10} cm^{-2} - , and the stress exponent varies between 3 and 3.6. This indicates class-I behaviour, i.e., here the creep is controlled by the viscous glide of the dislocations. In both cases only <100> dislocations have been observed. Obviously the driving force and the atom mobility which is necessary for subgrain formation is sufficient only in the Ni-rich phases.

Besides dislocation creep, grain boundary sliding was observed in (Ni,Fe)Al. The process is of course not an independent deformation mechanism since the resulting grain shifts lead to stress concentrations at grain boundary junctions and must be accommodated by deformation processes within the grains, i.e. by dislocation creep of the grains in the regarded stress-temperature range. For such coupled deformation processes the total creep rate is controlled by the slower process, which is dislocation creep in the present case as is indicated by the observed stress-strain rate relationship. However, dislocation creep is accelerated by the additional driving force - the more the smaller the grain size - and at very low grain sizes there is a transition to superplastic flow with grain boundary sliding as rate controlling mechanism [14,15].

At lower stresses which produce secondary creep rates below 10^{-8} s^{-1}, the observed stress-strain rate relationship deviates from the power-law behaviour, i.e., the apparent stress exponent is smaller than 3 and decreases with decreasing stress. This deviation indicates the contribution of diffusion creep which is a linear function of stress:

$$\dot{\varepsilon}_{diff} = A_{diff}(\Omega D/kTd^2)\sigma \qquad (2)$$

where A_{diff} is a dimensionless factor (usually $A_{diff} = 14$), Ω is the atomic volume, D is the effective diffusion coefficient which considers both the diffusion through the grain (Nabarro-Herring creep) and along the grain boundaries (Coble creep), and d is the effective diffusion length which is usually approximated by the grain size [1]. Dislocation creep and diffusion creep are independent creep processes which act in parallel in the grains, and the total creep rate is given by the sum of the partial rates. Because of the stronger stress dependence of dislocation creep (Eq. 1) the contribution of diffusion creep becomes more prominent with decreasing stress. Furthermore, a smaller grain size accelerates diffusion creep and thus shifts the transition from dislocation creep to diffusion creep to higher stresses.

2.2. Temperature Dependence

In view of Eqs. 1 and 2 it is expected that the temperature dependence of creep for a given stress is determined primarily by that of the diffusion coefficient since the other parameters in these constitutive equations show a significantly weaker temperature dependence. However, the temperature dependence of the creep resistance of the binary phases NiAl and FeAl and the ternary (Ni,Fe)Al phases cannot be characterized by a constant activation energy as is demonstrated by Fig. 3. Only at lower temperatures - about half the melting temperature - the activation energy of creep corresponds to that of self-diffusion whereas at higher temperatures the activation energy of creep is larger than that of self-diffusion.

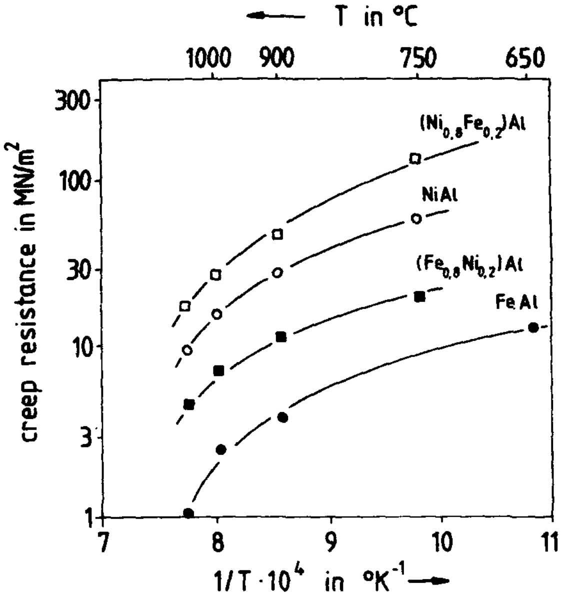

Fig. 3 - Creep resistance in compression (stress for $10^{-7}s^{-1}$ secondary creep rate) as a function of temperature for $(Ni_{0.8}Fe_{0.2})Al$, NiAl, $(Ni_{0.2}Fe_{0.8})Al$, and FeAl (for the latter two alloys the effective creep stress is shown at ≤750 °C which considers the observed threshold stress) [3,9].

In other cases, too, either the activation energies of diffusion or higher activation energies were found for creep, and the reasons for the activation energy increases are not yet clear - see e.g. [16-18]. This means that in contrast to conventional disordered alloys the microstructure-dependent parameter A in Eq. 1 may exhibit a strong temperature dependence, too, since the shear modulus G still depends only weakly on temperature [19].

2.3. Effects of Composition

Figure 4 shows the creep resistance of the ternary aluminide (Ni,Fe)Al as a function of composition, and it can be seen that the creep resistance depends sensitively on both the Al content and the Ni:Fe ratio. The B2 lattice is composed of two sublattices, one of which is occupied by the Al atoms whereas the other sublattice is occupied by the Ni and Fe atoms. This exclusive distribution of atoms on the respective sublattices represents the completely ordered state of these phases and is possible only for the stoichiometric composition with 50 at.% Al. Any excess or deficiency of Al leads to constitutional disorder, i.e. constitutional point defects.

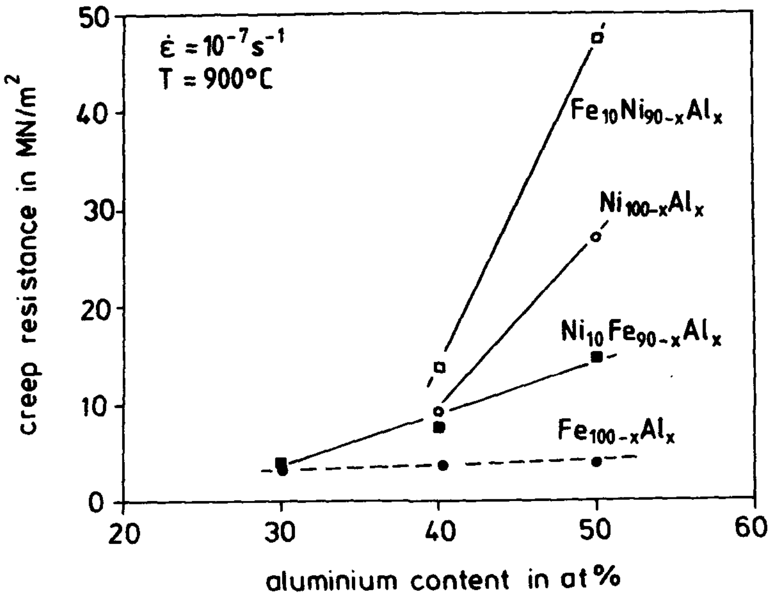

Fig. 4 - Creep resistance of binary and ternary B2 aluminides at 900 °C (in compression with 10^{-7} s^{-1} strain rate) as a function of Al content [3,12].

The presence of such point defects enhances diffusion [20] and thereby creep at sufficiently high temperatures, *i.e., the creep resistance reaches a maximum at the stoichiometric composition* as was shown for NiAl long ago [16]. At low temperatures the constitutional defects are immobile and act as point obstacles for moving dislocations. Consequently a minimum was found for the low-temperature strength at the stoichiometric composition [16].

The creep resistance of (Ni,Fe)Al (Fig. 4) indeed decreases with decreasing Al content - i.e. increasing deviation from stoichiometry - at 900 °C which corresponds to high-temperature behaviour. However, the strength decrease depends sensitively on the Ni:Fe ratio. In particular the binary FeAl shows nearly no effect of deviations from stoichiometry on creep resistance at 900 °C according to Fig. 4 which indicates the transition from low-temperature behaviour to high-temperature behaviour. Obviously the transition from low-temperature behaviour to high-temperature behaviour occurs at lower temperatures for the Ni-rich phases than for the Fe-rich phases. This is surprising since creep becomes dominant at about half the melting temperature which is higher for NiAl than for FeAl. In other words, creep scales with the melting temperature, and therefore the high temperature regime is expected for FeAl at lower temperatures than for NiAl. The reasons for the observed behaviour of (Ni,Fe)Al are not yet clear.

For a given Al content - in particular for the stoichiometric composition - the creep resistance of the binary NiAl is higher than that of FeAl which is expected in view of the higher melting temperature of NiAl. However, the highest creep resistance - see Fig. 5 - is shown by the ternary $(Ni_{40}Fe_{10})Al_{50}$ which is a solid solution of the softer FeAl (20 %) in the stronger NiAl. For (Ni,Fe)Al the diffusion coefficient has been estimated as a function of composition on the basis of available data - see Fig. 6. Clearly the creep resistance maximum for $(Ni_{40}Fe_{10})Al_{50}$ in Fig.5 results from a minimum of the diffusion coefficient. Such a creep resistance maximum is shown not only by (Ni,Fe)Al, but also by the other ternary B2 aluminides (Co,Ni)Al and (Co,Fe)Al as is illustrated by Fig. 5.

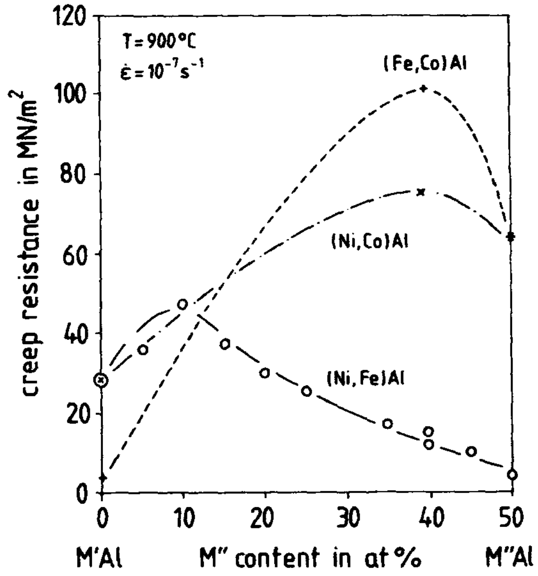

Fig. 5 - Creep resistance (in compression with $10^{-7}s^{-1}$ secondary creep rate) of various stoichiometric (M',M")Al with B2 structure at 900 °C as a function of M" content for M', M" = Ni, Fe, Co [8].

It has to be noted that the analysis of creep data with respect to diffusion coefficients poses problems because - apart from the scarcity of data - the diffusion coefficients in Eqs. 1 and 2 are effective ones depending on the particular creep process which determines the coupling of partial diffusion fluxes, i.e., the needed effective diffusion coefficients are not those which are measured in diffusion experiments. For binary solid solutions expressions for the effective

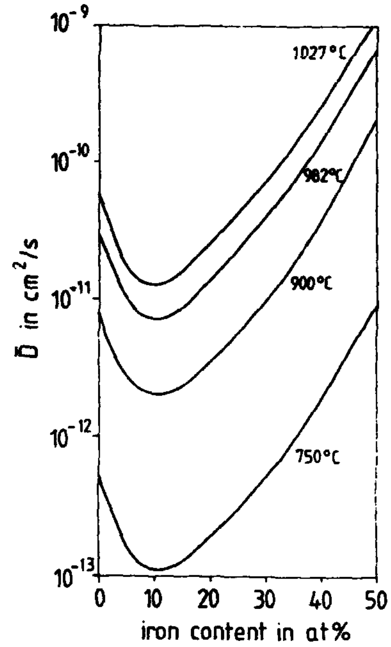

Fig. 6 - Estimated interdiffusion coefficient D as a function of iron content for stoichiometric (Ni,Fe)Al at various temperatures [3,12,21].

diffusion coefficients are available for various creep mechanisms [22,23], whereas for multinary phases an expression for the effective diffusion coefficient is known only for the case of diffusion creep [24]. Here more theoretical and experimental work is necessary.

The correlation between the observed creep resistances of various binary and ternary B2 phases and the respective diffusion coefficients as found in the literature or estimated on the basis of literature data is shown directly by Fig. 7 [3,9,12]. It can be seen that the correlation is surprisingly good and corresponds to Eq. 1 in spite of the problems with the appropriate determination of the effective diffusion coefficients. The question now is why the diffusion coefficient depends in the shown way on the composition of the B2 phases. As other properties the diffusion coefficient depends on the crystal properties, i.e. on the character and strength of atomic bonding and indeed the activation energy of diffusion increases with increasing heat of phase formation as is illustrated by Fig. 8. However, data for the effects of alloying additions on the diffusion behaviour which are necessary for any high-temperature materials design are scarce or not available for the intermetallic systems of interest. For understanding the effects of composition variations on the respective diffusion coefficients the correlation with the character and strength of bonding must be studied in detail. Here again much more theoretical and experimental work is necessary.

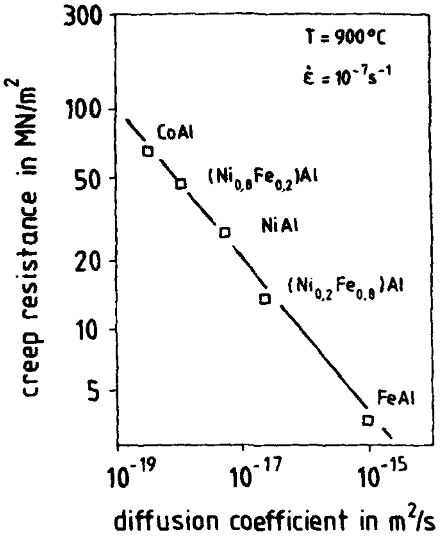

Fig. 7 - Creep resistance of binary and ternary stoichiometric B2 aluminides at 900 °C (in compression with 10^{-7} s^{-1} strain rate) as a function of diffusion coefficient as found in the literature or estimated from available data [2,3,9,21,25-27].

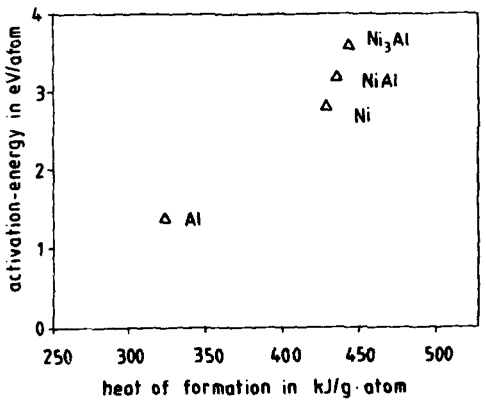

Fig. 8 - Activation energy of diffusion [1,28] as a function of total heat of phase formation for Ni, Al, NiAl and Ni_3Al [7,29].

In view of the discussed composition dependence of the creep resistance it is concluded that the effective diffusion coefficient is of primary importance for controlling the creep resistance. This of course does not mean that the other parameters in Eqs. 1 and 2 can be neglected. This is demonstrated by the apparent activation energy of creep which may vary with temperature as already mentioned in the preceding section.

3. Creep of Two-Phase Intermetallic Alloys

As with conventional metallic alloys, single-phase intermetallic alloys can be strengthened by second phases which may be disordered alloys or other intermetallics. Such second phases may be present as dispersed or precipitated particles in particulate alloys or as coarse phase distributions to form duplex structures or continuous lamellar or fibrous structures in non-particulate alloys. The creep behaviour of such two-phase intermetallic alloys has been studied up to now only to a small extent, and some examples are presented in the following.

3.1. Particulate alloys

The B2 aluminide (Ni,Fe)Al forms stable equilibria with other ordered or disordered Fe-Ni-Al phases [2]. In particular, Fe-rich particles with disordered bcc structure can be precipitated from Ni-rich (Ni,Fe)Al, and the creep behaviour of the resulting particle-strengthened intermetallic alloy was studied [30]. It was found that - as in the case of conventional alloys - the soft Fe particles act as obstacles to the movement of dislocations because of the attractive interaction between particle and dislocation. This interaction gives rise to a threshold stress in Eq. 1, and the creep resistance of the matrix alloy is increased by this threshold stress. The threshold stress is inversely proportional to the particle distance and of the order of the Orowan stress - see [6].

However, it has to be noted that in such a two-phase alloy the composition of the constituent phases cannot be chosen and optimized independently since the compositions of the two phases are determined by the particular two-phase equilibrium. In the regarded case the equilibrium between NiAl and Fe enforces an off-stoichiometric composition for the NiAl matrix which thus has a lower creep resistance than the stoichiometric NiAl. In this case the strength gain by the particles is more than outweighed by the strength loss by off-stoichiometry, and thus a finer distribution of particles by an appropriate pre-treatment or a shift of the two-phase equilibrium by alloying with further elements - or both - is necessary for an improved creep resistance.

Following the example of conventional ODS alloys, strengthening by dispersions of oxides, borides or carbides has been applied to intermetallic phases, too, and in particular to NiAl since its high-temperature strength is insufficient for structural applications - see e.g. [31-36]. Such alloys are produced by powder metallurgy methods and the resulting multiphase alloys are usually not in equilibrium. Thus reactions may occur between the constituent phases, i.e. chemical compatibility of the phases in such an alloy may be problem [37,38].

3.2. Non-particulate alloys

For describing the mechanical properties of alloys with coarse two-phase structures rules of mixtures are frequently used [39-43]. In the case of creep resistance σ_r this means a linear superposition of the creep resistances σ_{ri} of the constituents:

$$\sigma_r = \sum_i f_i \sigma_{ri} \tag{3}$$

(f_i = volume fraction of phase i), i.e., the alloy is regarded as composite with lamellae or fibres in stress direction.

Such a superposition, which refers to the secondary creep stage with stationary creep - after the initial primary stage with instationary creep -, would mean that the creep behaviour of the two-phase alloy is similar to that of a single-phase alloy. However, a rule of mixtures is only a phenomenologic first approximation which neglects effects of phase distribution. The effect of phase distribution on the creep behaviour was studied in detail in [44,45]. For this a Ni-40at.%Fe-18at.%Al alloy was chosen which was produced by directional solidification to produce a lamellar microstructure with the phases B2 NiAl and γ-Fe-Ni with equal volume fractions. It was found that the creep resistance of such a lamellar alloy is related to the creep resistances of the constituent phases according to a rule of mixtures as long as the lamellae spacing is larger than a critical spacing which is of the order of the free dislocation path. If the lamellae spacings are smaller than this critical value then the lamellae interfaces give rise to an additional strengthening effect. This strengthening effect can be described as in Eq. 3 by an additional threshold stress which again is proportional to the reciprocal lamellae spacing.

However, the above discussion has referred to secondary creep only. The situation is less clear for the transient primary creep stage which precedes secondary creep. As discussed in [8] the primary creep strain is reduced significantly by the presence of second phases and it decreases with increasing stress and with decreasing interface spacing at least in some NiAl-base alloys [44,46]. Such a behaviour is known for conventional alloys, too, but there are other alloys which show an opposite behaviour, i.e. an increasing primary strain with increasing stress (see [8]). Such effects are not yet understood even for disordered alloys. It is further noted that not only the normal primary creep with decelerating creep rate is observed for NiAl alloys with strengthening Laves phase, but also inverse primary creep with accelerating creep rate [47] as has already been reported for Ni_3Al [48,49]. Inverse creep results from an insufficient number of mobile dislocations, and a classic example for such a deformation behaviour is silicon where the deformation behaviour has been analysed in detail [50,51].

4. Conclusions and prospects

The creep behaviour of intermetallic phases and alloys is quite similar to that of conventional disordered alloys and can be described phenomenologically by the known constitutive equations. The particularities of the various intermetallic phases find expression in the respective materials parameters which are the effective diffusions coefficient D, the shear modulus G and the microstructure parameter A in the case of dislocation creep. The physical understanding of the rate controlling processes is, however, far from complete and much more experimental and theoretical work is necessary. In particular the fundamental data with respect to diffusion and elasticity are lacking in most cases.

Present materials developments on the basis of intermetallic phases aim at high strengths and creep resistances at high temperatures with reasonable fracture toughness at low temperatures. In view of this aim candidate phases are alloyed with further elements and processed in special ways to obtain optimum properties. However, the effects of alloying elements on diffusion which controls high-temperature deformation are not yet understood sufficiently for these intermetallic alloys. One should know in what way a composition change in a particular phase changes the elastic moduli on the one hand and the diffusion behaviour on the other hand. It is hoped that more diffusion work is done with respect to the alloy systems of interest to obtain the missing diffusion data and that more theoretical work - including quantum-mechanical ab initio calculations - is done to understand why the properties in general and the diffusion coefficients in particular change with specific alloying additions in specific ways.

References

1. H. J. Frost and M. F. Ashby, Deformation Mechanism Maps (Oxford: Pergamon Press, 1982.
2. I. Jung, M. Rudy and G. Sauthoff, "Creep in Ternary B2 Aluminides and Other Intermetallic Phases," High-Temperature Ordered Intermetallic Alloys II, ed. N. S. Stoloff, C. C. Koch, C. T. Liu et al. (Pittsburgh: Materials Research Society, 1987), 263-274.
3. M. Rudy, Untersuchung des Verformungsverhaltens der intermetallischen Phase (Fe,Ni)Al bei hohen Temperaturen (RWTH Aachen: Dr.Ing. thesis, 1986), 1-122.
4. G. Sauthoff, "Intermetallic Phases - Materials Developments and Prospects," Z. Metallkde., 80 (1989), 337-344.
5. G. Sauthoff, "Intermetallic Alloys - Overview on New Materials Developments for Structural Applications in West Germany," Z. Metallkde., 81 (1990), 855-861.
6. G. Sauthoff, "Mechanical Properties of Intermetallics at High Temperatures," High-Temperature Aluminides and Intermetallics, ed. S. H. Whang, C. T. Liu, D. P. Pope et al. (Warrendale: TMS, 1990), 329-352.
7. H.-J. Engell, A. Von Keitz and G. Sauthoff, "Intermetallics - Fundamentals and Prospects," Advanced Structural and Functional Materials, ed. W. Bunk (Berlin: Springer Verlag, 1991), 91-132.

8. G. Sauthoff, "Creep Behaviour of Intermetallics," Microstructure and Mechanical Properties of Materials, ed. E. Tenckhoff and O. Vöhringer (Oberursel: Deutsche Gesellschaft für Materialkunde, 1991), 141-149.
9. G. Sauthoff, "High Temperature Deformation and Creep Behaviour of BCC Based Intermetallics," Proceedings of the International Symposium on Intermetallic Compounds - Structure and Mechanical Properties - (JIMIS-6), ed. O. Izumi (Sendai: The Japan Institute of Metals, 1991), 371-378.
10. G. Sauthoff, "Creep Behaviour and Creep Mechanisms in Ordered Intermetallics," Ordered Intermetallics - Physical Metallurgy and Mechanical Behaviour, ed. C. T. Liu, R. W. Cahn and G. Sauthoff (Dordrecht: Kluwer Acad. Publ., 1992), 525-539.
11. M. Rudy and G. Sauthoff, "Creep Behaviour of the Ordered Intermetallic (Fe,Ni)Al Phase," High-Temperature Ordered Intermetallic Alloys, ed. C. C. Koch, C. T. Liu and N. S. Stoloff (Pittsburgh: MRS, 1985), 327-333.
12. M. Rudy and G. Sauthoff, "Dislocation Creep in the Ordered Intermetallic (Fe,Ni)Al Phase," Mater. Sci. Eng., 81 (1986), 525-530.
13. O. D. Sherby and P. M. Burke, "Mechanical Behaviour of Crystalline Solids at Elevated Temperature," Prog. Mater. Sci., 13 (1967), 325-390.
14. M. F. Ashby and R. A. Verrall, "Diffusion-Accomodated Flow and Superplasticity," Acta Metall., 21 (1973), 149-163.
15. M. F. Ashby, G. H. Edward, J. Davenport, et al., "Application of Bound Theorems for Creeping Solids and their Application to Large Strain Diffusional Flow," Acta Metall., 26 (1978), 1379-1388.
16. R. R. Vandervoort, A. K. Mukherjee and J. E. Dorn, "Elevated-Temperature Deformation Mechanisms in Beta Prime NiAl," Trans. ASM, 59 (1966), 930-944.
17. N. S. Stoloff, "Ordered Alloys - Physical Metallurgy and Structural Applications," Int. Materials Rev., 29 (1984), 123-135.
18. J. D. Whittenberger, "The Influence of Grain Size and Composition on Slow Plastic Flow in FeAl between 1100 and 1400 K," Mater. Sci. Eng., 77 (1986), 103-113.
19. M. R. Harmouche and A. Wolfenden, "Temperature and Composition Dependence of Young's Modulus in Polycrystalline B2 NiAl," JTEVA, 15 (1987), 101-104.
20. G. F. Hancock and B. R. McDonnell, "Diffusion in the Intermetallic Compound NiAl," phys. stat. sol., a 4 (1971), 143-150.
21. T. D. Moyer and M. A. Dayananda, "Diffusion in Beta2 Fe-Ni-Al Alloys," Metall. Trans., 7A (1976), 1035-1040.
22. R. Fuentes-Samaniego and W. D. Nix, "Appropriate Diffusion Coefficients for Describing Creep Processes in Solid Solution Alloys," Scr. Metall., 15 (1981), 15-20.
23. B. A. Chin, G. M. Pound and W. D. Nix, "The Role of Diffusion in Determining the Controlling Creep Mechanisms in Al-Zn Solid-Solutions: Part I," Metall. Trans., 8A (1977), 1517-1522.

24. C. Herring, "Diffusional Viscosity of a Polycrystalline Solid," J. Appl. Phys., 21 (1950), 437-445.
25. S. Shankar and L. L. Seigle, "Interdiffusion and Intrinsic Diffusion in the NiAl (Delta) Phase in the Al-Ni System," Metall. Trans., 9A (1978), 1467-1476.
26. H. C. Akuezue and D. P. Whittle, "Interdiffusion in Fe-Al System: Aluminizing," Met. Science, 17 (1983), 27-32.
27. G. H. Cheng and M. A. Dayananda, "Multiphase Diffusion in Fe-Ni-Al System at 1000 °C: II. Interdiffusion Coefficients for Beta and Gamma Alloys," Metall. Trans., 10A (1979), 1415-1419.
28. H. Wever, J. Hünecke and G. Frohberg, "Diffusion in Intermetallischen Phasen," Z. *Metallkde.*, 80 (1989), 389-397.
29. A. Von Keitz and G. Sauthoff, "The Effect of Chemical Bonding on Mechanical Properties in Transition Metal Intermetallics," *10th Int. Conf.* Solid Compounds of Transition Elements, Poster, 1991.
30. I. Jung and G. Sauthoff, "Creep Behaviour of the Intermetallic B2 Phase (Ni,Fe)Al with Strengthening Soft Precipitates," Z. Metallkde., 80 (1989), 484-489.
31. R. Bowman and R. Noebe, "Up-and-coming IMCs," Advanced Materials & Processes, 8/89 (1989), 35-40.
32. J. D. Rigney, P. S Khadkikar, J. J. Lewandowski, et al., "Strength and Toughness of Composite Materials Based on Nickel Aluminide Matrices," High-Temperature Ordered Intermetallic Alloys III, ed. C. T. Liu, A. I. Taub, N. S. Stoloff, et al. (Pittsburgh: Mat. Res. Soc., 1989), 603-608.
33. J. D. Whittenberger, R. K. Viswanadham, S. K. Mannan, et al., "1200 to 1400K Slow Strain Rate Compressive Behavior of Small Grain Size NiAl / Ni2AlTi - TiB2 Composites," J. Mater. Res., 4 (1989), 1164-1171.
34. J. D. Whittenberger, E. Arzt and M. J. Luton, "1300 K Compressive Properties of a Reaction Milled NiAl - AlN Composite," Intermetallic Matrix Composite, ed. D. L. Anton, P. L. Martin, D. B. Miracle, et al. (Pittsburgh: MRS, 1990), 211-218.
35. K. S. Kumar, "Discontinuously Reinforced Intermetallic Matrix Composites," ISIJ Intl., 31 (1991), 1249-1259.
36. K. S. Kumar and J. D. Whittenberger, "Intermetallic Matrix Composites via XD Synthesis," Proc.Int.Symp. Intermetallic Compounds - Structure and Mechanical Properties (JIMIS-6), ed. O. Izumi (Sendai: The Japan Institute of Metals, 1991), 927-934.
37. J. A. Moser, M. Aindow, W. A. T. Clark et al., "Compatibility of Potential Reinforcing Ceramics with Ni and Fe Aluminides," Intermetallic Matrix Composites, ed. D. L. Anton, P. L. Martin, D. B. Miracle et al. (Pittsburgh: MRS, 1990), 379-384.
38. D. M. Shah, D. L. Anton and C. W. Musson, "Feasibility Study of Intermetallic Composites," Intermetallic Matrix Composites, ed. D. L. Anton, P. L. Martin, D. B. Miracle et al. (Pittsburgh: MRS, 1990), 333-340.

39. M. N. Ahmed, M. Vedula and M. J. Koczak, "Composite Ferrous Powder Metallurgy Structures: Mechanical Properties and Stress Analysis," Metall. Trans., 21A (1990), 2943-2949.
40. G. Bao, J. W. Hutchinson and R. M. McMeeking, "Particle Reinforcement of Ductile Matrices against Plastic Flow and Creep," Acta Metall. Mater., 39 (1991), 1871-1882.
41. T. S. Byun and I. S. Kim, "Stress and Strain Partition in Elastic and Plastic Deformation of Two Phase Alloys," J. Mater. Sci., 26 (1991), 3917-3925.
42. M. Tanaka, T. Sakaki and H. Iizuka, "Creep Deformation of Ductile Two-Phase Alloys," Acta Metall. Mater., 39 (1991), 1549-1554.
43. M. -H. Poech and H. Fischmeister, "Mechanische Eigenschaften von Martensit-Austenit-Modellegierungen Teil I: Verformungsverhalten und Bruchfestigkeit," Z. Metallkde., 83 (1992), 176-182.
44. J. Klöwer, Untersuchung des Kriechverhaltens gerichtet erstarrter, lamellarer Eisen-Nickel-Aluminium-Legierungen (RWTH Achen: Dr.Ing. thesis, 1989), 1-112.
45. J. Klöwer and G. Sauthoff, "Creep Behaviour of Directionally Solidified Lamellar Nickel-Iron-Aluminium Alloys - Part I: Effect of Lamellae Spacing and Orientation," Z. Metallkde., 82 (1991), 510-518.
46. C. -P. Reip, Untersuchung des Verformungsverhaltens der D022-geordneten intermetallischen Phase Al3Nb (RWTH Aachen: Dr.rer.nat thesis, 1991), 1-118.
47. L. Machon, Untersuchung des Verformungsverhaltens hochschmelzender hexagonaler Laves-Phasen (Aachen: RWTH, Dr.rer.nat. thesis, 1992), 1-127.
48. K. J. Hemker, M. J. Mills and W. D. Nix, "An Investigation of the Mechanisms that Control Intermediate Temperature Creep of Ni3Al," Acta Metall. Mater., 39 (1991), 1901-1913.
49. J. H. Schneibel and P. M. Hazzledine, "Creep in L12 - Intermetallics," Ordered Intermetallics - Physical Metallurgy and Mechanical Behaviour, ed. C. T. Liu, R. W. Cahn and G. Sauthoff (Dordrecht: Kluwer Acad. Publ., 1992), 565-581.
50. H. Alexander and P. Haasen, "Dislocations and Plastic Flow in the Diamond Structure," Solid State Physics, ed. F. Seitz, D. Turnbull and H. Ehrenreich (New York: Academic Press, 1968), 27-47.
51. H. Alexander, "Dislocations in Covalent Crystals," Dislocations in Solids, ed. F. R. N. Nabarro (Amsterdam: North Holland, 1986), 113-234.

Environmental Embrittlement in Ordered Intermetallic Alloys

C. T. Liu[*] *and N. S. Stoloff*[+]

[*] Metals and Ceramics Division
Oak Ridge National Laboratory
P. O. Box 2008, Oak Ridge, Tennessee 37831-6115 USA

[+] Rensselaer Polytechnic Institute
Materials Engineering Department
Troy, New York 12180-3590 USA

Abstract

Ordered intermetallics based on aluminides and silicides possess many promising properties for elevated-temperature applications; however, poor fracture resistance and limited fabricability restrict their use as engineering material. Recent studies have shown that environmental embrittlement is a major cause of low ductility and brittle fracture in many ordered intermetallic alloys. There are two types of environmental embrittlement observed in intermetallic alloys. One is hydrogen-induced embrittlement occurring at ambient temperatures in air. The other is oxygen-induced embrittlement in oxidizing atmospheres at elevated temperatures. In most cases, the embrittlements are due to a dynamic effect involving generation and penetration of embrittling agents (i.e., hydrogen or oxygen) during testing. Diffusion of embrittling agents plays a dominant role in fracture of these intermetallic alloys. This chapter summarizes recent progress in understanding and reducing environmental embrittlement in these alloys.

Diffusion in Ordered Alloys
Edited by B. Fultz, R.W. Cahn, and D. Gupta
The Minerals, Metals & Materials Society, 1993

1. Introduction

Ordered intermetallics based on aluminides and silicides generally possess attractive high-temperature properties. However, brittle fracture and poor ductility at ambient temperatures have limited their use as structural materials for engineering applications [1-7]. For the past 15 years, substantial efforts have been devoted to understanding the brittleness in ordered intermetallics. As a result, significant progress has been made in understanding metallurgical factors governing the low ductility and brittle fracture in these intermetallics. Recent studies have shown that the poor fracture resistance in intermetallics is caused not only by intrinsic factors (such as lack of sufficient deformation modes, poor cleavage strength, etc.) but also extrinsic factors. Environmental embrittlement, an extrinsic factor, is found to be a major cause for brittle fracture in many ordered intermetallics [8-32], particularly in bcc- and fcc- ordered intermetallic alloys.

There are two types of environmental embrittlement observed in intermetallics. One is hydrogen-induced embrittlement occurring at ambient temperatures [8-25]. Surprisingly, it was found recently that many intermetallic alloys show a substantial decrease in room-temperature tensile ductility due to moisture-induced hydrogen embrittlement in moist air. The other is oxygen-induced embrittlement in air at elevated temperatures [26-32]. In most cases, the embrittlements are due to a dynamic effect involving generation and penetration of an embrittling agent (i.e., hydrogen or oxygen) during testing. In this chapter, these two types of environment-sensitive embrittlement are treated separately in sections 2 and 3. The last section discusses metallurgical means to alleviate the environmental embrittlement.

2. Ambient-Temperature Environmental Embrittlement

Hydrogen, introduced either by exposure to moist environments, by cathodic charging, or by testing in hydrogen gas, has been shown to embrittle a large number of single-phase intermetallics, as listed in Table 1. Most notable is the susceptibility of all $L1_2$ intermetallics which have been examined to date, i.e., Ni_3Al [21-23], Ni_3Al+Cr [32], Ni_3Fe [33], Ni_3Si [34, 35], Co_3Ti [13], $(Co,Fe)_3V$ [36, 37], and $Ni_3(Al,Mn)$ [14]. Therefore it is highly likely that all $L1_2$ intermetallics containing substantial amounts of the transition metals Fe, Ni or Co will prove to be susceptible to such embrittlement. Data for other superlattice structures remain scarce. Two B2 alloys are embrittled by hydrogen: FeCo-2%V and FeAl [9,11,12]. Fe_3Al alloys show severe environmental embrittlement when tested in air or hydrogen environment [10,38,39]. The $D0_{19}$ superlattice Ti_3Al (α_2) and its alloys with niobium are reported to form hydrides when exposed to hydrogen gas, and are therefore embrittled by hydrogen [40]. TiAl also is susceptible to embrittlement in air or in hydrogen gas, but the effect is much smaller than in α_2 alloys [41-43]. Ni_2Cr is highly susceptible to hydrogen embrittlement in both the ordered and disordered conditions [44].

$L1_2$	$D0_3$	B2	$L1_0$	$D0_{19}$
Ni_3Al				
Ni_3Al + Be	Fe_3Al	FeAl	TiAl	Ti_3Al
Ni_3Al + Cr	Fe_3Al + Cr	FeCo-V		Ti_3Al + Nb
Ni_3Fe				Ti_3Al + Nb + Mo
$Ni_3(Al,Mn)$				
Co_3Ti				
Ni_3Si				
$Ni_3(Si,Ti)$				
$(Ni,Fe)_3V$				
$(Co,Fe)_3V$				

Table 1: Intermetallic alloys subject to hydrogen embrittlement at ambient temperatures.

2.1 $L1_2$ Intermetallics

In terms of environmental embrittlement, ordered intermetallics can be grouped into two categories: (1) alloys containing no reactive elements and (2) alloys containing reactive elements (e.g., Al, Ti, Si). For the first category, the alloys are severely embrittled only when being forcefully charged with hydrogen, such as by cathodic charging. For the second category, the alloys themselves are capable of generating hydrogen from hydrogen-containing environments at ambient temperatures. The most striking case is the severe embrittlement of iron aluminides in moist air at room temperature.

Ni_3Fe is a model material for study of environmental degradation in ordered intermetallic alloys containing no reactive elements [33]. Ni_3Fe can be disordered by quenching from above its critical ordering temperature, T_c. This has permitted a direct comparison between the ordered and disordered conditions of Ni_3Fe (see Table 2) produced by quenching and aging treatments. In each case, hydrogen was cathodically charged for one hour prior to tensile testing at room temperature. Note that Ni_3Fe is slightly embrittled by precharging in both the ordered and disordered conditions;

simultaneous charging and testing cause greater loss of ductility than precharging, with an especially severe effect for the ordered condition. Similar effects are observed in ordered and disordered $(Fe,Ni)_3V$ [45]. Fractographic studies confirm a change in fracture mode from microvoid coalescence to intergranular fracture in hydrogen accompanying the reduction in elongation. However, the intergranular embrittlement zone is only about one third as deep in precharged samples of ordered Ni_3Fe as in disordered samples.

Embrittlement of the ordered condition is much more severe when charging occurs during testing, and unlike precharged samples, the entire fracture surfaces of the simultaneously charged samples are intergranular [33]. The fracture surfaces of disordered samples display a mixed mode. The diffusivity of hydrogen in ordered Ni_3Fe is undoubtedly lower than that in the disordered condition. Therefore, only a shallow layer can be embrittled by hydrogen. However, when plastic deformation accompanies hydrogen charging, dislocations can carry hydrogen inward to a much greater depth than through diffusion alone; hence embrittlement is more severe, and the fracture path is intergranular to a greater depth than in precharged material.

As shown in Table 2, both ordered and disordered Ni_3Fe display extensive ductility and ductile fracture in air, indicating that moisture does not embrittle the alloys. This can be explained from the fact that Ni_3Fe contains no reactive elements (such as Al, Ti, etc.) and is not able to release hydrogen from moisture in air [46]. Similarly, Ni_3Mn exhibits transgranular fracture and good ductility in air at room temperature [47].

	Disordered			Ordered		
	Air	Precharged	Simultaneously Charged	Air	Precharged	Simultaneously Charged
σ_{ys} (MPa)	111	112	110	180	176	177
UTS (MPa)	490	439	328	627	598	223
% El.	43	30.5	17.5	37	32	7
Avge. depth of IG zone (μm)	0	130	590	0	45	Totally IG fracture

Table 2: Room-temperature tensile properties of Ni_3Fe tested in various environmental conditions [33].

Most Ll2 intermetallics of interest for structural applications, on the other hand, contain reactive elements such as Al (for aluminides), Si (for silicides), Ti, and V. These intermetallics show severe environmental embrittlement not only in the hydrogen-charged condition but also in hydrogen-containing atmospheres such as moist air. Severe embrittlement has been observed in many Ll2 intermetallics, including $Ni_3(Al,Mn)$, B-doped Ni_3Al, Co_3Ti, $(Co,Fe)_3V$, Ni_3Si, and $Ni_3(Si,Ti)$ tested in moist air at room temperature. In this case, embrittlement involves the reaction of reactive elements with moisture in air and generation of atomic hydrogen which penetrates into crack tips and causes brittle crack propagation.

Figure 1 shows environmental embrittlement of $Ni_3(Al_{0.4}Mn_{0.6})$ tested at room temperature in various environments and at several strain rates [14]. Manganese at a level of 15 at. % was added for the purpose of enhancing grain-boundary cohesion in Ni_3Al. At a low strain rate of $10^{-5}s^{-1}$, the alloy showed about 40% elongation in vacuum but only 5% in air at room temperature. The ductility was further reduced by hydrogen charging, followed by testing in air. The loss in ductility was attributed to moisture-induced hydrogen embrittlement during the air tests. Consistent with the environmental effect, the ductility increases with increasing strain rate, and the yield strength is essentially independent of both test environment and strain rate (see Fig. 1). The decrease in ductility due to environmental embrittlement is accompanied by a change in the fracture mode from ductile transgranular, through mixed mode, to brittle intergranular. This observation suggests that hydrogen, generated either by the moisture/aluminum reaction or by hydrogen charging, diffuses mainly along grain boundaries and causes intergranular fracture.

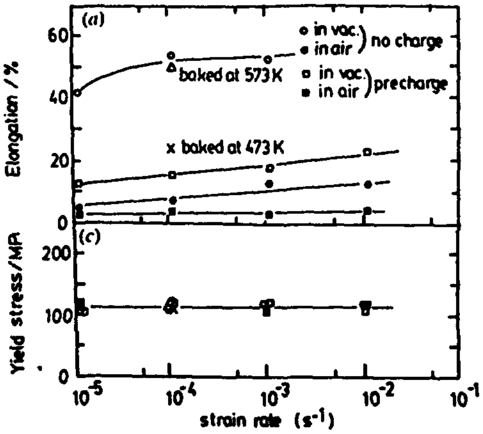

Figure 1: Effect of strain rate and hydrogen charging on tensile properties of $Ni_3(Al_{0.4}Mn_{0.6})$ tested at room temperature, in air and vacuum [14].

Similar to $Ni_3(Al_{0.4} Mn_{0.6})$, Co_3Ti [13, 18] and $(Co, Fe)_3V$ [36, 37] alloys have been found recently to be susceptible to environmental embrittlement at room temperature. As indicated in Fig. 2, $(Co_{78}Fe_{22})_3V$ shows ductile transgranular fracture, with a tensile ductility of 35.8% in vacuum [37]. The room-temperature ductility reduces to 20% in air and 15.3% in distilled water. The reduction in ductility is accompanied by a change in fracture mode from ductile transgranular to mixed transgranular and intergranular fracture. Grain-boundary fracture was observed mainly at the corner of the fracture surface, indicating that moisture-induced hydrogen diffuses from surface to interior, mainly through the grain boundaries, and causes intergranular fracture. The yield strength and work hardening behavior are insensitive to test environment. The environmental embrittlement in $(Co,Fe)_3V$ is completely eliminated by increasing the strain rate from 3.3×10^{-5} to $3.3 \times 10^{1} s^{-1}$ [36, 37]. Note that a similar reduction in ductility and change in fracture mode has been observed in other $L1_2$ intermetallic alloys (Table 1).

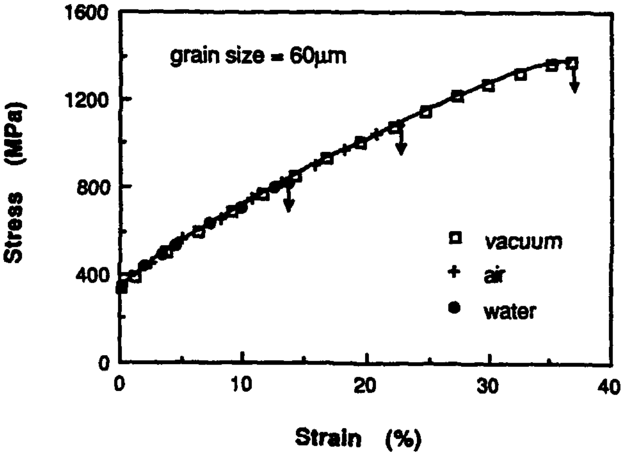

Figure 2: Effect of test environment on stress-strain curves of $(Co,Fe)_3V$ tested at room temperature [37].

Recently, intergranular fracture and environmental embrittlement have been studied in alloys based on Ni_3Si [35]. Ni_3Si showed no appreciable plastic deformation when tested in moist air but an elongation of 7.5% when tested in dry oxygen (Table 3), demonstrating that Ni_3Si is prone to environmental embrittlement. Since the elimination of the environmental effect by testing in dry oxygen does not lead to extensive ductility (e.g., 30% or more) and complete suppression of intergranular fracture in Ni_3Si, moisture-induced hydrogen embrittlement appears not to be the sole source of grain-boundary brittleness in the silicide. This is further indicated by comparison of the tensile data for Ni_3Si and $Ni_3(Si,Ti)$ [34]. As shown in Table 3, $Ni_3(Si,Ti)$ is also susceptible to environmental embrittlement. The $Ni_3(Si,Ti)$ alloy, however, exhibits considerable ductility (7%) when tested in air at room temperature. It displays excellent ductility (29%) when tested in vacuum, indicating that titanium enhances the intrinsic grain-boundary cohesion of Ni_3Si. The effect of boron additions on alleviation of environmental degradation will be discussed in section 4.

Alloy	Test environment	Tensile ductility (%)	Yield strength (MPa)	Fracture mode[b]
Ni_3Si	Air	0	---	GBF
Ni_3Si	Vacuum	4.7	677	GBF
Ni_3Si	Oxygen	7.5	685	GBF
Ni_3Si + B	Air	7.0	610	GBF
Ni_3Si + B	Oxygen	6.6	590	GBF
$Ni_3(Si,Ti)$[a]	Air	7	606	GBF + TF
$Ni_3(Si,Ti)$[a]	Vacuum	29	586	TF
$Ni_3(Si,Ti)$+B[a]	Air	36	593	TF
$Ni_3(Si,Ti)$+B[a]	Vacuum	34	613	TF

[a] Ni-11% Si-9.5% Ti [34]

[b] GBF = grain-boundary fracture ; TF = transgranular fracture

Table 3: Effect of test environment on room temperature tensile properties of Ni_3Si and $Ni_3(Si, Ti)$alloys [35].

Test environment affects mechanical properties of ordered intermetallics under both static and cyclic loading conditions. Hydrogen gas at 1 atm pressure has no effect on fatigue crack growth in a disordered $(Fe,Ni)_3V$ alloy at room temperature [45], but there is a marked effect on crack growth rate in the ordered condition (see Fig. 3). These results are consistent with those observed in tension under static loading in demonstrating the heightened susceptibility to hydrogen embrittlement when the lattice is ordered. The influence of hydrogen was severe at all cyclic stress-intensity levels studied, and the fracture surface revealed a primarily intergranular path. Embrittlement under cyclic loading also has been studied in Fe_3Al alloys, as described in the following section.

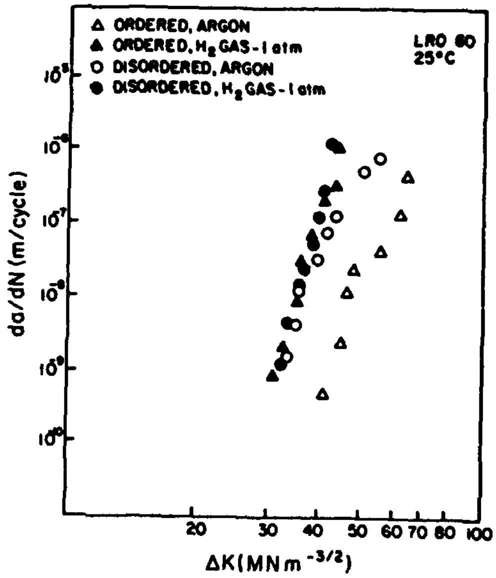

Figure 3: Effects of long-range order and test environment on crack growth of LRO-60 $(Fe_{50}Ni_{50})_3(V_{98}Ti_2)$ doped with 0.04 wt % Ce [45].

2.2 Iron Aluminides with BCC Ordered Structures

The two iron aluminides, FeAl and Fe_3Al, form the bcc ordered crystal structures B2 and $D0_3$, respectively. Despite this difference in crystal structure, these aluminides show similar embrittlement in hydrogen-containing atmospheres at room temperature. Both aluminides exhibit only a few percent ductility (1 to 4%) when tested at ambient temperatures in air. This led many workers to conclude that these alloys are inherently brittle. However, it has been demonstrated conclusively that when water vapor and hydrogen are eliminated from the external environment, both alloys exhibit considerable ductility [8-12, 39]. For an FeAl (36.5 at. % Al) alloy, tensile elongations up to 18% have been achieved in "dry" environments such as dry oxygen, see Fig. 4. The increase in ductility from 2 to 18% is accompanied by a change in fracture mode from transgranular cleavage in air to mainly grain-boundary separation in dry oxygen. This observation suggests that cleavage planes are more susceptible to embrittlement than are grain boundaries. The maximum degree of moisture-induced embrittlement occurs on either side of ambient temperatures [48] (Fig. 5). At higher temperatures in-situ protective oxide films can form readily on specimen surfaces and an entropy effect may reduce hydrogen concentration at crack tips, while at low temperatures the aluminum-moisture reaction is slowed and the equilibrium moisture content in air is lower.

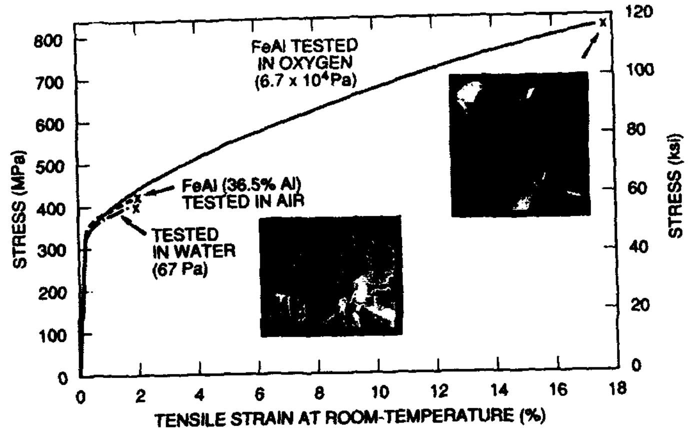

Figure 4: Influence of test environment on room-temperature tensile ductility of FeAl (36.5% Al).

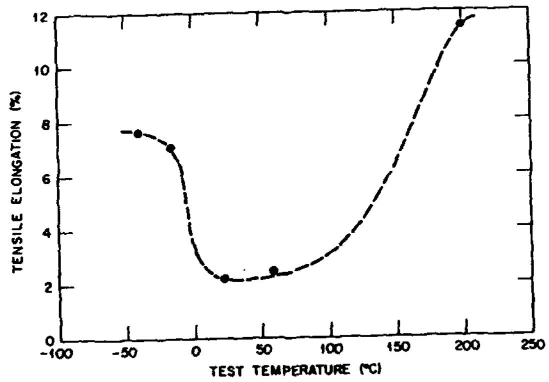

Figure 5: Effects of test temperature on tensile ductility of FeAl (36.5% Al) tested in moist air at room temperature [48].

The environmental sensitivity of FeAl is reduced markedly when the aluminum content is higher than 38 at. % [11,12]. For Fe-43 at.% Al, the ductility is nil in air as well as in dry oxygen; all specimens fail intergranularly. This difference in behavior with aluminum content suggests that grain boundaries in FeAl alloys with Al > 38% are intrinsically brittle. Therefore, environmental embrittlement and intrinsic effects must be distinguished in order to establish strategies for reducing brittleness. It has been demonstrated that the intrinsic grain-boundary brittleness in FeAl and other intermetallics can be alleviated by microalloying with boron.

Fe_3Al with a $D0_3$ crystal structure displays about 15% elongation in dry oxygen, but only 5% in moist air at room temperature [49], see Fig. 6. Its ductility drops to 3% in H_2 gas and to less than 1% when charged with hydrogen. Chromium additions to Fe_3Al increase its ductility in air, but do not suppress embrittlement by hydrogen gas or by hydrogen introduced by electrolytic charging. Under cyclic loading conditions, vacuum or oxygen environments raise the fatigue threshold, reduce crack growth rates and raise the stress intensity, K_c, at which cracks propagate in an unstable manner.

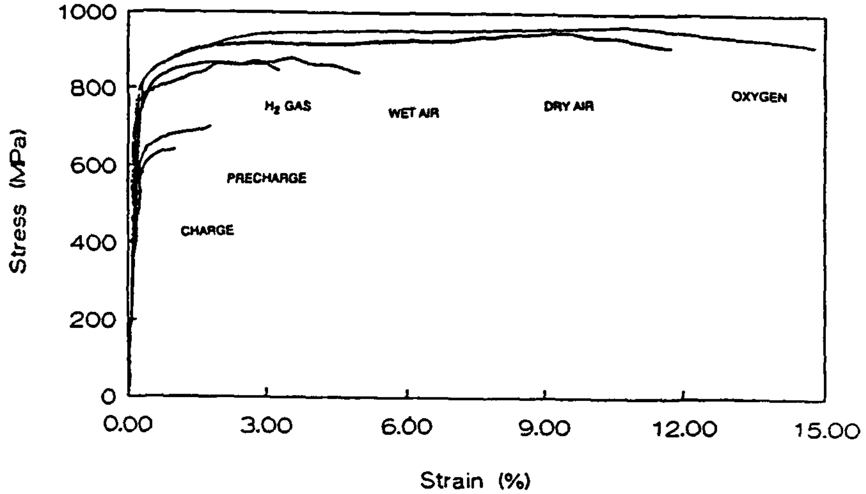

Figure 6: Comparison of hydrogen embrittlement as a result of various environments for Fe_3Al ($D0_3$) with grain size = 10-12 µm; strain rate = 3 × 10^{-6} s^{-1} [49].

2.3 Titanium Aluminides

Considerable effort has been devoted to determining the hydrogen susceptibility of γ TiAl ($L1_0$ structure) and α_2 Ti_3Al alloys ($D0_{19}$ structure). Ti_3Al takes up hydrogen much more readily than TiAl, but not as rapidly as titanium [40]. Hydride formation occurs in both binary Ti_3Al and Ti-Al-Nb alloys [50, 51]. Embrittlement due to gaseous hydrogen occurs in both Ti-24 at. % Al-11Nb and Ti-25Al-10Nb-3V-1Mo (super α_2). Severe embrittlement of super α_2 in 34.5 MPa hydrogen occurs at room temperature and at 204°C. Crack paths differ in the two environments: they followed the α_2/β interface in hydrogen, while in helium the cracks tend to remain in the ductile β phase. Super α_2 also is reported to crack after exposure to hydrogen at temperatures as low as 510°C.

Environmental embrittlement of TiAl (50-50) in air and in hydrogen gas has been studied recently by both bend tests and tensile tests at room temperature [41-43]. Figure 7 shows that bend ductility is considerably higher in vacuum than either in air or in hydrogen gas at 500 mm Hg pressure [43]. To date there have been few other published reports on hydrogen effects on mechanical properties of TiAl. Neither hydride formation nor embrittlement was detected in TiAl exposed to high pressure hydrogen gas at high temperatures [52]. The formation of hydrides appears to have the same embrittling effect as in the α_2 alloys.

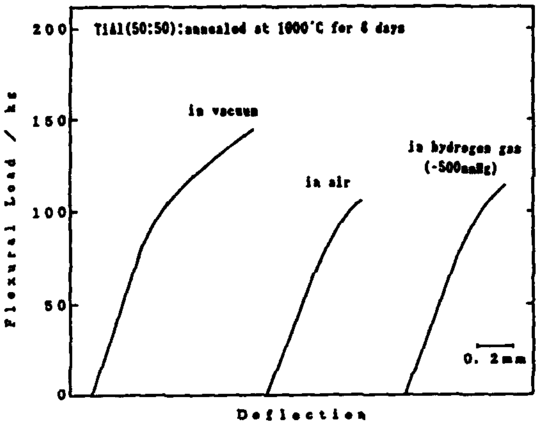

Figure 7: Effect of test environment on bend properties of TiAl at room temperature [43].

2.4 Embrittling Mechanisms

As mentioned in the previous sections, many ordered intermetallics show environmental embrittlement in hydrogen (charged or uncharged) environments or in moist air at ambient temperatures. It has been demonstrated that some intermetallics containing reactive elements (such as FeAl and Fe_3Al) exhibit more severe embrittlement in moist air than in dry hydrogen. The chemical reaction for the moisture-induced embrittlement involves [9, 46]:

$$xM + yH_2O \rightarrow M_xO_y + 2yH \qquad (1)$$

where M is a reactive element in intermetallics. It is the high-fugacity atomic hydrogen that rapidly penetrates into crack tips and causes severe embrittlement. Thus, the underlying mechanism of moisture-induced embrittlement in FeAl and other intermetallics is similar to embrittlement in hydrogen observed in Co_3Ti, Ni_3Al, $Ni_3(Al, Mn)$ and $(Fe, Ni)_3V$ alloys [13-15,38,45,53], with the principal difference being the manner in which atomic hydrogen is generated from water vapor and absorbed at crack tips. The yield strengths of the intermetallics are found to be insensitive to test environment. The highest ductility is generally obtained in dry oxygen environments because oxygen suppresses the reaction in Eq. (1) and the generation of atomic hydrogen through direct formation of oxides [54]:

$$2\,xM + yO_2 \rightarrow 2M_xO_y \qquad (2)$$

Both bcc- and fcc- ordered intermetallics show severe environmental embrittlement at ambient temperatures. In the case of iron aluminides with bcc-ordered crystal structures, the embrittlement occurs along cleavage planes, resulting in brittle cleavage fracture. The brittle cleavage is suppressed when FeAl alloys are tested in dry oxygen instead of moist environments. In the case of Ll_2 intermetallics, the loss in ductility is accompanied by a change in fracture mode from ductile appearance to brittle grain-boundary separation. The fcc-ordered intermetallics prone to environmental embrittlement include Co_3Ti, $(Co,Fe)_3V$, Ni_3Si, $Ni_3(Si,Ti)$, $Ni_3(Al,Mn)$, and TiAl alloys. The difference in the fracture between bcc- and fcc- ordered intermetallics may be due to differences in hydrogen diffusion along grain boundaries, with more rapid diffusion in the Ll_2 boundaries.

Hydrogen embrittlement is known to be a very complex phenomenon in metals and alloys. The underlying mechanisms suggested for hydrogen embrittlement in ordered intermetallics can be grouped into four categories [54]: (1) reduction of atomic bonding across cleavage planes, (2) reduction of cohesive strength across grain boundaries, (3) reduction of dislocation mobility and crack tip plasticity, and (4) formation of brittle hydrides. Environmental embrittlement in the bcc-ordered iron aluminides occurs mainly along cleavage planes, suggesting the reduction of cleavage strength by absorbed hydrogen. Experimental results are supported by recent first-principles quantum-mechanical calculations, which indicate that absorbed hydrogen significantly reduces the cleavage strength and energy of FeAl (by as much as 20 to 70%, depending on the hydrogen concentration) [55]. Superdislocations have been suggested to be the carriers for enhanced diffusion of hydrogen at crack tips. In the case of fcc-ordered intermetallics, hydrogen embrittlement takes place mainly along grain boundaries and reduces of the boundary cohesive strength.

Limited studies by in-situ TEM experiments indicate that hydrogen accumulated at crack tips may introduce a large number of defects which hinder the emission and motion of dislocations and thereby decrease the associated plastic work at crack tips

[18, 56]. Hydrides have been detected only in titanium aluminides [51] and they may be responsible for lowering tensile ductilities in hydrogen environments. However, embrittlement in the absence of hydrides cannot be excluded. Recent analyses of dislocation structures in B_2 intermetallics suggest that hydrogen can promote the formation of <100> edge dislocations and help the combination of them to form microcracks [57, 58].

3. Embrittlement at Elevated Temperatures

Environmental degradation in ordered intermetallics occurs not only at ambient temperatures but also at elevated temperatures. The embrittling mechanism and agent are, nevertheless, quite different in these two cases. Hydrogen is the major embrittling agent and oxygen is beneficial at room temperature, whereas oxygen is the major embrittling agent at elevated temperatures (typically above 300°C). At present, only a few intermetallic systems have been studied for environmental degradation at elevated temperatures, and data are available mainly for Ni_3Al, Ni_3Si, and $(Fe,Co)_3V$ alloys [26-31, 59].

3.1 Ni_3Al Alloys

Tensile properties of Ni_3Al are sensitive to test temperature and environment. Figure 8 compares the tensile elongation of a Ni_3Al alloy (Ni-21.5Al-0.5Hf-0.1B) tested in air and vacuum (10^{-3} Pa) as a function of test temperature [26, 32]. The alloy tested in air showed distinctly lower ductility than that tested in vacuum at temperatures above 300°C, and the severest embrittlement occurred around 750°C, despite the fact that Ni_3Al alloys exhibit good oxidation resistance in air. The loss in ductility is generally accompanied by a change in fracture mode from ductile transgranular to brittle intergranular. Similar embrittlement has been observed in other Ni_3Al alloys, such as B-doped Ni_3Al containing up to 16% Fe [60] and B-doped $(Ni,Co)_3Al$ alloys [28]. In these cases, oxygen has been identified as the embrittling agent.

Test environments also affect the fatigue life of boron-doped Ni_3Al (24 at. % Al) at elevated temperatures [27]. The alloy shows a sharp drop in fatigue life at temperatures above 500°C (Fig. 9), even when tested in conventional vacuum (10^{-3} Pa). This result suggests that a conventional vacuum may not be good enough to suppress the environmental embrittlement in Ni_3Al. The drop in fatigue life is accompanied by a change in fracture mode from transgranular to intergranular.

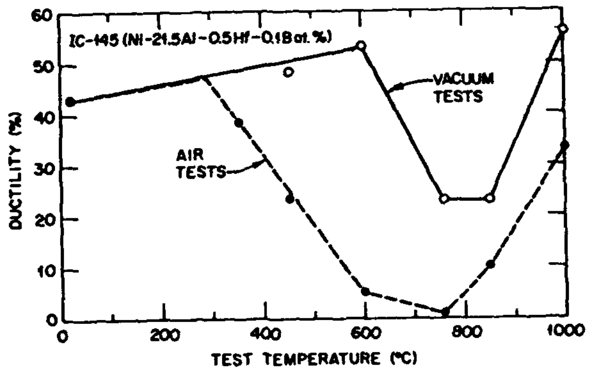

Figure 8: Change in tensile elongation with temperature for Ni-21.5% Al-0.5% Hf-0.1% B tested in vacuum and air [26].

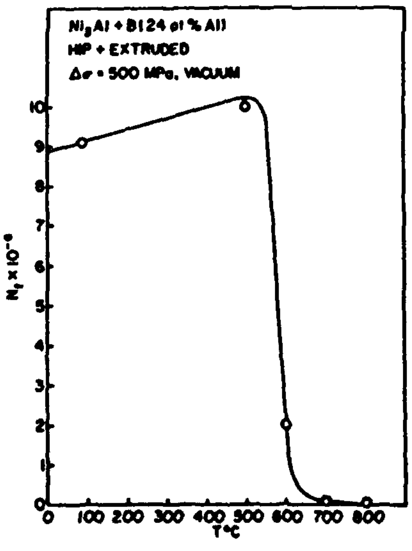

Figure 9: Change in high-cycle fatigue life with temperature for Ni3Al doped with boron and tested in vacuum [27].

3.2 Ni_3Si Alloys

Like Ni_3Al, Ni_3Si alloys also exhibit severe environmental embrittlement in oxidizing environments at elevated temperatures [61]. For Ni_3Si and $Ni_3(Si,Ti)$ alloys with and without B, tensile ductility decreases sharply at temperatures above 300°C in moist air [29]. The ductility of low silicon alloys (e.g., 19 at.%) reaches a minimum at 600°C, and above that temperature the ductility increases sharply. Tests in vacuum result in an increase in ductility at 600°C by a factor as high as 20. For high (Si+Ti) alloys (e.g., 21%), ductility decreases continuously with increasing temperature and approaches zero above 600°C. The alloys show no improvement in ductility at temperatures above 600°C in a conventional vacuum.

3.3 $(Fe,Co)_3V$ Alloys

$(Fe,Co)_3V$ alloys exhibit environmental embrittlement at ambient and elevated temperatures. Figure 10 shows the temperature dependence of the yield strength and tensile elongation of a $(Fe_{22}Co_{78})_3V$ alloy tested in air and vacuum (10^{-4} Pa) [59]. The yield strength shows a positive temperature dependence from 300°C to T_c ($\approx$ 910°C), the critical ordering temperature of the alloy. Anomalous yielding has been observed in many Ll_2 intermetallics and is generally explained by the cross-slip-pinning mechanism [62, 63].

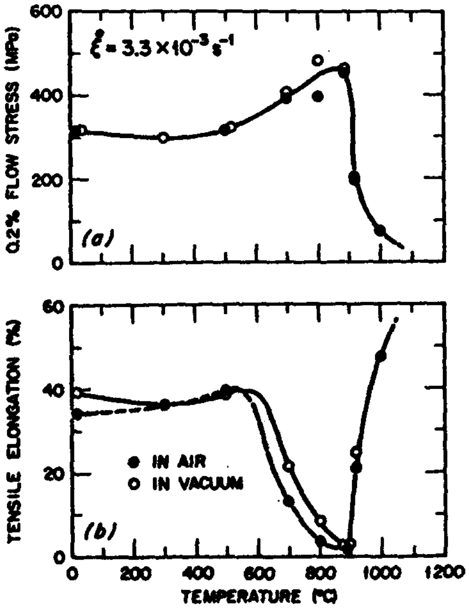

Figure 10: Temperature dependence of (*a*) the yield strength (0.2% offset) and (*b*) the tensile elongation of $(Fe_{22}Co_{78})_3V$ obtained in both air and vacuum [59].

The tensile ductility of the alloy decreases sharply at temperatures above 500°C and reaches a minimum around T_c when tested in air and vacuum [59]. The ductility in air is lower than that in vacuum in the temperature range of 500°C to T_c. The reduction in ductility is due to oxygen which penetrates and embrittles grain boundaries in the alloys. It is not clear at present that the decrease of ductility in vacuum with temperature is due to an intrinsic factor (such as increase in yield strength with temperature) or residual oxygen (extrinsic factor) existing in conventional vacuum systems, or both. The alloy exhibits a sharp increase in ductility and becomes insensitive to test environment at temperatures above T_c because of the loss of long-range order.

3.4 Other Intermetallics

The titanium aluminide Ti_3Al is prone to oxygen-induced embrittlement at elevated temperatures [64]. Iron aluminide alloys based on Fe_3Al-FeAl, on the other hand, exhibit no indication of elevated-temperature embrittlement in oxidizing environments [65], even though they show severe ambient-temperature embrittlement in moist air. The reason for the absence of elevated-temperature embrittlement in these aluminides is not well understood, but is possibly related to the lack of a substantial yield anomaly together with rapid formation of protective oxide films due to rapid diffusion in these bcc materials. Further studies are required to clarify these points.

3.5 Embrittling Mechanisms

Embrittlement at elevated temperatures is caused by a dynamic effect simultaneously involving high localized stress concentration, elevated temperature, and gaseous oxygen. Such a dynamic effect involves repeated weakening and cracking of grain boundaries as a result of oxygen absorption and penetration at crack tips. Based on a detailed study of crack growth in Ni_3Al alloys tested in oxidizing environments, a fracture mechanism of stress-assisted grain-boundary oxygen penetration has been suggested by Hippsley and Devan [30] to explain the elevated temperature embrittlement (Fig. 11). This model consists of four sequential steps: (i) occurrence of surface cracks at the initial stage of deformation, (ii) chemisorption of gaseous oxygen to the crack tips where a high localized stress field is involved, (iii) oxygen penetration in its atomic form to the stress field ahead of tips, and (iv) inward development of surface cracks preferentially along the grain boundaries, leaving some secondary cracks. Steps (ii) to (iv) proceed continuously and repeatedly during deformation, leading to premature fracture and severe loss in ductility at elevated temperatures in oxidizing environments.

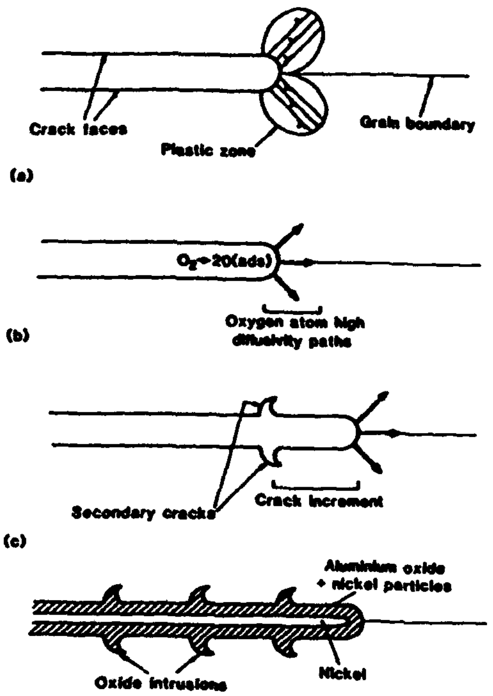

Figure 11: Schematic illustration of steps in the proposed fracture mechanism of dynamic embrittlement at elevated temperatures [30]

4. Alleviation of Environmental Embrittlement

Environmental embrittlement has been identified as a main cause of the low ductility and brittle fracture in many ordered intermetallics. This problem has to be solved satisfactorily if intermetallic alloys are to be used as engineering materials. Despite their different embrittling agents, ambient-temperature and elevated-temperature embrittlements can be treated together because both involve surface reactions and are sensitive to localized stress concentrations. Results generated to date indicate that the embrittlements can be alleviated or reduced by (i) control of surface conditions, (ii) control of grain size and shape, and (iii) alloy additions.

4.1 Control of Surface Conditions

Control of surface conditions is a simple way to alleviate environmental degradation involving surface reactions. In several cases, preoxidation and formation of protective oxide scales were proven to be beneficial in reducing environmental embrittlement at ambient and elevated temperatures. Preoxidation at 1000°C effectively reduces ambient-temperature embrittlement in boron-doped Ni_3Al charged with hydrogen [45].

Formation of protective oxide scales increases the tensile ductility of FeAl and Fe_3Al alloys in air at ambient-temperatures and the ductility of boron-doped Ni_3Al alloys at elevated temperatures [26]. Unfortunately, the oxide films crack after stretching a few percent, and their protective effect disappears. Surface coatings also should be useful in protecting underlying alloys from hydrogen or oxygen penetration along grain boundaries or bulk material; however, this effect has not yet been well demonstrated.

4.2 Control of Grain Size and Shape

Columnar grained structures have proven to be effective in increasing the ductility of Ni_3Al alloys tested in moist air at room and elevated temperatures. Liu and Oliver [66] first reported that the tensile elongation of cast hypostoichiometric Ni_3Al (24 at. % Al) increased from 1.2 to 14.1% with a change in grain shape from equiaxed to columnar. In this case, the columnar grain structure with a strong <100> texture was produced by a directional levitation zone remelting technique. The beneficial effect of the columnar grain structure tested in the direction parallel to the growth direction is attributed to minimizing the normal stress across the boundaries and thus reducing nucleation and propagation of cracks along the boundaries. Recently, even higher tensile ductilities were reported for stoichiometric and hyperstoichiometric Ni_3Al alloys with a columnar grain structure with a <100> + <111> or <110> + <111> texture [67]. For instance, a tensile ductility of >100% has been obtained in stoichoimetric Ni_3Al tested in the direction parallel to the growth direction. Surprisingly, the same material tested perpendicular to the growth direction also showed a high ductility (28 to 31%) and transgranular fracture. A detailed analysis of grain-boundary chemistry and character (e.g., low angle vs. random boundaries) as well as the influence of environment on different boundary types is required to fully understand these interesting results.

The role of grain size seems to be the same whether alloys fracture intergranularly (e.g., Ni_3Al) or transgranularly (e.g., Fe_3Al and FeAl) [11, 68]. As in the case of structural steels, refining grain size tends to reduce susceptibility to embrittlement.

4.3 Alloy Additions

Considerable effort has been devoted to alleviating environmental embrittlement by alloying additions in intermetallic alloys. The most prominent case involves Co_3Ti containing 23 at. % Ti. As shown in Fig. 12, the elements V, Ta, Cr, Mo, W, and Ge at a level of 3 at. % have no beneficial effects on moisture-induced embrittlement in air at room temperature, whereas the elements Fe and Al completely eliminate the moisture-induced embrittlement in air [18,15]. It has been suggested that iron may create a more homogeneous electron distribution at grain boundaries; however, there is no direct evidence to support this hypothesis.

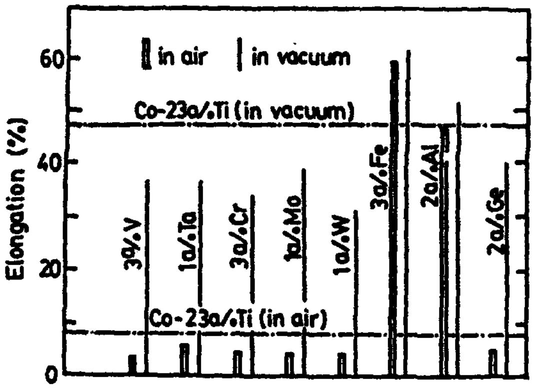

Figure 12: Effect of alloy addition on room-temperature tensile elongation of Co_3Ti(23 at. % Ti) tested in air and vacuum [15, 18].

Boron has been found to be effective in reducing moisture-induced embrittlement of grain boundaries in certain $L1_2$ intermetallics. As shown in Table 3, boron-free Ni_3Si and Ni_3(Si,Ti) are prone to environmental embrittlement, whereas boron-doped Ni_3(Si,Ti) is insensitive to test environment at room temperature [34, 35]. This result clearly indicates that boron is very effective in alleviating ambient-temperature embrittlement in Ni_3(Si,Ti). Carbon-doped Ni_3(Si,Ti) also exhibits high ductility, independent of test environment. Boron and carbon are known to segregate strongly to grain boundaries in Ni_3(Si,Ti), and their beneficial effect has been suggested to arise from slower hydrogen diffusion through reduction in site occupation by hydrogen at the boundaries. Boron, on the other hand, does not alleviate embrittlement in Co_3Ti [13], possibly because there is no strong segregation of boron to grain boundaries. Note that boron eliminates environmental embrittlement of Ni_3Al in moist air [69], but it does not prevent embrittlement induced by hydrogen charging in Ni_3Al alloys [16, 17].

Fe_3Al and FeAl exhibit severe embrittlement when tested in moist air at ambient temperatures. Recent efforts on alloy design show that the ductility of Fe_3Al in air can be substantially improved by increasing the aluminum concentration from 25 to 28% and by an addition of chromium to a level of 2 to 6% [69-72]. The increase in aluminum concentration sharply lowers the yield strength of the aluminide. The chromium additions double the tensile ductility when there are oxide scales formed on specimen surfaces during hot rolling or subsequent heat treatment in air. Refinement of grain structure and control of the degree of recrystallization are effective in improving the ductility of Fe_3Al and FeAl alloys tested at room temperature in moist air. Also, avoidance of water lubrication during machining of FeAl alloys has been shown to prevent surface cracking during fabrication [73].

A systematic study of alloying additions on the tensile ductility of Ni_3Al shows that no element, except chromium, significantly alleviates elevated-temperature embrittlement in air [32]. Alloying Ni_3Al+B with 8% Cr is effective in alleviating oxygen embrittlement at elevated temperatures (Fig. 13). The chromium addition increases the minimum ductility of Ni_3Al and Ni_3Al+Fe alloys at 700°C from 6% to above 20%. Chromium is also effective in reducing elevated-temperature embrittlement in Ni_3Si alloys [61]. Cyclic loading tests indicate that chromium additions improve the fatigue resistance of Ni_3Al alloys tested in air at elevated temperatures [74]. The beneficial effect of chromium is related to the rapid formation of protective chromium oxide films that reduce the penetration of oxygen into Ni_3Al grain boundaries.

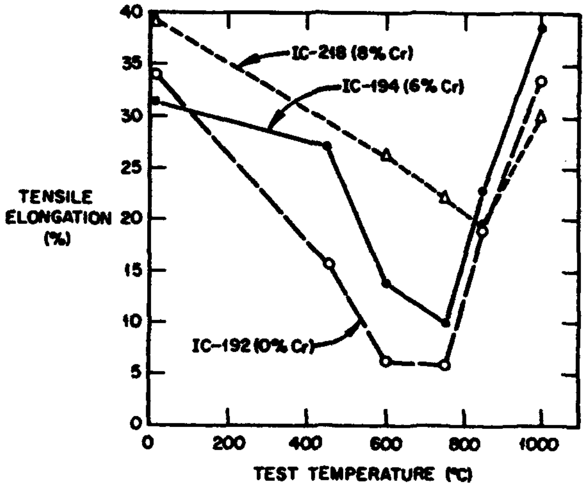

Figure 13: Effect of chromium on elevated temperature ductility of Ni_3Al [32].

Acknowledgments

This research was supported by the Division of Materials Science, United States Department of Energy under contract DE-AC05-84OR2100 with Martin Marietta Energy Systems, Inc. Thanks are due to Patty Boyd for manuscript preparation.

References

1. Liu, C. T. and Stiegler, J. O., *Science*, **226**, 636, (1984).
2. *High-Temperature Ordered Intermetallic Alloys, Vol. 39,* Proc. Mat. Res. Soc. Symp., ed. C. C. Koch, C. T. Liu, and N. S. Stoloff, in Materials Research Society, Pittsburgh, PA (1985).
3. *High-Temperature Ordered Intermetallic Alloys II, Vol. 81,* Proc. Mat. Res. Soc. Symp., ed. N. S. Stoloff, C. C. Koch, C. T. Liu, and O. Izumi, Materials Research Society, Pittsburgh, PA (1987).
4. *High-Temperature Ordered Intermetallic Alloys III, Vol. 133,* Proc. Mat. Res. Soc.Symp., ed. C. T. Liu, A. I. Taub, N. S. Stoloff, and C. C. Koch, Materials Research Society, Pittsburgh, PA (1989).
5. *High-Temperature Aluminides and Intermetallic,* Proc. TMS/ASM Symp., ed. S. H. Whang, C. T. Liu, D. P. Pope, and J. O. Stiegler, TMS Publication, Warrendale, PA (1990).
6. *High-Temperature Ordered Intermetallic Alloys IV, Vol. 213,* Proc. Mat. Res. Soc, Symp., ed. L. Johnson, D. P. Pope, and J. O. Stiegler, Materials Research Society, Pittsburgh, PA (1991).
7. Liu, C. T., Stiegler, J. O., and Froes, F. H, "Ordered Intermetallics", pp. 913-42 in *ASM Handbook, Vol. 2,* 10th Edition, ASM International Publication, Metals Park, OH (1990).
8. Liu, C. T. and McKamey, C. G., pp. 133-51 in ref. 5.
9. Liu, C. T., Lee, E. H., and McKamey, C. G., *Scr. Metall.* 23: 875 (1989).
10. Liu, C. T. and McKamey, C. G., and Lee, E. H., *Scr. Metall.* 24: 385-90 (1990).
11. Liu, C. T. and George, E. P., *Scr. Metall.* 24: 1285-90 (1990).
12. Liu, C. T. and George, E. P., pp. 527-32 in ref. 6 (1991).
13. Takasugi, T. and Izumi, O., *Acta Metall.* 34: 607 (1986).
14. Masahashi, N., Takasugi, T., and Izumi, O., *Metall. Trans.* 19A: 353 (1988).
15. Izumi, O. and Takasugi, T., *J. Mater. Res.* 3: 426 (1988).
16. Kuruvilla, A. K., Ashok, S., and Stoloff, N. S., p. 629 in *Proc. Third Intl. Congress on Hydrogen in Metals,* Pergamon, Paris, Vol. 2 (1982).
17. Kuruvilla, A. K. and Stoloff, N. S., *Scr. Metall.* 19: 83 (1985).
18. Liu, Y., Takasugi, T., Izumi, O., and Yamada, T., *Acta Metall.* 37: 507-17 (1989).
19. Stoloff, N. S., *J. Met.* 40: 18 (1988).
20. Takeyama, M. and Liu, C. T., *Mater. Sci. and Eng.* A153: 538 (1992).
21. George, E. P., Liu, C. T., and Pope, D. P., *Scr. Metall.* 27: 365 (1992).
22. Liu, C. T., *Scr. Metall.* 27: 25 (1992).
23. Wan, X. J., Zhu, J. H., and Jing, K. L., *Scr. Metall.* 26: 473 (1992).

24. Nishimura, C. and Liu, C. T., *Mat. Sci. and Eng. A*, **A152:** 146 (1992).
25. Casagna, A. and Stoloff, N. S., *Scr. Metall.* **26**: 673 (1992).
26. Liu, C. T. and White, C. L., *Acta Metall.*, **35**: 643 (1987).
27. Stoloff, N. S., Fuchs, G. E., Kuruvilla, A. K., and Choe, S. J., ib(id) 3, p. 247.
28. Taub, A. I., Chang, K. -M., and Liu, C. T., *Scr. Metall.*, **20:** 1613 (1986).
29. Takasugi, T., Suenaga, H., and Izumi, O., *J. Mater. Sci.*, **26:** 1179 (1991).
30. Hippsley, C. A. and DeVan, J. H., *Acta Metall.*, **37:** 1485 (1989).
31. Takeyama, M. and Liu, C. T., *Acta Metall.*, **37**: 2681 (1989).
32. Liu, C. T. and Sikka, V. K., *J. Metals*, **38:** 19 (1986).
33. Camus, G. M., Stoloff, N. S., and Duquette, D. J., *Acta Metall.* **37**: 1497 (1989).
34. Takasugi, T., Suenaga, H., and Izumi, O., *J. Mater. Sci.* **26**: 1179 (1991).
35. Liu, C. T. and Oliver, W. C., *Scr. Metall.* **25**: 1933 (1991).
36. Nishimura, C. and Liu, C. T., *Scr. Metall.* **25**: 791-94 (1991).
37. Nishimura, C. and Liu, C. T., *Acta Metall.* **40**: 723-31 (1992).
38. Scott, J., Duquette, D. J., and Stoloff, N. S., Rensselaer Polytechnic Institute, unpublished research (1992).
39. Lynch, R. J., Heldt, L. A., and Milligan, W. W., *Scr. Metall.* **25**: 2147 (1991).
40. Ronald, T., *Summary Proc. 2nd Workshop on Hydrogen-Materials Interactions*, NASA Workshop Publ. **1004**: 137 (1988).
41. Sastry, S. M., Soboyejo, W. O., and Lederick, R. J., *Proc. 3rd Workshop on Hydrogen-Materials Interactions*, ed. H. G. Nelson, NASP Workshop Publ. 1007: 191 (1990).
42. Kane, R. J. and Chakachery, E. A., in *Environmental Effects on Advanced Materials*, eds. R. H. Jones and R. E. Ricker, TMS, Warrendale, PA, p. 35 (1992).
43. Nakamura, M., National Research Institute for Metals, Tokyo, Japan, unpublished work (1991).
44. Bukowitz, B. J., and Miller, C., *Metall. Trans.* **11A**: 1877 (1980).
45. Kuruvilla, A. K. and Stoloff, N. S., *Metall. Trans* A **16A**: 815 (1985).
46. Liu, C. T. and Takeyama, M., *Scr. Metall. Mater.*, **24**: 1583.47 (1990).
47. Stoloff, N. S., and Davis, R. G., *Progress in Mat. Sci.* **13**: 1 (1991).
48. Liu, C. T., Fu, C. L., George, E. P., and Painter, G. S., *International Journal of Iron and Steel Institute, Japan (ISIJ)*, Special Issue on Advanced High-Temperature Intermetallics, October 1991.
49. Stoloff, N. S., unpublished results, Rensselaer Polytechnic Institute (1992).
50. Thompson, A. W., in *Environmental Effects on Advanced Materials* , eds. R. H. Jones and R. E. Ricker, 21-33, TMS, Warrendale, PA (1991).

51. Gao, Ming, Boodey, J., and Wei, Robert P., in *Environmental Effects on Advanced Materials*, ed. R. H. Jones and R. E. Ricker, p. 47, TMS, Warrendale, PA (1991).
52. Fritzmeyer, L. G. and Jacinto, M. A, Hydrogen Effect on Material Behavior, TMS, Warrendale, PA, 533 (1990).
53. Kuruvilla, A. K. and Stoloff, N. S., *Scr Metall.* **19**: 83 (1985).
54. Liu, C. T., pp. 703-712 in *Proc. Intermetallic Compounds, Structure and Mechanical Properties,* (JUMIS-6), ed. O. Izumi, The Japan Institute of Metals, 1992.
55. Fu, C. L. and Painter, G. S., *J. Mater. Res.* **6**: 719-723 (1991).
56. Bond, G. M., Robertson, I. M., and Birnbaum, H. K., *Acta Metal.* **37**: 1407-13 (1989).
57. Mandziej, S., *Scr. Metall.* **25**: 213-18 (1992).
58. Li, J. C. M. and Liu, C. T., *Scr. Metall.* **27**: 1701-06 (1992).
59. Miura, S. and Liu, C. T., *Scr. Metall.* **26**: 1753-58 (1992).
60. Liu, C. T., pp. 222-37 in Micon 86, ASTM, Philadelphia, PA (1988).
61. Oliver, W. C., *High-Temperature Ordered Intermetallic Alloys III,* C. T. Liu, A. I. Taub, N. S. Stoloff, and C. C. Koch (eds.),Vol. 133, MRS, Pittsburgh, PA, p. 397 (1989).
62. Pope, D. P. and Ezz, S. S., *Int. Metall. Rev.* **29**: 136 (1984).
63. Yoo, M. H., Horton, J. A., and Liu, C. T., *Acta Metall.* **36**: 2935 (1988).
64. Balsone, S. J., *Oxidation of High-Temperature Intermetallics,* eds.T. Grobstein and J. Doychak, TMS, Pennsylvania, p. 219 (1988).
65. Baker, I. and Gaydosh, D. J., ib(id) 3, p. 315.
66. Liu, C. T. and Oliver, B. F., *J. Mater. Res.* 4: 294 (1989).
67. Hirano, T., *Scr. Metall.* **25**: 1747 (1991).
68. Gaydosh, D. J. and Nathal, M. V., *Scr. Metall.* **24**: 1281 (1990).
69. Masahashi, N., Takasugi, T., and Izumi, O., *Acta Metall.* **36**: 1823 (1988).
70. McKamey, C. G., Horton, J. A., and Liu, C. T., *J. Mater. Res.* **4**: 1156-63 (1989).
71. McKamey, C. G., Horton, J. A., and Liu, C. T., *Scr. Metall.* **22**: 1679 (1988).
72. McKamey, C. G., DeVan, J. H., Tortorelli, P. F., and Sikka, V. K., *J. Mater. Res.* **6**: 1779 (1991).
73. Ferguson, P. A. and Liu, C. T., *Scr. Metall.* **26**: 1669 (1992).
74. Matuszky, W., Camus, G., Duquette, D. J., and Stoloff, N. S., *Metall. Trans A* **21A**: 2967 (1990).

Bibliography

Camus, G. M., Stoloff, N. S., Duquette The effect of Order on Hydrogen Embrittlement of Ni_3Fe. *Acta Metall.* **37**: 1497-1501 (1989).

Hippsley, C. A., DeVan, J. H. A Study of High Temperature Crack Growth in Nickel Aluminide. *Acta Metall.* **37**: 1485-96 (1989).

Izumi, O., Takasugi, T. Mechanisms of Ductility improvement in $L1_2$ compounds. *J. Mater. Res.* **3**: 426-40 (1988).

Kuruvilla, A. K., Stoloff, N. S. Hydrogen embrittlement of Ni_3Al+B. *Scr. Metall.* **19**: 83-87 (1985).

Liu, C. T., Lee, E. H., McKamey, C. G. An environmental effect as the major cause for room temperature embrittlement in FeAl. *Scr. Metall.* **23**: 875-80 (1989).

Liu, C. T., White, C. L. Dynamic embrittlement of boron-doped Ni_3Al alloys at 600°C. *Acta Metall.* **35**: 643-49 (1987).

Liu, Y., Takasugi, T., Izumi, O., Yamada, T. The influence of hydrogen on deformation and fracture processes in Co_3Ti polycrystals and single crystals. *Acta Metall.* **37**: 507-18 (1989).

Masahashi, N., Takasugi, T., Izumi, O. Hydrogen embrittlement of pseudobinary $L1_2$-type $Ni_3(Al_{0.4}Mn_{0.6})$ intermetallic compound. *Metall. Trans. A* **19A**: 353-58 (1988).

Oliver, W. C. The development of alloys based on Ni_3Si in High temperature ordered intermetallic alloys III, MRS Proc. Vol. 133, 397-402 (1989).

Shea, M., Castagna, A., Stoloff, N. S. Hydrogen embrittlement of FeAl and Fe_3Al in high temperature ordered intermetallics IV, MRS Proc. Vol. 213, 609-16 (1991).

Stoloff, N. S. in Hydrogen effects on materials behavior ed. N. R. Moody and A. W. Thompson, TMS-AIME, Pittsburgh, PA, 483-97 (1990).

Takasugi, T., Izumi, O. Factors affecting the intergranular hydrogen embrittlement of Co_3Ti. *Acta Metall.* **34**: 607-18 (1986).

Takasugi, T., Suenaga, H., Izumi, O. Environmental effect on mechanical properties of recrystallized $L1_2$-type $Ni_3(Si,Ti)$ intermetallics, *J. Mater. Sci.* **26**: 1179-86 (1991).

Thompson, A. W. in Environmental effects on advanced materials ed. R. H. Jones and R. E .Ricker, TMS-AIME Warrendale, PA, 21-33 (1991).

Microelectronic Applications of Thin Films of $\mathrm{TiAl_3}$

D. Gupta, K. Vieregge, K. P. Rodbell, and K. N. Tu*

IBM Research Division, T. J. Watson Research Center
P. O. Box 218, Yorktown Heights, New York 10598 USA

* Present Address: Hoogovens Aluminum GmBH
Karl Spacter Strasse 10, 5400 Koblenz, Germany

Abstract

Modern microelectronic devices rely, almost exclusively, on the use of Al(Cu) thin films for interconnection metallurgy. As density of these devices increases, stringent demands are imposed on their performance where failures occur by diffusion-induced mechanisms, *notably electromigration* and hillock growths. To suppress diffusion processes of various kinds, diffusion barriers are interposed between thin film structures. A novel approach in this regard is the *in-situ* formation of diffusion barriers of the $\mathrm{TiAl_3}$ intermetallic compound which has been successfully employed in the IBM bipolar transistors and 512Kb SRAMs. The resulting devices have exceeded the electromigration performance of the earlier metallization schemes. In this article, the diffusion processes operating during the growth of the $\mathrm{TiAl_3}$ films are described. New measurements of the $^{67}\mathrm{Cu}$ radiotracer in $\mathrm{TiAl_3}$(0.5wt%Cu) polycrystalline films have been made, and are compared with the intrinsic diffusion of Ti and Al obtained earlier from the growth kinetics. Finally, the implications of the diffusion kinetics of the various atomic species involved are examined in context to the outstanding improvements achieved in the electromigration performance of the thin film package employed for interconnections in the above mentioned IBM devices.

Diffusion in Ordered Alloys
Edited by B. Fultz, R.W. Cahn, and D. Gupta
The Minerals, Metals & Materials Society, 1993

Introduction

Aluminum metallization has been the mainstay of metal-oxide-semiconductor (MOS) devices in the microelectronic industry since their inception. However in the modern devices, pure Al metallization has given way to complex structures incorporating multilevel thin films of Al alloy as conductors, diffusion barriers, stacked contact vias etc. The driving force in these complex ULSI circuits has been high density and operating speeds in the nanosecond range which have become possible coupled with high reliability against failure mechanisms such as spiking[1], electromigration and unacceptable materials reactions. Diffusion barriers are critical components of such structures as they separate Al and other metals from Si. Since diffusion processes are significantly slower in intermetallic compounds compared to their constituent metals, transition metal aluminide thin films have been studied extensively for their formation kinetics and diffusion barrier properties. These studies have been recently reviewed by Colgan[2].

Of the numerous transition metal aluminide systems investigated during the last decade, $TiAl_3$ films have shown the best properties for application in the IBM bipolar logic and array chips[3] and 512Kb SRAM[4] devices. This is due to the ease of *in-situ* formation at low temperatures in the 300-400° C range, accompanied by such needed properties as thermal stability, good adhesion, low level of stresses and defect-free planar interfaces over the entire area of the 200mm dia Si wafers currently used in the VLSI industry. In Fig.1(a and b), schematic cross sections of the IBM four-level bipolar transistor[3] and three-level 512Kb CMOS SRAM[4] are shown. During device processing, the Ti over and under the Al(Cu) metallization results in the formation of $TiAl_3$(Cu) thin film diffusion barriers. In the final product, the electromigration resistance improved by a factor of ~100 with respect to the Al(Cu) metallization[5] and current density limits could be raised to as high as 500,000A/cm^2. In the past, the electromigration lifetimes for pure Al thin film conductors have been only about 45 hours at a current density of ~10^6 A/cm^2 and at an average temperature of 86°C, and addition of 4%Cu resulted in improvements by a factor of ~70[6].

In this article, we will describe diffusion properties of the binary $TiAl_3$ and ternary $TiAl_3$(0.5wt%Cu) blanket thin films. Incorporation of Cu into $TiAl_3$ films is important to prevent chemical divergence in the multilevel metallizations during electromigration. Two kinds of measurements will be discussed: (1) The instrinsic diffusion of Ti and Al during the formation of the $TiAl_3$ films from the evaporated Ti/Al thin film couples with or without Cu which have been studied earlier by Tardy and Tu[7]. In these studies Rutherford Back Scattering(RBS) technique was employed. (2) Grain boundary diffusion studies employing ^{67}Cu radiotracer and sectioning techniques in the pre-reacted $TiAl_3$(0.5wt%Cu) films.

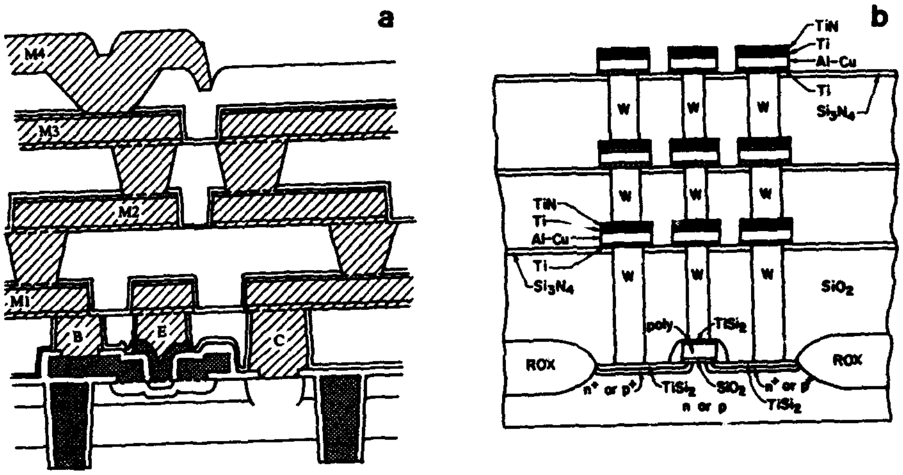

Fig. 1 Schematics of multilayer metallizations in ULSI applications, (a) IBM bipolar transistor with four-level wiring of Ti/Al(Cu)/Ti and Al(Cu) via contacts, B = base, E = emitter, C = collector (after Brown et. al Ref. 3 *IBM copyright 1992 reprinted with permission*), and (b) 512Kb SRAM with 3-level wiring of Ti/Al(Cu)/Ti and CVD W via contact (after Joshi et. al Ref.4)

Materials, Methods and Results

(a) Reaction studies in Ti/Al and Ti/Al-0.6wt.%Cu thin film couples (Intrinsic diffusion studies)

Tardy and Tu[7] have studied interdiffusion and formation of $TiAl_3$ in thin film couples of Ti/Al and Ti/Al-0.6wt%Cu. Each metal had an initial thickness of 200nm, and a temperature range of 350-500° C was investigated. The growth kinetics were measured by the RBS technique. For extraction of the intrinsic diffusion coefficients of Ti and Al from the growth data, tungsten markers were placed at the interface in the form of discontinuous films of 1nm thickness. In Fig. 2(a, b, and c) RBS spectra of the two kinds of thin film couples are shown with or without W markers. The thickness "x" of the $TiAl_3$ layer showed square-root-of-time dependence during growth from which chemical interdiffusion coefficients were computed as function of temperature:

$$x^2=4\tilde{D}_a t, \tag{1}$$

where x is the thickness of the $TiAl_3$ film formed at time t, $\tilde{D}_a$ is the chemical diffusion coefficient and t is the time for annealing. The chemical diffusivity is related to the intrinsic diffusion of Ti and Al as:

$$\bar{D}_a = D^{\beta}_{Ti}/(\beta + 1) + \beta D^{\beta}_{Al}/(\beta + 1), \qquad (2)$$

where β is the atomic ratio equal to 3 in $TiAl_3$, and D^{β}_{Ti} and D^{β}_{Al} are the intrinsic diffusion coefficients for Ti and Al, respectively in $TiAl_3$. In Fig. 2c, W marker displacements are seen clearly at 400° C for annealing periods of 30, 180 and 600 minutes. Unequal intrinsic diffusion of Ti and Al species is responsible for the marker shift. They are related as:

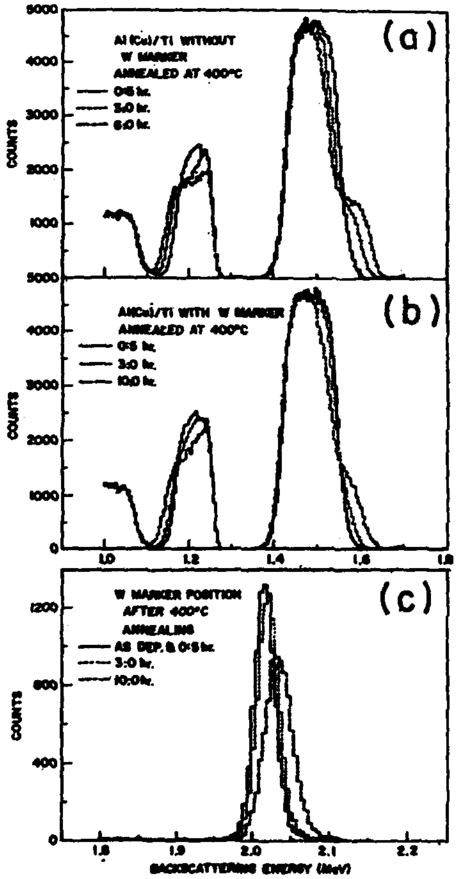

Fig. 2 Rutherford Back Scattering Spectra: (a) of Al-Ti bilayer films after several annealing periods at 400 ° C, (b) of Al/1nm W/ Ti structure where slowing of the growth of $TiAl_3$ occurred, and (c) high energy part of spectra (b) showing displacements in W peaks upon annealing at 400 ° C (Tardy and Tu Ref. 7)

$$\frac{D^{\beta}_{Ti}}{D^{\beta}_{Al}} = \beta \frac{(x_2 - x_m)}{(x_m - x_1)}, \qquad (3)$$

where x_1, x_2 and x_m are the positions of $Ti/TiAl_3$, $Al/TiAl_3$ interfaces and W marker, respectively. These positions are referred to the free surface. Tardy and Tu solved Eqs. 1, 2 and 3 and obtained values of intrinsic diffusion coefficients for the Ti and Al species in $TiAl_3$ as a function of temperature. Corrections were made for the drag effect by the W film on the reaction kintics. In Fig.3, the intrinsic diffusion coefficients for Ti and Al in the $TiAl_3$ reaction are shown with or without Cu. Addition of 0.6wt.%Cu to the $TiAl_3$ films resulted in slowing of the kinetics with the activation energy for Ti intrinsic diffusion increase from 1.68 to 2.17eV. The change in the Al intrinsic diffusion was, however, relatively small and perhaps negligible.

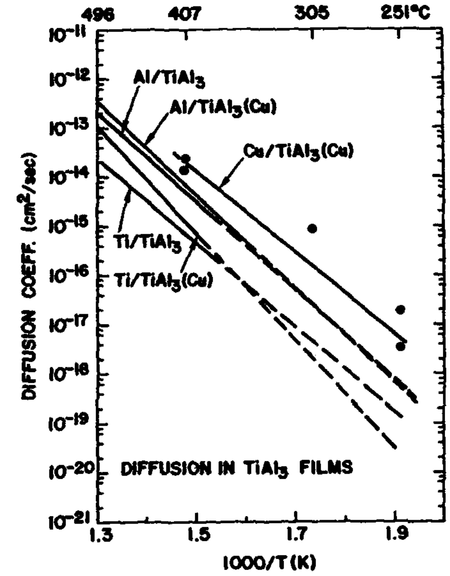

Fig. 3 Grain boundary diffusion of ^{67}Cu tracer in evaporated $TiAl_3$(0.5wt%Cu) films shown by • and compared with the intrinsic diffusion coefficients of Ti and Al obtained from the growth kinetics of $TiAl_3$ and $TiAl_3$0.6wt.%Cu films (after Tardy and Tu Ref. 7)

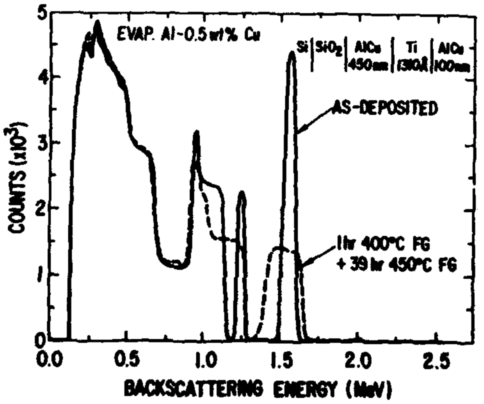

Fig. 4 Rutherford Back Scattering spectra of three-level $TiAl_3$(0.5wt%Cu) evaporated films used in ^{67}Cu tracer diffusion study. solid line — as deposited, broken line — annealed at 400 ° C for a total of 40 hours in forming gas.

(b) ^{67}Cu diffusion studies in $TiAl_3$(0.5wt%Cu) films

As mentioned earlier, spatial variation of Cu concentration in the multilevel metallization is detrimental for electromigration resistance. Hence, diffusion of Cu was studied in pre-reacted $TiAl_3$(0.5wt%Cu) films using ^{67}Cu radiotracer and serial microsectioning techniques.

For the Cu diffusion studies, three-layered evaporations were made consisting of 450nm Al(0.5wt.%Cu)/131nm Ti/100nm Al(0.5wt%Cu) films on oxidized Si wafers in a vacuum of $5x10^{-7}$ Torr at room temperature. The details of the deposition have been described earlier by Rodbell et. al [8] Following deposition, the composite films were annealed initially for 1 hour at 400° C and later for 39 hours at 450° C. Moisture free 90 $N_2/10H_2$ gas mixture was used for ambient in both cases. In Fig. 4, the RBS spectra for the as deposited and annealed $TiAl_3$(0.5wt%Cu) films are shown. The resulting films were further characterized by x-ray diffraction(XRD), selected area diffraction(SAD) and cross-section and plan-view transmission electron microscopy(TEM). In Fig. 5(a, b, and c), SAD patterns, plan-view and cross-section TEM micrographs are shown. From the SAD patterns, a dominant presence of $TiAl_3$ phase was inferred, and the extra rings were indexed for the long-period superlattice Ti_9Al_{23} phase. In the plan-view and cross-section TEM micrographs well formed columnar grains of $TiAl_3$ phase are seen which are free from the presence of a secondary phase such as $CuAl_2$ or a high density of dislocations.

The radiotracer diffusion techniques and the subsequent microprofiling of the diffused tracer into the thin film specimens have been described earlier[9] and will not be repeated here. In Fig. 6, several plots of the log of the fractional specific activity of the ^{67}Cu tracer versus the penetration distance to the power 6/5 are shown for typical diffusion measurements in the 251-407° C range. It is seen that these plots have linear regions indicating that a grain boundary diffusion process is opertive. The penetration profiles were therefore analyzed using the Whipple[10] and Suzuoka[11] asymtotic solution:

$$\delta D_b = 0.661 \left(\frac{\partial \ln C}{\partial y^{6/5}} \right)^{-5/3} \left(\frac{4D_l}{t} \right)^{1/2}, \tag{4}$$

where D_b and D_l are the grain boundary and lattice diffusion coefficients respectively, C is the specific activity of the ^{67}Cu radiotracer at distance y into the sample at time t, t is the time for diffusion and δ is the effective width of the grain boundary. To be able to extract the product δD_b, values of D_l are required at the temperatures of measurement but these data are not available for the $TiAl_3$ phase. In their absence, the activation energy Q_l for lattice diffusion was estimated from the empirical relationship $Q_l \sim 34T_m$(cal/mole), where T_m is the melting temperature of $TiAl_3$(1614K) and a value for the D_{ol} of 1 cm²/sec was assumed. Furthermore, the grain boundary width δ was assumed to be 10^{-7} cm.

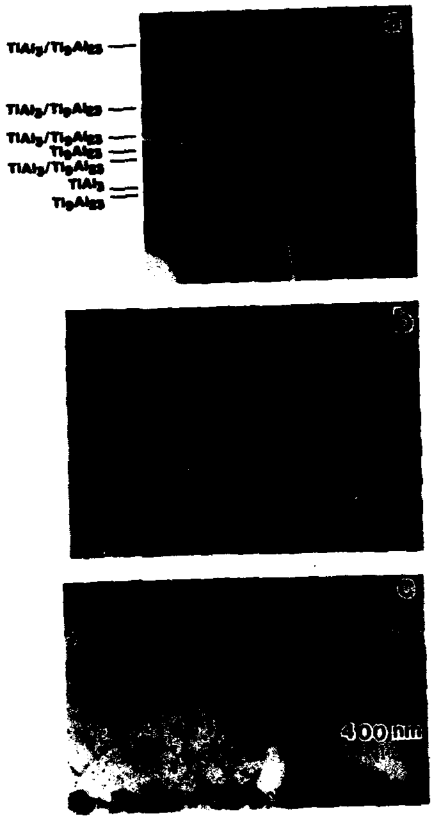

Fig. 5 Characteristics of the evaporated $TiAl_3$ (0.5wt%Cu) films grown at 400° C for at total of 40 hours in forming gas: (a) Transmission electron diffraction patterns, (b) TEM plan-view and (c) TEM cross-section. Note columnar equiaxed grains of $TiAl_3$ phase and absence of $CuAl_2(\theta)$ particles.

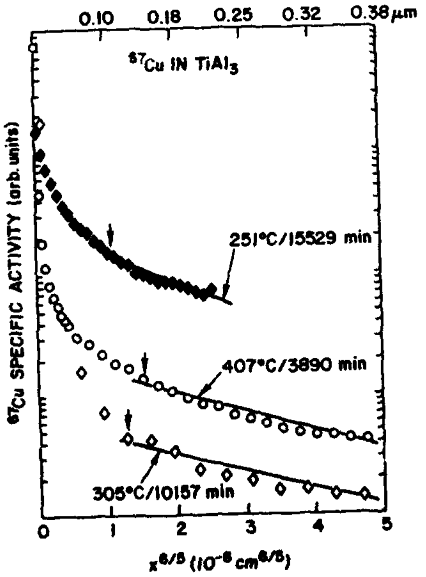

Fig. 6 Typical diffusion profiles of the ^{67}Cu tracer in $TiAl_3$(0.5wt%Cu) films. The slopes from the linear regions to the right of arrows in these plots of the specific activity versus 6/5 power of penetration distance were used in Eq. 4 for computation of δD_b values listed in Table I.

The grain boundary diffusion coefficients for Cu in the $TiAl_3$(0.5wt%Cu) films evaluated using the above procedure are listed in Table I and displayed in Fig. 3. It is seen that these data are not too different from those obtained by Tardy and Tu(7). The Cu diffusion parameters in the grain boundaries of $TiAl_3$(0.5wt%Cu) films are described by $Q_b(Cu) = 1.46eV$ and $D_{ob}(Cu) = 1.37x10^{-3}$ cm²/ sec. The parameters for intrinsic diffusion of Ti and Al in Cu-free $TiAl_3$ films measured by Tardy and Tu are $Q_{in}(Ti) = 1.68eV$, $Q_{in}(Al) = 1.81eV$, $D_{ino}(Ti) = 2x10^{-3}$ cm²/sec and $D_{ino}(Al) = 0.14$ cm²/sec respectively. The intrinsic diffusion parameters for Ti in the $TiAl_3$ films containing 0.6wt%Cu, however, changed to $Q_{in} = 2.17eV$ and $D_{ino}(Ti) = 15$ cm²/sec, while those for Al remained unaffected.

Table I. Grain Boundary Diffusion Data of ^{67}Cu Tracer in $TiAl_3$(0.5wt%Cu) Films.

T / °C	t / min	$\partial \ln c/\partial x^{6/5}$	$\sqrt{4\frac{D_l}{t}}$ *)	δD_b / cm^3s^{-1} +)	D_b / cm^2s^{-1} +)
251	15529	36346	$6.23x10^{-15}$	$2.24x10^{-24}$	$2.24x10^{-17}$
		1044332	$6.23x10^{-15}$	$3.80x10^{-25}$	$3.80x10^{-18}$
305	10157	198987	$9.20x10^{-14}$	$8.98x10^{-23}$	$8.98x10^{-16}$
407	3890	471171	$5.55x10^{-12}$	$1.27x10^{-21}$	$1.27x10^{-14}$
		332368	$5.55x10^{-12}$	$2.26x10^{-21}$	$2.26x10^{-14}$

*) assuming $Q_l = 2.46eV$ and $D_{0l} = 1cm^2s^{-1}$ using an empirical approximation.

+) $\delta = 10^{-7}cm$, $Q_b = 1.46eV$ and $\delta D_{0b} = 1.37x10^{-10} cm^3s^{-1}$.

Discussion

In this section we discuss: (a) the nature of the intrinsic (Ti and Al) and impurity (Cu) diffusion in the polycrystalline $TiAl_3$ films with or without ~0.5wt%Cu, and (b) the characteristics of the $TiAl_3$(0.5wt%Cu) films as diffusion barriers and their application for enhancement of the electromigration resistance.

(a) Intrinsic diffusion of Ti and Al and impurity diffusion of Cu in $TiAl_3$ films

Intrinsic diffusion coefficients of Al in the $TiAl_3$ films with or without Cu are higher compared to Ti(Fig.3). This difference is inherent in the diffusion mechanism in ordered alloys such as $TiAl_3$ and has been discussed by Tardy and Tu[7]. In their model, diffusion of both species was assumed to take place via a vacancy mechanism. It is to be noted in the $TiAl_3$ lattice, shown in Fig. 7, that there are three kinds of planes where the atomic arrangements of the Ti and Al atoms are distinctly different. In the basal (0 0 0) plane, Ti atoms occupy the cor-

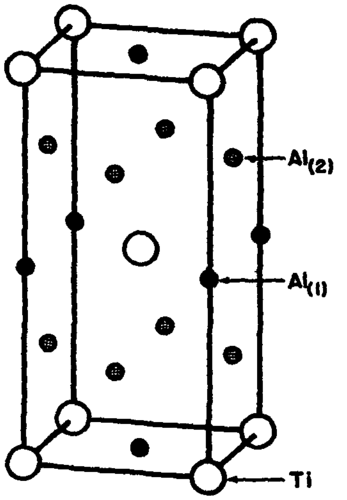

Fig. 7 TiAl$_3$ Unit cell; Tetragonal (14/mmm) a = b = 3.8537Å, c = 8.5839Å with Ti at (0 0 0), Al$_{(1)}$ at (0 0 1/2) and Al$_{(2)}$ at (0 1/2 1/4).

ners of the tetragonal cell and an Al atom resides in the face center, in the (0 0 1/2) plane the arrangement of the Ti and Al atoms is reversed, but still they remain near neighbors. These Al atoms are denoted by Al$_{(1)}$ in Fig. 7. Finally, sandwiched between these two planes is the (0 1/2 1/4) plane where only Al atoms reside, let us denote them by Al$_{(2)}$. The Al$_{(2)}$ atoms diffuse without any interference from Ti atoms but Al$_{(1)}$ atoms have to undergo highly correlated motion to preserve long range order with Ti atoms, and consequently they are substantially slower. Thus, the Al$_{(1)}$ and Al$_{(2)}$ atoms together diffuse at a much faster rate than the Ti atoms since they too must maintain long range order with Al atoms, but a plane wholly occupied by Ti atoms is lacking. Broadly speaking, in ordered lattices having unequal population of the two kinds of atoms, the majority species diffuses faster than the minority species since the latter is caged. This is sometimes known as the A$_3$B rule, and has been discussed by d'Heurle in these symposia proceedings. Also, several articles in these proceedings cover the topic of correlation effects in ordered alloys. Consequently, the diffusion mechanisms in the TiAl$_3$ lattice will not be discussed further.

In the TiAl$_3$ films containing Cu, Cu has been considered by Tardy and Tu to substitute for the Al atoms, and its diffusion also occurs by vacancies. In Fig. 3, the activation energy for Ti intrinsic diffusion is seen to be enhanced by the presence of Cu, but that for Al atoms remains unaffected. This difference has been attributed to the strong binding between Al and Ti atoms, and relatively weak binding between Al and Cu atoms. In the evaporated films, the long-period Ti$_9$Al$_{23}$ compound also forms along with the TiAl$_3$ phase. *A priori*, diffusion processes in the long-period Ti$_9$Al$_{23}$ compound are also expected to have constraints similar to the TiAl$_3$ phase since the local atomic arrangements in both remains essentially the same.

Diffusion of Cu impurity in $TiAl_3$(0.5wt%Cu) films is important because of its role in electromigration resistance which will be discussed in the following section. As mentioned in the preceding section, combined parameters δD_b were first computed according to Eq. 4 from the linear segments of the ^{67}Cu profiles shown in Fig. 6. The reduced grain boundary diffusion coefficients, after taking out the grain boundary width parameter, δ, were then obtained and are compared with the intrinsic diffusion coefficients of Ti and Al in $TiAl_3$ phase in Fig. 3. The grain boundary diffusion coefficients are seen to be, on average, an order of magnitude higher than the intrinsic diffusion of Ti and Al. This is contrary to general findings in most metals and alloys where grain boundary diffusion coefficients are typically 4-6 orders of magnitude higher than in the lattice. There are two possible explanations for this observation. (1) The intrinsic diffusion of Ti and Al in the $TiAl_3$ phase is already higher due to the presence of extra vacancies needed to balance small departures from the stoichiometry which may occur in these films. The extra vacancies have been known to elevate diffusion coefficients by several orders of magnitude in many ordered alloys such as NiAl, Ni_3Al, AuZn, AuCd[12]. Alternatively, (2) the grain boundaries in the $TiAl_3$ phase as well may be considered to have special or ordered structure so that diffusion in them would be slower compared to more open grain boundaries commonly found in other metals and alloys. It is not yet possible to single out one or the other possibilities. However, the similarity between the grain boundary diffusion and intrinsic diffusion of Ti and Al in $TiAl_3$ does have important implications in the enhanced electromigration lifetimes of the metallization structures containing $TiAl_3$ (shown in Fig. 1) and will be discussed in the following section.

(b) Diffusion barrier characteristics of $TiAl_3$(0.5wt%Cu) films and their role in enhancing of the electromigration resistance

As seen in Fig. 1, Ti films have found application in IBM bipolar transistors and 512Kb CMOS SRAMS. In the Ti-Al(Cu)-Ti sandwich structures with via contacts filled with Al(Cu), the electromigration performance exceeded the earlier Al(Cu)-Hf-Al(Cu) metallization by a factor of almost 100(5). Furthermore, they appear to have more immunity to void formation under thermal stresses. Full understanding of this remarkable gain in the electromigration performance is not yet possible. Before we discuss the diffusion data in the $TiAl_3$(0.5wt%Cu) films, we will briefly summarize the factors which may be responsible for electromigration failures.

In the older planar technology, electromigration failures occurred as a result of atomic flux divergences at the grain boundaries, notably triple points and mixed grain regions. Incorporation of 4wt% Cu to Al films was found to reduce electromigration by a complex process which involved reduction of grain boundary diffusion of Al by Cu. The Cu is readily available from the $CuAl_2(\theta)$ precipitates which acted like reservoirs(6). It is noteworthy that Cu atoms themselves electromigrate. It was later discovered that the reservoirs were not infinite and with time the supply of Cu atoms was depleted as the $CuAl_2$ phase dissolved. At that point, electromigration of Al atoms accelerated again and led to failures. In the new technology consisting of multilevel conductors with stacked via contacts shown in Fig. 1, the Al(Cu)/W interface provides an additional source of flux divergence which has been recently investigated by Hu et. al[13] They found an incubation time before degradation commenced at the atomic flux divergence site, which was correlated with the dissolution of the $CuAl_2$ precipitates and was accompanied by void formation close to the cathode and growths at the anode. Due to the unavailability of Cu atoms at the depleted sites, Al started to migrate more rapidly until another $CuAl_2$ particle was encountered which blocked the migration. It was this acceleration and retardation of the Al migration which resulted in extrusions and hillocks. The presence of W via contacts results in an interruption of the Cu supply. All the $CuAl_2$ precipitates were swept away in the Al(Cu) above the W via in 120 hours, thereby causing electromigration failures. In the case of Al(Cu) vias, which also contained the $TiAl_3$(0.5wt%Cu) films, no such problem was encountered. Obviously, continuity of the Cu migration needs to be maintained throughout the structure.

We now discuss the diffusion data in the $TiAl_3$(0.5wt%Cu) films (Fig. 3) in the context of their use as diffusion barriers and as electromigration resistant layers. The Al and Ti intrinsic diffusion in the $TiAl_3$ films with or without Cu is very slow compared to the electromigration kinetics. The activation energies for these two elements, in the 1.68-2.17eV range, are much larger than the the activation energies for electromigration in Al and Al alloys films (commonly in the 0.5 - 1.00eV range[6]). Furthermore, the activation energy for interdiffusion in Al/Cu films is 1.0eV[14]. Hence, $TiAl_3$(0.5wt%Cu) films can be considered diffusion barriers against the migration of Al atoms, contingent on the film continuity and adequate thickness. Although, $TiAl_3$(0.5wt%Cu) films may retard migration of Cu atoms compared to the Al(Cu) films, Cu migration still remains substantial compared to that in CVD W films which has been recently reported[15]. Hence it is not surprising that Al(Cu) stacked vias perform better in comparison with the W stacked vias.

The electromigration behavior of films containing $TiAl_3$ layers has been found to be superior to films which contain Ti_9Al_{23} [8]. The formation of these latter superlattice structures in the Ti - Al system results in Ti-rich unit cells, i.e. Al deficient structures. Such intermetallics tend to form large unit cells due to slight shifts in the atomic positions of the Ti and Al atoms from the symmetric positions found in the closely-related line compounds, e.g. $TiAl_3$, see Fig. 7. A larger point defect density, which more readily allows for atomic diffusion, would also be expected in Ti - Al superlattices than in $TiAl_3$ stoichiometric compounds. This would result in faster diffusion of Al through the superlattice redundant layers than through similar $TiAl_3$ layers resulting in inferior electromigration performance.

Concluding Remarks

Thin films of $TiAl_3$ intermetallic compound have been employed in the multilevel interconnection metallization of IBM bipolar transistors and 512Kb CMOS SRAMs. In these applications, significant enhancements in the electromigration performance have been reported. Implications of the diffusion kinetics of the various atomic species involved in the $TiAl_3$ phase are examined in this article.

The diffusion parameters, the activation energy and the pre-exponential factors, for intrinsic diffusion of Ti and Al[7] are: Q_{in} = 1.68ev, $D_{ino}(Ti) = 2x10^{-3}$ cm²/sec; $Q_{in}(Al)$ = 1.81eV, and $D_{ino}(Al)$ = 0.14 cm²/sec. Incorporation of 0.6wt%Cu in the $TiAl_3$ films resulted in slowing of the intrinsic diffusion of Ti and its diffusion parameters change to: $Q_{in}(Ti \rightarrow TiAl_30.6wt\%Cu)$ = 2.17eV and $D_{ino}(Ti \rightarrow TiAl_30.6wt\%Cu)$ = 15 cm²/sec.

Grain boundary diffusion of Cu in $TiAl_3$(0.5wt%Cu) films has also been measured and the parameters are: $Q_b(Cu \rightarrow TiAl_3(0.5wt\%Cu))$ = 1.46eV and $D_{ob}(Cu \rightarrow TiAl_3(0.5wt\%Cu)) = 1.37x10^{-3}$ cm²/sec. Grain boundary diffusion of Cu in $TiAl_3$(0.5wt%Cu) has been found to be unexpectedly slow and may, perhaps, be atttributed to the presence of special grain boundaries in this class of ordered intermetallic compounds.

Several factors may be responsible for the remarkable improvements in the electromigration performance of the interconnection metallization containing $TiAl_3$(0.5wt%Cu) in the devices mentioned above. Diffusion kinetics of all the constituent atomic species of the $TiAl_3$(0.5wt%Cu) metallization are slower than the electromigration kinetics reported in the pure Al or Al(Cu) alloy structures. Slower diffusion kinetics are also expected to retard electromigration damage. Along with $TiAl_3$, a long-period superlattice phase, Ti_9Al_{23}, co-exists in the evaporated $TiAl_3$(0.5wt%Cu) which contains, a high density of point defects. The $TiAl_3$(0.5wt%Cu) layers are also expected to provide redundancy for current flow when the underlying Al(Cu) conductor becomes discontinuous during electromigration.

Acknowledgements

The authors would like to thank R. Rosenberg and M. B. Small for helpful discussions.

References

1. R. Rosenberg, M. J. Sullivan and J. K. Howard, Thin Films - Interdiffusion & Reactions, Eds. J. M. Poate, K. N. Tu and J. W. Mayer, (John Wiley & Sons, 1978), 13-55.
2. E. G. Colgan, Materials Science Reports (North Holland), **5**, (1990), 1-44.
3. K. H. Brown, D. A. Grose, R. C. Lange, T. H. Ning and P. A. Totta, IBM J. Res. Develop., **36**, (1992), 821-828.
4. R. V. Joshi, S. Basavaiah, L. Hsu and M. Jaso, Adv. Met. for ULSI Applications, Eds. V. S. Rana, R. V. Joshi and Iwao Odhomari, (Conf. Proceedings ULSI-VII Materials Res. Soc., 1992), 35-47.
5. John E. Kelly and Daniel J. Fleming, ibid, 13-23.
6. F. M. d'Heurle and P. S. Ho, Thin Films - Interdiffusion & Reactions, Eds. J. M. Poate, K. N. Tu and J. W. Mayer, (John Wiley & Sons, 1978), 243- 303.
7. J. Tardy and K. N. Tu, Phys. Rev., **B32**, (1985), 2070- 2081.
8. K. P. Rodbell, P. W. DeHaven and J. D. Mis, Mat. Res. Soc. Symp., **225**, (1991), 91- 97.
9. D. Gupta, Diffusion Phenomena in Thin Films and Microelectronic Materials, Eds. D. Gupta and P. S. Ho, (Park Ridge NJ, Noyes Publications, 1988), 1-72.
10. R. T. P. Whipple, Philos. Mag., **45**, (1954), 1225.
11. T. Suzuoka, Trans. Jpn. Inst. of Metall., **2**, (1961), 25.
12. H. Bakker, Diffusion in Crystalline Solids, Eds. Graeme E. Murch and Arthur S. Nowick, (Academic Press, 1984), 189-256.
13. C-K. Hu, P. S. Ho and M. B. Small, J. Appl. Phys., **72**, (1992), 291- 293.
14. M. B. Chamberlain and S. L. Lehoczky, Thin Solid Films, **45**, (1977), 189-194.
15. D. Gupta, Encyclopedia of Appl. Phys., **5**, (VCH Pblishers Inc., 1993), 75-86.

SUBJECT INDEX

AUTHOR INDEX